Ultrafast Imaging of Molecular Processes in Small Molecules Using Coulomb Explosion Imaging

by

Benjamin Wales

A thesis
presented to the University of Waterloo
in fulfillment of the
thesis requirement for the degree of
Doctorate of Philosophy
in
Physics

Waterloo, Ontario, Canada, 2017

Examining Committee Membership

The following served on the Examining Committee for this thesis. The decision of the Examining Committee is by majority vote.

External Examiner	David Villeneuve Adjunct Professor
Supervisor	Joseph Sanderson Associate Professor
Internal Member	Kazi Rajibul Islam Assistant Professor
Internal-External Member	Marcel Nooijen Professor
Other Member	Wing-Ki Liu Adjunct Faculty

I hereby declare that I am the sole author of this thesis. This is a true copy of the thesis, including any required final revisions, as accepted by my examiners.

I understand that my thesis may be made electronically available to the public.

Abstract

Molecular structure and dynamics of three molecules (carbonyl sulfide, acetylene, and ethylene) are examined using various implementations of the Coulomb Explosion Imaging (CEI) technique. Soft x-rays from the Canadian Light Source synchrotron are used to ionize OCS doubly, triply, and quadruply. The structural changes and dynamics of the ionization processes and subsequent fragmentation processes are imaged through coincident measurements of ionic fragment momenta. Variations in these processes are explored as a function of photon energy from 90 eV to 173 eV, imaging structural changes as a result of fast (<1 fs) and slow (>1 fs) ionization processes.

Fragmentation processes in OCS^{3+} and OCS^{4+} are also examined using short, intense, infrared laser pulses of variable pulse length (7 - 500 fs) at the Advanced Laser Light Source. Here, several sequential fragmentation pathways are observed along with pulse-length dependent bond stretching and bending. The extreme case of the latter is shown to open up a new fragmentation pathway for pulse lengths greater than 200 fs.

Proton migration in both the acetylene (HC_2H) and ethylene ($H_2C_2H_2$) cations are imaged using a short pulse (32 and 40 fs) UV-IR pump-probe ionization scheme in order to access the excited cation states which lead to isomerization. For the acetylene molecule, the probe pulse removes two more electrons allowing us to map the momentum vectors of fragments in the channel $CH^+ + C^+ + H^+$ as a function of time, and thus image the isomerization from HC_2H^+ into $C_2H_2^+$. The isomer yield is shown to match theory. Similarly, isomerization of ethylene into ethylidene is imaged, measuring a peak isomerization yield at 100 fs.

Acknowledgements

I would like to acknowledge the invaluable aid provided by the expert members of our collaborators; specifically Dr. Shiromaru and Dr. Matsumoto of Tokyo Metropolitan University; Dr. MacDonald and Dr. Zuin of the Canadian Light Source; and the large team at the Advanced Laser Light Source including both Dr. Legare and Dr. Ibrahim from whom I have learned much of what is here, and much more that is not.

My supervisor, Dr. Joseph Sanderson has been a pillar of insight and leadership throughout this long campaign. He has offered me countless opportunities and advised me in directions true. My committee members, Dr. Wing-Ki Liu and Dr. Marcel Nooijen for many educational conversations and meaningful courses; Dr. Donna Strickland for answering my many optics questions; and Dr. K. Rajibul Islam and Dr. David Villeneuve for their timely commitment to review this thesis.

My colleagues, Dr. Reza Karimi for his many technical ways, his high spirits, and his many rides. Ali Ramadhan and his reliable resourcefulness. All of the undergraduate students who made working in the lab a pleasure.

My family for their tireless support, both edible and non. My friend, Chris McMahon, for his sobering views and willingness to drive eleven thousand kilometers, without which this could not be done. Sayaka Tiessen for keeping me from komakai pitfalls and encouraging dedication. My many friends at the University of Waterloo, Dr. Wesolowski, Laura Roncone, Stephanie Theis, Kier von Konigslow, Kevin Liu whose special influence has always been appreciated.

And to you, the reader.

Dedication

Dedicated to my parents, my brother, my sister, and my nephews.

Table of Contents

List of Tables

List of Figures

List of Abbreviations

ADC Analog-to-Digital Converter

ALLS Advanced Laser Light Source

AMO Atomic Molecular Optics

CAD Computer Aided Design

CE Coulomb Explosion

CEI Coulomb Explosion Imaging

CLS Canadian Light Source

COLTRIMS Cold-Target Recoil-Ion-Momentum Spectroscopy

CPA Chirped Pulse Amplification

CREI Charge Resonance Enhanced Ionization

CW Continuous Wave

DAQ Data Acquisition System

FEL Free Electron Laser

FEMPULS FEmtosecond Multi-PUlse Length Spectroscopy

FLASH Free-electron-LASer in Hamburg

HCI Highly Charged Ion

HHG High Harmonic Generation

HOMO Highest Occupied Molecular Orbital

IP Ionization Potential

IR infrared

KER Kinetic Energy Released

LCLS Linac Coherent Light Source

MBWC Modified Backgammon method with Weighted coupling Capacitors

MCP Microchannel Plate

MRMI Mass-Resolved Momentum Imaging

PES Potential Energy Surface

PIPICO Photoion-Photoion Coincidence

PSD Position Sensitive Detector

RIMS Recoil Ion Mass Spectrometer

SACLA SPring-8 Angstrom Compact free electron LAser

TDDFT Time-Dependent Density Functional Theory

TMU Tokyo Metropolitan University

TMUECRIS Tokyo Metropolitan University Electron Cyclotron Resonance Source

TOF Time Of Flight

TOFMS Time Of Flight Mass Spectrometer

UW University of Waterloo

VLS-PGM Variable Line Spacing Plane Grating Monochromator

VMI Velocity Map Imaging

VUV Vacuum Ultraviolet Light

XFEL X-Ray Free Electron Laser

XUV X-ray Ultraviolet Light

Chapter 1

Introduction

1.1 Motivation

The historic relationship between science and technology is an exchange of leadership: technology may expand on our native senses, allowing scientific inquiry to tread new grounds; or the curiosity of yet unknown realms may drive the development of investigative tools. At the intersection of physics and chemistry, this to-and-fro relationship has immensely increased our understanding of and access to the molecular world. In one hundred years, the scientific body has gone from a theory of hooks and eyes [166] and microscropic images, to comprehensive quantum mechanical descriptions of electron wave functions and Angstrom-level imaging of femtosecond processes.[1] The staggering variety of imaging tools and realms of inquiry are justified by the volume of phenomena unseen and questions unanswered.

Among this world of research is the mission to image, directly, molecular structure and its defining processes. Currently, the geometry of small molecules can be easily calculated and inferred through spectroscopic means, structures defined by molecules in electronically excited states - such as those that allow access to chemical breakup and isomerization - are significantly more difficult to capture. When we include the dimension of time for geometries that naturally evolve between nuclear states, a world of unseen behaviour opens up and along with it, a need for specialized techniques.

One of these techniques is the method of Coulomb Explosion Imaging. Popularized by Vager *et al.* [183], it provides generalized access to molecular geometry through a

[1] For a detailed history of the development leading to the field of femtochemistry, refer to Dr. Ahmed Zewail's Nobel Price lecture [200]

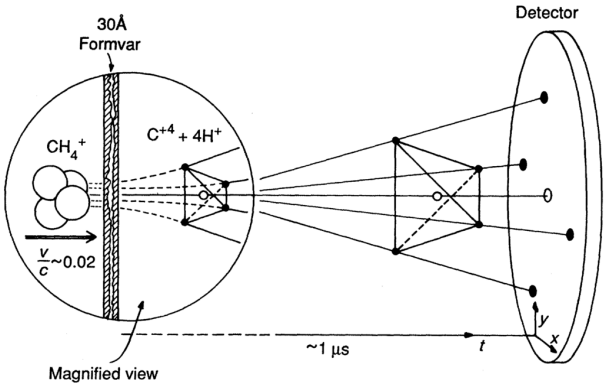

Figure 1.1: Beam-foil induced imaging of CH_4^+ stereochemical structure, demonstrating one of the earliest implementations of CEI. [183] Reprinted with permission from AAAS.

paradoxical process. Specifically, a target molecule is multiply ionized to the point that chemical bonds are replaced with purely Coulombic repulsion; the momentum imparted on the constitutent ionic fragments encode the original geometry through the definition of Coulomb's law, and so measurement of the asymptotic momentum yields a view of the initial molecular structure. Imaging of stereochemical structure with this method was first performed on H_3^+, where complete ionization into three protons was achieved by passing the ion through a thin foil at relativistic speeds [62]. Since then, increasingly sophisticated measurements of structure and structural dynamics have been realized for small molecules as the technique continues to evolve. In the forty years since the first H_3^+ structural measurement, much of the promise of CEI has not yet been realized. The work described here intends to contribute and connect elements of this growing mosaic.

1.2 Organization

The work documented in this thesis attempts to explore the extents of CEI in terms of ionization sources and targets. Since the common thread is the use of Coulomb Explosion Imaging, Chapter 2 is dedicated to an explanation of this system in general. The details of its application to specific ionization schemes are presented in the following relevant chapters.

Chapter 3 provides historical context and the theoretical frameworks for laser-initiated ionization of molecules and subsequent imaging of molecules through CEI. Similarly, Chapter 4 documents examples of single x-ray photon initiated spectroscopy, multiple ionization,

and imaging of molecular structure.

Four publications, edited for completeness, are presented in Chapters 5 through 8. Specifically, Chapter 5 follows the 2014 publication [189], examining the structural deformation of OCS under short infrared pulses (from 7 to 200 fs). By varying the pulse length of the ionization field, molecular deformation and fragmentation processes are controlled. A large addition is made in the later sections detailing the observation of a new process: single pulse control of laser-driven molecular isomerization.

Chapter 6 follows the 2016 publication [153]. Here, the OCS molecular structure is examined using x-ray ionization of various energies. Due to the novelty of this particular experiment, additions to the publication are made to expand on the results as well as details on the specific implementation of the CEI apparatus at the Canadian Light Source (CLS) synchrotron.

Chapter 7 is a largely unedited version of the 2013 publication [188]. It compares the dynamics of OCS when ionized with highly charged ions and femtosecond laser sources.

Chapter 8 follows the 2014 publication [87]. The structure of the acetylene molecule (C_2H_2) is examined in a novel UV-IR femtosecond pump-probe scheme. Proton migration is observed in the cation of acetylene, hereto unseen under UV laser initiated ionization.

Lastly, Chapter 9 documents unpublished results imaging the proton migration in ethylene (C_2H_4) under the same experimental conditions of the previous chapter. In addition, the production of the isomer moeities CH_3 and H_3 as a function of pump-probe delay is examined.

Chapter 2

Experimental Methods

An experiment using the CEI technique requires three major components: an ionization method (high flux x-rays, Highly Charged Ion (HCI), high intensity laser fields, and beam-foil stripping); a CEI apparatus; and sophisticated data acquisition and analysis. In this chapter, the details of these three components are elucidated. Since the published research associated with this work made use of three different implementations of the CEI technique, a general case is described in this chapter, while the specifics of each implementation are detailed in the relevant chapters to follow.

2.1 Principles of Coulomb Explosion Imaging

Fundamentally, molecular structures exist in their specific geometries due to the energy minimization caused by bonding electrons. In the simplest case, diatomic molecular geometry is defined by a single bond length. At stretched bond lengths, the shared electrons between atoms creates an attractive force, keeping the atoms' proximity with some energy barrier. For compressed lengths, the Coulombic repulsion from atomic nuclei overpowers the attractive inter-atomic electron density, resulting in a potential barrier of the form $E \sim 1/r$. These competing forces result in the familiar potential energy curve shown in Figure 2.1. Should the bonding electrons be removed altogether, the potential takes the complete Coulombic form following Equation 2.1.

$$E(r_{12}) = \frac{1}{4\pi\epsilon_0}\frac{q_1 q_2}{r_{12}} \tag{2.1}$$

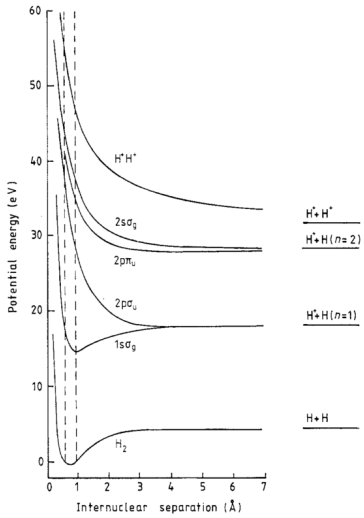

Figure 2.1: Potential energy curves for H_2, two states of H_2^+, and $H^+ + H^+$. H_2 ground state and the $1\sigma_g$ state of H_2^+ exhibit bonding potential wells. The fully ionized $H^+ + H^+$ follows the Coulomb potential. [37] Reprinted with permission from IOP.

For diatomic molecules, the entire geometry is encoded in the bond length r_{12}. If the bonding electrons for such a molecule were removed, resulting in purely Coulumbic repulsion, then the energy would provide a direct measure of r_{12}, and thus structure. Experimentally, this is a feasible task as it is relatively easy to measure the kinetic energy of ions at the electron-volt level (as is produced in this process).

For triatomic molecules, the potential energy curve becomes a potential energy volume defined by two dimensions of bond length (r_{12} and r_{23}) and one bond angle (θ_{123}). Without bonding electrons, the repulsive system is described by Equation 2.2 where charges on three constituent atoms result from missing valence electrons. The measure of total energy released for three charges q_1, q_2, and q_3 along such a volume are not unique to the initial geometry, and so energy cannot be used as a direct measure of structure.

$$E(r_{12}, r_{23}, \theta_{123}) = \frac{1}{4\pi\epsilon_0}\left(\frac{q_1 q_2}{r_{12}} + \frac{q_2 q_3}{r_{23}} + \frac{q_1 q_3}{\sqrt{r_{12}^2 + r_{23}^2 - 2r_{12}r_{23}\cos(\theta_{123})}}\right) \tag{2.2}$$

The momentum imparted on the constituent atoms provides much more information. In the case of complete triatomic breakup, momentum measures 9 degrees in real space (3 dimensions per atom). Due to momentum conservation, this space reduces to 6 degrees of

freedom. If the molecular frame is considered this space reduces to 3 degrees of freedom, matching the 3 geometric parameters defining a triatomic molecule (usually identified as two bond lengths and one bond angle). In the CEI experiment, the asymptotic momentum vectors $\vec{p_i}$ for each ion are measured in 3-dimensions. Through Equation 2.3 and the defining Coulombic force 2.4, it is possible to relate the momentum measurements to the absolute geometries defined in real space by $\{\vec{r_i}\}$.

$$\vec{p_i} = \sum_{j \neq i}^{n_{ions}} \int_0^\infty \vec{F_{i,j}}(t) dt \tag{2.3}$$

$$\vec{F_{i,j}}(t) = \frac{1}{4\pi\epsilon_0} \left(\frac{q_i q_j}{|\vec{r_i}(t) - \vec{r_j}(t)|^2} \right) \tag{2.4}$$

However, Equation 2.3 is not invertible, and, in fact, degeneracies exist where two sets of geometries $\{\vec{r_i}\}$ result in the same set of momentum vectors $\{\vec{p_i}\}$. CEI cannot therefore explicitly measure exact geometries - additional information must be added to clarify which geometry was the genesis of the measured momenta. To determine the initial geometry (or possible geometries), one of two routes are taken: simulation of momenta [180, 81], or geometry reconstruction [25, 24, 112, 17].

Beginning with a set of geometries, classical trajectory calculations are performed using well defined routines such as the Runge-Kutta method. Asymptotic momenta (Equation 2.3) are calculated in this process and compared with measured momenta; when there is agreement, the geometries are said to have been identified. It is prudent to simulate a wide scope of geometries to ensure uniqueness in this result. For many spaces, degenerate geometries can be found and argued away when their shape is extreme compared with the domain of expected geometries.

The second technique is to reconstruct the geometries for each set of measured momenta. Beginning with a set of geometries, momenta are calculated. The geometries are then manipulated in a manner that minimizes the difference between calculated and measured momenta. Again, this system can yield degenerate results and so special care should be taken to limit a false claim of reconstructed geometry.

2.2 Ionization and Electronic Excitation

CEI may be used to image molecular structure of a single state, or, through pump-probe schemes, image molecule structure as it evolves along a state, as depicted in Figure 2.2. In

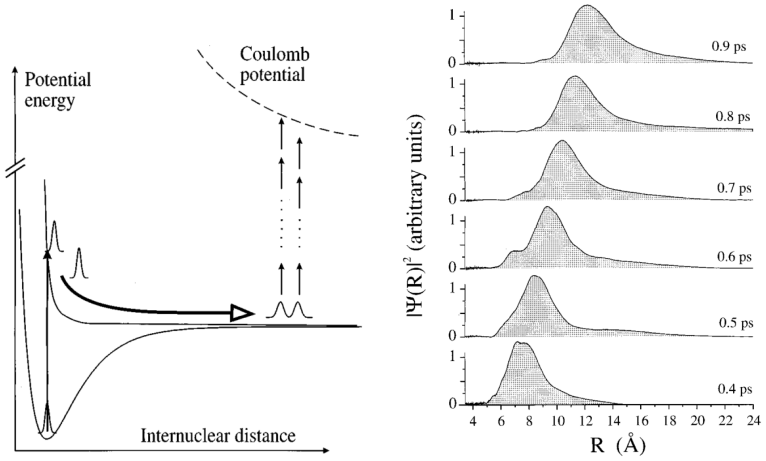

Figure 2.2: [LEFT] Pump-probe scheme imaging I_2 geometry. I_2 is excited to the dissociative curve then ionized along the Coulombic curve. [RIGHT] Measures of I_2^* bond length (converted from total kinetic energy release) at various pump-probe delays. Imaged here is the stretching of the I_2^* bond as it evolves along the repulsive curve. [173] Reprinted with permission from APS.

either case, controlled excitation and controlled ionization are required. Additionally, these excitation / ionization schemes should occur on timescales faster than nuclear dynamics (on the order of tens of femtoseconds) if high resolution imaging is desired.

These requirements are very general and as a result a number of ionization means have been employed to measure molecular structure in CEI-like experiments. Beam-foil ionization as a means to image structure first developed this field [95], inspiring the popular use of CEI [183], and continues to be a succesful ionization technique for imaging complex structures today [73]. This ionization mechanism is appropriate because multiple ionization is possible and the process occurs within a single femtosecond [183]. However, the process produces ions with a variety of electrical, rotational, and vibrational states [183], which may be unwanted for imaging of specific processes. Additionally, beam-foil experiments suffer from their high operating costs and inability to image neutral molecules. Following beam-foil initiated CEI came HCI impact as an ionization technique in molecular imaging. Similar to beam-foil ionization, such impact mechanisms occur over a relatively short period of time, result in multiple ionization, but also leave the target in a variety of states.

Another tool for ionization entered the field of structural imaging shortly after its invention: the high intensity short pulse laser. Short pulse lasers, with pulse lengths down to few femtoseconds, are ideal candidates for ionization in CEI experiments. They are highly

tunable in energy and pulse length while also produced with dependable repetition rates. They did not see use in this field, however, until the Chirped Pulse Amplification (CPA) technique was developed, allowing short pulse lasers to carry enough energy such that multiple ionization became possible [175]. As this technology developed, reliable sub 10 fs sources are available with staggering repetition rates ($\sim$100 kHz) with central frequencies from the ultraviolet into the infrared - all delivered in manageable tabletop systems. Not surprisingly, the development of this technology has lead to leaps in short pulse delivery, where attosecond pulses in the ultraviolet are being used for CEI experiments.

Finally, the use of x-rays as ionization mechanisms for CEI is intuitive due to their tune-ability, state selection, and ionization time-scale. Similar to beam-foil systems, sources of x-rays with sufficient photon flux, such as large synchrotron facilities, have natural drawbacks both economic and technological. Additionally, the process of multiple ionization via x-ray absorption is itself a collection of different schemes including direct ionization, Auger ionization, and shake-off, result in an added layer of complexity when deciphering molecular states and structure. Synchrotron sources for the requisite x-ray photon fluxes have now been out done by X-Ray Free Electron Laser (XFEL); providing all of the tune-ability of an x-ray laser but delivered in a femtosecond pulse, opening the door for x-ray pump-probe experiments.

2.3 Coulomb Explosion Imaging Apparatus

A CEI apparatus is an evolution of the Time Of Flight Mass Spectrometer (TOFMS). TOFMS are engineered to maximize the time-of-flight of ions as they travel from their origin to detection while minimizing signal broadening from initial velocity distributions. They do so by making use of extended drift chambers and sophisticated extraction fields. These systems sacrifice (indeed, purposefully reduce) measures of velocity to maximize a single measure of time of flight. A CEI apparatus simplifies a TOFMS by making use of one single homogeneous extraction field applied across the entire system volume - from the ionization center through to the detector. All cations produced at the target end of this system accelerate along predictable parabolic trajectories towards a detector. The Position Sensitive Detector (PSD) (unique to CEI), timestamps the location of each detected ion, measuring the 3-tuple (x, y, t). A schematic of the spectrometer employed in Chapter 5 is shown in Figure 2.3 and a photo of this spectrometer shown in Figure 2.4.

By time-stamping detected ions, the CEI apparatus can operate identically to a TOFMS, identifying ions through their mass-to-charge ratio via measuring their Time Of Flight

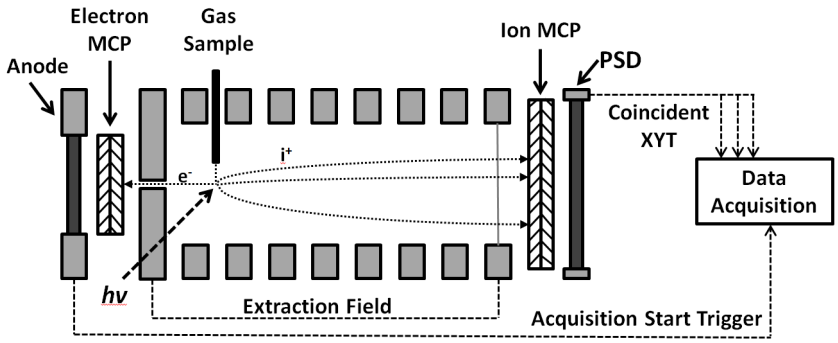

Figure 2.3: Schematic of the spectrometer implemented at CLS for X-ray initiated CEI. Photoelectrons signal an ionization event in lieu of photodetectors used in short pulse laser systems.

(TOF)[1] (an example TOF spectrum is shown in Figure 2.5). The simple field structure and geometry of the CEI apparatus define the relationship shown in Equation 2.5, where d is the distance from the ionization location to the detector, E is the extraction field, and m and q are the specific ion's mass and charge.

$$t_{0,m,q} = \sqrt{\frac{2d}{E}}\sqrt{\frac{m}{q}} \tag{2.5}$$

The expected TOF for an ionic species with zero initial momentum is referred to as the zero-time-of-flight, $t_{0,m,q}$ (signal peaks in Figure 2.5 result from ions produced with zero momentum, arriving at their characteristic TOF $t_{0,m,q}$). Similarly, the expected location for ions to be measured across the detector when produced with zero initial momentum is referred to as the zero-x and zero-y locations, (x_0, y_0). Unlike the $t_{0,m,q}$, (x_0, y_0) is the same for all ions. An ion (identified by m/q) measured with a 3-tuple (x, y, t) any different than $(x_0, y_0, t_{0,m,q})$ must have been produced with some momentum. Classical mechanics provides a straightforward calculation[2] of this momentum, shown in Equations 2.6, 2.7, and 2.8.

[1]The colloquial *time-of-flight* often refers to the true ion TOF, while TOF measurements (and often the reported spectra) have not accounted for the signal delay, resulting in systematic error. Measured TOF spectra reported in this work are uncalibrated in this manner, but calculation of other parameters such as momentum and energy are performed from calibrated TOF measurements.

[2]To make accurate measures of momentum, the 3-tuple measures (x, y, t) must be calibrated. For details of this process, refer to Appendix A.1.

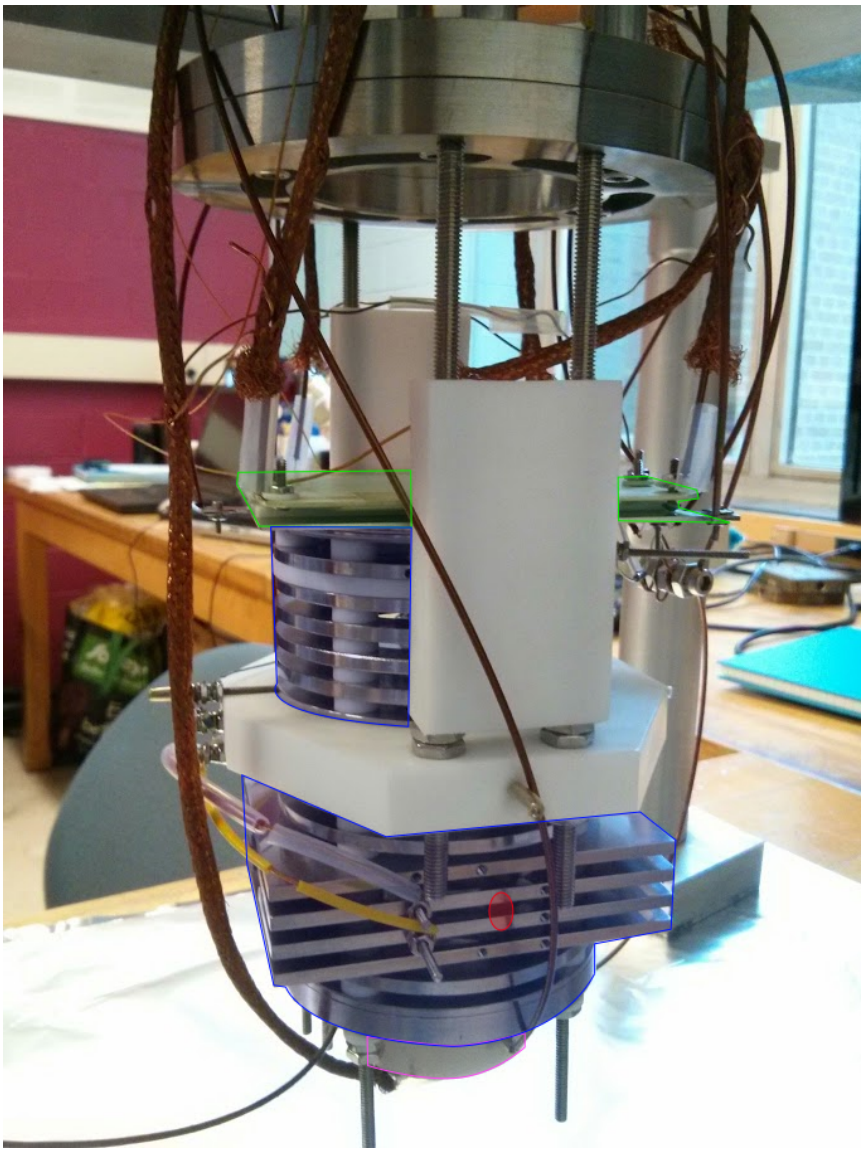

Figure 2.4: Photo of the CEI spectrometer depicted schematically in Figure 2.3 out of its high vacuum chamber. (Green) Cation PSD. (Blue) Concentric rings defining extraction field. (Red) X-ray entrance. (Pink) Electron detector.

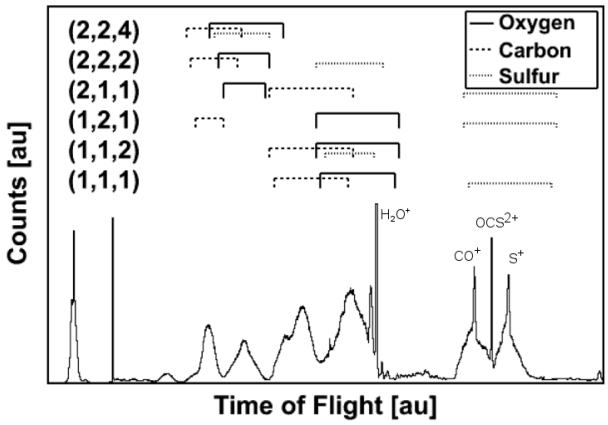

Figure 2.5: TOF of OCS and its fragments measured in a CEI experiment. Narrow peaks in the spectrum indicate ions with zero momentum (four have been labeled), while broad regions result from detecting ions with non-zero momentum. Regions in the TOF where ions are expected for triple coincidence are shown with solid, dashed, and dotted lines for O^{p+}, C^{q+}, and S^{r+} respectively (labeled as (p,q,r)). [190] Reprinted with permission from Elsevier

$$p_x = m\frac{x - x_0}{t} \tag{2.6}$$

$$p_y = m\frac{y - y_0}{t} \tag{2.7}$$

$$p_z = \frac{qE}{2}\frac{t_0^2 - t^2}{t} \tag{2.8}$$

The apparatus and calculations outlined hereto may measure the true 3D momentum of ionic fragments, but the goal is to measure $\vec{p_i}$ for *all* ions produced from a *single* molecule. Such coincidence measurements of fragment momentum put additional constraints on the CEI system. Namely, it is required that the PSD detector operate quickly in the sense that it can measure the (x, y, t) 3-tuple, transmit this information to the Data Acquisition System (DAQ), and ready itself for the following fragment due to appear on the order of tens of nanoseconds. Various types of detectors have been designed to do just that, such as the hexagonal delay line anode [88] and the Modified Backgammon method with Weighted coupling Capacitors (MBWC) [133], both of which are used in the work presented here. Naturally, the flood of data measured in such coincident experiments also requires high-speed storage infrastructure, available in high-end commercial PCs.

Measuring coincident ionic momenta on a per-molecule basis places a new demand on data analysis. Where TOFMS, Velocity Map Imaging (VMI), and the Mass-Resolved Momentum Imaging (MRMI) methods work with non-coincident measurements in one dimension, CEI requires deconvolving n-coincident measurements of 3-tuples, for each triggered acquisition, for millions of events. Therefore, successful systems making the most use of comprehensive coincidence momentum measurements require sophisticated coincidence analysis algorithms [190].

A homogeneous extraction field, fast PSD for coincident detection of the ionic 3-tuple (x, y, t), high-speed digital storage, and coincidence analysis algorithms define the basic necessities for a CEI apparatus. Details of the electrical hardware and software now follow.

2.4 Data Acquisition

The data acquisition system begins with a reliable trigger. For pulsed laser initiated ionization, the system's RF clock or a fast photodiode along the beamline can gate the DAQ with sufficient precision. For highly charged ion impact and synchrotron radiation where ionization is bunched into packets larger than the spectrometer timing precision, triggering of the DAQ is performed from the ionization directly. In these latter systems, an electron detector is added on the opposite end of the cation PSD. When an electron is detected, a signal is sent triggering the beginning of an acquisition.

From here, the DAQ awaits signals from the PSD. Depending on the type of detector, additional processing may be required to readout the 3-tuple measures of position and time (x, y, t). The DAQ records $(x, y, t)_i$ for each detected ion until a sufficient amount of time has passed. The end of acquisition for one trigger is predetermined by the expected TOF for the heaviest and slowest ions and is on the order of microseconds. The set of 3-tuples is stored, and the DAQ resets, awaiting again a trigger from the ionization system.

Ionization systems used in the research presented here have repetition rates from approximately 1 kHz up to 5 kHz, while average ionization rates often result in between one and six detected ions per trigger.[3] Total acquisition times were on the order of hours or tens of hours for each ionization setting (for example, a specified pulse length or photon

[3]The ion production rate in such Cold-Target Recoil-Ion-Momentum Spectroscopy (COLTRIMS) systems has traditionally been a limiting factor in the amount of data a single experiment may feasibly acquire, ultimately limiting the possibility of measuring rare processes with statistical significance. Systems were tuned to measure less than one event per trigger, but recent developments in analysis techniques have allowed for this limit to be surpassed [190]. As a result of these developments, increasingly rare processes can be measured with statistical significance.

energy). Therefore, each completed acquisition records on the order of 10 and 100 million ions. Where digitization is done with 2 bytes per dimension (such as with the RazorMax 16 ADCs by GaGe), each acquisition records between 10 MB and 1 GB of raw data. In the case of a MBWC type detector, each triggered acquisition records a 4 kB signal before $(x, y, t)_i$ can be deconvolved, resulting in data files upwards of 100 GB.

These staggering data sets are required in part to make statistically significant measures of rare processes and in part to compensate for an inherent challenge of detection efficiency in CEI. The inherent inefficiency of CEI results from the Microchannel Plate (MCP) at the front end of the PSD itself. The area of the MCP sensitive to ions makes up approximately 65% of the entire face, resulting in an emperical detection efficiency of approximately 58% [174]. This inefficiency is compounded by the need to detect ions in coincidence for CEI. Therefore, the likelihood of detecting all fragments in a three-body process is below 20%, and below 10% for a four-body process. Typically, a breadth of processes are available for a specific excitation / ionization scheme, where the desired phenomenon may occur with marginal probability. The large combinations of dissociative fragmentation pathways and detection possibilities demands sophisticated analysis.

2.5 Coincidence Analysis

The principle task of preliminary data analysis in CEI experiments is to first identify the detected events as specific ions and then determine which of these ions are truly coincident (that is, fragmented from the same parent ion). This is done for each triggered acquisition in succession. Ultimately, a large set of truly coincident ions is identified, labelled, and set aside for further analysis. This process is now described in detail, but first a note on nomenclature.

After ionization, molecular targets may fragment through a number of pathways. For diatomic molecules, the process $AB^{n+} \longrightarrow A^{p+} + B^{q+}$ is referred to as the (p,q) fragmentation channel. For triatomic molecules, the process $ABC^{n+} \longrightarrow A^{p+} + B^{q+} + C^{r+}$ is referred to as the (p,q,r) fragmentation channel. This nomenclature is useful for complete fragmentation, but in the case of partial breakup into larger moeities, the channel should be explicitly described as $(AB^{p+} + C^{q+})$. In any case, the fragmentation channel description is a useful label in this research because it describes the end state of the molecular process under investigation, which happens to be exactly what is detected in a CEI apparatus (that is, ions produced from a single molecule and detected in coincidence).

To begin with, events can be identified through their measured TOF, up to a degeneracy in the mass-to-charge ratio. An event recorded with the TOF of O^+ could in fact be S^{2+}

since both have the same mass-to-charge ratio ($(m/q)_{O^+} = 16/1$ and $(m/q)_{S^{2+}} = 32/2$). What's more, the momentum kick imparted to fragment ions displaces their TOF, requiring that a wide TOF window be used to identify events as specific ions. This can be seen using the coincidence map technique where a histogram plotting TOF vs. TOF is made, $\sum_j^{triggers} \mathbf{T_j T_j}'$.[4] (See, for example Figure 8.2.)

Both the TOF spectrum and the coincidence map provide averaged views of coincident ions, but they do not explicitly identify events as belonging to one channel. To do so, the technique of coincident momentum analysis is performed. For this technique, fragmentation channel is first specified, such as the (1,1,1) channel in OCS. Then each triggered acquisition is examined for the existence of coincident ions in this channel. That is, three TOF windows are defined surrounding the expected TOF of O^+, C^+, and S^+, and the raw data is parsed for triggered acquisitions with at least one detected ion in each of these three ranges. The set of triggers with ions in the (1,1,1) channel have not necessarily measured true coincidences (due to multiple molecules in the focus). To discriminate against false coincidences, the momentum of each ion is first calculated (using equations 2.6-2.8), then checked against the zero-momentum sum condition defined by Equation 2.9. Overwhelmingly, the momentum sum for true coincidences is zero and non-zero for false coincidences [190].

$$\sum_{i=1}^{n=ions} \vec{p_i} = 0 \tag{2.9}$$

Of course, thermal distributions in parent molecule momentum and limits on measurement precision require that a momentum threshold be applied to Equation 2.9 on the order of 1×10^{-23} kgm/s, or <5% of the measured ionic momenta.

Once filtered, the complete set of coincident ions make-up the measured fragmentation channel. From here, more detailed analysis follows.

[4] An improvement on this technique capable of highlighting especially rare processes is the covariance mapping method popularized for use with CEI-like experiments by Frasinski *et al.* [60]. For the purposes of identifying fragments and potential channels, the computationally less intensive coincidence map works well.

Chapter 3

Review of Laser and X-Ray Initiated Ultrafast Molecular Imaging

3.1 Low Intensity Long Pulse Interaction

The application of lasers to spectroscopy is natural given the field's photon flux, narrow line widths, and phase coherence. The arena of physics that could be investigated with this tool expanded as the field intensities increased. Non-linear photo-absorption spectroscopy, for example, is only achievable with intensities large enough to make use of χ^2. Beyond simply amplifying the field, gating the laser-field as pulses allows for time-resolved spectroscopy. The intensities and time scales required for such experiments are met in concert through the reduction of the laser pulse length, as can be seen in equations 3.1 and 3.2 where P_{peak}, E, τ, I_{peak}, and A are the peak power, pulse energy, pulse length, peak intensity and spot size respectively.

$$P_{peak} = \frac{E}{\tau} \tag{3.1}$$

$$I_{peak} = \frac{P_{peak}}{A} \tag{3.2}$$

Large intensities needed for driving increasingly exotic physical processes demand achieving diffraction limited beam waists and spot sizes. The area defined by the Gaussian beam waist is shown in equation 3.3 [176] where λ, f, w_0 are the wavelength, focal length, and

beam diameter at the focusing optic respectively. The inverse square relationship between the peak intensity and the focal length suggests the selection of short focal length optics with broad-band reflectivity to produce high intensity fields.

$$A = \pi w^2 = \frac{1}{\pi}\left(\frac{\lambda f}{w_0}\right)^2 \tag{3.3}$$

The swift development of laser technology from the invention of the optical Continuous Wave (CW) laser in 1960 [121] to nanosecond Q-switched systems in 1961 and finally picosecond mode-locked pulses in 1966, ushered in a new area of light-matter interaction, demanding parallel developments in theory explaining emerging observations.

3.2 Intense Field Ionization of Atoms and Diatomic Molecules

The story of molecular ionization by intense alternating electromagnetic fields begins with tunnelling auto-ionization in single atoms. The need for new theory developed as the threshold for strong-field intensities became comparable to the binding Coulomb field in atoms ($1 \times 10^{14}\,\mathrm{W/cm^2}$). At this point, low-order perturbation theory is no longer applicable, requiring an updated description. To begin this development, a new region was defined making use of two assumptions: the single electron approximation and a quasisatic field. The former considers only a single electron in the highest occupied orbital of the ground state.[1] The latter ensures the AC field changes slowly with respect to electron dynamics.

In low frequency domain (down to radio waves), the potential felt by the ionizing electron can be considered static with respect to the alternating field when the time required for an electron to tunnel through its perturbed barrier is less than the alternating period of the ionizing field. This frequency, Equation 3.4, is derived by Keldysh in [98] where e is the electron charge, E the applied field amplitude, m the mass of the electron, and V the ionization potential. Indeed, for the low intensity, nanosecond lasers available at the time, $\mathrm{E} = 1 \times 10^7\,\mathrm{V/cm}$ applied on a hydrogen atom with an Ionization Potential (IP) of 13.6 eV yields an upper frequency in the radio band at 1 GHz.

[1] Later work on HCl by Akagi *et al.* showed the importance of ionization from lower lying states, specifically the Highest Occupied Molecular Orbital (HOMO)-1 state [1]. They postulate that the significance of tunnelling ionization from such states plays an even greater role in molecules where the energy difference between orbitals is smaller.

$$w_t = eE/\sqrt{2mV} \tag{3.4}$$

For a given driving field with frequency w, the Keldysh parameter (eq. 3.5) is defined. It provides a soft border between the two major ionization regimes: tunnelling ionization ($\gamma \ll 1$) and multiphoton ionization ($\gamma \gg 1$).

$$\gamma = w/w_t = w\sqrt{2mV}/eE \tag{3.5}$$

Despite the contentious use of electron tunnelling time (developments on this topic continue today [202]), the Keldysh parameter remains as a jumping off point for Atomic Molecular Optics (AMO) research remaining relevant with the increase of field intensities, shrinking of pulse widths, and broadening of field frequencies laser development has seen in the following half-decade.

From Keldysh' work, ionization rates in alternating intense fields were calculated by Perelomov *et al.* for the most ideal case, the hydrogen atom [145, 44]. Then, Ammosov *et al.* published the seminal work extending field ionization predictions to include arbitrary atoms and states (categorized by principal quantum numbers $n*$ and $l*$ and charge state Z)[5]. In the relatively simple case where the effective angular quantum number $l*$ is far less than the effective principle quantum number $n*$, the following rates were derived.

$$w_{m=0} = \left(\frac{3e}{\pi}\right)^{1/2} \frac{Z^2}{n^{*4,5}} \left(\frac{4eZ^3}{\mathscr{E} n^{*4}}\right)^{2n^*-1,5} \exp\left(-\frac{2Z^3}{3n^{*3}\mathscr{E}}\right) \tag{3.6}$$

$$w_{|m|=1} = \left(\frac{3e}{\pi}\right)^{3/2} \frac{2eZ^2}{n^{*5,5}} \left(\frac{4eZ^3}{\mathscr{E} n^{*4}}\right)^{2n^*-2,5} \exp\left(-\frac{2Z^3}{3n^{*3}\mathscr{E}}\right) \tag{3.7}$$

Equations 3.6 and 3.7 compared favourably with ion detection experiments [198] on neutral, singly charged, and one doubly charged noble gases ionized with field intensities of $1 \times 10^{14}\,\mathrm{W/cm^2}$ from a CO_2 nanosecond laser ($\lambda = 9.55\,\mathrm{um}$ and $10.55\,\mathrm{um}$) [35]. This work also extended to include arbitrary orbital quantum numbers as well as arbitrary field polarizations. The theory developed for the above tunneling rates are in the quasiclassical realm, requiring that (among others) the following two conditions be met: $\hbar w \ll E$ and $\mathscr{E} \ll \mathscr{E}_{atom}$. The first condition states that the photon energy in the ionizing field ($\hbar w$) be less than the binding energy of the atom (E) where, otherwise, the direct photoelectric effect would apply. Implied by this requirement as well is that the probability is low for absorbing more than one photon, i.e. multiphoton ionization is not considered. The second

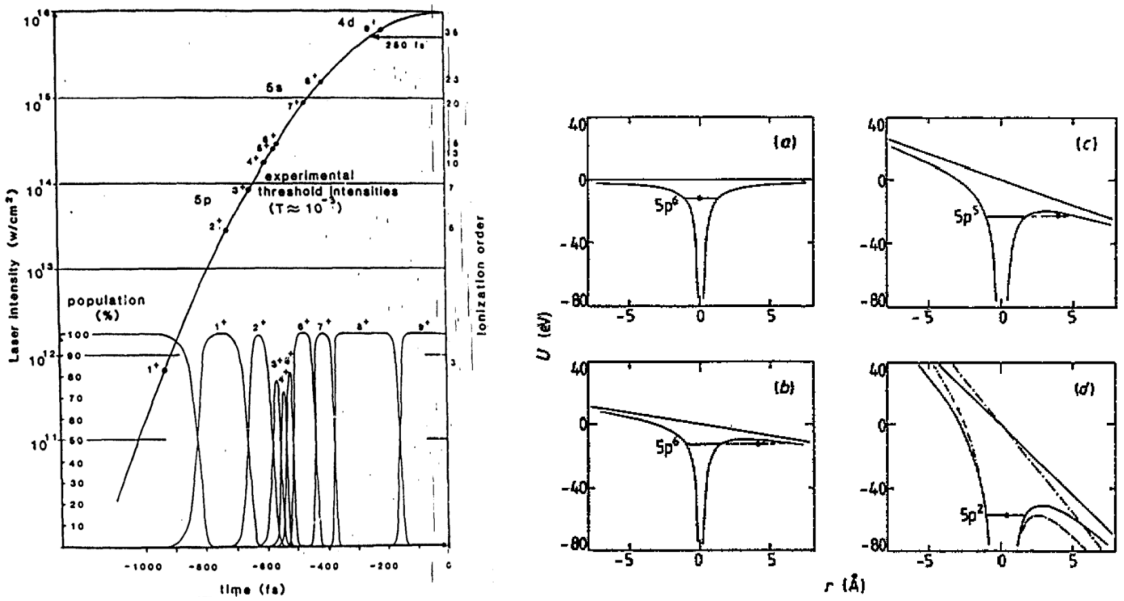

Figure 3.1: [LEFT] Calculation showing the dependence of multiphoton multiple ionization of Xe in a short intense UV field. [RIGHT] Barrier suppression followed by tunneling ionization for an atom in a long-wavelength field. Increased field strength over time explains the possibility of increased ionization states. [93] Reprinted with permission from AIP.

condition requires that the ionizing field voltage ($\mathscr{E}$) be far less than the Coulombic well voltage ($\mathscr{E}_{atom}$). Again, this ensures that direct, over the barrier ionization cannot occur. Measurements of ionization rates to support the above theory were made [9] for 1 µm intense fields, and simplification to the theory proposed in the form of barrier-suppression ionization.

At this point, laser-induced multiple ionization for short intense fields of atoms is well understood. From the multiphoton view (short wavelengths), it is a sequential process where the increasing ionization state demands an increase in absorbed photons which is met by an increasing intensity over the pulse duration [93] (See LEFT Figure 3.1). For longer wavelengths, right in Figure 3.1 depicts the mechanism for sequential ionization through tunnelling ionization resulting from laser-field induced barrier suppression.

The success of this theory found its limits when both higher laser field intensities were developed and atomic targets were replaced with molecular targets. Early experiments under these conditions galvanized laser-molecule interaction in this domain [59, 72, 37, 38, 60, 41, 108].

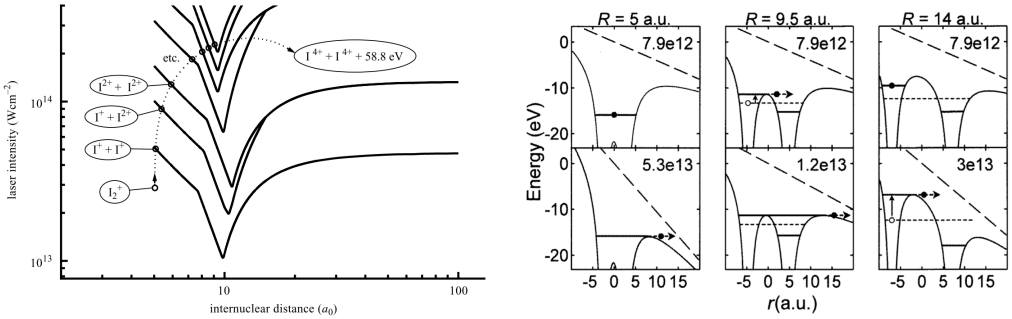

Figure 3.2: [LEFT] Appearance intensities for highly ionized states of I_2 in an intense laser field [127]. [RIGHT] Model illustrating ionization dependence on the stretched bond of a diatomic ion, highlighting the dependence of ionization on bond length. Enhanced ionization occurs at $r = 9.5$ au where less intensity is required for over the barrier ionization [149]. Reprinted with permission from The Royal Society and IOP

These relatively long pulse experiments (compared with nuclear dynamic timescale), consistently estimated molecular bond lengths much longer than neutral ground state geometries. Explanation for this came in the form of enhanced ionization wherein stretched bonds lead to increased ionization rates (depicted in Figure 3.2). Initially, the largely symmetric charge distributions of ionic fragments was explained by [23]. However, this was later corrected by [165], who emphasized the necessity for charge localization in enhanced ionization, yielding, ultimately, asymmetric fragmentation channels. The complete quantum mechanical description of enhanced ionization was publish by [203] and title Charge Resonance Enhanced Ionization (CREI), remaining relevant in today's scope of laser pulse lengths, intensities, and wavelengths. Classical interpretation of enhanced ionization models were developed by [186], and direct evidence of enhanced ionization made by [39].

Much of the molecular ionization theory is summarized in an experiment on D_2 performed by Legare *et al.* [113]. Here 8.6 fs laser pulses completely ionized D_2 - first singly ionized, then after a short period, doubly ionized. The resulting repulsive $D^+ + D^+$ were detected in a TOFMS. The kinetic energy of these fragments were measured and used as timing signature of the second ionization step. Shown left in Figure 3.3, two ionization processes, bond-softening, and enhanced ionization can be resolved with the long pulse. Again, the low energy release in the enhanced ionization process results from the second ionization step occurring long (10s of fs) after the bond has stretched to a critical bond length. If the second ionization step occurs quickly enough (< 10 fs), higher energy release can be measured due to the deuterium nuclei's proximity. Such is the cause of the new peak seen at 5.5 eV using the 8.6 fs pulse. A fourth process is resolved using linear and

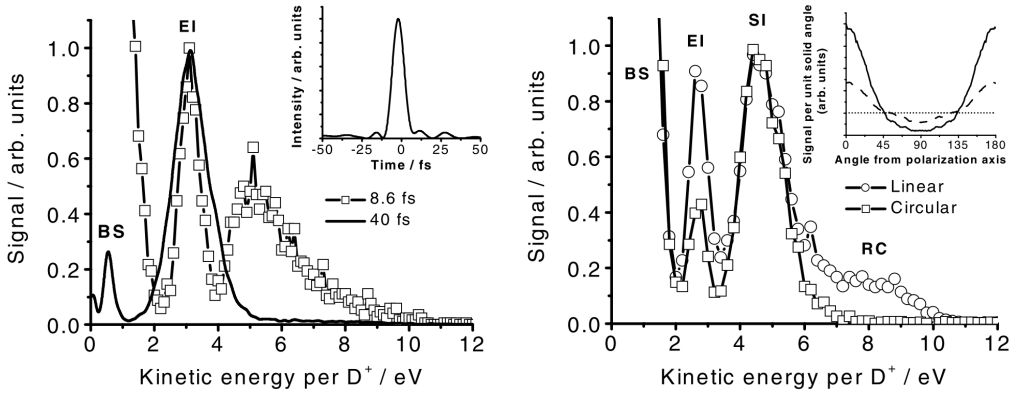

Figure 3.3: [LEFT] KER spectra for $D_2^{2+} \longrightarrow D^+ + D^+$ fragments ionized by short (8.6 fs) and long (40 fs) pulses. BS = Bond Softening; EI = Enhanced Ionization; Peak at 5 eV indicates sequential ionization. [RIGHT] KER spectra for $D_2^{2+} \longrightarrow D^+ + D^+$ fragments ionized by linear and circular polarization. Similar to spectrum at left, a fourth ionization process (RC) resulting from the first electron colliding with the second not-yet-ionized electron can be seen with linear polarization. [113] Reprinted with permission from APS.

circularly polarized ultrashort pulses (shown right in Figure 3.3). Fragments with higher energy than the identified sequential ionization result from recollision ionization - a very fast process where the first ionized electron, driven by the laser field, collides with the second electron ionizing the molecule (1 to 2 fs as seen by Niikura *et al.* [139]).

3.3 Triatomic structure and dynamics

3.3.1 Laser Initiated Ionization

In developing models for multiple ionization of small molecules, commensurate studies of molecular structure occurred. This interest in molecular structure drove the field into studying more complicated systems such as triatomic molecules, resulting in a number of studies on both electronic excitation and nuclear motion. The availability of ever shrinking pulse lengths allowed research to focus on structures nearly frozen in time. This vast field of research is now summarized as it applies to the work presented in this thesis.

Triatomic molecules provide numerous challenges both experimental and theoretical above the earlier work on diatomic molecules. On the experimental end, the planar ge-

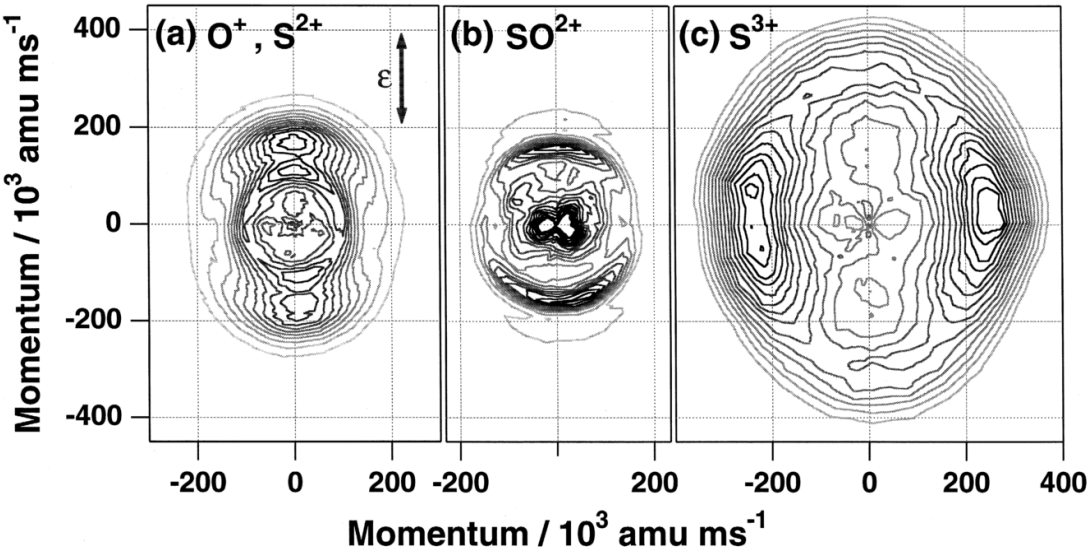

Figure 3.4: MRMI of SO_2 fragments ionized by 100 fs, 795 nm laser pulses with 5.4×10^{15} W/cm^2 intensity. [77] Reprinted with permission from Elsevier

ometry demands increased detector size with efficiencies capable of measuring a breadth of fragmentation pathways. The theoretical models need to work in a larger space, reducing the possibility of intuitive descriptions while increasing the demand for sophisticated computational techniques.

An early experiment exemplifying the improvement in experimental practices while yielding measures of triatomic fragmentation was performed by Hishikawa *et al.* on SO_2 [77]. Here, the MRMI technique is used as an extension of typical time-of-flight mass spectroscopy. The apparatus is built as a TOFMS with an aperture mask mounted in front of the cation detector, thereby only detecting ions with momentum narrowly directed along the TOF-axis. TOF spectra are measured and fragment momenta along the TOF-axis are calculated; then, the field polarization is rotated with respect the TOF-axis, resolving momentum mesaurements as a function of the angle between the fragment ion momentum and the field polarization. In [77], SO_2 was multiply ionized with a 100 fs, 795 nm laser field with an intensity of 5.4×10^{15} W/cm^2. MRMI maps are shown in Figure 3.4 for a few fragments. The magnitude of these momentum measurements confirmed that SO_2 fragments from a stretched geometry for 100 fs pulse lengths. Measuring the direction of the S^+ ion with respect to the polarization field (right-most diagram in Figure 3.4), shows that the SO_2 molecule must be extremely bent by the field during ionization. Similarly, MRMI

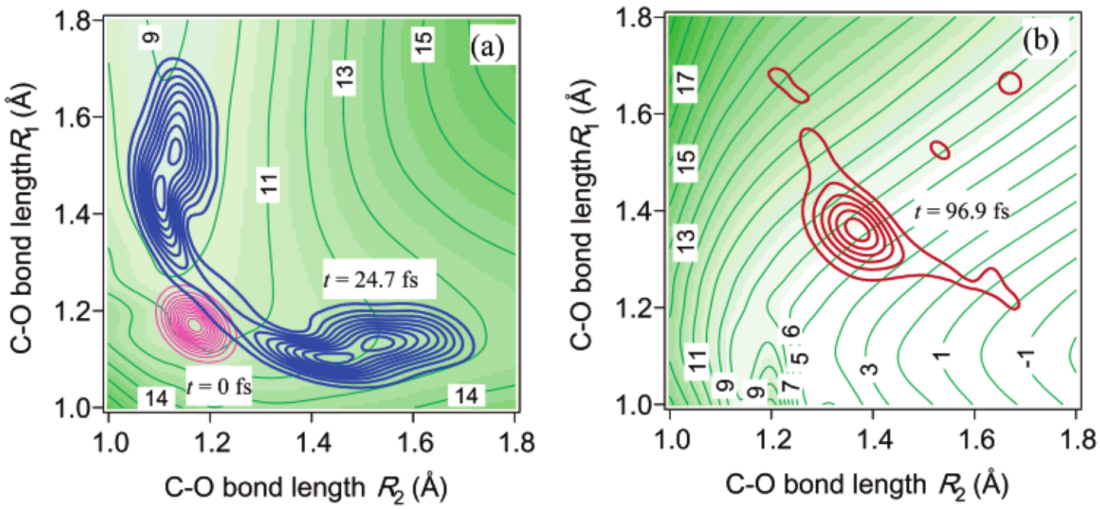

Figure 3.5: PES and nuclear wave packet calculations for CO_2^{2+}. Beginning with a vertical transition from the ground state of CO_2, the square of the wavepacket is plotted after t=0 fs (pink), t=24.7 fs (blue), and t=96.9 fs. The instantaneous adiabatic potentials are shown for t=24.7 fs [LEFT] and t=96.9 fs [RIGHT]. [163] Reprinted with permission from ACS.

work done by Sanderson *et al.* [161] with a shorter pulse (60 fs) on CO_2 measured molecular orientation in the field as well as dramatic bending. In an improved MRMI experiment, Sanderson *et al.* made measures of H_2O deformation during multiple ionization by a 50 fs 790 nm laser pulse [159]. The measures reveal significant reorientation of the molecule in the laser field and, more importantly, a linearization of the H_2O molecule. Theory explaining this bond straightening phenomeonon is given by Rottke *et al.* [154]

As with diatomic molecular multiple ionization, the nuclear dynamics of triatomic molecules is an interplay between the intense laser field, its effect on electronic states, and the resulting nuclear motion. Sato *et al.* explained characteristic bending and two-bond stretching of CO_2 using a time-depenent adiabatic state approach [163]. Snapshots of the nuclear dynamics and adiabatic potentials are shown in Figure 3.5 and 3.6. This model successful explained reported MRMI measurements of bending CO_2 molecule before fragmenting into a 3+ charge state under short pulse laser initiated ionization [78].

The first implementation of CEI on a triatomic molecule where ionization was initiated by a short pulse laser was perforemd by Hasegawa *et al.* [71]. 60 fs, 3.6×10^{14} W/cm^2 were used to doubly, triply, and quadruply ionize CS_2 molecules. Coincident momentum measuremets were made on ions in the fragmentation channel $CS_2^{3+} \longrightarrow S^+ + C^+ + S^+$

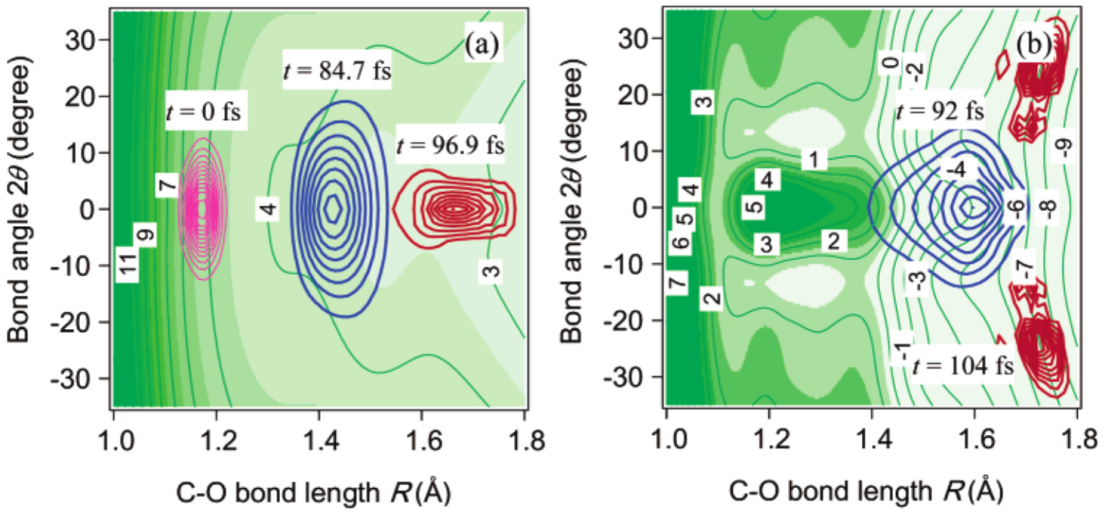

Figure 3.6: PES and nuclear wave packet calculations for CO_2^{2+}. Beginning with a vertical transition from the ground state of CO_2, the square of the wavepacket is plotted after time delays indicated by $t = x$fs. The instantaneous adiabatic potentials are shown for t=84.7 fs [LEFT] and t=92 fs [RIGHT]. [163] Reprinted with permission from ACS.

(PSD measurements of ions shown left in Figure 3.7). Reconstruction of the CS_2 molecule was performed, revealing stretched bond lengths ($R_{measured}/R_{neutral}$ = 1.6) and significant bending ((θ_{SCS} =145°). The extreme deformation occurring as a result of sequential ionization process relatively slow compared with nuclear evolution. These inaugural measurements on triatomic molecules in laser-initiated CEI were followed by similarly themed research continuing to this day.

Improving on the measurements of SO_2 by [77] and H_2O by [159], Legare *et al.* performed complete 3D momentum measurements in CEI apparatus [112] using 8 fs, 800 nm pulses. Fragment momenta in the channel $D_2O^{4+} \longrightarrow D^+ + D^+O^{2+}$ were measured, revealing a slightly stretched and bent geometry as well as expectedly low KER. To explain this pathway, step-wise simulations were performed for the D_2O. In these simulations, the molecule was singly ionized, then propagated along the resultant PES until a short period where it was again ionized, where it propagated along the dicationic curve. This was performed until the 4+ state was reached under the laser pulse duration resulting in remarkable agreement with measurements. The same experiment was performed for SO_2 looking at the $SO_2^{7+} \longrightarrow O^{2+} + S^{3+} + O^{2+}$ fragmentation channel. The increase in mass from D_2O to SO_2 suggests that the heavier molecule would not evolve quickly during ionization. However, the reduced ionization potential of SO_2 ensures that it is ionized more

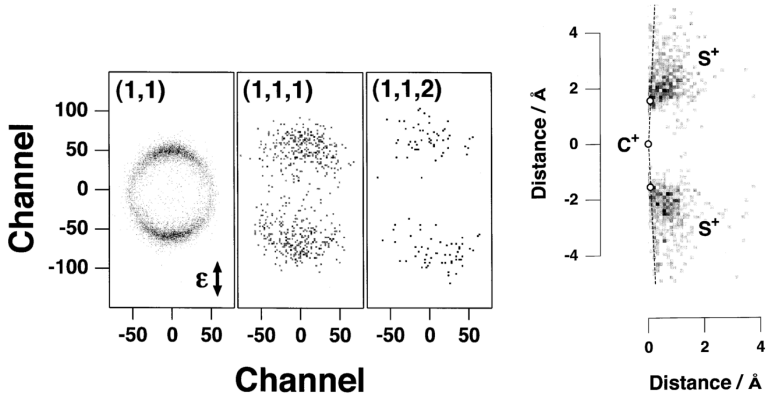

Figure 3.7: [LEFT] PSD measurements for coincident ions in the channels $CS^+ + S^+$ (1,1), $S^+ + C^+ + S^+$ (1,1,1), and $S^+ + C^+ + S^{2+}$ (1,1,2). [RIGHT] Reconstructed geometries for CS_2. [71] Reprinted with permission from Elsevier.

easily, allowing it more time to deform. These competing elements result in relatively similar fragmentation dynamics. Ultimately, the measured KER for these channels nearly matched the Coulombic values, showing that the molecules fragment from geometries much shorter than the CREI limit, and very nearly frozen in their ground state positions. The *ab initio* calculations matching initial geometries to measured momenta for D_2O and SO_2 are shown in Figure 3.8.

Comprehensive measurements of CREI were performed on CO_2 with pulse lengths from 7 fs to 200 fs [17]. Measurements were made with a CEI apparatus, acquiring full 3D momentum vectors for fragmentation channels from low charge states ($CO_2^{3+} \longrightarrow O^+ + C^+ + O^+$) up to high charge states ($CO_2^{6+} \longrightarrow O^{2+} + C^{2+} + O^{2+}$). They show that 100 fs is the time scale to initiate 4+ state CREI, and this occurs at a critical geometry with bond lengths nearly twice the ground state bound length and bent bond angle ($\theta_{OCO} \approx 163^\circ$ vs $\theta_{OCO} \approx 172^\circ$ for the ground state). Geometry reconstruction is performed (Figure 3.9), revealing the time-dependent structure of CO_2.

From this work, the technique FEmtosecond Multi-PUlse Length Spectroscopy (FEMPULS) was defined, wherein structural dynamics of molecules can be investigated through the control of the ionizing pulse length. The first formal research with this technique was performed by Karimi *et al.* [96]. This research focused on the N_2O molecule and, similar to [17], measured the time dependent CREI. Additionally, the 3D momentum measurements offered by CEI allowed for direct measurement of a sequential dissociative pathway. Specifically, the complete fragmentation of N_2O^{3+} and N_2O^{4+} through metastable formation of

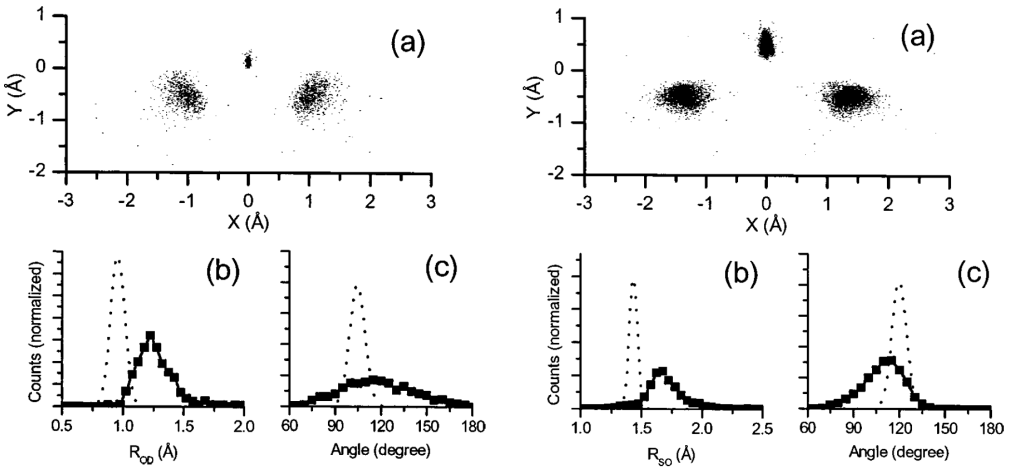

Figure 3.8: [LEFT] Reconstructed geometries of D_2O. [RIGHT] Reconstructed geometries for SO_2. [112] Reprinted with permission from APS.

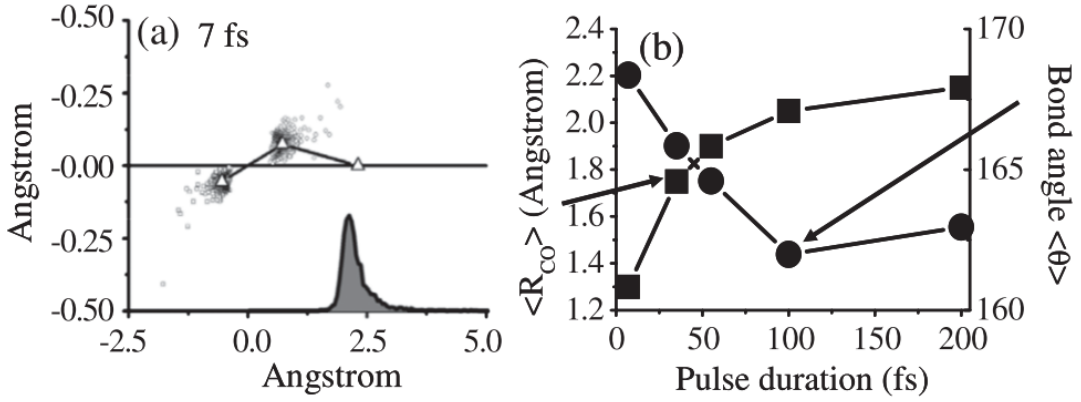

Figure 3.9: [LEFT] Reconstructed geometry of CO_2 measured in the $CO_2^{2+} \longrightarrow O^{2+} + C^{2+} + O^{2+}$ channel initiated by 7 fs pulses. [RIGHT] Bond length and bend angle dependence on pulse length. [17] Reprinted with permission from APS.

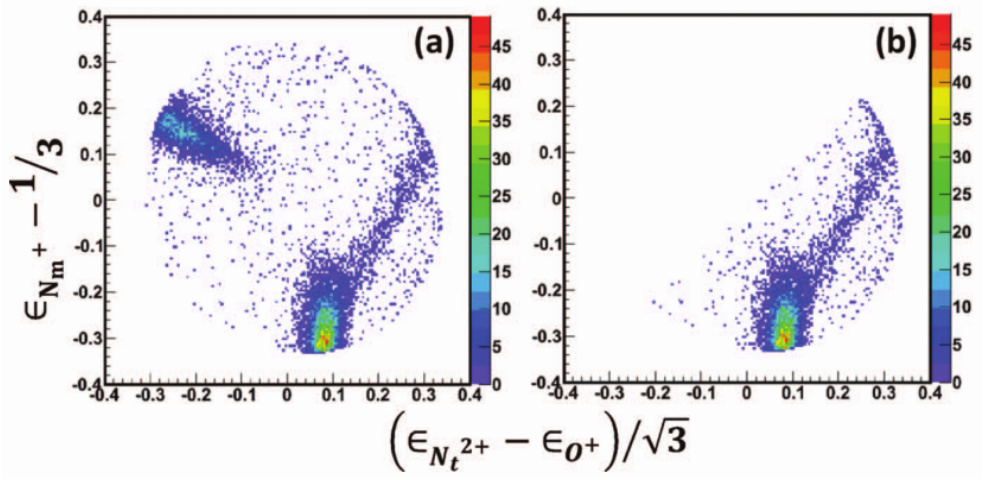

Figure 3.10: [LEFT] Dalitz plot visualizing the channel $N_2O^{4+} \longrightarrow N^{2+} + N^+ + O^+$. [RIGHT] same as [LEFT] but with a filter removing misidentified events. [RIGHT] The central node indicates concerted 3-body breakup; diagonal signal indicates breakup through the channel $N_2O^{4+} \longrightarrow N^{2+} + NO^{2+*} \longrightarrow N^{2+} + N^+ + O^+$ with the rotating metastable ion NO^{2+*} [96] Reprinted with permission from AIP.

rotating moeties NO^{2+} and N_2^{2+} (shown in Figure 3.10).

3.3.2 X-Ray Initiated Ionization

The mulitple ionization of molecules over short time scales can also be achieved with x-rays, where the demand for photon flux is met by increasingly brilliant synchrotron facilities such as the MAX-lab in Lund, Sweden, Indus-1 in Indore, India, the CLS in Saskatoon, Canada, and others. Although the process of single-photon absorption is considered instantaneous with respect to nuclear motion, subsequent multiple ionization (through either direct or Auger processes) can occur over a large enough window for the nuclei to evolve along new PES. This gives rise to the opportunity to measure molecular structure on an ultrashort timescale.

Imaging of x-ray initiated nuclear dynamics of carbonyl sulfide (OCS) were performed by Laksman *et al.* using a momentimg imaging TOFMS [106]. Coincident momentum measurements of fragments resulting from OCS^{2+} and OCS^{3+} fragmentation were performed by ionizing OCS through excitation at $C1s \rightarrow \pi^*$, $C1s \rightarrow \sigma^*$, and off-resonance transitions (using incident photon energies of 288.2 eV, 311.5 eV, and 286 eV respectively). The effect

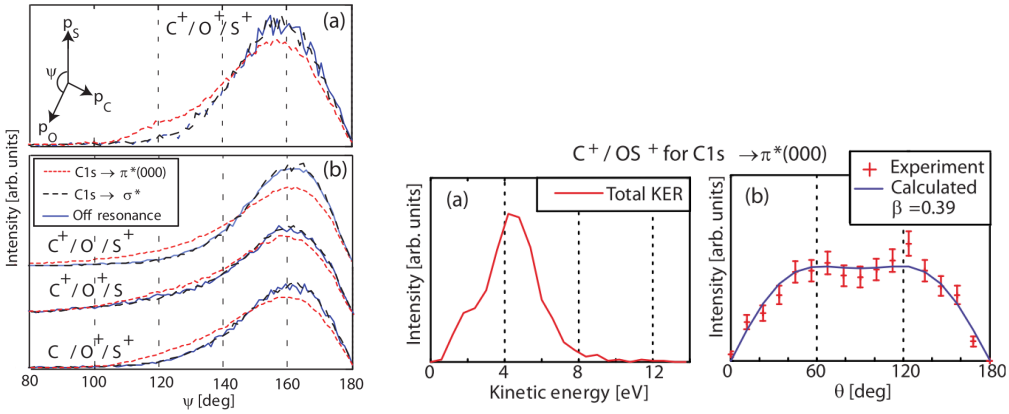

Figure 3.11: [LEFT] Angle distributions between terminal momentum vectors for several channels ionized at two resonance and one off resonance. [RIGHT] KER distributions for the $OS^+ + C^+$ channel when excited at the $C1s \rightarrow \pi^*$ resonance. [106] Reprinted with permission from AIP.

on molecular structure can be seen left in Figure 3.11 by examining the angle ψ between the momentum vectors $\vec{p_S}$ and $\vec{p_O}$. The increase in signal at lower angles show bending of the OCS molecule when excited through $C1s \rightarrow \pi^*$ compared with off-resonance transition and the near-resonance transition, $C1s \rightarrow \sigma^*$. Additionally, the authors observe isomerization of OCS through the measurement of the OS^+ fragment when excited at the $C1s \rightarrow \pi^*$ resonance (shown right in Figure 3.11).

In a similar experiment, both the OCS fragment KER and photoelectron energy were measured by Saha *et al.* at the Indus-1 synchrotron [156]. Tuning the x-ray energy to 172 eV (the sulfur $2p_{1/2}$ threshold in OCS), the photoelectron energy was measured giving rise to the Auger spectrum shown left in Figure 3.12. The Recoil Ion Mass Spectrometer (RIMS) was then triggered at select Auger electron energies, giving rise to KER measurements through specific states shown right in Figure 3.12.

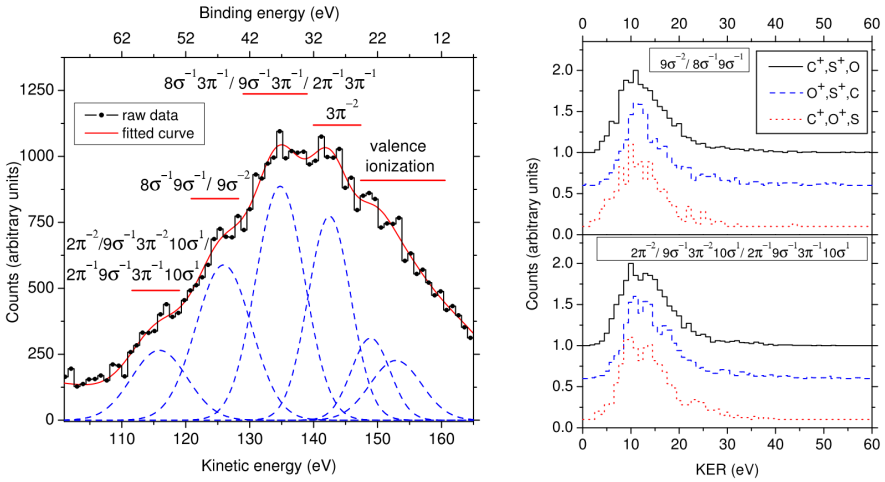

Figure 3.12: [LEFT] Photoelectron energy from ionizing OCS with 172 eV photons, measured with a cylindrical mirror analyser. [RIGHT] KER distributions for triple fragmentation, state selected by the photoelectrons detected left. [156] Reprinted with permission from IOP.

3.4 Pump-Probe Imaging

3.4.1 IR and UV Tabletop Systems

The increased availability of table-top high intensity laser sources has led to more sophisticated ionization schemes. The first ultrafast pump-probe scheme implemented for CEI was done by Legare *et al.* [111]. Beginning with 8 fs IR pulses generated through a hollow-core fiber (same as those in [112])[2], the beam was split into a pump and probe arm by passing the whole beam front through a donut-shaped piece of fused silica. Inside the donut sat a separate piece of fused silica. By rotating the inner silica with respect to the outer silica, an optical path difference was created, allowing the inner beam to be delayed with respect to the outer beam. Focusing this piece-wise beam as usual with a focusing mirror resulted in a pump-probe ionization scheme with an intensity ratio of $I_{probe}/I_{pump} \approx 3.3$. Targeting D_2, the pump-pulse ionized D_2, launching a vibrational wave-packet along the $X^2\Sigma_g^+$ state. The to-and-fro vibration is then imaged using the probe pulse, resulting in the oscillatory signal in Figure 3.13. Similar to [112], the SO_2 target was considered and its geometry

[2]Although the generation of ultrashort pulses can be performed a number of ways, the hollow-core fiber technique [142], now standard in this field, is prefered due to its generation of both short and high energy pulses, allowing for intensities capable of multiple ionization

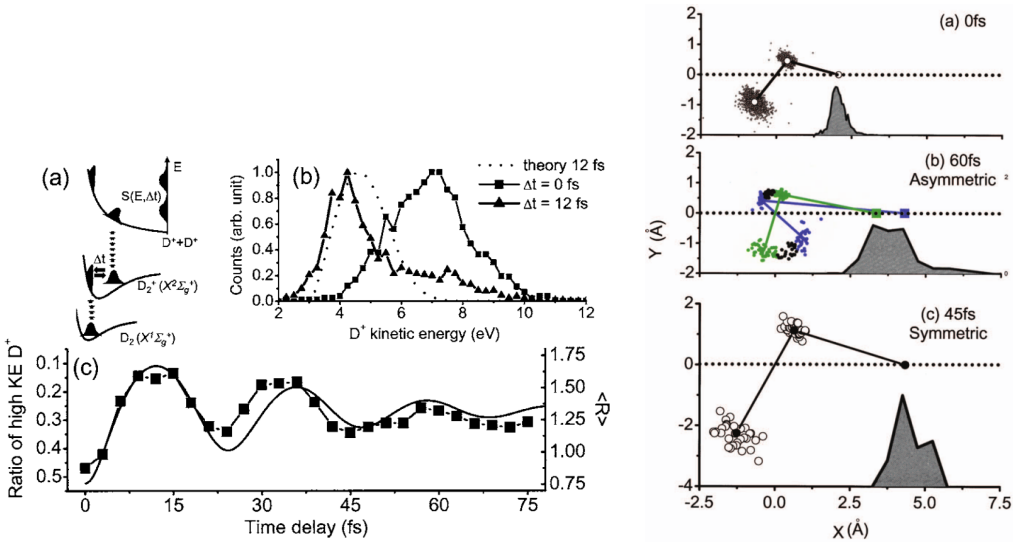

Figure 3.13: [LEFT] Imaging D_2^+ vibration oscillations with Angstrom and femtosecond resolution. [RIGHT] SO_2 stucture at three pump-probe time delays. The colour concrentrated regions indicate imaged rotational wave packets of SO_2 under asymmetric dissociation [111]. Reprinted with permission from APS.

again imaged. Using pump-probe, Figure 3.13 shows the structure of SO_2 for short and longer time delays. At 60 fs, the heavily bent geometries are seen to result from a rotational wave packet of the SO fragment, transferred during asymmetric dissociation.

Another ionization scheme, making use of commercial high intensity Titanium-Sapphire short pulse lasers, involves again splitting the beam into pump and probe arms. The pump arm, however, is passed through a gas cell initiating High Harmonic Generation (HHG), resulting in short EUV pulses in the energy range 20 - 25 eV. The result is a femtosecond level EUV-IR pump-probe ionization scheme. Tilborg *et al.* employed such a system in a CEI apparatus and targeted ethylene in order to image the isomerization of H_2CCH_2 into $HCCH_3$ [184]. Here, the EUV pump arm singly ionizes C_2H_4 where proton migration occurs, isomerizing into the assymmetric form ethylidene, $HCCH_3^+$. Then, the IR probe further ionizes, allowing the molecule to fragment along many pathways including $HCCH_3^+ \longrightarrow CH^+ + CH_3^+$. The state of isomerization at the time of the probe should then be encoded in the yield of this channel, which is a function of the pump-probe delay. They also measure the production of H_2^+, which is expected to increase when ethylene is in the ethylidene structure. The results shown in Figure 3.14 match the theory well, resolving an isomerization time of approximately 100 fs.

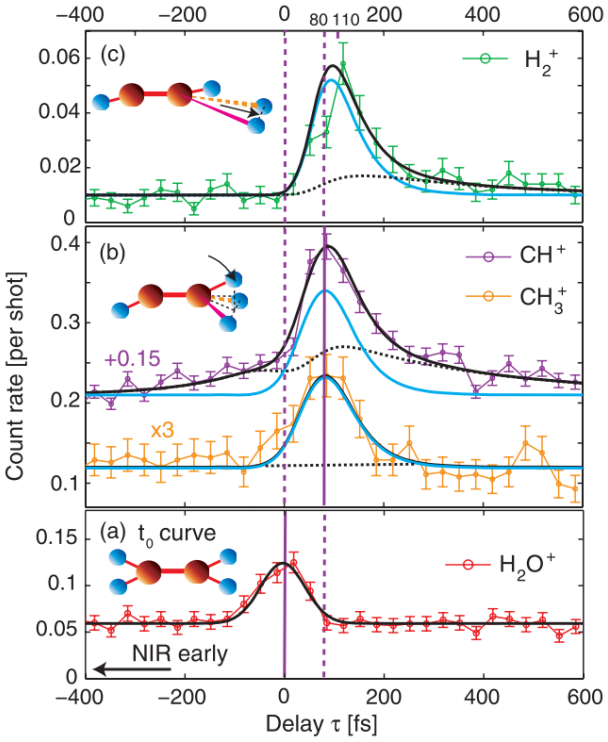

Figure 3.14: Production of various fargments from the ethylene dication measured as a function of pump-probe delay. The peaks at 100 fs confirm theory of isomerzation timescales for the ethylene cation into the ethylidene cation [184]. Reprinted with permission from IOP.

3.4.2 XUV pump-probe

In recent years, several Free Electron Laser (FEL) sources have come online (Linac Coherent Light Source (LCLS), SPring-8 Angstrom Compact free electron LAser (SACLA), Free-electron-LASer in Hamburg (FLASH), etc.), generating tunable, coherent, x-ray beams with high photon-flux delivered as short, femtosecond, pulses. Following the success of tabletop ultrashort IR and UV pump-probe schemes as mechanisms to investigate molecular dynamics, apparatuses have been developed to irradiate and image single molecule targets in an XUV pump-probe scheme. The technical challenges abound, Jiang *et al.* showcased the promise of 30 fs X-ray Ultraviolet Light (XUV) sources at FLASH with a reaction microscope outfitted with a pair of half-moon focusing mirrors[3] [90]. By translating one mirror longitudinally along the beam path, a pump-probe delay is controlled with single femtosecond resolution. In this experiment, isomerization of the acetylene cation into the vinylidene cation ($HCCH^+ \longrightarrow CCH_2^+$) is initiated through single photon absorption and probed by secondary ionization and fragmentation into 2-body 2-ion channels (dynamics process shown left in Figure 3.15). KER measurements for fragments in the $C_2H_2^{2+} \longrightarrow C^+ + CH_2^+$ channel were made in coincidence and are shown right in Figure 3.15.

[3]In addition to measuring the fragment cation momeneta, this device also measures the ejected electron momentum. By considering the ionization potential of the molecule, the measured electron energy can be used to deduce the excited state of the target molecular cation.

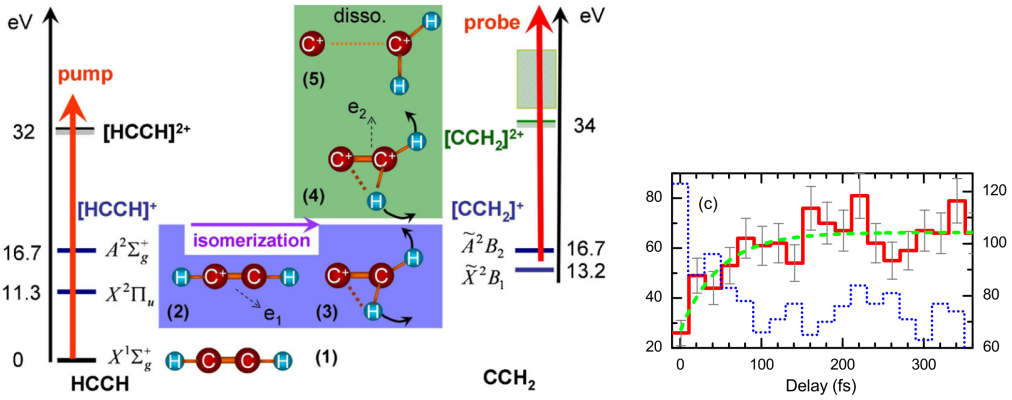

Figure 3.15: [LEFT] Pump-probe energy level diagram. Molecular diagrams 1 through 5 show ionization of acetylene, isomerization, second ionization, and dissociation of vinylidene. [RIGHT] Red measures integrated counts for detected fragmens in the isomerized channel $C^+ + CH_2^+$. The exponential curve (green) fits the signal confirming the isomerization timescale of ∼50 fs. [90] Reprinted with permission from APS.

3.5 Polyatomic Structure

Pushing the limits of complete molecular imaging through CEI, Gagnon *et al.* succesfully made measurements on the structure of the 5 atom molecule CH_2CHI_2 [61]. Relatively long laser pulses of 40 fs were used, allowing for fragmentation along non-Coulombic pathways to occur before complete Coulombic breakup into the $CH_2Cl_2^{6+} \longrightarrow C^+ + H^+ + H^+ + Cl^+ + Cl^{2+}$ channel. The tetrahedral structure was imaged, showing some stretched bond lengths and bond angle deformation (shown in Figure 3.16). The limitation of completely imaging such complex structures can be summarized by the number of geometries successfully reconstructed from coincidence momentum measurements: five.

Similiarly, Pitzer *et al.* looked to image the complete structure of the large molecule, CHBrClF [146]. After multiphoton ionization of CHBrClF using a 40fs laser pulse, five ion coincident detection of the fragment ions in the channel $CHBrClF^{5+} \longrightarrow C^+ + H^+ + Br^+ + Cl^+ + F^+$ was performed in a CEI system. The two enantiomers of this chiral species were detected and discriminated against by examining the relative angles between ion fragment momenta. Here, the geometries were not reconstructed as they are in the work on CH_2Cl_2 by Gagnon *et al.*, rather the orientation of the momenta themselves are used as indicates of structure in general. For identification of chiral species, the authors show that such measurements are sufficient. They also note that making measurements on

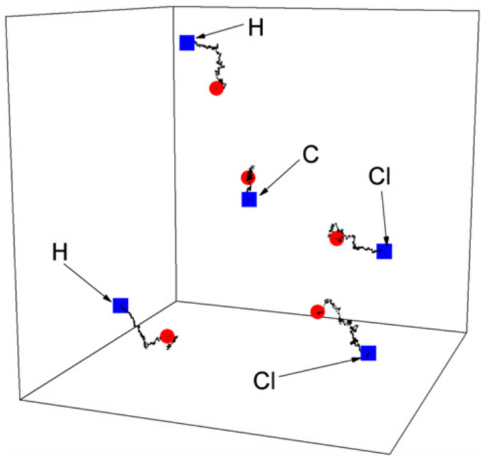

Figure 3.16: Visualization of geometry annealing algorithm used to reconstruct the CH_2Cl_2 structure from CEI momentum measurements. Red circles indicate initial guess and blue squares show final coordinates [61]. Reprinted with permission from IOP.

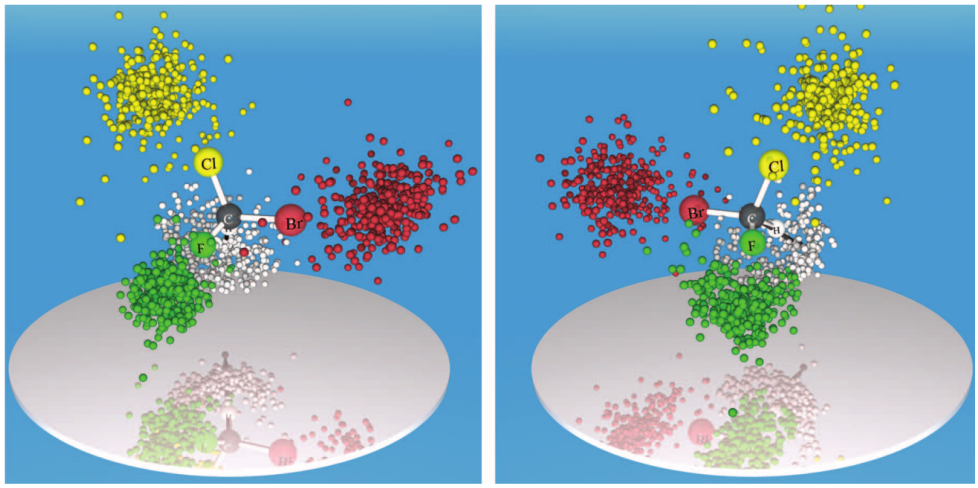

Figure 3.17: 3D momentum measurements of CHBrClF showing the detection and identification of mirror enantiomers [146]. Reprinted with permission from AAAS.

isotopically chiral molecules like $CHBrCl_2$ is not possible given the unambigious assignment of ion identification to the degenerate chlorine atoms - a limitation that might be overcome by the succesfull disentanglement of ion degeneracy performed by Karimi *et al.* [96]

Chapter 4

Imaging of OCS structure and dynamics

4.1 Introduction

This chapter includes edited text from the publication [189].

Intense femtosecond (fs) lasers are ideal tools for imaging molecular structure and dynamics, and have been used for more than twenty years initially through uncorrelated methods such as momentum imaging [78, 159, 162, 76] but more latterly through the powerful coincidence method of glscei [71, 81, 180], in particularly since the advent of hollow fibre compressors the equilibrium structure of molecules has been within reach [112, 111, 80, 79, 17, 96]. More recently methods such as electron ion coincidence [199] and high harmonic tomography have also shown promise [64, 67, 187, 171]. Theoretical advances have identified the origin of phenomena observed experimentally such as CREI [203] and laser induced dynamics [163].

We have recently made an experimental advance [17, 96] by varying the pulse duration from few cycles (<10 fs) to 100s of fs and making a series of careful measurements of fragmentation. Crucially we maintain a nearly constant ratio of final dissociation products from triply and doubly charged molecular ions which ensures we are exploring the same break up processes for each pulse duration. This has revealed aspects of lasermolecule interaction not visible in earlier work which used a fixed pulse duration [78, 159, 162, 76, 71, 81, 180, 112, 111, 80, 79]. This improvement is analogous to the increase in information retrieved about dynamics from a movie compared to a single snapshot. The new multidimensional approach is referred to as FEMPULS and has enabled us

to make significant advances in the understanding of dynamics and ionisation dynamics in triatomic molecules. Firstly in the case of CO_2 [17], by monitoring the total Kinetic Energy Released (KER) of the observed dissociation channels from 3+ to 6+ using the 3D-ion-momentum coincidence method [71], we were able to show that the KER from fragmentation on the 3+ charge state is nearly constant with pulse duration even for few cycle pulses. When we compare the KER with a simulation of the Coulomb Explosion (CE) assuming point-like ions, we found that the measured energy release is around 70 of the Coulombic energy. This contrasted with the higher channels such as 6+ (2,2,2) which exhibited low energy release of close to 50 for long pulses, and high energy release up to 90 for short 7 fs pulses. The pattern not only revealed that the 3+ state is never Coulombic but also pinpointed it as the state from which CREI to higher charge states is initiated. In addition, by monitoring the individual energy released by the respective fragment ions, we showed that there was a progression in the deformation of molecular structure with pulse duration. In the case of N_2O [96] we focused on the low molecular charge 3+ and 4+ and were able to observe a new break up channel for the shortest pulses (sub 7 fs) in which a metastable N_2^{2+} ion is generated, $N_2O^{3+} \longrightarrow N_2^{2+} + O^+ \longrightarrow N^+ + N^+ + O^+$ as well as a new stepwise channel for 4+, $N_2O^{4+} \longrightarrow N^{2+} + NO_2^+ \longrightarrow N^{2+} + N^+ + O^+$. Crucially we used the Dalitz plotting method [42] to express the structure of the molecule for different lengths of exposure to the intense laser radiation, and were able to effectively deduce aspects of stretching and bending.

Here we use the FEMPULS method, along with both Dalitz and Newton plots, to determine the changes in structure and break up processes for OCS in femtosecond laser pulses varying in pulse length from less than 7 fs to 200 fs. OCS structure and break up has been studied previously using femtosecond laser interaction [27, 160, 188] or highly charged ion impact [188, 191, 89] but here we expect to be able to reveal new aspects of processes such as metastable break up channels $OCS^{3+} \longrightarrow CO^{2+} + S^+ \longrightarrow O^+ + C^+ + S^+$, and how they change with pulse length.

4.2 Experimental

The experiments were performed at the Advanced Laser Light Source (ALLS) using the multi-kHz titaniumsapphire (TiSa) laser system (KMLabs Dragon laser system; 5 kHz, 5 mJ, 35 fs pulse duration). Few-cycle pulses (7 fs) are obtained using nonlinear propagation in a hollow core fibre filled with Ar and by dispersion compensation using chirped mirrors. To achieve longer pulse duration, the fibre was evacuated. Using an acousto-optic programmable dispersive filter located in the stretcher of the TiSa amplifier, we applied

second order dispersion ($\Phi^{(2)}(\mathrm{fs}^2)$) to achieve the desired pulse duration. As in [17, 96] we maintain the appearance of our TOF spectrum by adjusting the peak laser power so that the relative amounts of final triply and doubly charged fragment ions stays constant. Because enhanced ionisation becomes more important for longer pulses, this results in intensities which vary between $3 \times 10^{15}\,\mathrm{W/cm^2}$ for 7 fs pulses and $2 \times 10^{14}\,\mathrm{W/cm^2}$ at 500 fs. The laser pulses are focused by a parabolic mirror (f = 10 cm) on a well-collimated supersonic jet of OCS inside a uniform-electric-field ion imaging spectrometer. The fragments are detected and their full 3D momenta are determined using a time- and position-sensitive delay-line anode detector at the end of the spectrometer (RoentDek Handels GmbH). The atomic and molecular fragment ions were measured in double or triple coincidence: $CO^{a+} + S^{b+}$ and $O^{a+} + CS^{b+}$ or $O^{p+} + C^{q+} + S^{r+}$ (a + b = 2 or 3, p + q + r = 3 or 4). Ions are identified as the result of the fragmentation of a single molecule only if their total momentum is close to zero ($< 5 \times 10^{-23}\,\mathrm{kgm/s}$), using this criteria we can distinguish between the degenerate S^+ and O^{2+} ions as well as discriminate against ions resulting from more than one molecule [190].

4.3 Results

One feature which emerges from the coincidence search for modes of molecular ion break up for OCS at a pulse length of 7 fs is the strong signal from binary dissociation channels which include doubly charged molecular ions and result from multiply charged molecular ions OCS^{3+} and OCS^{4+},$CO^{2+} + S^{2+}$ and $O^{2+} + CS^{2+}$ are both present in addition to $CO^{2+} + S^+$ and $O^+ + CS^{2+}$ previously observed in highly charged ion collision [191, 89]. Although it is a new observation for laser induced dissociative ionisation the existence of channels which involve these species is not necessarily surprising as the nuclear interaction potential for the triply charged state [53] as with CO_2 [163] is expected to be a saddle point in which expansion of one bond is the energetically favourable dissociation path. To confirm the form of the potential for OCS^{3+} we measure the kinetic energy release distribution of the (1,1,1) channel. Figure 4.1 shows that the distribution for (1,1,1) [97] is largely unaffected by pulse length up to 100 fs and peaks at around 64% of the expected Coulombic value. Since, for the shortest pulses, we expect that the molecule will be ionised before the bonds have a chance to expand, this is a strong indicator that the 3+ potential is not Coulombic near to equilibrium and in fact has a shallow minimum or 'quasi bound' region which stretches out to a local maximum. The position of this maximum can be estimated from the ratio of energy released to the expected Coulombic value, $E/E_{Coulombic}$ = 0.64 indicates that at around $1.56R_{eqilibrium}$ there is a maximum after which the potential

becomes Coulombic. This is in good agreement with calculations of low lying potentials in OCS^{3+} [53]. Only for pulses of 200 fs and higher, do the bonds stretch to the Coulombic region, where energy begins to decrease with pulse length. By contrast the (1,1,2) channel shows significant decrease in energy for all increases in pulse length, until the critical distance for enhanced ionisation is reached. It appears from this that the OCS^{4+} potential is purely repulsive when both bonds break. We will return to this later.

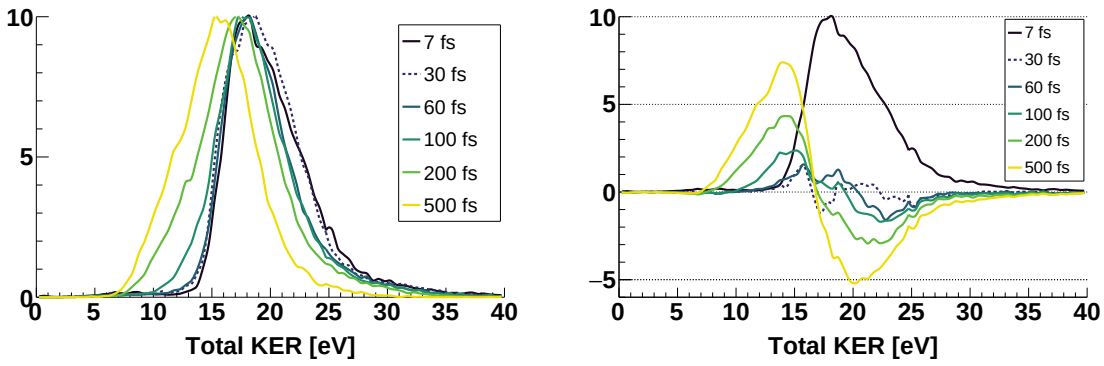

Figure 4.1: [Left] KER Distributions for the (1,1,1) fragmentation channel. Peak normalized. [Right] Difference KER Distributions for the (1,1,1) fragmentation channel. 7 fs is plotted as reference and all other pulse length distributions are subtracted from it.

In order to categorise the possible break up channels for the 3+ and 4+ channels we use the Dalitz plot method, a well established technique for displaying the possible molecular dissociation geometries in a two dimensional histogram [42]. The plot is typically used for symmetrical molecules but functions in a similar fashion for the asymmetric OCS molecule where the total geometrical phase space is represented by a diagonal oval. The histogram is simply generated by plotting the fraction of energy carried by the carbon ion along the y-axis while the difference in the fraction of energy between the sulfur and oxygen ions is plotted along the x-axis. The resulting space is a well defined oval where each point represents specific arrangements of momentum vectors (Figure 4.7). Though the geometry of the molecule and the momentum vectors are related in a nontrivial way, a simple simulation shows that the equilibrium geometry should appear on the Dalitz plot at (0.11,-0.29).

Bending of the molecule in a concerted dissociation process results in a reduced angle between the outside momentum vectors and is associated with approximately vertical changes from the equilibrium point on the Dalitz plot. This is indicated by a black oval shown in Figure 4.7 which shows the (1,1,1) channel for a 7 fs pulse. Points further sepa-

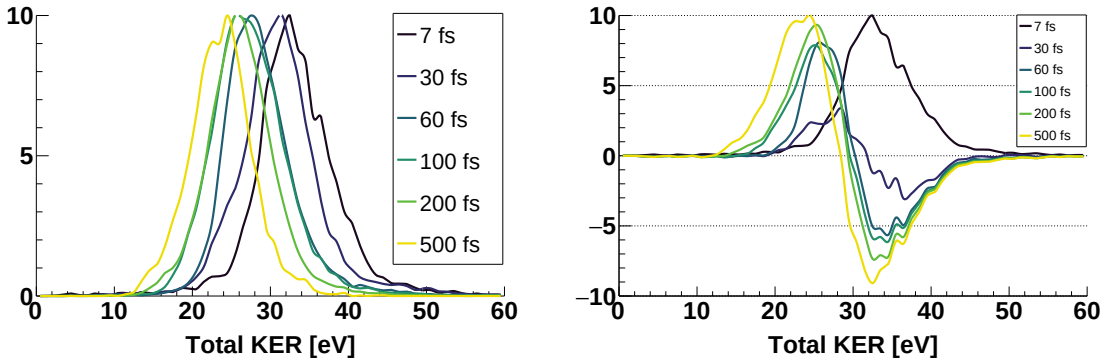

Figure 4.2: [Left] KER Distributions for the (1,1,2) fragmentation channel. Peak normalized. [Right] Difference KER Distributions for the (1,1,2) fragmentation channel. 7 fs is plotted as reference and all other pulse length distributions are subtracted from it.

rated horizontally from the main distribution represent increasing amounts of asymmetry in bond length and are indicative of asynchronous break up. Fragmentation of OCS into a metastable CO ion appears as a diagonal indicated by the dashed red ovals in Figure 4.7 while a break up which involves a metastable CS ion appears as data along a diagonal indicated by the dashed yellow ovals. The uniform density of the diagonals indicates the molecular fragment behaves as a rigid rotor spinning away from the remaining atomic ion [81, 136]. It is worth noting that both of these processes are strong in the case of OCS and are represented on a linear intensity scale, whereas for the CO_2 and CS_2 molecules [81, 136] the stepwise process needed to be shown on log plots. To further examine the stepwise processes we use normalised Newton plots [136] of the (1,1,1) channel at 7 fs firstly with the O^+ ion as the frame of reference and secondly with S^+. Figure 4.4 shows the momentum vectors of the C^+ and S^+ ions relative to O^+ with the concerted channel represented by two intense islands, and the stepwise channel $CS^{2+} + O^+$ represented by two diffuse half rings (which are offset from each other), a more faint feature consisting of horizontal jets is explained by plotting momentum relative to the sulfur ion, in Figure 4.3 here a similar picture emerges but the diffuse ring now represents the $CO^{2+} + S^+$ channel and consists of the data points which were present in the jets of Figure 4.4. Figure 4.5 shows the Newton plot for the (1,1,2) channel relative to S^{2+} again showing a diffuse ring which represents $CO^{2+} + S^{2+}$, in this case there are no faint jets because there is no alternative stepwise channel. One feature of these rings is their uniformity, which indicates the stability of the molecular ion, such that it can perform many rotations before dissociating. Estimates for CO^{2+} and CS^{2+} have ranged from 100 fs [136] to picoseconds [81].

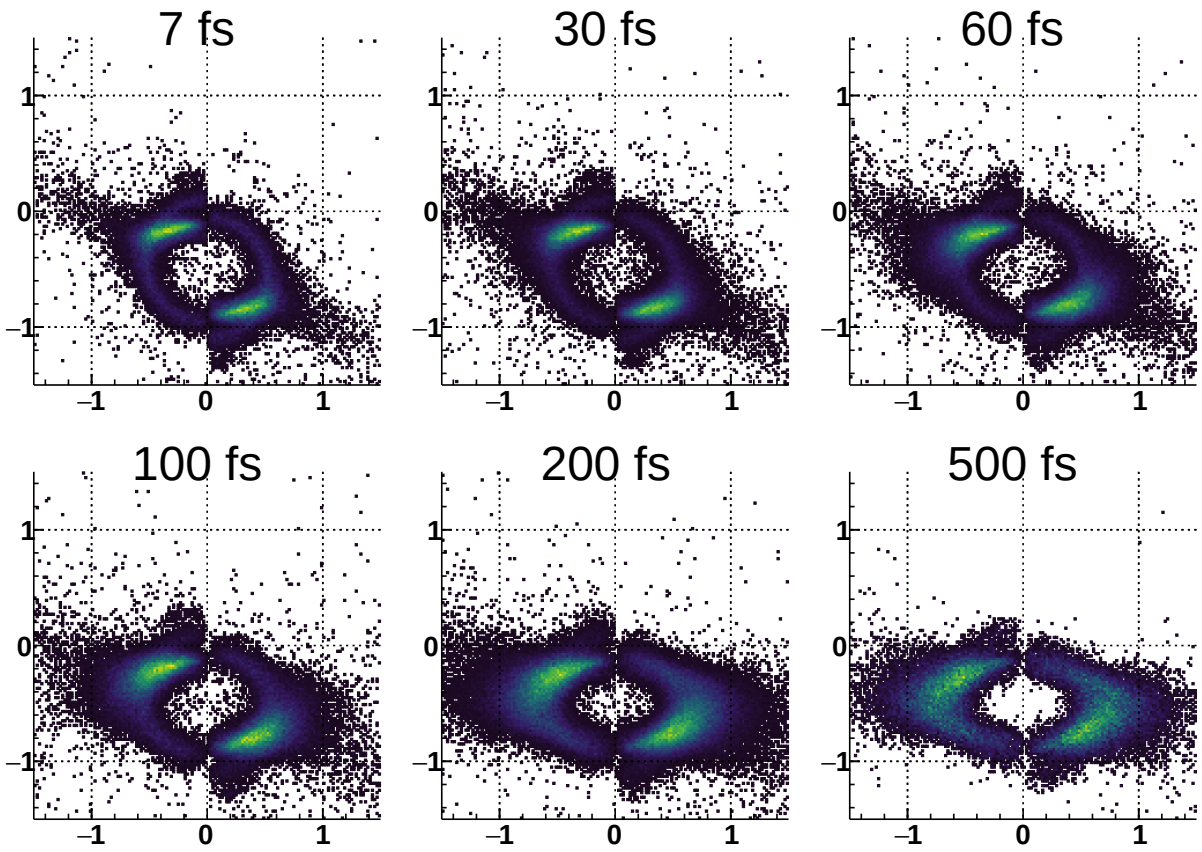

Figure 4.3: Newton plots for the (1,1,1) channel normalized to the S^+ momentum vector at (0,1).

Figure 4.8 shows the Dalitz plots from 7 to 200 fs, normalised so that the peak signal is always the same colour, revealing morphological differences as a function of pulse length. These Dalitz plots indicate the progression of the molecular wave packet on the 3+ and 4+ states, for short pulses the geometries are close to equilibrium for the concerted channel. As the pulse gets longer the concerted process spreads out along the vertical bending axis indicating that the laser induced bending process proposed for CO_2^{6+} [17] also exists for OCS. As in CO_2, it is the potentials of lower charge states in the laser field where the molecular bending takes place, before it reaches 3+ and 4+. We can also see that the central region of the Dalitz plot (indicated by the black oval in Figure 4.7), showing the concerted process, becomes wider with pulse length (in the x-dimension) and that for longer pulses the region becomes wider at the top than the bottom of the plot. Points

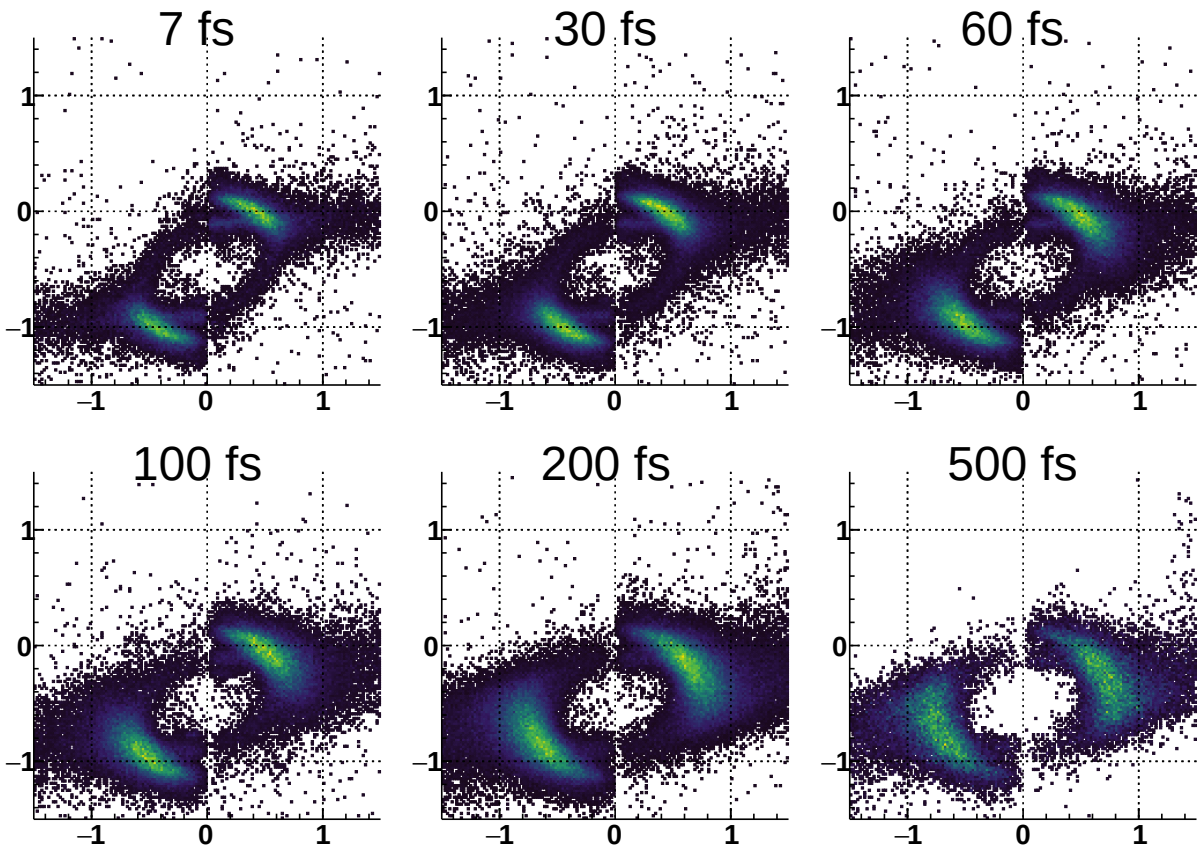

Figure 4.4: Newton plots for the (1,1,1) channel normalized to the O^+ momentum vector at (0,1).

on the Dalitz plot to the left or right of x = 0.11 indicate less concerted or progressively asynchronous bond breaking while points above y = -0.29 indicate more bending. The trend indicates that as the pulse length increases, molecules bend more and bonds break more asynchronously. This is not clear from the energy release of Figure 4.1, which seems to indicate that bonds are not changing below 200 fs because energy release is not decreasing. In fact bonds are almost certainly stretching as they bend as observed for higher channels [17] but the stretch must be in a region of the potential which is relatively flat and so does not lead to decreased kinetic energy release. The effect of pulse length can be revealed more precisely in the Dalitz plot by examining the upper arms of the metastable signal region as the pulse length increases in Figures 4.8 and 4.9. As the pulse length is increased up to 60 fs, the diagonal signal representing the stepwise process fades, and then begins to

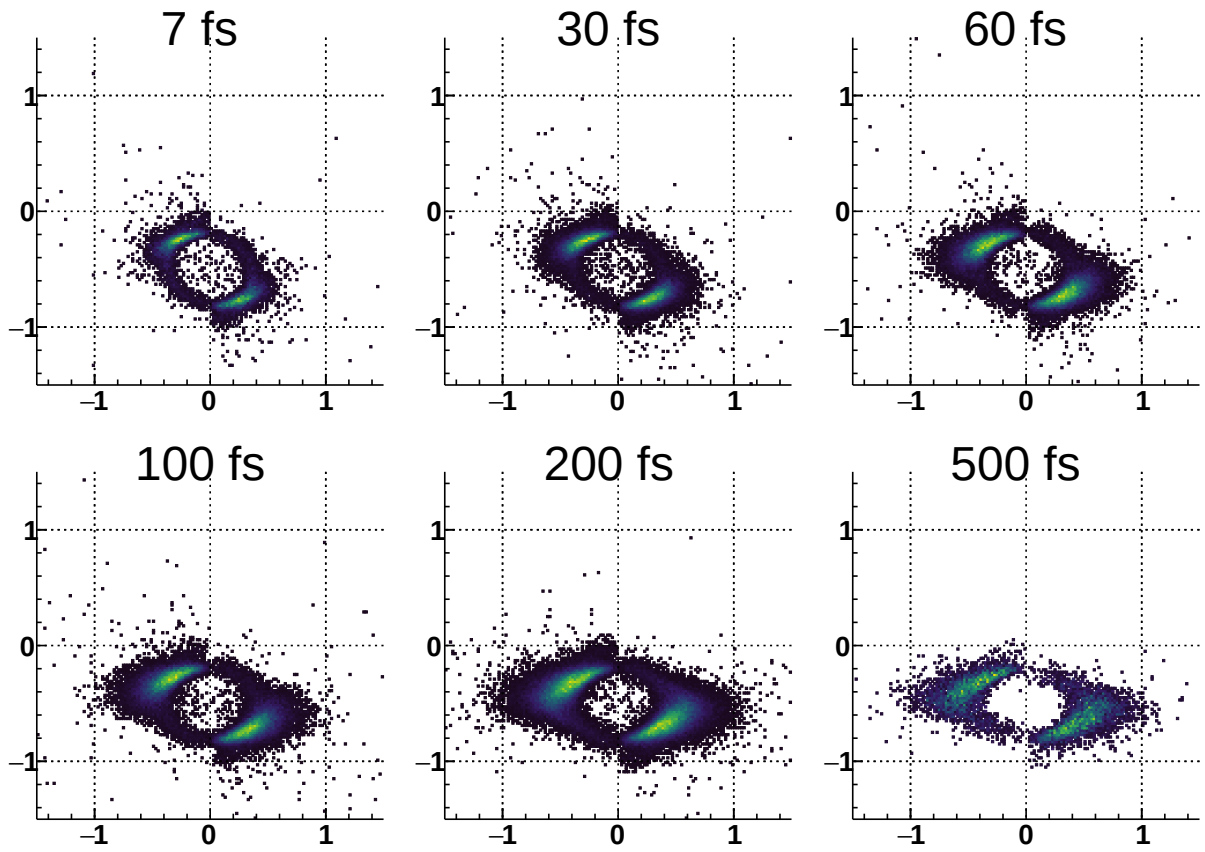

Figure 4.5: Newton plots for the (1,1,2) channel normalized to the S^{2+} momentum vector at (0,1).

become more prominent again for longer pulses. This process can be seen more explicitly in Figure 4.10 which shows how the ratio of stepwise to concerted processes vary with pulse length. This surprising control mechanism can be understood within the framework of field induced bending and stretching [163]. Sato *et al.* showed that for CO_2, not only was bending initiated on the light dressed 2+ potential but that this was coupled with stretching, of the bonds. Their calculations indicated that the light induced potential pushes the molecule along the concerted coordinate stretching both bonds symmetrically, and giving the molecule momentum along the concerted break up coordinate. An important aspect of their calculation was that the timescale for this process was on the order of tens of femtoseconds. We can understand the behaviour by thinking of the wave packet on the 3+ potential as a classical ball rolling on a two dimensional saddle point surface similar in form

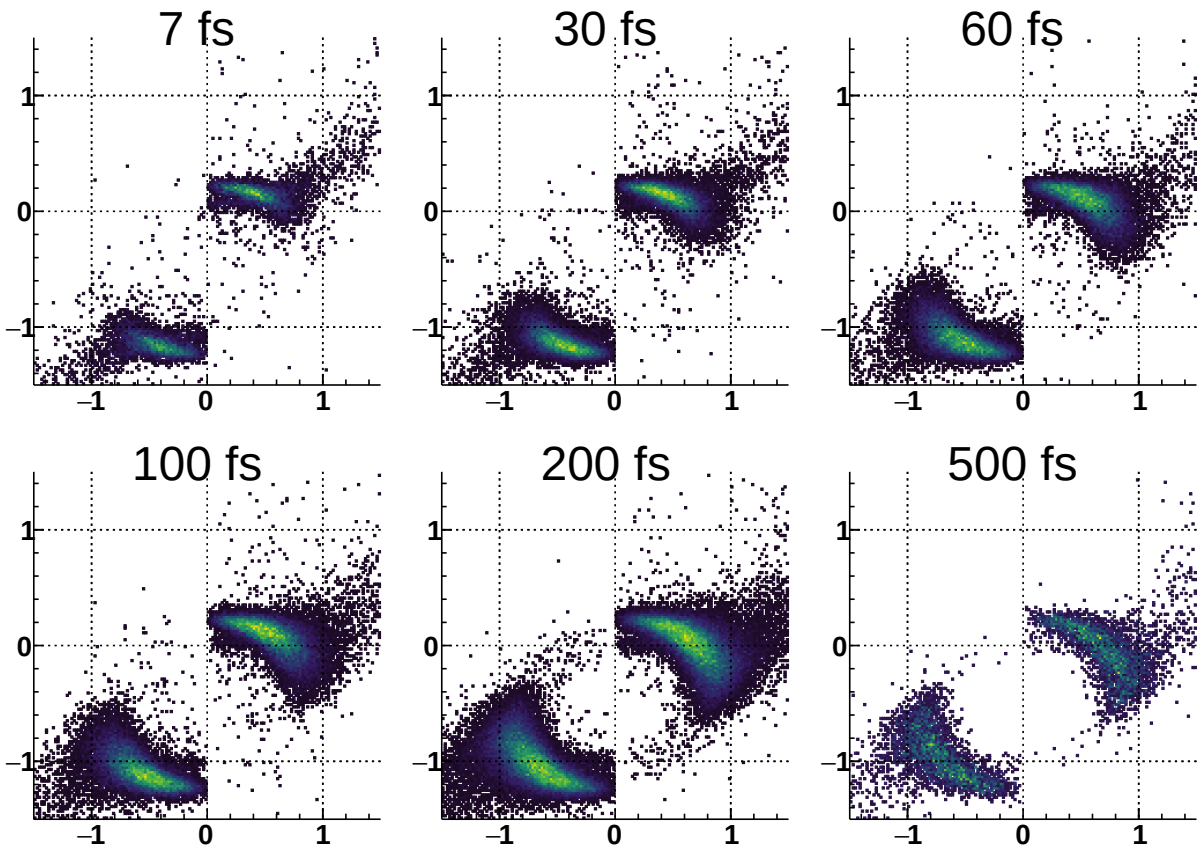

Figure 4.6: Newton plots for the (1,1,2) channel normalized to the O^+ momentum vector at (0,1).

to that of the potential of Figure 4.8 of [163]. As with CO_2 the 3+ potential has a local minimum followed by a maximum along the $(y = x)$ diagonal (concerted bond expansion) and deep valleys along the x and y coordinates which correspond to stretching of the CO or CS bond only, with the CS being the deeper. Similarly for the 4+ state, the potential must have a valley along the CS stretch coordinate giving rise to the stepwise channel and this is likely accompanied by a shallow local minimum along the concerted coordinate. Evidence for this minimum from Figure 4.2 is contained in observation that the peak energy released is only slightly lower for 30 fs than it is for 7 fs. For OCS we can see that for the shortest pulse length (sub 7 fs) the molecule passes through the intermediate channels quickly and the wave packet arrives on the 3+ and 4+ potential with little momentum. This lack of momentum along the concerted coordinate means some of the wave packet is directed down

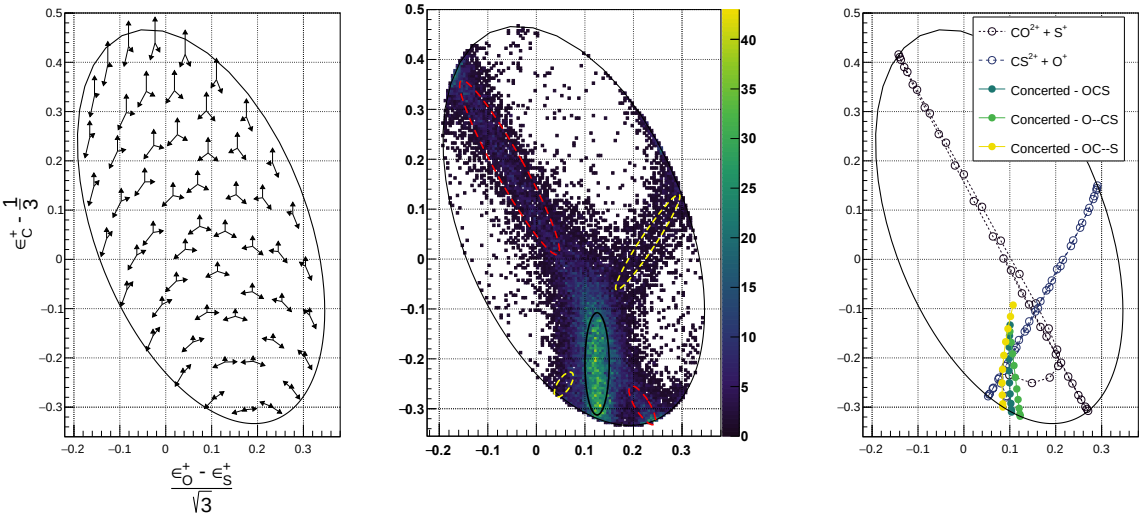

Figure 4.7: Dalitz plot for the (1,1,1) channel of OCS. The x-axis indicates the difference between the fraction of total energy release (epsilon) by the O and S ions and the y-axis is fraction of energy release of the C ion. [LEFT] The relationship between the points on the plot to the momentum vectors of the three fragments, the C is vertical, S to the left and O to the right. [CENTRE] Measurements with 7 fs pulses with ovals highlight specific processes: (black) concerted breakup; (red oval) CO^{2+} metastable sequential breakup; (yellow) CS^{2+} metastable sequential breakup. [RIGHT] Simulations for concerted and sequential breakup. Three curves (solid circles) show simulations originating from three types of bond lengths: ground state, stretched CO bond, and stretched CS bond. Each curve begins with 180° bond angle (lowest point in y-axis) and ends at 160° (highest point in y-axis). Sequential breakup curves (open circles) are shown for the metastable processes $OCS^{3+} \longrightarrow CO^{2+} + S^+ \longrightarrow C^+ + O^+ + S^+$ (black) and $OCS^{3+} \longrightarrow CS^{2+} + O^+ \longrightarrow C^+ + O^+ + S^+$ (blue). Each process begins with slightly bent and slightly stretched geometries (near the concerted region). Points along each curve result from the metastable ion existing for specific times (beginning with 0 fs and increasing by 10 fs increments).

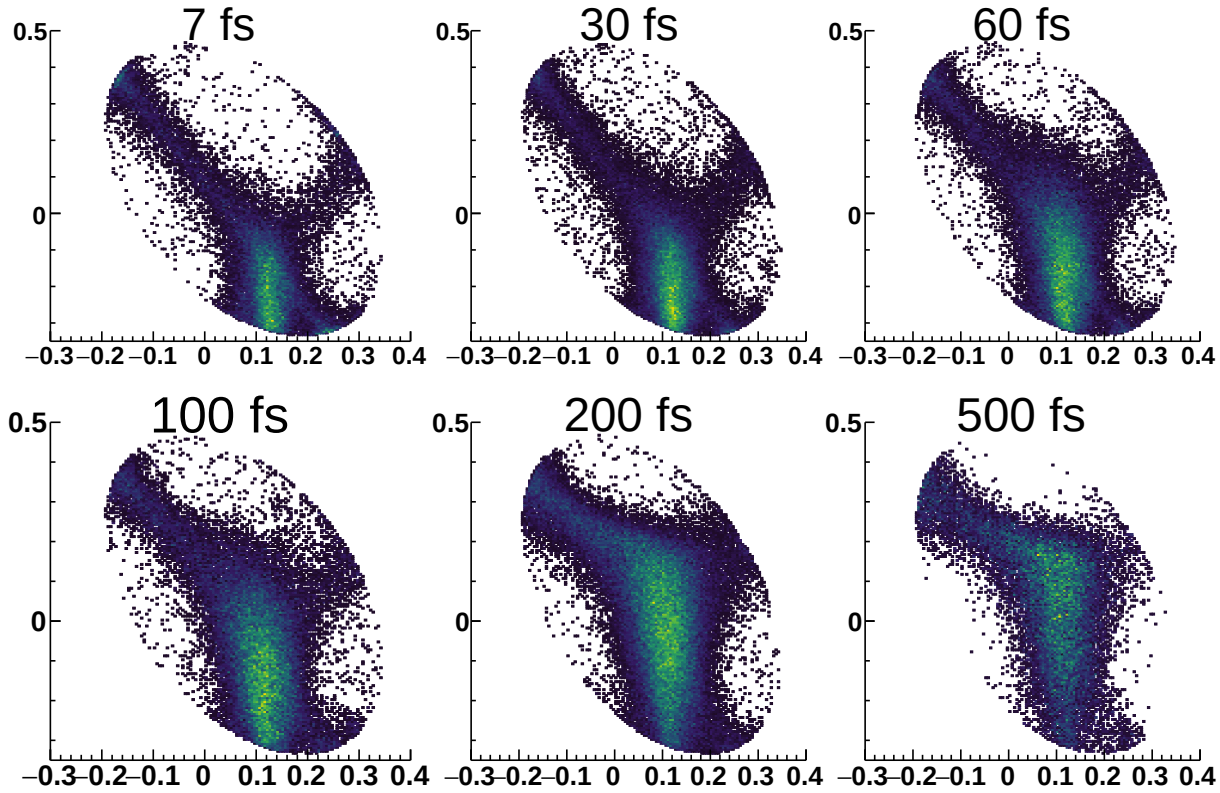

Figure 4.8: Dalitz projections for the (1,1,1) channel with various pulse lengths.

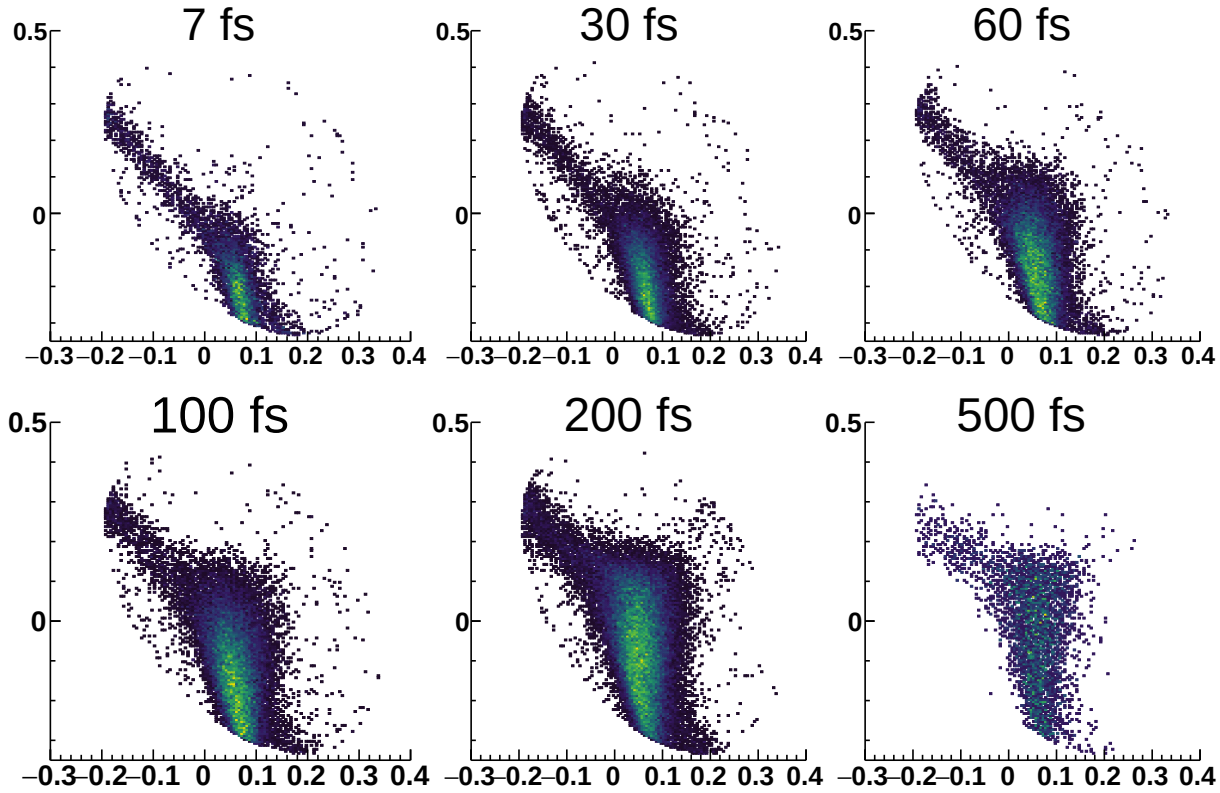

Figure 4.9: Dalitz projections for the (1,1,2) channel with various pulse lengths.

the favourable two body valleys in which only one of the bonds stretch. As the pulse length increases the impulse delivered on the 2+ potential increases because the molecule spends more time climbing the ionisation ladder and the wave packet arrives on the 3+ and 4+ states with momentum in the concerted coordinate direction allowing it to overcome any local maximum and diminishing the stepwise channel. With still further increase in pulse length however this concerted momentum is again reduced because the peak intensity of the laser decreases, now the wave packet again has a chance to slide down the valleys rather than overcome the saddle point maximum.

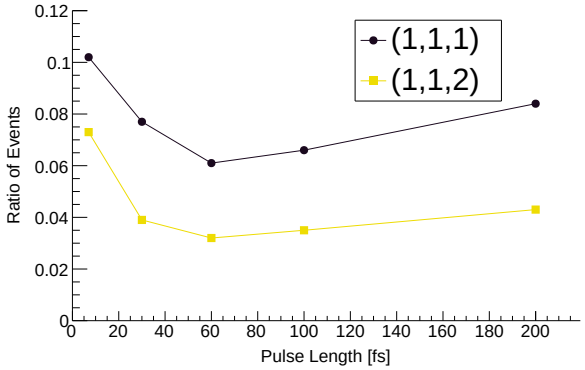

Figure 4.10: Ratio of counts in the stepwise region to concerted processes region of Figure 4.8 and Figure 4.9 as a function of pulse length.

4.4 New Results - Extreme Molecular Deformation

In addition to the (1,1,1) and (1,1,2) fragmentation channels discussed thus far, measurements of the (1,2,1) and (2,1,1) channels were also performed. Dalitz plots for these channels are shown in Figures 4.11 and 4.15 respectively. Similarities and differences between these channels and the more common (1,1,1) and (1,1,2) channels are now discussed, with a focus on a new process observed at 200 fs for both (1,2,1) and (2,1,1).

The strong central mode imaged in the (1,2,1) channel with 7 fs is similar to those measured for other channels - (1,1,1) 4.8, (1,1,2) 4.9, (2,2,2) 6.5, and (2,2,3) 6.5. Due to the short pulse, the ionization occurs quickly enough so as to preserve the initial molecular geometry until Coulombic explosion occurs. The breadth and height of the signal in the Dalitz plots are similar to those for the (1,1,1) channel and can be modelled by Coulombic fragmentation from stretched and bent geometries. Simulations for such geometries are

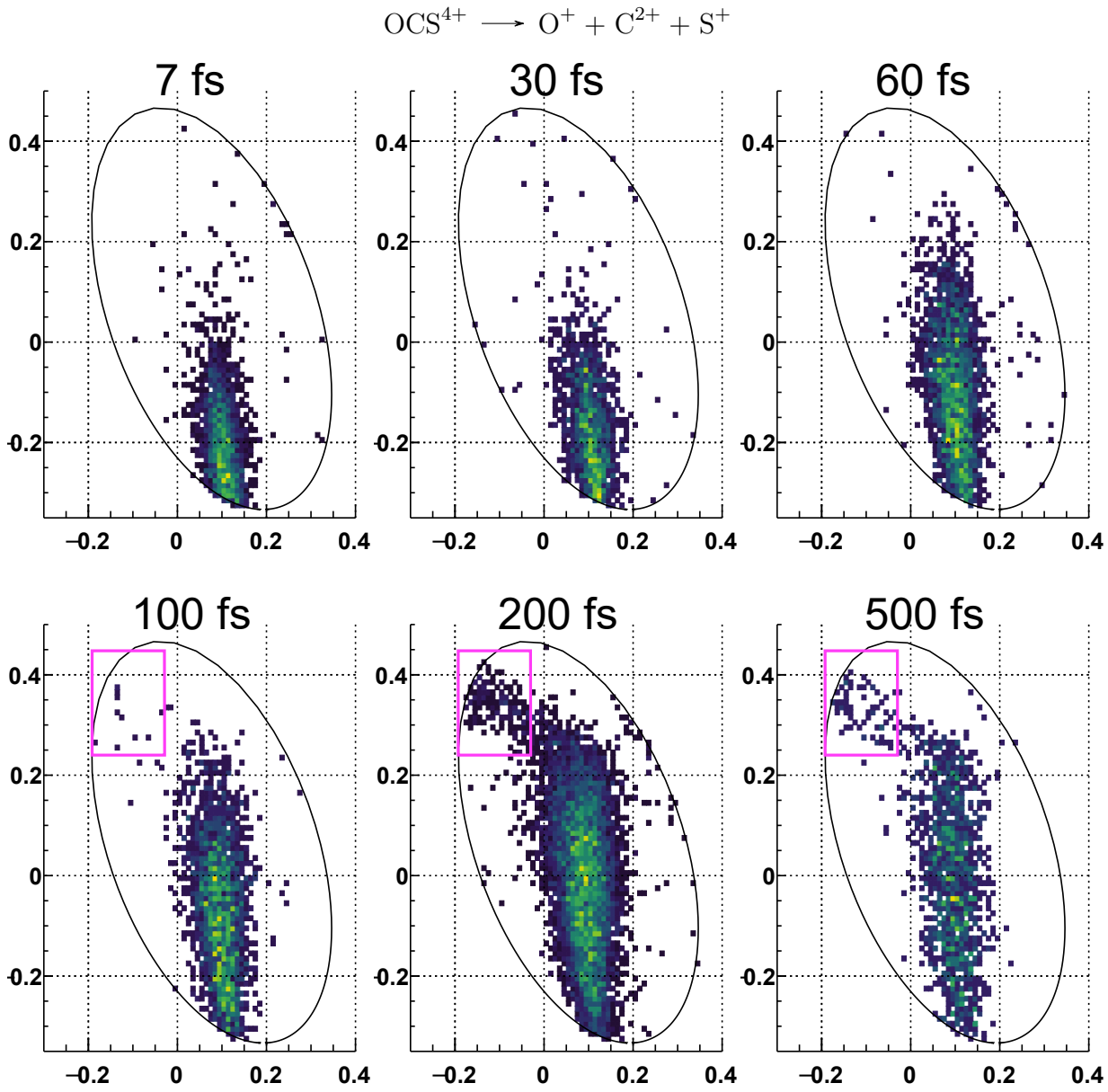

Figure 4.11: Dalitz plots for the (1,2,1) channel for various laser pulse lengths.

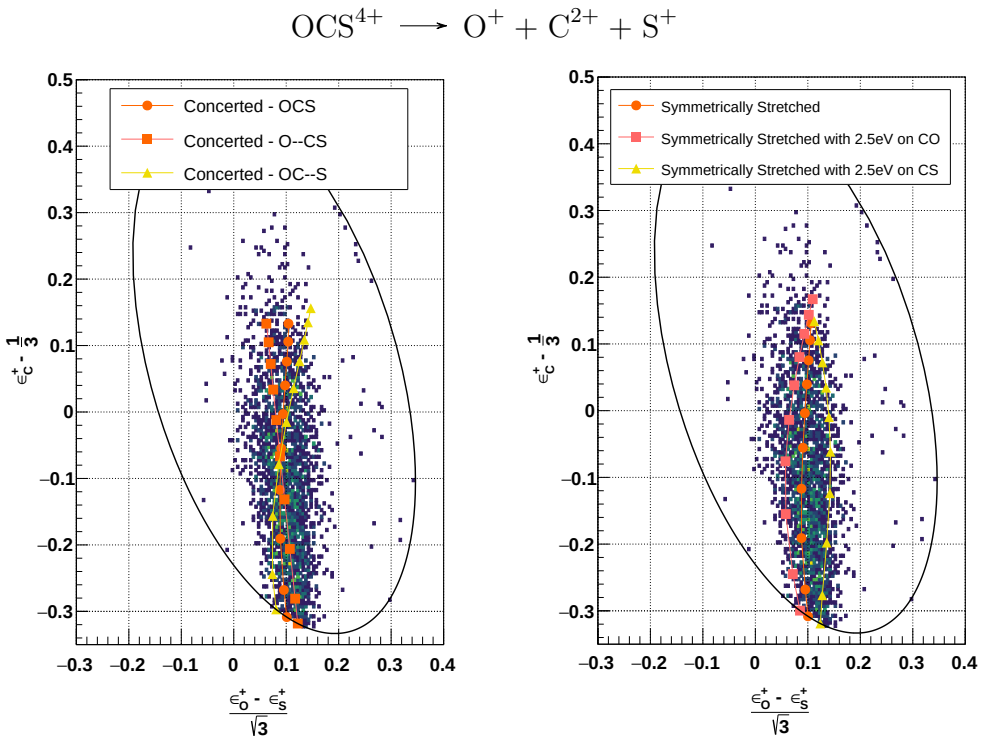

Figure 4.12: [LEFT] Breakup simulations of OCS into the channel $OCS^{4+} \longrightarrow O^+ + C^{2+} + S^+$ beginning with ground state bond lengths (orange circles), stretched C-O bond lengths (pink squares), and stretched C-S bond lengths (yellow triangles). Points along each curve correspond to decreasing bond angle, beginning at 180° (bottom) and ending at 135° (top). [RIGHT] Breakup simulations of OCS into the channel $OCS^{4+} \longrightarrow O^+ + C^{2+} + S^+$. (Orange Circles) Coulombic fragmentation from geometries with bondlengths stretched 1.5x ground-state lengths; each point upwards along curve indicates decreasing bond length from 180° to 135°. (Pink Squares) Same as (Orange circles) but 2.5 eV is split between C^{2+} and O^+ to simulate the initial break of the C-O bond. (Yellow Triangles) same as (Orange circles) but 2.5 eV is split between C^{2+} and S^+ to simulate the initial break of the C-S bond.

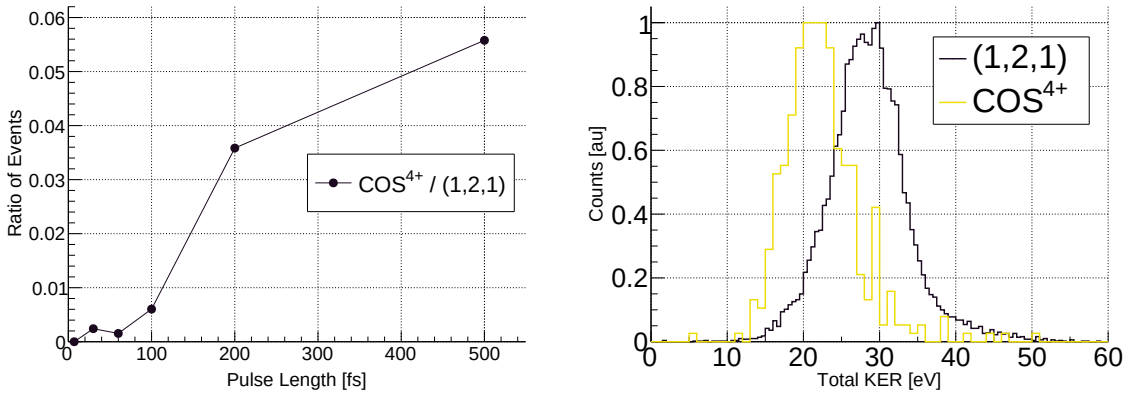

Figure 4.13: [LEFT] Ratio of events measured corresponding to the C-O-S structure in the (1,2,1) channel against all events measured in the (1,2,1) channel. [RIGHT] Total KER measurements for these regions. Integration of C-O-S events performed on Daltiz plots in Figure 4.11 with the indicated window.

shown in Figure 4.12. The simulations shown here bend the molecule from 180° to an extreme 135°. At approximately 160°, the three simulation curves converge. If the phase space below this convergence point is considered (bend angles between 180° and 160°), the simulated region takes a tall triangular shape, mimicking closely the measurements made with 7 fs shown in Figure 4.7. So, the signal measured with 7 fs pulses can be understood as direct imaging of stretched and bent OCS structures.

As the pulse length increases, the signal in the Dalitz plots move upwards along the y-axis, indicating an increase in bend angle as suggested by the simulations shown left in Figure 4.12. However, the simulations show a narrowing at y = -0.1 while measurements are especially wide in this region. In fact, no amount of simulated stretching at this critical bond angle (160°) provides noticeable spread in fractional energy along the x-axis. To account for the wide signal measured here, a second simulation was performed shown right in Figure 4.12. Here, small amounts of energy (<1 eV) were added to the ions in the stretched bond while conserving momentum. In doing so, the boundaries of the simulation widen and the entire signal in the Dalitz plot can be modelled (shown in Figure 4.12 for the 60 fs pulse).

By adding energy to the ions in the stretched bond, an approximation of sequential ionization has occurred. For the stretched CO bond, the simulation has effectively taken into account the initial ionization of carbon and oxygen and their subsequent stretching and repulsion by both stretching the bond before complete Coulomb repulsion occurs and

providing some momentum kick along the bond coordinate. In the neighbouring simulation, the same is done for the CS bond. Here the initial ionization of carbon and sulfur is mimiced by stretching the CS bond while adding a momentum kick along the CS bond coordinate. After adding these energy kicks, the fragmentation is simulated with classical Coulombic repulsion. This sequential ionization modelling is similar to that done by Legare *et al.* [112]. The broadening of the central signal along both the x and y axes in the Dalitz plots for all pulse lengths can be accurately modelled with sufficient stretching, bending, and momentum kicks simulating sequential ionization.

In addition to these dynamics, a new process appears in the top left corner of the Dalitz plot when the pulse length is increased to 200 fs. This process is unique to the rest of the imaged structures for three reasons. One, it appears to have a distinct time-dependent switch occurring between 100 and 200 fs. This is shown by integrating the signal in the region of interest and plotting this value as a function of pulse length (shown left in Figure 4.13). Two, the process has a KER peak ∼8 eV lower than the central process (shown right in Figure 4.13). And three, the signal results from low oxygen momentum, but significant carbon and sulfur momentum. Considering what has been stated about the effect of bending on the OCS structure of increasing pulse lengths, this last point suggests that the OCS molecular ion has isomerized into a COS structure (as seen in [106] with x-ray initiated ionization). However, purely Coulombic simulations of the ground state COS structure (shown in Figure 4.14) does not exactly reproduce the signal shown in the Dalitz plot. This signal can be reproduced using one of two simulations. One, performing Coulombic breakup simulations with severely stretched CO bond lengths ($r_{CO} \approx 10$ Å) and bent geometries ($\theta \approx 90°$); two, performing the Coulomb breakup simulations with a symmetrically stretched COS geometry and include some initial vibrational energy ~ 1 eV. It is also possible that CREI is being observed here for triangular structure. This would explain the low KER measurements as well as the need for bending over long time scales. Ultimately, the possibilities are currently too many to definitively conclude which structure has been created, but it can be said that the new fragmentation pathway originates from a severely bent geometry and the degree to which this process occurs can be controlled by the laser pulse length.

The Dalitz plots for the (2,1,1) channel (shown in Figure 4.15) measure features and trends similar to those found in the (1,2,1) channel. Unlike the (1,2,1) channel, the (2,1,1) channel features diagonal signal characteristic of the metastable process $OCS^{4+} \longrightarrow O^{2+} + CS^{2+*} \longrightarrow O^{2+} + C^{+} + S^{+}$. Much like the (1,2,1) channel, however, signal appears at the top left of the Dalitz plot when the laser pulse length reaches 200 fs. Additionally, a similar pathway opens on the right side of the Dalitz plot, highlighted by the pink box. Among the possible explanations for this new signal is the possibility of isomerizing OCS into the

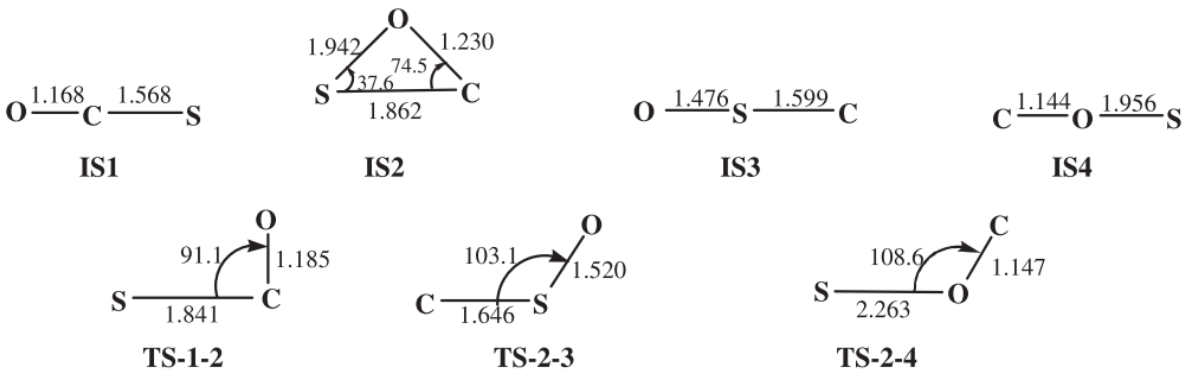

Figure 4.14: Geometry of isomers of carbonyl sulfide and their inter conversion transition states at MP2/6-311++(2d,2p) level. [63] Reprinted with permission from Taylor & Francis.

OSC structure (perhaps along the 2+ PES, as calculated by Briets *et al.* [26]). As before, a few simulations can account for both of these features and so no conclusion can be drawn other than the pulse-length dependence of this new deformation pathway.

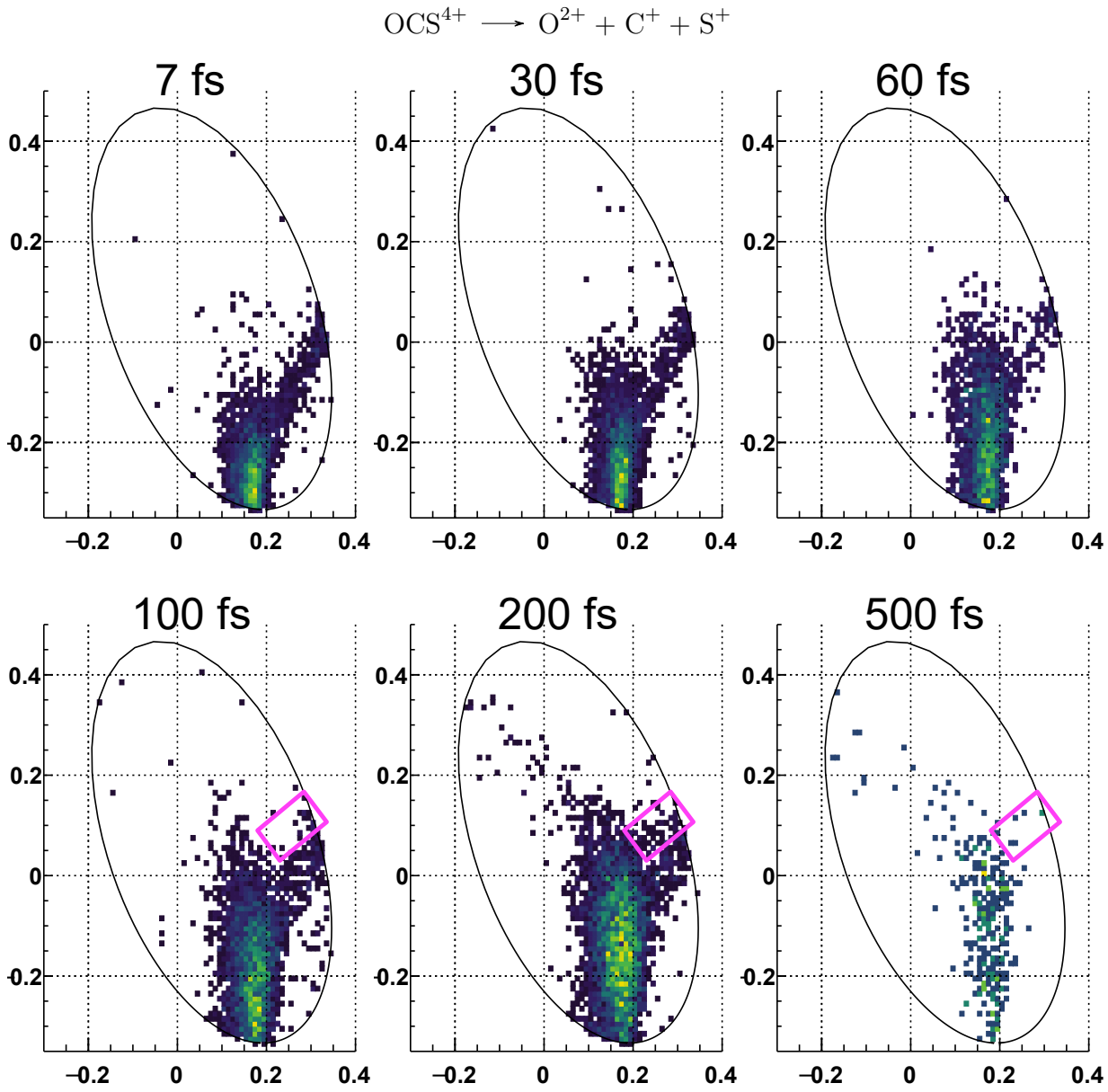

Figure 4.15: Dalitz plots for the (2,1,1) channel for various laser pulse lengths.

4.5 Conclusions

By using a compact representation offered by the Dalitz plot we can see, without attempting any complex molecular reconstruction process [25], how processes of molecular deformation and break up develop as pulse length is changed. Three stepwise channels have been identified, including one for the 4+ state. Furthermore, by careful control of laser pulse length, from few cycle to 200 fs, we can exert a degree of control over the final state molecular dissociation channel for the OCS molecule. The behaviour observed fits well into the picture predicted by [163] where the molecule is given momentum by the laser field, along the concerted bond breaking coordinate with bending. That this could lead to an intermediate isomerization is previously unpredicted. Control over molecular deformation and, perhaps, isomerization, has been highlighted by measuring the appearance of a deformation process fragmenting in the (1,2,1) and (2,1,1) channels as a function of pulse length.

Chapter 5

Imaging of Ultrafast Processes in OCS using X-rays

5.1 Introduction

This chapter includes edited text from the publication [153].

CEI is a developing technique designed to image the geometry of small molecules (<10 atoms) as they bend, stretch, and separate on a femtosecond time scale (10^{-15} s). The technique usually relies on ultrafast infrared laser pulses [96, 17] or highly charged ion impacts [191] but x-ray and UV laser pulses from free-electron laser sources have also been used [90]. Here we use CEI utilizing ionization by single x-ray photons from a third generation synchrotron source.

The (near) simultaneous ejection of more than one electron from an atom in response to absorption of an x-ray photon is the result of electron-electron correlations and as a result has been extensively studied in helium and other atoms [10]. At energies away from threshold this is dominated by two mechanisms. The first TS1, or knock-out, is where the outgoing photoelectron scatters off the other electrons to produce multiple ionization [157]. The second, shake-off [29], is where the rapidly outgoing photoelectron leaves the atom in a suddenly different charge state. In this case there is a possibility that an electron experiencing this sudden difference in effective charge may find itself in the continuum. The end result is that the branching ratio of double to single ionization in atoms generally rises from zero at threshold to a plateau where the total excess energy is around 100 eV (e.g for helium [48]) and that the energy sharing between the two electrons involved is

generally unequal [99]. Hartman *et al.* [69, 70] have extended these mechanisms from atoms to moderately large molecules. We assume that these mechanisms are available for the double and triple ionization of OCS at 90 eV. As well as direct ionization the processes above may leave an intermediate ion in a highly excited state, which can then shed a further electron through autoionization. Depending on the lifetime(s) involved this may occur at any point in the dissociation process up to and including a fragment atom. For a diatomic molecule this can be described as $AB + hv \longrightarrow (AB^+)^* \longrightarrow A^+ + B\cdot \longrightarrow A^+ + B^+$. Price and Eland [151] describe a particularly nice example for O_2. Extensions to a triatomic molecule are easily imagined. This may produce a low energy electron.

Above an energy where a core electron can be excited another mechanism for double and multiple ionization becomes available: Auger ionization. Here a core electron is either excited into a vacant orbital (resonant Auger) or into the continuum (normal Auger). Subsequently the core hole is filled by an electron in a higher energy level, with the excess energy being carried away by the ejection of a third electron. This process has a distinct timescale and typically produces electrons of a distinct energy. During this Auger lifetime the nuclei of the molecule may move, as determined by the potential energy surfaces of the excited neutral (resonant Auger) or excited ion (normal Auger). Of course the Auger electron may interact with the remaining electrons in the atom or molecule through the TS1 or shake-off mechanisms described above. Excitation at 167 eV gives access to resonant Auger processes, while excitation at 172 and 173 eV gives access to normal Auger processes.

After a triatomic molecule absorbs a photon in the soft x-ray wavelength range, it ionizes and loses up to 4 electrons through direct or Auger ionization. It can then dissociate into two or three fragments, two or more of which are ions. In the case when the molecule decays into its constituent atomic ions, the break up can be modeled as a decay through the Coulomb repulsion, in which an imprint of the initial molecular shape is left on the final fragment momenta. The extent to which this is an accurate description depends in part on the speed of a multiple ionization event, by which we refer to the time between the initial and final ionization steps, during which the charge builds up. The removal of the initial electron in both direct and Auger processes is on an attosecond timescale. If the multiple ionization is rapid compared to nuclear motion ($t < 10$ fs) then the initial molecular geometry may be preserved, but if the event is slow, ($10 < t < 100$ fs), and the initial geometry is known, then nuclear dynamics during the ionization process can be revealed in the pattern of momentum release [17].

We attempt to vary the ionization timescale in this work by scanning the photon energy through the sulfur 2p edge at ∼172 eV. Below this edge, ionization is dominated by direct ionization in which electrons are removed promptly by photon absorption, while above the edge the ionization is dominated by electron ejection due to Auger decay which through

its lifetime (t $\sim$ 10 – 100 fs), extends the duration of the ionization event.

5.1.1 Valence absorption and ionization

The photoabsorption, photoionization, and photofragmentation of OCS has been well studied. The ultraviolet absorption cross section has been measured [21] as has the valence photoionization cross section [40], threshold photoelectron spectrum [46], He(i) photoelectron spectrum [103, 45, 192], and electron energy loss spectrum [110]. The inner valence region has been probed by photoabsorption [196], electron energy loss [56], photoelectron spectroscopy using synchrotron [83, 43], He(ii) [150] and Mg K-α [2] radiation, and studied theoretically [50, 168]. Autoionization from the S atom has been observed from photoexcited OCS [75].

5.1.2 Inner valence ionization and double ionization

Coincidence spectroscopies allow higher electronic states and higher charge states to be probed. The dication of OCS has been probed by TEPEsCO [68] with the threshold found at 30.0 $\pm$ 0.1 eV. Various electron multi-ion time-of-flight spectroscopies have been used to study the fragmentation of valence [124, 123, 122] and inner valence [131, 138, 57] excited OCS. We note that Masuoka and Doi [123] give the threshold for double photoionization as 32 eV and the threshold for triple ionization as 52.5 eV. The maximum in the triple ionization cross section (below any S(2p) absorption threshold) is reported to occur at 95 eV. Excitation of OCS at 90 eV can result in the direct production of a triply ionized molecule through the knock out process, without the effects of a S(2p) core-hole lifetime. Masuoka also reports the branching ratios for all ion production up to 100 eV photon energy [124]. Eland *et al.* have reported double [54] and triple [52] coincidences between O^+,C^+, and S^+ from ionization of OCS at 65 eV with the S^+ and O^+ fragments in the triple ionization taking away more initial kinetic energy than in the double ionization case.

5.1.3 Sulfur 2p edge ionization

Absorption spectra and total ion yield spectra have been recorded in the region of the sulfur 2p edge [104, 8, 55, 120]. Theoretical multi-reference, single and double-excitation configuration interaction, *ab initio* (MRD-CI) calculations have lent weight to the peak assignments [22]. Using dipole (e, e plus ion) coincidence spectroscopy, Feng *et al.* [57] have measured branching ratios for the production of fragment ions at equivalent photon

energies from the first ionization threshold up to 300 eV. Ion fragmentation studies have been carried out using the time-of flight coincidence method near the sulfur 2p edge. Erman *et al.* [55] have measured the photofragment ion asymmetry parameter (β) across the sulfur 2p absorption edge, as well as the PePIPICO maps for double ionization events, which have also been measured by Franzen *et al.* [58]. Ankerhold *et al.* [8] have measured the total charge production in OCS as one scans across the sulfur 2p edge. In the same paper they report the maximum kinetic energy of the fragments from both double and triple photoionization. As expected, the fragments from triple ionization events take away considerably more energy than those from double ionization events. Another class of electron ion measurements is molecular frame photoelectron angular distributions (MFPADs). Here the photoelectron is measured in coincidence with an ionic fragment from the parent molecule to give a fixed in space angular distribution of photoelectrons. This has been reported for OCS by Golovin *et al* [66] for OCS at the S2p$_{3/2}$, S2p$_{1/2}$, C1s, and O1s electrons.

Sulfur 2p photoelectron and Auger electron processes have been well studied. Carrol *et al.* [30] have recorded Auger spectra for C(1s),O(1s), and S(2p) ionization and determined level assignments for the final states of the 2+ ion. Bolognesi *et al.* [18] have measured the S L23MM Auger electron spectrum in coincidence with the photoelectron, since the energy range of the Auger electrons is 127 - 141 eV this double ionization energy ranges from 30 eV (threshold) to 45 eV. Niskanen *et al.* [140] have measured the energies of core valence doubly excited OCS though double ionization photoelectron spectroscopy which is essentially a variant on TOF-PEPECO. This allows them to directly measure OCS S2p^{-1} v^{-1} double ionization energies. These start at approximately 190 eV and are above the photon energies used in this study. Saha *et al.* [156] have measured the fragmentation of OCS in coincidence with the Auger electron. Their experimental set-up - a cylindrical mirror analyser for the electron detection and an ion time-of-flight system with position sensitive detection for the ions - allowed them to measure the mean kinetic energy release (KER) upon fragmentation of OCS^{2+} for different Auger states. The fragmentation of the molecule was found to be highly dependent on different Auger decays through which the precursor molecular ions are formed. Carlson *et al.* [28] have reported that following resonant absorption the excited electron acts as a spectator electron in the subsequent Auger decay.

5.1.4 Higher energy ionization

Of the papers cited above only the dipole coincidence spectroscopy papers of Feng *et al.* [56, 57] cover the sulfur 2s edge. The photofragmentation studies and ion coincidence

studies above, likewise, do not cover the S(2s) absorption edge.

Hikosaka *et al.* [74] have studied the sulfur (2s) Auger spectrum at sub natural linewidth resolution. This was done by exciting the OCS S(2s) photoelectron at threshold and measuring Auger threshold coincidences. Exciting the S(2s) electron differs from exciting the S(2p) electron in that the major Auger component is the Coster-Kronig decay of the 2p electron to fill the 2s hole, producing an Auger electron of energy 45 eV or lower. They find that the core-hole lifetime of the 2s hole corresponds to a width of 1.8 eV (0.37 fs). By contrast the S 2p core-hole lifetime is 65 meV (10.1 fs) [105] in OCS. Following the CosterKronig decay the 2p hole may be filled by further Auger transitions leading to higher charge states of OCS and its fragments being detected.

Sham *et al.* [167] present a total ion yield spectrum for OCS across the C(1s) edge, as do Erman *et al.* [55]. The PePIPICO studies of Franzen [58] and Erman [55] also cover the C(1s) edge with Erman [55] also including a total electron yield spectrum across the C(1s) edge. Using a momentum imaging TOF spectrometer, Laksman *et al.* [106] have measured the anisotropy parameter (β) for OCS dissociated to$O^+ + CS^+$ and $S^+ + CO^+$. The dissociation necessarily produces two ions at 180° separation. They found that the intensity for the $S^+ + CO^+$ channel was always 10× to 15× greater than the $O^+ + CS^+$ channel. They also found that the anisotropy of the $O^+ + CS^+$ channel was greater than that of the $S^+ + CO^+$ channel, which they suggest, implies the dication state leading to $S^+ + CO^+$ has significant bending vibrational excitation. The paper also describes the total KER and momentum correlations for OCS producing three ions ($O^+ + C^+ + S^+$) when excited near the C(1s) edge, with the total KER ranging from 10 to 30 eV both on the 1s-π^* and 1s-σ^* resonances and off resonance. They investigated bending of OCS for the C(1s) and O(1s) excitations and observe effects of Renner-Teller splitting for C(1s) excitation only, which were distinguishable by their respective molecular orientations relative to the photon polarization.

5.1.5 Ionization at the S(1s) edge

Ankerhold *et al.* [7] have measured the charged particle production in coincidence for photoexcitation of OCS both above and below the S(1s) edge. They find the most abundant combination excited below the edge (2449 eV) to be $O^+ + C^+ + S^+$ and above the edge to be $O^+ + C^+ + S^{2+}$. They also plot the relative abundances of the various (total charge = 2 and 3) channels across the S(1s) edge. Neville *et al.* [137] have recorded a total ion yield spectrum across the S(1s) edge with traces for various individual ion channels as well as PePIPICO maps for double ion and triple ion production. Bomme *et al.* [19] present

a total ion yield spectrum for OCS excited near the S(1s) edge, complete 2D TOF maps for the production of $CO^+ + S^+$, $CO^+ + S^{2+}$, $CO^+ + S^{3+}$, and $CO^{2+} + S^{2+}$ dissociation channels. They also present complete 3D MFPADs for dissociation to $S^+ + CO^+$ at 10 eV above threshold.

5.1.6 Excitation by highly charged ions and ultrafast laser pulses

Recent electron capture work employing highly charged ion impact experiments with Ar^{4+} and Ar^{8+} projectiles at 15 keV/q [191, 155, 188] has also probed the break up of OCS from 2+ up to 6+. Findings showed the kinetic energy release from the 3+ state to be lower than the calculated Coulombic value, in agreement with recent femtosecond laser induced ionization work [189]. Higher charge states peaked closer to the Coulombic value but with distributions wider than the laser work results, indicating the presence of more excited states in the HCI impact induced ionization than the tunnel ionization process associated with the femtosecond laser induced ionization.

5.2 Experimental

The experiment was performed at the Variable Line Spacing Plane Grating Monochromator (VLS-PGM) x-ray beam line at the 3rd generation CLS synchrotron in Saskatoon, Saskatchewan, Canada [85]. A portable CEI apparatus from the University of Waterloo was installed at the beamline behind a differential pumping chamber. Adapted from the single stage TOF apparatus of [24], an effusive gas beam of OCS is injected into a high-vacuum chamber through a hypodermic needle placed one millimeter away from an orthogonal 1 mm diameter, collimated beam, of variable energy x-ray photons (5.5 - 250 eV) with a resolution of $>$ 10000 E/ΔE. The beam enters the chamber horizontally and the electric vector of the 100 linearly polarized beam is horizontal (perpendicular to the TOF axis). The photon flux was reduced using the entrance and exit slits and baffles such that a typical count rate was of the order of 100 per second. Electrons produced via direct ionization and Auger processes in the interaction region are accelerated downward with a constant electric field (26 710 V/m) through a 2.9 mm diameter aperture and are detected with a microchannel plate, operating as the TOF start signal. The aperture and field are such that electrons with a kinetic energy component orthogonal to the electric field of more than 1 eV will not pass through the aperture. Thus the aperture becomes an increasingly efficient filter for electrons with a total kinetic energy above 1 eV and our apparatus biases in favor of low

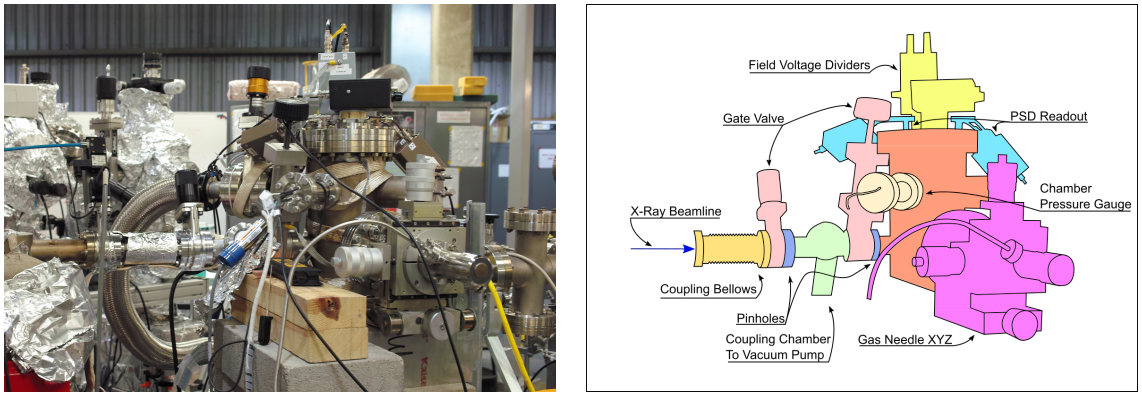

Figure 5.1: Photograph of the UW CEI apparatus installed at CLS on the VLS-PGM beamline. Colourized cut-out indicates functional sections.

energy electrons. This energy filtering biases our detector in favor of (1) low energy photoelectrons produced by the photoionization of S(2p) core states at 172 and 173 eV and (2) low energy electrons produced through the TS1 and shake-off mechanisms described in the introduction section. This biases us against straightforward single ionization from valence states [123]. The electron aperture is aligned directly below the interaction region in order to filter out interactions with the background gas, allowing us to define a zero momentum position for all fragments, which is crucial in calculating fragment momenta. Positive ion fragments on the other hand are accelerated upwards. The fragments are detected and their full 3D momenta are determined using a time and position- sensitive capacitively coupled film anode detector at the end of the spectrometer [85, 185]. The four outputs from the anode are recorded by a pair of GaGe branded oscilloscope cards interfaced with a PC giving a sampling rate of 500 MHz. The atomic and molecular fragment ions were measured in double or triple coincidence: $CO^{a+} + S^{b+}$, $O^{a+} + CS^{b+}$, or $O^{p+} + C^{q+} + S^{r+}$ ($a + b = 2$ or 3, $p + q + r = 3$ or 4). Ions are identified as the result of the fragmentation of a single molecule only if their total momentum is close to zero ($< 5 \times 10^{-23}$ kgm/s). Although the asynchronous nature of the data acquisition means that the probability of detecting ions from more than one molecule for any electron start is small, data analysis which can distinguish between all possible combinations of ions given their arrival times is used to identify true coincidences [190].

A photo of the CEI apparatus coupled to the CLS VLS-PGM beamline along with a simplified schematic are shown in Figure 5.1. Details on the additions made to the CEI apparatus so as to couple with synchrotron radiation are now described.

5.2.1 Gas Injection

When CEI experiments are performed with optical laser pulses, the required high intensities necessitate the use of an optic short focal length to produce a narrow beam waist and a subsequently small focal volume. One beneficial side effect of this small focal volume is the generation of ions at the projected centre of the PSD. By positioning the focal volume here, two major benefits are realized: the possibility of fragment ions striking the apparatus material is minimized, and the coincidence momentum imaging technique is improved (by assuming a point-centre for ion production). Current x-ray optics do not allow for similarly sized focal volumes, nor are they required to increase the field intensity in these single-photon experiments. As such, the x-ray beams enter and exit the apparatus volume with nearly unchanging beam waist. Should the chamber pressure be simply increased using a cylinder of the target gas, ionized particles would be created along the entirety of the beam path. In order to achieve a high production of ions at the projected centre of the PSD, a gas injection needle was implemented, thereby increasing the target gas pressure in a small volume at the center of the spectrometer, crossing the beam path.

The gas input needle is a hyperaemic needle coupled to the target gas source and mounted on a three-dimensional micrometer controlled XYZ stage. A photo of this system in place is shown in Figure 5.1. The stainless steel rings used to generate the homogeneous extraction field were cut to create a hole for the gas needle to pass through. To minimize perturbation of the extraction field resulting from the gas needle's proximity, the needle was biased to a voltage matching that of the rings through which it passed.

5.2.2 Electron Detector

CEI experiments making use of short pulses gate the timing of their acquisition systems using electronic synchronization from the laser amplifier. The timing jitter of this signal (as well as the femtosecond pulse itself) is below the $\sim$1 ns TOFMS detection precision. For x-ray pulses generated in long bunches at CLS, this is not the case. In order to gate the CEI acquisition with the ionization of a target molecule, an electron detector was introduced on the opposite end of the apparatus' extraction field. A photo of this device is shown bottom in Figure 2.4 and a simple schematic shown left in Figure 2.3.

A voltage threshold on the anode signal was used to discriminate true electron triggered events from noise. The last plate defining the extraction field closest to the electron detector was modified to include a 2.9 mm aperture. This opening discriminates the detection of electrons in two ways. Firstly, it allows the detector to preferentially accept

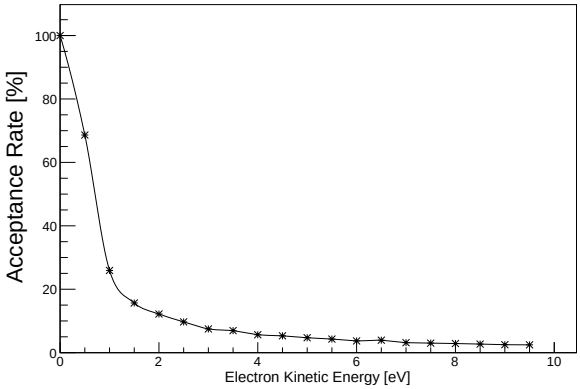

Figure 5.2: Electron acceptance rate through the electron aperture used in the CEI apparatus design at CLS. Monte Carlo simulation performed using the classical trajectorie sof electrons in an extraction field. Initial velocity vectors are isotropically distributed while the starting positions were placed at the approximate interaction centre used throughout the following experiments.

electrons generated in the volume projecting normally to the aperture opening. Secondly, the relatively small ratio between the aperture diameter and its distance from the interaction region discriminates against the detection of high energy electrons. To verify this, a Monte Carlo simulation calculating the classical trajectories of electrons from the interaction region was performed. Figure 5.2 shows the relative detection efficiency for electrons of energies ranging from 0 to 10 eV.

The extent to which the x-ray beam, needle-fed gas volume, and electron aperture overlap can be resolved by plotting the raw positions of detected events. Shown in Figure 5.3, a strong signal peak appears at the center of the detector, measuring ions fragmenting from the overlap of these three elements. The weaker signal forming a line from left to right results from events generated along the x-ray beam leading up to and moving beyond the target gas volume.

5.2.3 X-Ray Photodiode

For the purposes of alignment, a photodiode was built from copper and mounted down stream just beyond the extraction field rings (shown left in Figure 5.4. A readout line was connected to a picoammeter. The current measurement from this detector was maximized through fine adjustments of the vacuum chamber itself, resulting in beam alignment passing

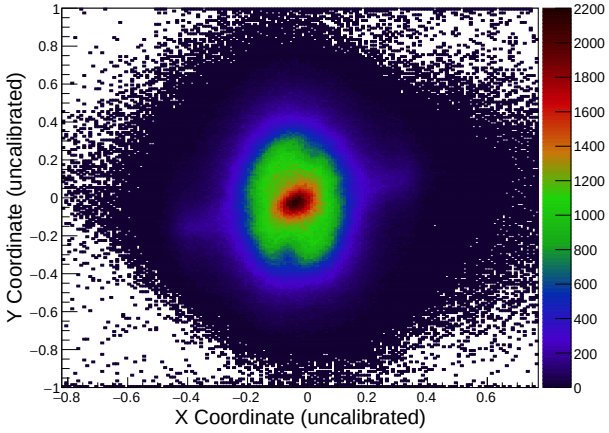

Figure 5.3: Raw PSD measurements of OCS initiated with 90 eV photons. Strong signal at center indicates good overlap between the x-ray beamline, injected gas volume, and electron aperture. Weak, linear, signal results from ionization occurring along the beam-path, outside of the target volume.

directly through the space between two spectrometer rings (schematic shown right in Figure 5.4).

5.2.4 Data Analysis Technique

Although the algorithm described in [190] makes use of momentum discrimination, the same effect can be yielded by performing discrimination on the calculated ionization position (a straight forward calculation performed by first *assuming* net zero momentum, then *determining* the central position of the initial ionization). Filtering the data in such a manner provides a metric of position in real 3D space - one that can be compared with the specific apparatus geometry. The experimental conditions for this work yielded an approximately spherical interaction volume with a 1 mm radius. The data acquisition and analysis system confirm this in a Figure 5.5 (typical results for the (1,1,1) channel). The bottom left and bottom middle histograms show distributions of target positions - the left 2D distribution shows real XY positions in the plane parallel to the detector, while the middle shows positions relative to the expected target position parallel to the extraction field. The strong peaks in XY and Z confirm that this data selection process yields events originating from an expected interaction volume.

In the following analysis, coincidence measurements are made on the three-body breakup

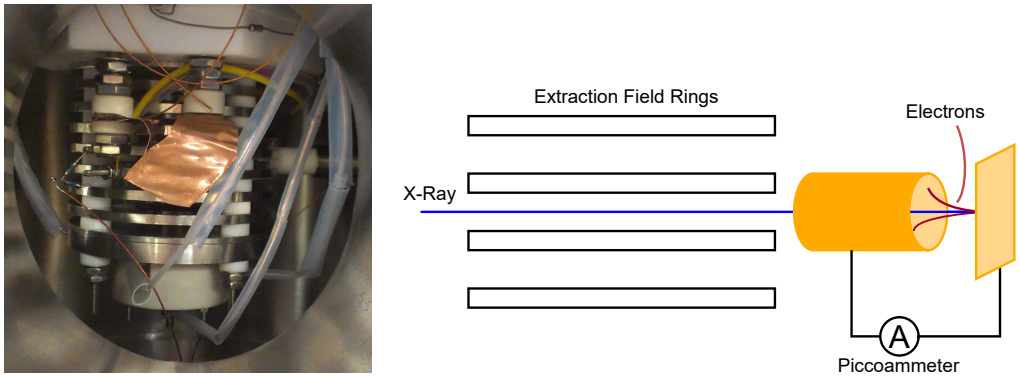

Figure 5.4: XRay Photodiode at CLS and schematic.

of OCS into two ions and a neutral atom. The CEI apparatus is not designed for such reactions since coincident momentum measurements require the explicit detection of moving ions (and ideally those with high momenta). Therefore, a judicious analysis of detected fragments in the desired pathways is now described in order to ensure that the three neutral pathways of interest $O^+ + C^+ + S$, $O^+ + C + S^+$, and $O + C^+ + S^+$ are correctly identified.

The principle issue with using the established coincidence analysis techniques is the possibility of misidentifying a neutral channel with its analogous triply ionic channel where one of the ions has gone undetected. For example, where only the oxygen and carbon ions are detected from the (1,1,1) channel, it is possible to identify these events as being fragments in the (1,1,0) channel. What's more, should the undetected sulfur ion in this example be produced from a pathway resulting in little S^+ momentum, then it cannot be easily determined from which pathway these ions originate. However, some statements can be made with certainty. The expected KER for 2-ion and 3-ion fragmentation channels should be substantially different, with the additional charge increasing the KER by $\sim$10 eV. So, should 3-ion channels be misidentified as neutral channels, this data will appear having much higher energy than that for the true 2-ion coincidences. Therefore, coincidence events from neutral channels can be confidently detected for low energies while the same cannot be said for high energies. Unless another metric (such as molecular orientation) is preferentially realized in the 2-ion neutral versus the 3-ion case, this region will remain unconfirmed.

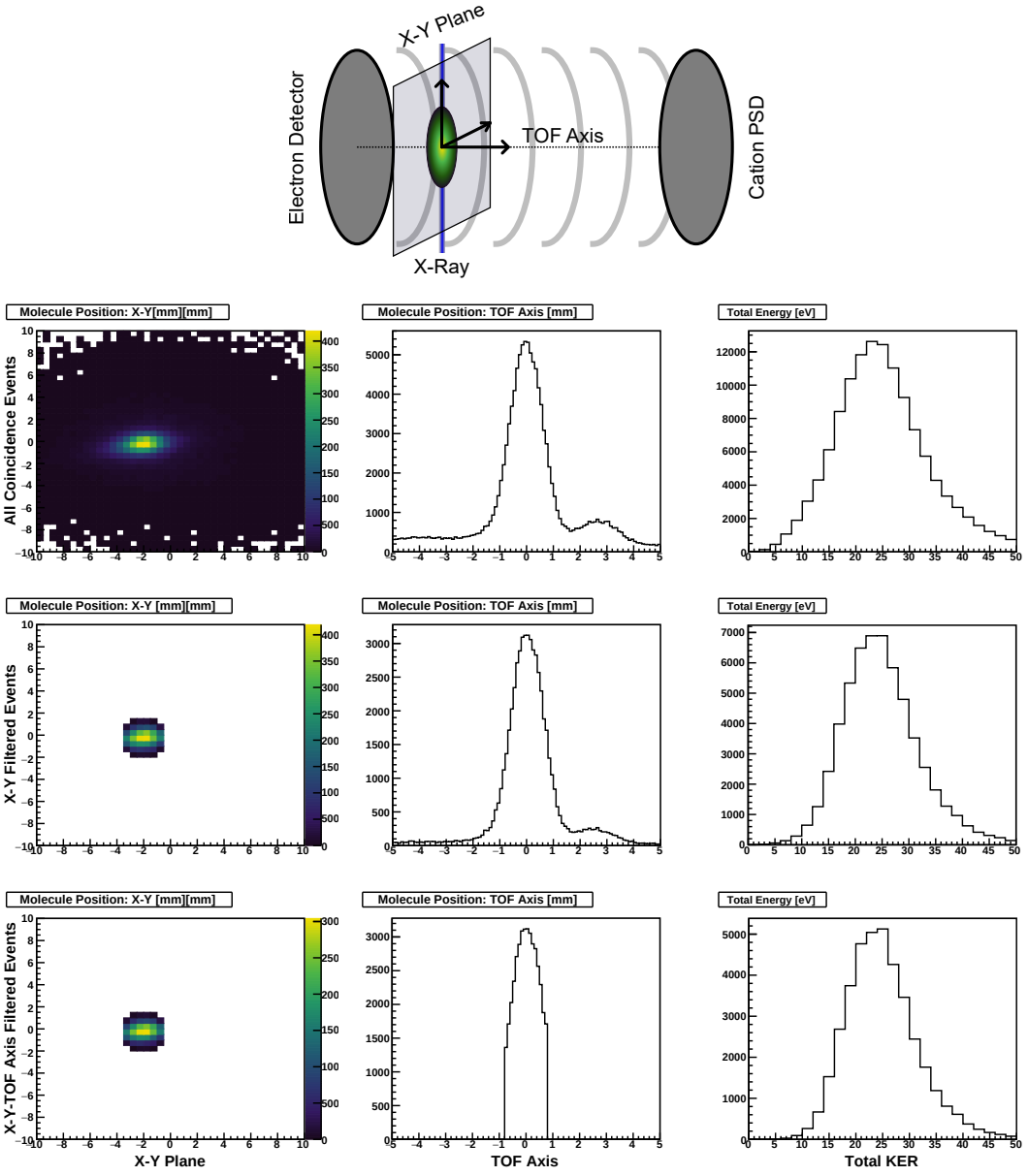

Figure 5.5: Calculated positions for molecular ionization in the plane perpendicular to the detector [LEFT column] and along the TOF axis [MIDDLE column]. [RIGHT column] shows the total KER. The top rows are produced from all coincident measurements fitting the TOF windows for this channel. The second row shows distributions after filtering for a small circular area perpendicular to the detector plane. The third row results from additional filtering along the TOF axis. The strong peaks at the filter center result from true coincidences; the homogeneous background that is filtered out results from false coincidences.

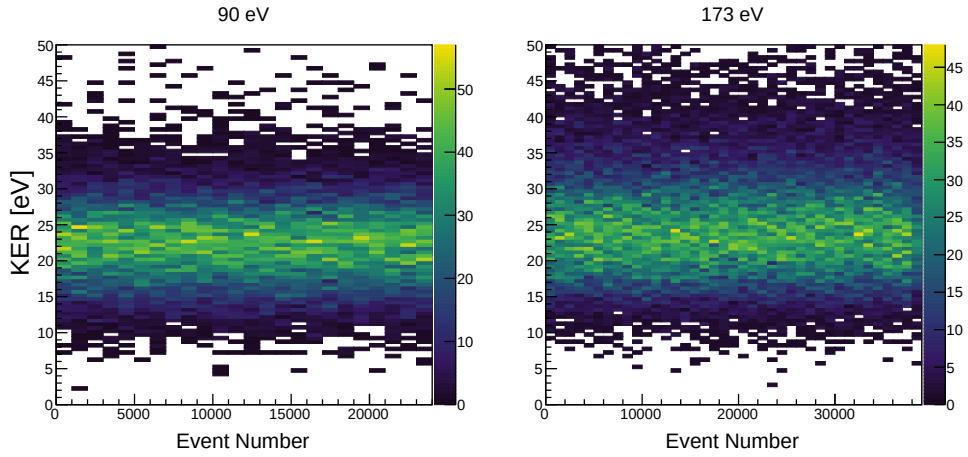

Figure 5.6: KER of the (1,1,1) channel as a function of event number and thus time. The entire acquisition periods for 90 and 173 eV photon energy are approximately one and two days respectively.

5.2.5 Stability

Due to the relatively low count rates of this experiment, data acquisition occurred over several days. As such, it is possible for experimental parameters critical to the accuracy of CEI measurements (such as gas needle position, apparatus alignment, etc.) to drift. To check that this is not the case, the KER spectrum for various channels were plotted as a function of event number (and thus as a function of time). As an example, such data is shown for the (1,1,1) channel in Figure 5.6. Clearly, variation of the KER measurements for long time scales extend the period of the experiment, while variations within the experimental time scale do not yield observable differences larger than 0.5 eV. It can be concluded that drift is not a significant factor in these measurements.

5.3 Results

Data was collected at 90, 166.94, 171.6, and 172.6 eV. 90 eV was chosen to observe the ground state geometry and locally maximizes ionization efficiency [123]. 166.94 eV was chosen as it was below the S(2p) edge and coincided with the $S(2p_{3/2})^{-1} \rightarrow 4s$ Rydberg state transition [55]. 171.6 eV was chosen as it ionized the $S(2p_{3/2})$ electron to the continuum, while 172.6 eV was chosen as it ionized both the $S(2p_{3/2})$ and $S(2p_{1/2})$ electrons to the

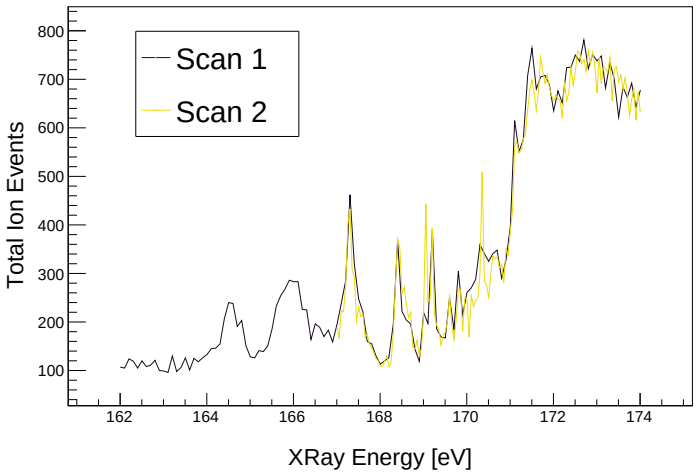

Figure 5.7: Integrated counts from the electron detector as a function of X-ray energy. Scan 1 and scan 2 were performed sequentially to check the reproducibility of signal peaks.

continuum [53]. Throughout this section, photon energy figures are rounded to the nearest eV for brevity, thus the 90, 166.94, 171.6, and 172.6 eV energies are referred to as 90, 167, 172, and 173 eV respectively. For three body breakup, we observe and discuss the (0,1,1), (1,0,1), (1,1,0), (1,1,1), (1,1,2), (1,2,1), and (2,1,1) channels. For two body breakup, the$O^+ + CS^+$, $CO^+ + S^+$, and $CO^+ + S^{2+}$ channels are observed and discussed. All other possible fragmentation channels were too rare to offer enough statistics for discussion.

5.3.1 Two-ion breakup kinetic energy release

KER distributions for various double coincidence (2-ion) fragmentation channels are plotted in figure 5.8. The kinetic energy of each fragment ion is calculated from its mass and experimentally measured momenta.

For the 2-ion 3-body fragmentation channels that included a neutral atom, only the energy of the two ions is included in the total energy release plots, in order to compare with previous work [156, 125] but the complete energy release can be calculated from conservation of momentum. In practice the difference is negligible with the neutral taking away less than 0.5 eV.

We observe several points of comparison between our KER distributions in figure 5.8 and those of Saha *et al.* [156] and Masuoka *et al.* [125]. Qualitative comparisons regarding

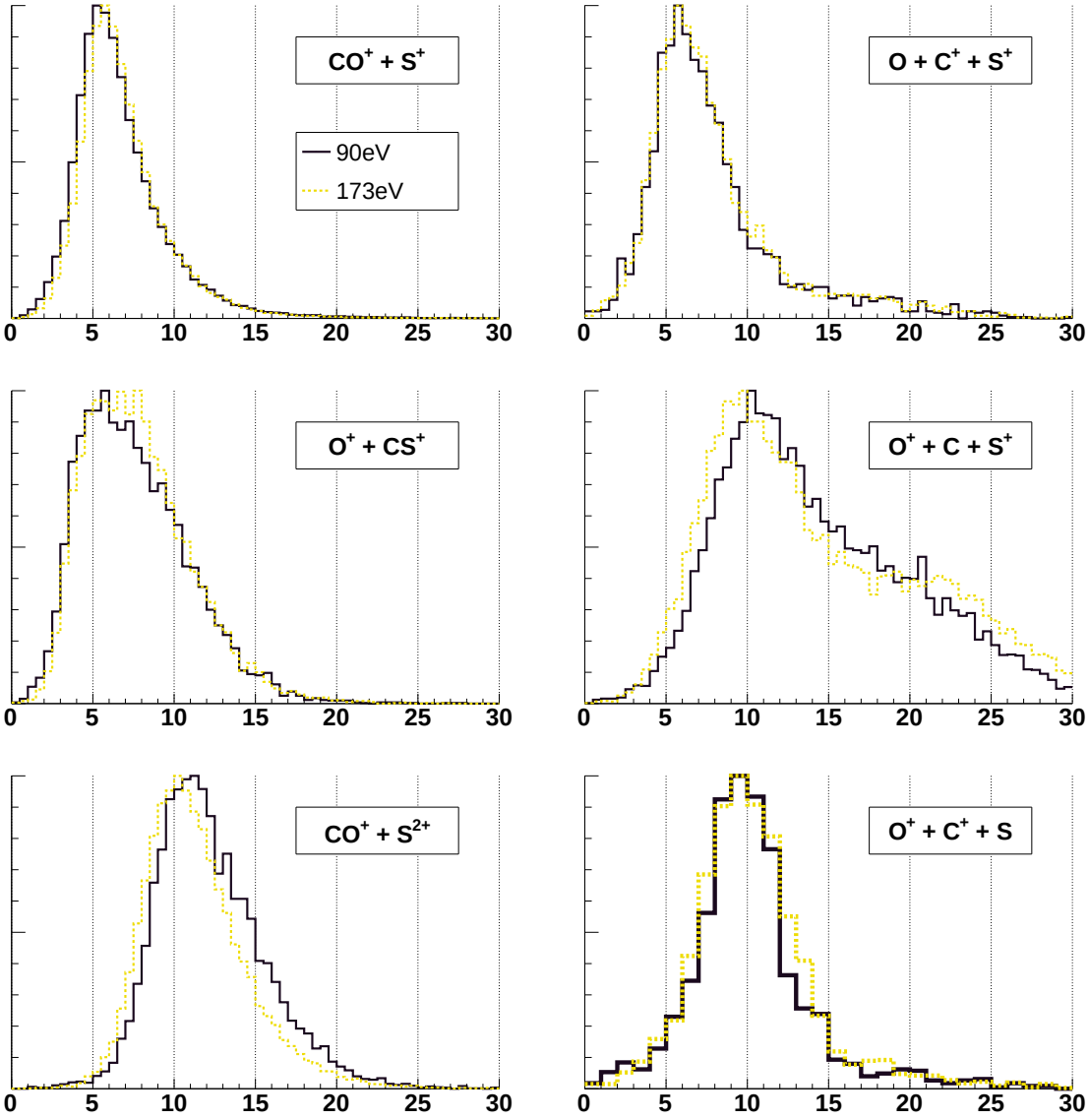

Figure 5.8: KER distributions (in units of eV) of the three possible 2-ion three-body OCS^{2+} fragmentation channels; (1,1,0), (1,0,1), and (0,1,1), and the KER distributions of the observed 2-ion two-body OCS^{q+} (q = 2, 3) fragmentation channels; $CO^+ + S^+$, $O^+ + CS^+$, and $CO^+ + S^{2+}$.

	90 eV		173 eV	
	Measured	Masuoka *et al.*	Measured	Saha *et al.*
$CO^+ + S^+$	5	5	6	6-7
$O^+ + CS^+$	6, 9 (bimodal)	∼6	7	7-9
$O + C^+ + S^+$	6 (long tail)	6, 10 (bimodal)	6	10
$O^+ + C + S^+$	10 (broad, asymmetric)	7, 10, 20 (trimodal)	10 (broad)	10
$O^+ + C^+ + S$	9 (long tail)	Not observed	10 (broad)	9

Table 5.1: Qualitative comparisons between our measured KER distributions in figure 1 and those measured by Saha *et al.* [156] and Masuoka *et al.* [125] highlighting the peak KER energies in units of electron-volts and the qualitative nature of the observed distributions.

the KER distributions are detailed in table 5.1. We first note that excitation at 173 eV produces relatively simple KER distributions with a single peak. At 90 eV, multimodal distributions are observed indicating that several different electronic states are being accessed, in agreement with the observations of Masuoka *et al.* [125]. Magnuson *et al.* [120] have calculated potential energy curves for OCS indicating that the energy available to the molecule is greater than that found in the measured KER in figure 5.8. This suggests that these processes are not limited by energetics, but rather by dynamics. Furthermore, this also suggests that several electronic states are being accessed which all dissociate and auto-ionize at different rates. Overall, we find nothing to contradict earlier observations. Additionally, in the case of S(2p) or 172 eV excitation, the Auger decay seems to result in a narrower KER distribution, or at least a more symmetric distribution relative to the case of 90 eV excitation.

Contamination in the $O^+ + C + S^+$ Channel

As discussed earlier, momentum measurements on fragmentation pathways resulting a neutral species are not complete as the neutral atom is itself never detected. Under these conditions, the reliability of coincidence momentum measurements falters as the strict momentum sum condition (Equation 2.9 is not met. Therefore, it is possible that signal measured in the neutral fragmentation channels (0,1,1), (1,0,1), and (1,1,0) shown in Figure 5.8 has contamination from foreign channels. This contamination would rise from similar

channels that have been misidentified as the neutral pathways listed here. For example, fragments from the (1,1,1) channel could be identified as those in the (0,1,1) channel if the oxygen ion from a true (1,1,1) channel was ejected with little momentum. Then, the momentum sum condition would be met for both the (1,1,1) and (0,1,1) channels.

Re-examining Figure 5.8, the unique high energy shoulders measured for the $O^+ + C + S^+$ channel at both 90 and 173 eV can be explained by false coincidences from the (1,1,1) channel. Firstly, the shoulder peaks between 20 and 25 eV, just as for the (1,1,1) channel shown in Figure 5.9. This peak is unique to the (1,0,1) channel precisely due to the reason for the false identification of (1,1,1) fragments. Namely, for false identification the carbon must have nearly zero momentum - which is often the case for the three-body breakup of OCS where carbon is sandwiched between oxygen and sulfur. The other two neutral channels, (0,1,1) and (1,1,0), would only falsely identify (1,1,1) events when the terminal ions have near zero momentum - an unlikely event in the complete 3-body fragmentation of OCS. For this reason, high energy shoulders in these channels resulting from the false identification of (1,1,1) events is suppressed.

Interestingly, Masuoka *et al.* also measure a high energy shoulder exclusively in the (1,0,1) channel and not the (0,1,1) channel. On the other hand, Saha *et al.* do not measure any high energy shoulder. In the former, KER measurements are made using the Photoion-Photoion Coincidence (PIPICO) method where only two ions are measured in coincidence with the third one inferred. Similar to the coincidence momentum analysis technique used here, such a measurement cannot distinguish between events from the (1,0,1) channel and those from the (1,1,1) channel. Without discriminating against false coincidences through the use of the zero-momentum-sum equation, all (1,1,1) events are identified as (1,0,1), resulting in the significant peak between 18 and 20 eV [125]. Saha *et al.*, however, do not measure a significant high energy shoulder because of the coincidence electron measurements. By selecting electron energies for coincident events in the (1,0,1) channel, they discriminate against events from the (1,1,1) channel and its uniquely different photo-electron energies.

Ultimately, the misidentified signal in the (1,0,1) channel is a result of applying the coincidence momentum technique where not all momentum vecotrs are measured in coincidence. This issue is mitigated in the two-ion two-body fragmentation as well as the three-ion three-body fragmentation analysis to come.

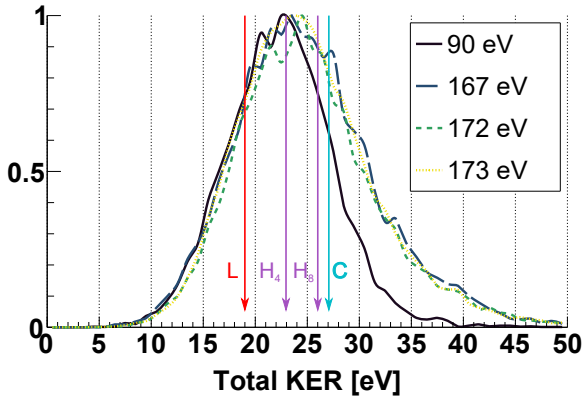

Figure 5.9: The total kinetic energy release (KER) distributions for the (1,1,1) fragmentation channel of OCS_3^+ at 90, 167, 172, and 173 eV excitation. Arrow C indicates the expected KER (26.96 eV) when fragmenting from the ground-state geometry assuming a purely Coulombic potential and point-like particles. Arrow L indicates the experimentally measured KER after ionization by a few cycle infrared femtosecond laser pulse [189]. Arrows H4 and H8 indicate the experimentally measured KER for ionization by highly charged Argon ions, Ar^{4+} for H_4 and Ar^{8+} for H_8 [191]

5.3.2 (1,1,1) kinetic energy release

The total KER by OCS^{3+} fragmenting into three singly charged ion fragments is shown in figure 5.9 for multiple x-ray energies. The arrow marked 'C' indicates the expected KER when fragmenting from the most probable ground-state geometry ($r_{CO} = 115.78$ pm, $r_{CS} = 156.01$ pm [116], and $\theta = 175°$ [191]) assuming a purely Coulombic potential and point-like particles [25]. For the (1,1,1) fragmentation channel of OCS^{3+} we find this Coulombic KER to be 26.96 eV. The KER distributions for each photon energy peak at energies between 24 and 26 eV, making the (1,1,1) KER 89 - 96% of the Coulombic value.

The KER distributions for each excitation energy peak at approximately the same energy (24 - 26 eV), which is slightly less than that of a perfectly Coulombic explosion (indicated by arrow C). KER distributions from previous HCI impact work peak at a similar energy (23 and 26 eV, indicated by arrows H_4 and H_8 respectively) to those in figure 5.9, with impact by Ar^{8+} peaking at the higher energy (26 eV) and being more Coulombic than impact by Ar^{4+} which peaks at 23 eV [191]. KER distributions for the (1,1,1) fragmentation channel of OCS^{3+} by femtosecond induced Coulomb explosion [189] always peak at lower energies (maximum of 19 eV indicated by arrow L) than those of

figure 5.9 even for very short pulses (7 fs).

From this we can identify that the x-ray and HCI impact excite a similar group of excited states but the femtosecond laser pulse experiment [189] accesses preferentially not only the ground state of the 3+ molecular ion, but its outer regions where the quasi bound nature is dominant [52, 188]. Both exhibit a small tail although the KER distribution of Ar^{4+} impact is quite symmetric while that of Ar^{8+} is noticeably asymmetric about their peaks. They also exhibit a steeper low-energy rise and a shallower high-energy fall with a significant tail for all pulse lengths.

In comparing the overall energy distributions resulting from the different photon energies we immediately notice that the maximum KER for the (1,1,1) fragmentation channel from 90 eV excitation is 40 eV whereas for 167, 172, and 173 eV it goes up to 50 eV. It also has a steeper high-energy falloff than the KER distributions for other excitation energies, suggesting that energetics are limiting the available KER. This is a consequence of conservation of energy as the total amount of energy available to the molecule is determined solely by the absorbed photon from the x-ray beam.

In the case of excitation at 90 eV it takes 49.520 eV to produce $O^+ + C^+ + S^+$ from OCS with three zero energy electrons leaving a maximum of 40.480 eV available for the fragments and electrons. To obtain the value of 49.520 eV, we used the fact that the bond dissociation energy of S-CO to produce S + CO is 3.120 eV, and for C-O to produce C + O is 11.162 eV [82, 170]. The first ionization energies of C, O, and S are 11.260 eV, 13.618 eV, and 10.360 eV respectively [115], giving a total of 49.520 eV. This corresponds with the triple ionization threshold measured by Masuoka [123] of 52.3 eV. Thus when excited by a 90 eV photon a maximum of 40.480 eV is available to the (1,1,1) KER. The KER measured for the (1,1,1) fragmentation channel at 90 eV cuts off at almost exactly 40 eV, supporting this argument. To our knowledge this is the first time that such a clear KER cut off has been observed, associated with a limit to the input energy.

Laksman *et al.* measured the total KER for excitation near the C(1s) edge [106]. Their KER distributions for OCS^{3+} looks quite similar to our 167, 172, and 173 eV data, but with possible calibration differences. They show a peak from 10 to 30 eV with the high energy cut off having a slightly elongated tail compared to the low energy rise. Their KER distributions peak at a slightly lower energy (by only about 3 - 5 eV) compared to the current results in figure 5.9.

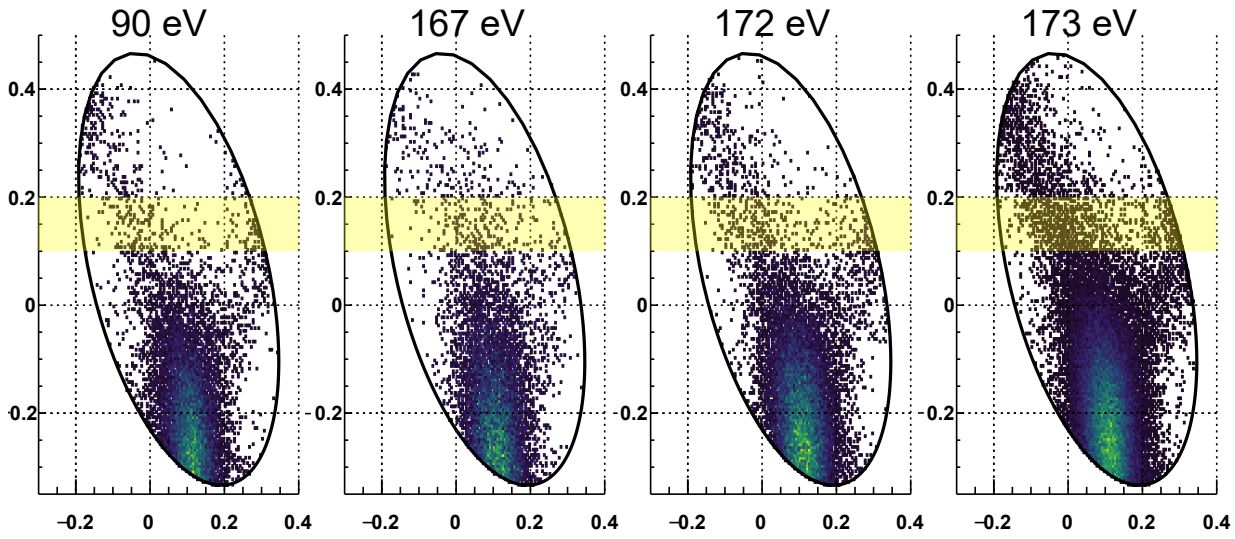

Figure 5.10: Dalitz plots for the (1,1,1) fragmentation channel of OCS^{3+} at 90, 167, 172, and 173 eV excitation. The x-axis indicates the difference between the fraction of total energy released by the O and S ions divided by a scaling factor, and the y-axis is the fraction of energy released by the C ion minus an aesthetic factor to get the plot roughly centered about $y = 0$. Data was used exclusively from the region highlighted in yellow to produce a plot of the number of counts along the x-axis in figure 5.12. Each Dalitz plot is individually normalized such that the maximum is 1. The red crosses indicate the location on the Dalitz plot of a purely Coulombic fragmentation, that is, when fragmenting from the ground-state geometry assuming a purely Coulombic potential and point-like particles.

5.3.3 (1,1,1) geometry and dynamics

To identify the possible break up channels for the OCS^{3+} states in more detail we use the Dalitz plot method, a well-established technique for displaying the possible molecular dissociation geometries in a two dimensional histogram [42]. Dalitz plots for the (1,1,1) channel are shown in figure 5.10. The experimental signal peaks near the red crosses at (0.11, -0.29) which indicate the location on the Dalitz plot of a purely Coulombic fragmentation, that is, when fragmenting from the ground-state geometry assuming a purely Coulombic potential and point-like particles. It is important to note that the geometry of the molecule and the momentum vectors are related in a nontrivial way and so the molecular bond angle is not the same as the angle between the momentum vectors of the terminal ions although sometimes simplified to such [106]. The momentum vector angle is typically smaller than the molecular bond angle but can be larger for extreme bending.

Bending of the molecule in a concerted dissociation process, the most common process, results in a reduced angle between the outside momentum vectors and is associated with approximately vertical changes from the equilibrium point on the Dalitz plot.

The significance of areas to the left or right of the equilibrium point have a more subtle origin, there is not a direct relationship to asymmetry of bond length but there is an association with the simultaneity with which bonds break, also known as the concertedness of the bond breaking reactions. As an illustration of this relationship, fragmentation of OCS^{3+} into a metastable CO^{2+} ion which itself breaks up after some life time (tens to hundreds of femtoseconds [136]), appears as a diagonal region, stretching from the bottom right (around 0.25, -0.33) to the top left (-0.15, 0.35). The neat linear relationship between how stepwise the bond breaking occurs and the amount of bending is simply related to conservation of angular momentum causing the metastable molecular ion to rotate as it separates from the S^+ ion. The amount of rotation experienced by the metastable ion before breakup correlates to different positions along the diagonal arms on the Dalitz plot, though not homogeneously. Therefore statistics are built-up with a higher density at the edges of the sequential breakup features

Three fragmentation channels are visible in the Dalitz plots for 90, 172, and 173 eV excitation; concerted breakup and two sequential breakup channels. The first sequential process proceeds via the metastable CO^{2+} ion, as described above and the second via a metastable CS^{2+} molecule, which appears as a diagonal region from the bottom left towards the top right. It is worth noting that both of the stepwise channels are strong in the case of OCS^{3+} and are represented on a linear intensity scale, whereas for the CO_2 and CS_2 molecules [136, 81] the stepwise process required the use of a logarithmic scale. Sequential

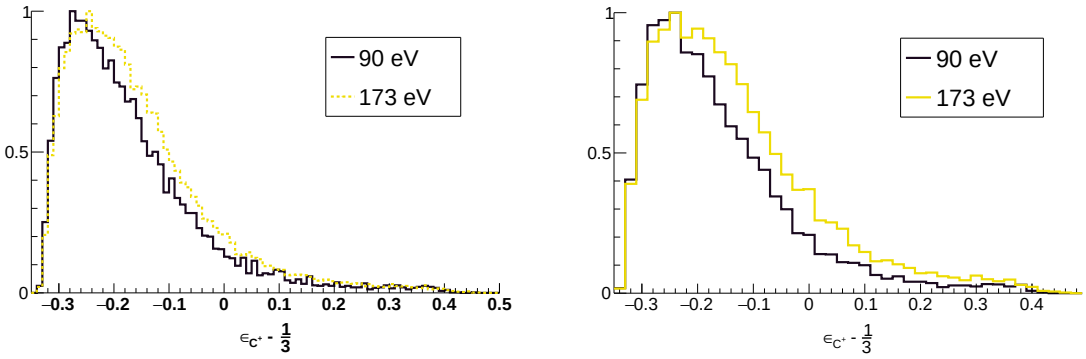

Figure 5.11: (a) Projections on the y axes of the Dalitz plots of figure 3 comparing the direct ionization process of 90 eV with the Auger ionization process at 173 eV. Each curve is individually normalized such that the maximum is 1. Gray drop lines indicates the location on the Dalitz plot of a purely Coulombic fragmentation, that is, when fragmenting from the ground-state geometry assuming a purely Coulombic potential and point-like particles. (b) Same as (a) but from data limited to the region of identical kinetic energy release - the range [15 ev, 22 eV] as can be seen in figure 5.9

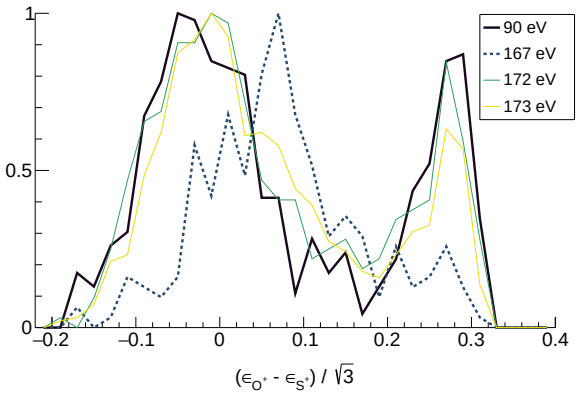

Figure 5.12: A count of the number of events with $0.1 \leq \epsilon_{C^+} - 1/3 \leq 0.2$ from the region highlighted in yellow in figure 5.10 for photon energies of 90, 167, 172, and 173 eV. The two arms due to sequential breakup (or stepwise) processes in the 90, 172, and 173 eV Dalitz plots can be seen as two peaks at $x \sim 0$ and $x \sim 0.3$. However, for 167 eV only a single peak can be observed at $x \sim 0.1$.

breakup channels appear weak in the Dalitz plots of Laksman *et al.* [106] for the case of C(1s) excitation and for highly charged ion impact work [191] although this may be due to the method of trigger which can lead to loss of sensitivity to the generally low energy process. Both of these cases may be resolved by further experimental attention. In the current work, the 167 eV data shows a much lower stepwise signal which we will return to later. By comparison, Dalitz plots produced from previous femtosecond laser work [189] show narrower and more pronounced arms suggesting that the metastable molecular ion is more vibrationally excited by the synchrotron ionization processes, leading to increased range of energy release by its breakup.

The final dissociation process, the concerted breakup in which both bonds break at the same time, is the most significant channel. In the Dalitz plots of figure 5.10 the concerted process is represented by a zone from the bottom edge up to about zero on the y-axis. Although as mentioned above, the peak signal is found to be near to the equilibrium geometry, the vertical and horizontal spread are consistent with bending and a degree of stepwise breakup respectively. This is a similar region to that exhibited under ionization by 7 fs laser pulses and HCI impact [191, 189] and in contrast to the progressively vertically stretched region characteristic of longer pulses (up to 200 fs) where the molecule has time to bend in the laser field, and indeed is bent by the field [189].

The concerted process offers us the best opportunity to see differences due to the slower (10 fs) multiple ionization event associated with the Auger process, which therefore affords increased time between ionization steps and so more time is spent on the singly and doubly ionized potentials than is possible for the direct ionization process ($<$1 fs). The result of these increased residence times would include a greater degree of stepwise nature and increased bending exhibited in the Dalitz plots for 172 and 173 eV compared to the direct process best exemplified by 90 eV. There are indeed small but discernible differences between the direct and Auger ionization plots, particularly in the vertical direction, which can be seen more clearly by integrating over the vertical axes and constructing a new plot shown in figure 5.11.

As expected, the 173 eV data shows both more bending in the form of a peak which is at higher y-value and a wider distribution than the 90 eV data. The shift of the peak although small is significant as the 90 eV distribution is peaked very close to the predicted equilibrium value, marked by the gray dropline, indicating that for the fastest multiple ionization events at 90 eV, very little motion is possible for the molecule during the ionization process whereas for 173 eV even the fastest multiple ionization event allows time for some bending to occur. The conclusion that this is a time-scale effect depends on the assumption that the states of the molecular ions occupied are the same. The only certain way to determine this is to observe the electrons emitted during the ionization process, but in the absence of this a

good indicator is the total KER by the ionic fragments. Although the patterns of energy release are very similar for all photon energies, we can restrict the energy range over which we compare the bending parameter to one where the total KER for 90 eV and 173 eV photons is nearly identical. This region (15 - 22 2eV) can be seen to be identical in 5.9. The right-most distribution in figure 5.11 shows the corresponding comparison between the Dalitz plot y projection exhibiting the same enhanced peak bend and wider range of bending.

The data at 167 eV which is just below the S(2p) edge has some significant differences to the other plots in figure 5.10. For 167 eV the stepwise arms appear diminished and a single central distribution stretching upwards is apparent. This difference becomes clear when we consider the highlighted region in figure 5.10, for which the signal is plotted in figure 5.12 is integrated in the vertical direction. At a photon energy of 167 eV, the distribution is dominated by a maximum peaking close to $x = 0.1$ compared to the other energies which are dominated by two maxima near $x = 0$ and $x = 0.3$, each corresponding to an arm on the Dalitz plot. Although some stepwise events still exist at $x = 0.3$ for 167 eV, the dominant distribution near $x = 0.1$ represents processes leading to enhanced bending.

In order to gain some insight into the difference, we consider that excitation by a 167 eV photon corresponds to exciting OCS to the $(2p_{3/2})^{-1} \rightarrow 4s$ Rydberg state [55]. The Rydberg state (and the direct ionization) should only show vibrational excitation in the symmetric stretch (v_1) and asymmetric stretch (v_3) modes. The molecular state we are exciting to is linear and so we do not expect to observe any bending dynamics. Therefore as a major channel we should see no difference between 90, 167, 172, and 173 eV.

However the OCS molecule may be excited by a 167 eV photon to other states with similar energies. Excitation at $(2p_{3/2})^{-1} \rightarrow 4s$ (167 eV photon) sits on the tail of the highly bent $\pi^*_{1/2}$ state at 165.4 eV. Thus as well as exciting the 4s Rydberg state which is expected to be linear, we are additionally exciting the $\pi^*_{1/2}$ state which is expected to be highly bent due to the strong interactions between the excited electrons and the remaining core electrons [55]. Thus following excitation at 167 eV we see the stepwise arms due to the excitation of the 4s Rydberg state, and we additionally see a central distribution stretching upwards due to excitation to the $\pi^*_{1/2}$ state. This central arm is indicative of a bending process occurring. Typically, bending of molecules during single photon ionization is accepted to occur but be incomplete on the timescale of the multiple ionization event, differing degrees of bending have been inferred using the photo electron - photo ion - photo ion - coincidence method depending on the photon energy [135, 109], though not because of differing timescales, but in the context of our current discussion, timescales are important. The extent to which the molecule is allowed to bend significantly during the fast multiple ionization process needs to be addressed, and with the current time and position sensitive

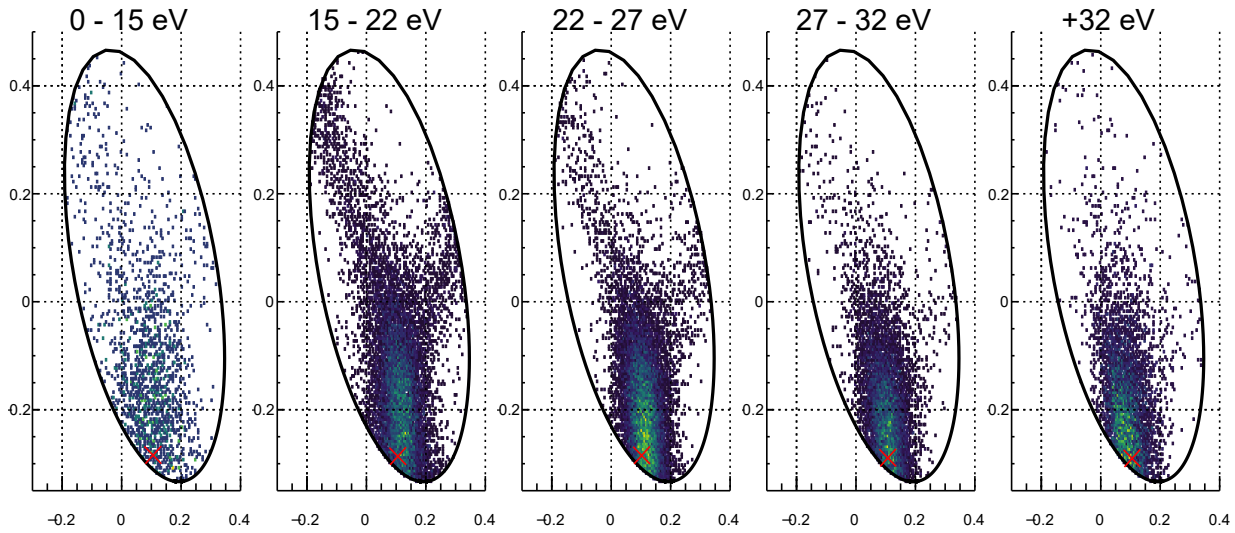

Figure 5.13: Dalitz plots for the (1,1,1) fragmentation channel of OCS^{3+} at an excitation energy of 173 eV for different ranges of KER. The red crosses indicate the location on the Dalitz plot of a purely Coulombic event, that is, when fragmenting from the ground-state geometry assuming a purely Coulombic potential and point-like particles.

method we can determine the full bend distribution. The important factor is that the peak in the Dalitz plot y projection in left disribution in figure 5.11 is still close to the equilibrium indicating that the fastest ionization events occur before any bending can happen, but the slower ionization events can image the molecular dynamics induced by the $(2p_{3/2})^{-1} \rightarrow$ 4s excitation. Slower multiple ionization events do of course happen, when metastable excited states are accessed, as with the stepwise processes, which can take hundreds of femtoseconds to complete.

In order to consider the connection between the KER and the dynamics taking place during breakup, figure 5.13 shows the Dalitz plot for 173 eV data sliced into five energy ranges. At low values of KER (0 - 15 eV), the Dalitz distribution is almost uniformly distributed around the simulated Coulombic center indicated by a red cross. There are events in the regions associated with stepwise processes but the arms are not well-defined. At mid values of KER (15 - 22 and 22 - 27 eV), the concerted distribution is centered a little to the right of the Coulombic simulation ($x = 0.11$) in contrast to the overall distribution which is centered horizontally close to this equilibrium point as indicated by figures 5.10 and 5.12. This implies that for molecules near equilibrium in the bending

coordinate, the S-C bond is breaking shortly before the CO bond resulting in relatively more energy deposited in the O^+ ion than the S^+ ion. The long timescale stepwise arms are well defined and strongest in the 15 - 22 eV range showing that they originate from excitation to specific metastable states which can only result in significantly lower than Coulombic KER. A possible mechanism at this KER range is that during the Auger cascade a dication is formed as OCS^{2+} rapidly dissociates to $S^+ + (CO^+)^*$ which at a later stage during the dissociation process autoionizes to CO^{2+} to eventually form $C^+ + O^+$. It is interesting to note that the stepwise arms are most prominent in the 15 - 22 eV KER range, which overlaps with, or is only slightly greater than, the 2 ion KER (section 5.3.1). At higher values of KER (27 - 32 and >32 eV) the concerted process shifts to the left until it is centered horizontally on the simulation, indicating a higher degree of simultaneity, consistent with the assumption of instantaneous bond breaking. This is the first such observation of a horizontal shift in the position of the concerted process but inspection of [74] shows the existence of an overall shift for the few cycle laser results which also exhibit an overall lower peak in KER consistent with the trend observed here. A further significant feature of the plots is the progressive restriction of the concerted region in the vertical direction towards the equilibrium point with increasing KER, which is consistent with both bonds breaking more rapidly.

5.3.4 OCS^{4+} kinetic energy release

The KER distributions for the three OCS^{4+} channels producing triple ion fragments are shown in figure 5.14 for 173 eV excitation.

OCS^{4+} events are significantly rarer than OCS^{3+} events (10 - 100 times rarer) hence the poorer statistics. The most commonly observed fragmentation channel of OCS^{4+} is the (1,1,2) channel, followed by the (1,2,1) and then the (2,1,1) channel. This can be explained by the increasing second ionization energies of S, C, and O, which are 23.34, 24.38, and 35.12 eV respectively [115]. These distributions are also very similar at 167 and 172 eV. At 90 eV excitation, OCS^{4+} production is energetically unfavourable and so events are extremely rare and the fragment ions are left with little kinetic energy. The KER distributions in figure 5.14 all have similar shapes and peak at similar energies (40 - 42 eV). They are broader than the KER distributions for the (1,1,1) fragmentation channel in figure 5.9. The (1,1,2) distribution peaks exactly at the Coulombic value, while the (2,1,1) distribution peaks at a slightly lower energy than the Coulombic value, and the (1,2,1) distribution peaks at a noticeably lower energy than the Coulombic value.

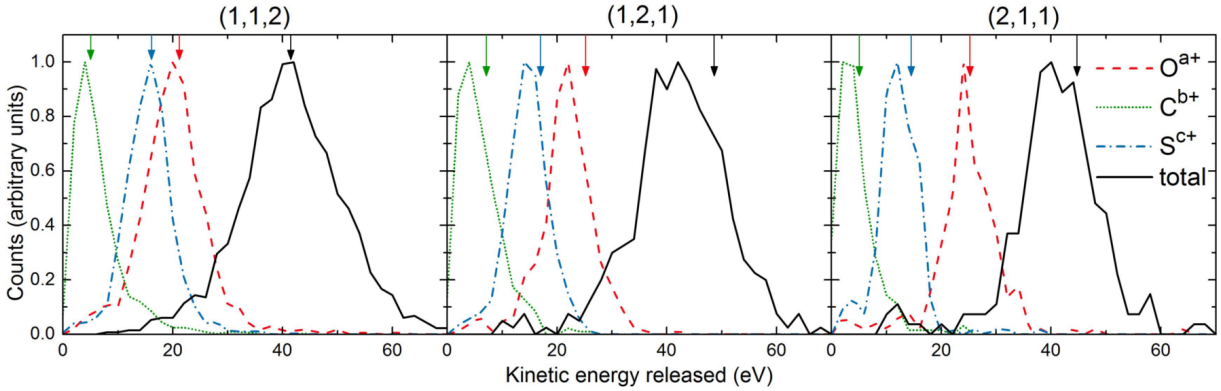

Figure 5.14: KER distributions for the three OCS^{4+} channels producing triple ion fragments; (1,1,2), (1,2,1), and (2,1,1) at 173 eV excitation. The total KER distributions are plotted as well as the KER distributions of the individual fragments. The arrows indicate the expected KER when fragmenting from the ground-state geometry assuming a purely Coulombic potential and point-like particles. Reprinted with permission from IOP.

5.3.5 OCS^{4+} geometry and dynamics

Dalitz plots for the three possible fragmentation channels of OCS^{4+} at an excitation energy of 173 eV are plotted in figure 5.15. In the case of the (1,1,2) fragmentation channel, the majority of observed events are concerted and centered around the Coulombic simulation indicated by the red cross. Some CO^{2+} metastable sequential events exist giving a diagonal background. The (1,2,1) fragmentation channel is similarly centered around the equilibrium position and no stepwise channels are possible. The (2,1,1) fragmentation is unusual however because it is far from centered on the equilibrium cross and shifted to the right which means the O^{2+} ion carries a significantly higher fraction of the total KER than for the equilibrium Coulombic case. As in the less extreme case of the low energy release (1,1,1) channel this can be seen as indication that the CS bond breaks before the CO bond. In order to formulate a possible cause for this phenomenon, we should first consider how an initial ionization process which results in removal of a core 2p electron from the sulfur atom can finally result in fragmentation involving a more highly ionized oxygen ion than the sulfur ion, despite its distance from the initial ionization site and its higher double ionization potential. In order to do this we should consider the molecular orbitals of neutral OCS [144]. The HOMO (2π) is anti-bonding with respect to the O-C bond and has considerable overlap with the S. Thus involvement (loss) of this valence orbital in the Auger cascade will result in the relative strengthening and shortening of the O-C bond.

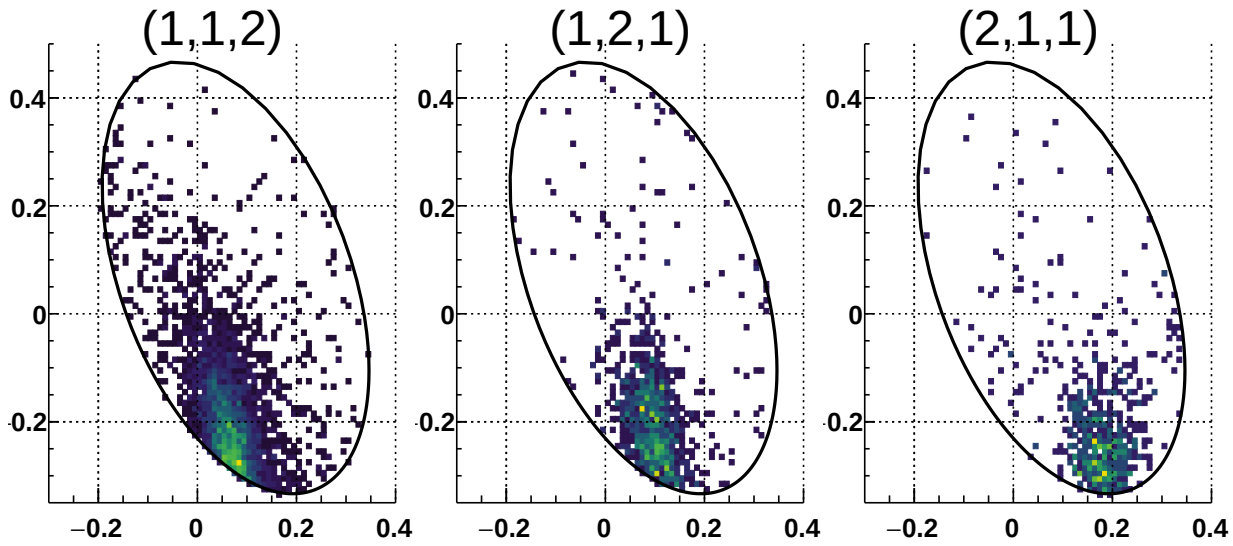

Figure 5.15: Dalitz plots for three possible fragmentation channels of OCS^{4+} at a photon energy of 173 eV. The red crosses indicate the location on the Dalitz plot of a purely Coulombic fragmentation, that is, when fragmenting from the ground-state geometry assuming a purely Coulombic potential and point-like particles.

The HOMO-2 (1π) is extremely bonding with respect to O-C and has negligible overlap with the S, thus the retention of this orbital during the Auger cascade will again result in a shortening of the O-C bond and strengthening it with respect to the C-S bond, while increasing the amount of charge being retained near the O atom. As mentioned earlier, the Dalitz asymmetry cannot be simply linked to asymmetry of bond length, but implies breaking of the C-S before the C-O bond as a result of the asymmetry inducing cascade. To our knowledge this is the first such observation.

5.4 Conclusions

We have attempted to compare the ionization by direct (90 and 167 eV) and Auger processes (172 and 173 eV) resulting from the S(2p) core ionization, in order to discern any timescale effects which might be manifested in the plethora of processes which are initiated. Both methods can be thought of as ultrafast in terms of the speed with which electrons are removed from the molecule, but the direct process has the potential to be the faster, at the femtosecond scale as opposed to the tens of femtoseconds scale. For the low ionization processes we see little difference between the current measurements and those of previous work [124, 156] irrespective of the photon energy, although we are able to add considerable detail due to the high photon flux available in the CLS. The consistency is perhaps not surprising given that these processes release relatively little energy as they are not dominated by Coulombic potentials and are therefore relatively robust to time scale changes. Even for triply ionized states the major difference between energy release is dominated by the limitation imposed by a photon energy of 90 eV. It is only when we look at the pattern of momentum release in comparing 90 and 173 eV Dalitz plots that we can see distinct evidence of timescales effects. A pattern, particularly imprinted in the peak position of the bending distribution, indicates that there is very little dynamics before ionization is complete, for the direct process, but that there is a small but significant bend characteristic of stepwise ionization, present for the Auger process. In fact the equilibrium bond angle of OCS is remarkably well imaged for the (1,1,1) channel by the peak of the energy integrated Dalitz plot. This is in contrast to the results of 7 fs laser pulses [189], suggesting that the ionization process is considerably faster for the synchrotron case, in fact this would be faster than any tabletop multiphoton systems [87] which shows great promise in imaging molecular dynamics on femtosecond time scales. Our results show that below the S(2p) edge, we can see ionization events which involve metastable steps and result in large amplitude angular motion in both concerted (167 eV) and stepwise processes. We have identified, for the first time, a connection between low KER and breaking of the S-C bond

before the C-O bond. Finally for the 4+ ionization, we see evidence that in generating the (2,1,1) channel the molecule is excited to even more asymmetric dissociation. This phenomenon is only observable because of the large photon flux, but indicates that more exotic phenomena may be observable using other energies available at the third generation synchrotron source. In conclusion we have been able to identify a surprisingly rich set of dynamics, on a femtosecond timescale resulting from Auger decay after ionization of the S(2p) electron and see evidence that direct ionization takes place on shorter timescales. In order to confirm the exact timescales, with which the processes proceed, it is possible that pump probe studies could be carried out utilizing pulses from a free electron laser or high harmonic attosecond source.

5.5 Acknowledgments

We gratefully acknowledge research funding from NSERC (Natural Sciences and Engineering Research Council of Canada). Part of the research described here was conducted at the CLS, which is supported by the Canadian Foundation for Innovation, the Natural Sciences and Engineering Research Council of Canada, the University of Saskatchewan, the Government of Saskatchewan, Western Economic Diversification Canada, the National Research Council Canada, and the Canadian Institutes of Health Research.

Chapter 6

Comparison of OCS Dynamics Initiated by HCI and Femtosecond IR Pulses

6.1 Introduction

This chapter includes edited text from the publication [188].

The experimental study of multiple ionization and complete breakup of small molecules in collision with HCI [136, 94] or in intense femtosecond laser pulses [17] is a field of considerable interest to molecular physics. This is especially so since the development of the multiple coincidence method using time and position sensitive detection [132]. The technique allows the detection of every fragment ion produced by a single molecule, and furthermore the determination of momentum for each fragment, revealing a rich variety of molecular parameters.

HCI impact initiated ionization allows the dependence of final ionization state parameters (such as the total energy release and the angles between the momentum vectors of the fragments) to be determined typically as a function of projectile energy and charge state [169, 158]. These parameters can then in turn be used to determine how closely the dissociation reaction can be described by a purely Coulombic potential and to what extent the bonds break simultaneously in a concerted dissociation reaction or one at a time in a stepwise manner [136]. For femtosecond laser initiated ionization, the emphasis has been more on the effect of pulse length, which until the advent of hollow fiber pulse compression [142] was limited to tens of femtoseconds [71]. This is a regime in which molecular

motion was fast compared to pulse length and so ionization was dominated by enhanced ionization [17] which limited energy release to around 50% of the Coulombic level expected from equilibrium. The first experiments to use sub ten femtosecond pulses [112] immediately found energy release in bent triatomic molecules (D_2O and SO_2) at around 85% of the Coulombic value while more work on the linear triatomic CO_2 using sub 7 fs pulses recently [17] achieved above 95% for some channels.

Here we look at new measurements from femtosecond ionization of the molecule carbonyl sulfide (OCS) using sub 7 fs pulses at the ALLS which we compare to new and recent measurements made with Ar^{8+} at 120 keV made at the Tokyo Metropolitan University Electron Cyclotron Resonance Source (TMUECRIS). We then concentrate on the peak energy released by the many channels and compare to previous work by our groups and others on CO_2 and CS_2 using both HCI impact and few cycle pulses. We assess the comparison in the context of whether or not the current few cycle pulse results are still limited by molecular deformation on the pulse timescale.

6.2 Experimental

The HCI impact data was recorded in Tokyo Metropolitan University (TMU) with a setup described in [191] where Ar^{8+} ions from the TMUECRIS were accelerated to energies of 120 keV. The beam was trimmed with a 0.5 mm aperture and crossed a target gas beam of OCS introduced through a multicapillary plate. Ejected electrons were accelerated in the opposite direction and passed through a 1 mm hole as well as an array of capillaries before being detected by a channel electron multiplier. The detection of these electrons produces the trigger for the data acquisition system. The fragment ions drifted through a 204 mm TOF region until striking a pair of 120 mm diameter microchannel plates in Chevron formation. The electron avalanche from the second microchannel plate was collected by a backgammon type anode [132, 133]. The four output signals from the anode were amplified by charge-sensitive preamplifiers (Ortec: 142B) and sent to a four channel Analog-to-Digital Converter (ADC) equipped PC. The four channel spectra were analyzed with a sophisticated algorithm to extract the xy position and time-of-flight of each detected event in coincidence.

The femtosecond laser experiments were performed at the ALLS using the multi-kHz TitaniumSapphire (TiSa) laser system (KMLabs). Few-cycle pulses (7 fs) are obtained using nonlinear propagation in a hollow core fiber filled with Ar and by dispersion compensation using chirped mirrors. To achieve longer pulse duration, the fiber was evacuated. Using an acousto-optic programmable dispersive filter located in the stretcher of the TiSa

amplifier,we applied second order dispersion ($\Phi^{(2)}$ (fs^2)) to achieve the desired pulse duration. The laser pulses are focused by a parabolic mirror (f = 10 cm) on a well-collimated supersonic jet of CO_2 or OCS inside a uniform-electric-field ion imaging spectrometer. The fragments are detected and their full three-dimensional momenta are determined using sophisticated software and a time- and position-sensitive delay-line anode detector at the end of the spectrometer (RoentDek Handels GmbH).

6.3 Results

We concentrate on the highest channels observed which for both methods are the six times ionized channel [191] (referred to as (2,2,2)) and the seven times ionized molecule in which the oxygen and carbon fragments are doubly charged and the sulfur is triply charged (referred to as (2,2,3)). Figure 6.1 shows that by reducing the laser pulse length systematically from 200 fs down to below 7 fs the energy released in fragmentation increases. We express the energy as a percentage of the amount of energy released if the molecule fragmented into point-like ions along a purely Coulombic potential from the ground state equilibrium geometry.

The value increases from around 50% (a characteristic of enhanced ionization) to values above 80%. The higher charge state gives rise to a slightly higher ratio of energy released, but perhaps more significant is the fact that the peak of the energy released as the result of HCI impact is still significantly higher (greater than 90% of Coulombic).

To confirm this is a trend across the possible channels we compare the current sub 7 fs laser results for all channels observed here and the current and previous results for HCI impact [169], in Figure 6.2 which shows a clear trend of lower energy release for the laser pulse ionization. Furthermore, Figure 6.3 confirms that this trend exists for CO_2 for channels higher then (1,1,1). It should also be noted that although [169] is high energy impact with Xe^{18+} where the ionization process differs somewhat from that expected for Ar^{8+}, previous work on CO_2 [158] also using Ar^{8+} showed fragmentation energies greater than 100% Coulombic energy released for the high channels recorded. To investigate this further we need to consider more than simply the peak in energy release. Figure 6.4 shows the energy distributions recorded for two fragmentation channels in OCS, clearly depicting a qualitative difference between the two ionization modes, with the 7 fs laser pulse producing significantly narrower distributions at around $E_{FWHM} = E_{Peak}/5$ compared to the HCI initiated case $E_{FWHM} = E_{Peak}/2$.

This phenomenon indicates that the electron capture process characteristic of low energy HCI impact excites a wide range of electronic states in the final ionic level. The

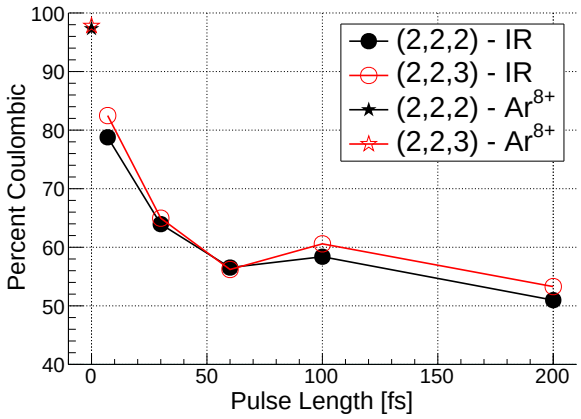

Figure 6.1: Pulse length dependence (circles) of the percentage of Coulombic energy released by the complete molecular disintegration of OCS for the (2,2,2) and (2,2,3) channels. Indicated are 0 fs are the measurements through HCI initiated CEI with Ar^{8+} impact at 120 keV (stars)

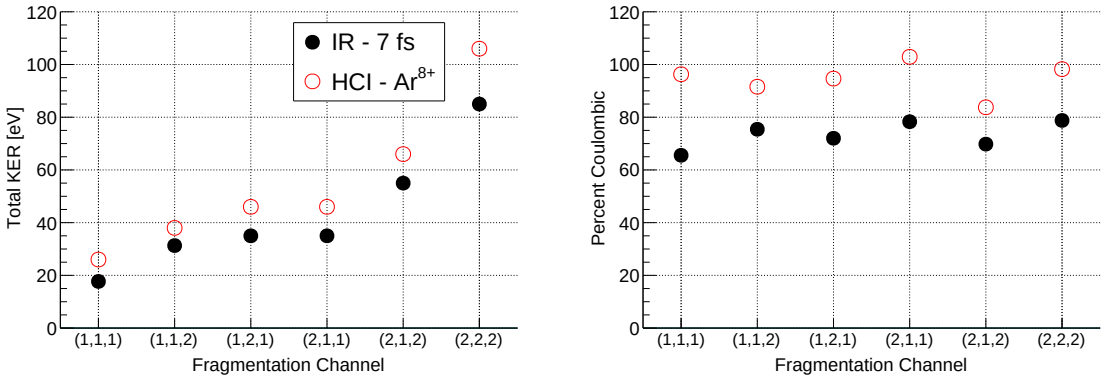

Figure 6.2: [LEFT] Total KER for various fragmentation channels of OCS initiated by Ar^{8+} HCI and sub-7 fs IR pulses. [RIGHT] Same as [LEFT] but KER measured as a percentage of the Coulombic value.

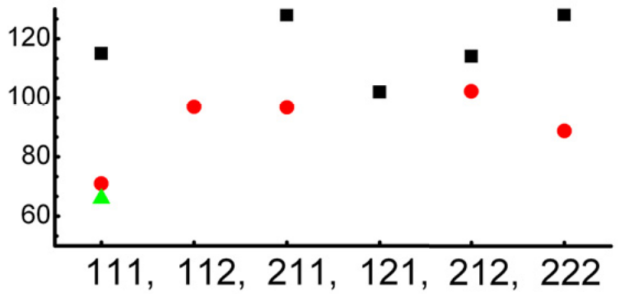

Figure 6.3: KER peaks measured as percent Coulombic for CO_2 fragmentation channels. Sub 7 fs laser pulse initiated ionization (red circles) and ion impact Xe^{18+} (black squares) [94] and Ar^{8+} ion impact green triangle [17, 169]. Reprinted with permission from IOP.

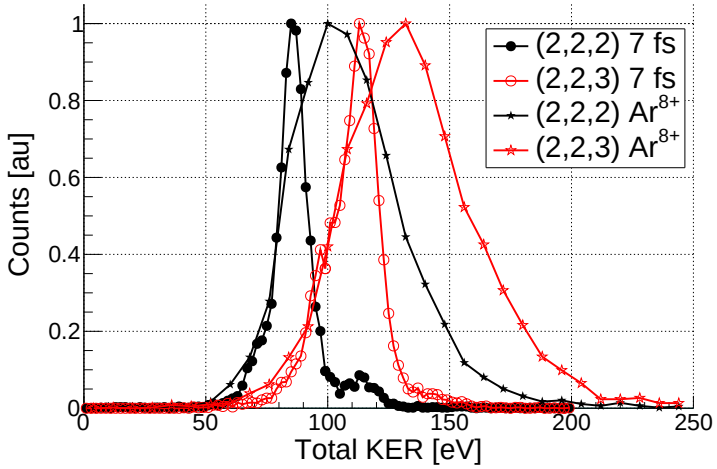

Figure 6.4: Energy distributions of the (2,2,2) (black) and (2,2,3) (red) channels of OCS ionized by sub 7 fs (circles) laser pulses and 120 keV Ar^{8+} (stars) respectively.

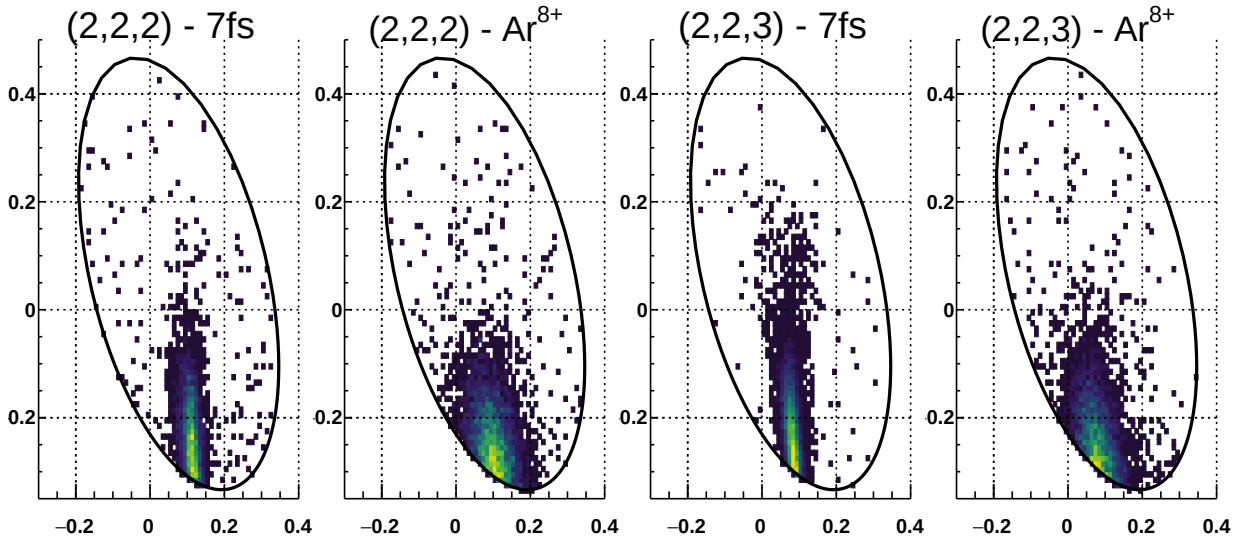

Figure 6.5: Comparison of Dalitz pots for the (2,2,2) and (2,2,3) channels of OCS ionized by sub 7 fs laser pulses and Ar^{8+} at 120 keV

range of geometries which the exploding molecules can exhibit is best depicted using the Dalitz plotting method [136, 191]. The plot compares the energy of the ions at the ends of the molecule on the x-axis with the energy of the central ion on the y-axis. Because OCS is an asymmetric molecule the complete geometric space is not a circle. The range of equilibrium geometries would be represented by a small region around (0.10, -0.28) for (2,2,2) and (0.09, -0.28) for (2,2,3) where bending gives more energy to the central ion and so results in vertical translation while asymmetry in the bond lengths result in data to the left or right of the equilibrium point. Figures 6.5 show how the laser initiated and HCI initiated ionization process affects the explosion geometry in quite distinct ways. Although the data regions of all the plots stretch for similar vertical ranges indicating considerable bending is introduced in both ionization process, plots b and d show that there is a wider range of asymmetry in the bond lengths for the HCI initiate process.

6.4 Conclusion

The new results presented here for OCS and the previous works on CO_2 shown alongside each other for the first time indicate several intriguing possibilities depending on their

interpretation. Firstly that the laser ionized molecule still has the opportunity to relax slightly on the few femtosecond timescale, stretching to longer bond lengths during the stepwise ionization process, characteristic of multiple ionization by a few cycle laser pulse. This would mean that shorter laser pulses such as sub 5 fs might result in energy release at the Coulombic level or higher for linear triatomic molecules. It is also possible that the higher bandwidth necessary to produce these pulses would result in wider energy release spectra such as seen in the HCI impact. From the Dalitz plots, it is possible that the greater asymmetry in structure observed for HCI impact could be a function of momentum transfer during the electron capture process. This could be investigated further by detecting the projectile final charge state in order to categorize the energy release and break up geometry in terms of ionization process.

Chapter 7

Proton Migration in Acetylene

7.1 Introduction

This chapter includes edited text from the publication [87].

Since the introduction of femto-chemistry [201, 193, 16, 67, 195], electron or X-ray diffraction have been the most commonly used techniques to track nuclear rearrangement in molecules [32, 130, 51, 12]. Unfortunately, these techniques are largely insensitive to the more subtle and irregular structural changes that can occur within a single small molecule undergoing a chemical reaction. Pump-probe CEI allows observation of these changes on a femtosecond timescale with atomic resolution [112, 17, 126, 79]. So far, however, important phenomena such as proton migration in the acetylene cation have only been observed using vacuum ultraviolet light Vacuum Ultraviolet Light (VUV) from a FEL [90].

Since laser-driven tunnel ionization preferentially ionizes a neutral molecule to the electronic ground state of the cation, any subsequent nuclear dynamics will generally occur on that state. The ability to readily initiate dynamics on an excited electronic state of the cation would enable a variety of new and complex experiments. Using the intuitive Koopmans approximation picture of ionization [100], the ground electronic state of a cation is generated by removal of an electron from the HOMO of the neutral, whereas excited states are generated by ionizing electrons from the lower-lying HOMO-n orbitals. It had, for example, been assumed that only ionization of the HOMO contributes to HHG because of the low frequency fields used. However, recent results, obtained at 800 nm, demonstrate that ionization of HOMO-n orbitals may also contribute to an HHG spectrum [128, 1, 171]. Given the coherent nature of HHG process, even a small excited state contribution can

have a significant impact on the observed signal due to interference effects. However, in CEI, these contributions add linearly, and thus a small contribution from ionization of the HOMO-n would be difficult to observe.

To efficiently launch dynamics in excited states of molecules with a large energy gap between ground and excited states, it is common to use high photon energy sources such as FELs (acetylene) [90] or HHG (ethylene) [184]. If sub-fs resolution is required, one can use an XUV pump/XUV probe arrangement based on HHG for this kind of experiments [177, 179], however, at the price of a highly demanding experimental setup.

Even though acetylene (C_2H_2) has been serving as a model system for decades, proton migration dynamics in its cation is not yet fully elucidated, and has recently attracted attention of both experimental and theory groups [126, 79, 90, 118, 49, 92]. Given its small size, it is an ideal candidate for the application of quantitative electronic structure theory, which can be brought to bear on its ground and excited states.

Actually, proton migration pumped by 800 nm pulses has been observed solely in the dication of deuterated acetylene by Hishikawa and co-workers [126, 79]. Very recently, optimal control experiments confirmed that excitation with 800 nm pulses leads to isomerization in the dication [194]. These 800 nm pump schemes, however, are not capable of launching proton migration in other charge states such as in the cation[4].

This is because it is quite challenging to overcome the potential energy barrier of 2 eV (ref. [20]) that separates the acetylene cation $[HC{=}CH]^+$ in its ground state $X^2\Pi_u$ from vinylidene. Therefore, to obtain sufficient energy to overcome this isomerization barrier [118], it is necessary to populate the A-state ($A^2\Sigma_g^+$) of $[HC{=}CH]^+$ (5.3 eV above the ground state), which requires ionization from the HOMO-1. This cannot be achieved in the adiabatic regime with 800 nm pulses [4]. To remain in the adiabatic regime for long conjugated molecules that display small energy gaps, Lezius *et al.* [114] have suggested increasing the laser wavelength. Inverting this idea, it appears sensible to reach the non-adiabatic regime for small molecules by using UV wavelengths with larger photon energies.

We present a generalized approach using 266 nm pump-pulses that unites the convenience and flexibility of a tabletop setup with excitation ranges of FELs, and unveils the isomerization process in unprecedented detail allowing us to record a high-resolution molecular movie of proton migration from the linear acetylene cation ($[HC{=}CH]^+$) to the vinylidene cation ($[C{=}CH_2]^+$). This movie shows that multiple oscillations can occur between the two isomers acetylene and vinylidene, revealing that results obtained in a tabletop multiphoton approach can go well beyond the FEL results [90]. Thus, multiphoton ionization with ultrashort UV laser pulses provides a powerful alternative to demanding VUV sources. This paper is structured as follows: first, in a single- pulse experiment, we verify that ex-

citation with 266 nm pulses leads to the same spectral signatures as those obtained with an FEL [90], confirming that we populate the first excited electronic state of the acetylene cation ($A^2\Pi_g^+$) that initiates proton migration. Second, we present time-resolved pump-probe experiments of the two-body breakup. Based on the single-pulse experiments, the presence of CH_2^+ in the dynamics of the vinylidene channel in the cation ($C^+ + CH_2^+$ correlation) is a clear indicator of proton migration since one proton has been migrating to the other side of the molecule. In addition to proton migration resulting in the formation of bound vinylidene molecules in the cation, new channels that lead to dissociation of the cation are observed in both, the vinylidene and the acetylene ($CH^+ + CH^+$) correlations. And finally, we investigate the three-fragment correlations from the same experimental data set ($C^+ + CH^+ + H^+$) and construct a molecular movie of proton migration that exhibits excellent agreement with new numerical simulations of non-adiabatic wavepacket propagation on the ground and excited electronic states of the cation. These *ab initio* trajectory simulations use definitive levels of electronic structure theory in the description of the relevant potential energy surfaces.

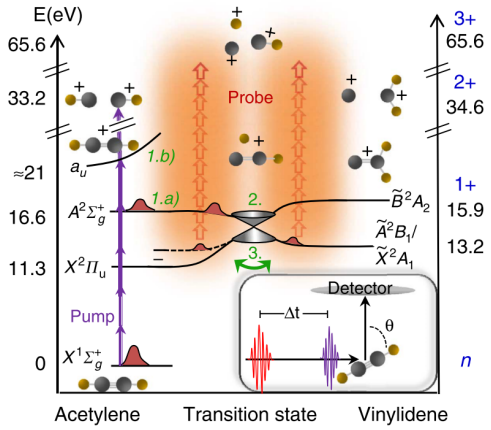

Figure 7.1: (1.a) a 266 nm pump-pulse populates the first excited state $A^2\Sigma_g^+$ of $[HC{=}CH]^+$ in a four-photon ionization process. Proton migration pathway: (2) within 40 fs, the wavepacket enters a region of strong non-adiabatic coupling with the ground $X^2\Pi_u$ state of $[HC{=}CH]^+$ (1+). Passage through this region involves relaxation to the X-state via a conical intersection. (3) Following this transition, the molecule, now in a highly vibrationally excited state, may undergo isomerization to the vinylidene cation $[C{=}CH_2]^+$. A to and fro isomerization between acetylene and vinylidene takes places, indicated by the green double arrow. Dissociation pathway: (1.b) while the 32 fs pump-pulse is present, a fifth photon can be absorbed on the A-state thus exciting population to higher lying states that have sufficient energy to dissociate along the C=C bond. Pictograms show the molecular structure in each configuration, starting from neutral acetylene (n) in the lower left corner. After excitation, $[HC{=}CH]^+$ remains in linear configuration ($D_{\infty h}$), reaches the trans-geometry (Figure 7.6), followed by the transition state and changes to a 'Y-shape' once a proton migrates from one C-atom to the other in the vinylidene structure (C_{2v}). To probe the nuclear structure, either further 266 nm photons are absorbed to reach the dication of acetylene and vinylidene (single-pulse experiment) or a second time-delayed 800 nm pulse leads to Coulomb explosion of the charged molecule (pump-probe experiment). With the latter, we reach the doubly charged (2+) as well as the triply charged ionic states (3+), and thus correlate either two fragments ($CH^+ + CH^+$ or $C^+ + CH_2^+$) or three fragments $H^+ + C^+ + CH^+$ with each other. In the inset, a sketch of the experimental setup with orientations of molecules, laser pulses and TOF direction towards the detector is given, with θ being the angle between molecular axis and laser polarization. Molecules being oriented parallel to the laser field correspond to θ=0°. Energy levels are taken from [20] and our calculations. Reprinted with permission from NPG.

7.2 Experiment Implementation

7.2.1 Experimental Technique

Experiments were carried out at the ALLS (INRS-EMT, Varennes, Canada). We use pump-probe CEI: a pump-pulse (266 nm, 32 fs and 3.2 mJ) ionizes the system to the cation and launches proton migration dynamics. A time-delayed probe-pulse (800 nm, 40 fs and 44 mJ) further ionizes it to higher charged states. Its electric field stripes off electrons almost immediately, leaving positively charged fragments behind that undergo Coulomb explosion. They represent the molecules geometric configuration at the arrival time of the probe-pulse. The strength of CEI is its ability to directly image geometrical structures. It does not provide direct observation of electronic states, as photoelectron spectroscopy would do. Nevertheless, we are able to draw conclusions about the electronic states populated in the initial ionization from the angular distribution of the molecular fragments and theoretical support.

Intense 266 nm pulses were obtained by sum frequency generation of the fundamental beam (800 nm, 2.5 KHz and 35 fs, KM labs) with its second harmonic (400 nm) in a 40 mm thick type-I BBO crystal (Altos Photonics). Pulse duration was controlled by chirped mirrors (Ultrafast Innovation) and/or fused silica plates from almost Fourier-transform limited (32 fs) to above 250 fs by adding a positive chirp. Measurements were obtained with a homebuilt TG-FROG [164]. Pulse energy was varied between 11.2 and 3.2 mJ. For the pump-probe experiments, a 32 fs, 3.2 mJ pump-pulse of 266 nm was combined with a 40 fs, 44 mJ probe-pulse of 800 nm. Laser polarization was vertical for both, pump- and probe-beams. Laser pulses were focussed (f=100mm) into a collimated acetylene gas jet (Praxair AC 2.6AA-A5). A schematic of this setup is shown in Figure 7.2. Pump intensity on target was estimated to 3×10^{14} W/cm^2 for the pump-probe experiment. Ionic fragments resulting from Coulomb explosion are collected with a uniform-electric-field ion imaging spectrometer. Their full three-dimensional momenta are retrieved using a time- and position-sensitive delay line detector at the end of the 23 cm ion TOF spectrometer (RoentDek Handels GmbH). Owing to the vertical polarization direction two fragments of same mass and charge but opposite momenta (for example, CH^+/CH^+, the acetylene channel) will hit the same detector position, but at different times. Thus choosing the correct TOF range enables us to distinguish them.

Owing to a significantly increased intensity when pump- and probe-pulses overlap temporally, the effective focal volume is increased within which the threshold for ionization is reached, leading to an increase in ionized molecules. This allows determining time zero by the appearance of a 60% increase in total ion yield (sum of all ion fragments) when

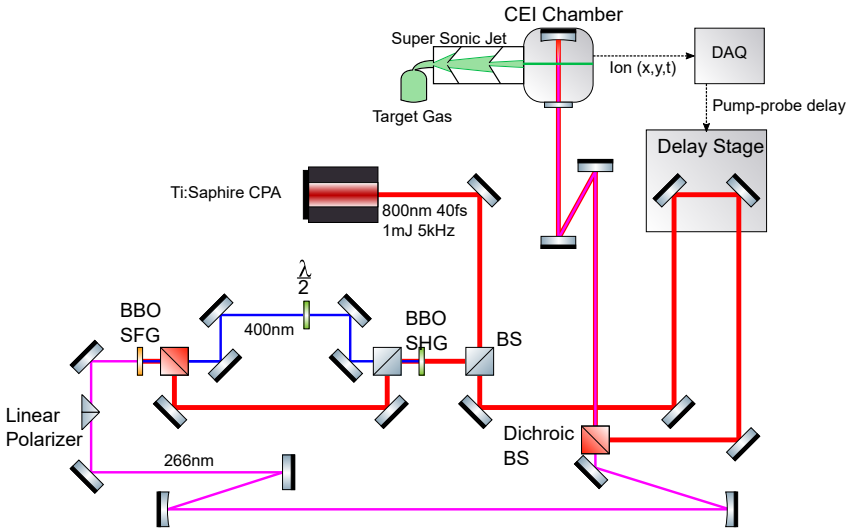

Figure 7.2: Schematic of UV-IR pump-probe laser system

scanning the delay stage. Error of time zero assignment is around ±5 fs, partially due to drifts over typical acquisition times of 24 48 h. Even though the pulse durations of 32 and 40 fs for pump- and probe- pulses appear quite long, we like to point out that both - pump and probe step - are highly nonlinear. A four-photon excitation effectively shortens the pump-pulse to 16 fs, and also the effective tunnel ionization time for the probe-pulse will be much shorter than the actual pulse duration.

7.2.2 Data Analysis

Owing to the large count rates produced in this experiment (typically >3 ions per laser shot), a sophisticated algorithm is used to parse the data for true coincidences [190]. A TOF window is defined in order to identify events registered by the position-sensitive detector as specific ions - either H^+, C^+, CH_2^+, or CC^+. The data is then parsed, laser shot by laser shot, for the existence of a specific fragmentation channel, for example, (H^+, C^+, and CH^+) for the three- or for the two-body breakup (CH^+ and CH^+), as the acetylene channel and (C^+ and CH_2^+) giving the vinylidene channel. If data from a laser shot yield the desired ions for the fragmentation channel, the momentum for these ions is calculated. If the momentum sum is near zero ($< 10^{-23}$ kgm/s), the group of ions is considered as

a true coincidence, originating from the same molecule. The momentum information for this channel is stored for further calculation of various metrics, for example, KER, θ (inset of Figure 7.3) and so on. It is possible with these high count rates that multiple ions are detected in the TOF windows defined for a specific channel, leading to several possible combinations of ions - the majority of which are false. In this case, all ion combinations are considered and only that which yields near zero momentum is stored as a true coincidence. Each laser shot excites a neutral molecule in the ultrasonic jet. From this molecule, we detect the full-fragment momentum information (CH^+, C^+ and H^+) in coincidence. This experiment is repeated many thousand times. All this information together is fed into the Newton plots that gives us the molecular movie. This represents not only a standard experimental approach but also a prerequisite to detect the square of a quantum mechanical wavepacket. So every point in the Newton plot originates from a single detected molecule where all molecules started with the same initial conditions.

7.2.3 Theoretical Methods

The excited non-adiabatic molecular dynamics on the $A^2\Sigma_g^+$ state were simulated using the full-multiple spawning approach [13], a semi-classical method. In this methodology, the vibronic wavepacket is represented in a basis of direct products (over each Cartesian coordinate) of frozen Gaussian functions. These basis functions, or trajectories, are propagated classically, with the potential energy surfaces determined 'on-the-fly' using *ab initio* electronic structure methods. The number of trajectories expands dynamically, to account for regions of non-adiabatic coupling between electronic states, by 'spawning' (approximating non-adiabatic transitions) new basis functions onto different electronic states as needed. The requisite energy gradients and derivative couplings required to propagate the trajectories were computed at a very high level of electronic structure theory, using atomic natural orbital basis sets and a first-order multireference configuration interaction treatment of electron correlation [117]. The underlying complete active space reference functions for the multireference configuration interaction procedure were determined using a 7 electron, 7 orbital (7e,7o) active space. The initial distribution of nuclear positions and momenta for the simulation were generated by sampling the ground vibrational state of neutral acetylene [172]. From 20 initial conditions, 1,480 spawned trajectory basis functions were generated. On the basis of these simulations, the adiabatic state populations as a function of time, as well as the geometric character of the wavepacket (that is, acetylenic versus vinylidenic) could be readily determined.

Assuming a Coulomb potential for the 3+ charge state ($C_2H_2^{3+} \longrightarrow C^+ + CH^+ + H^+$), momentum positions within the Newton plot have been calculated for the following four

structures using classical mechanics: (1) C_2H_2 at equilibrium; (2) $C_2H_2^+$ in the trans-geometry; (3) $C_2H_2^+$ at the transition state at the conical intersection; and (4) $C_2H_2^+$ in vinylidene geometry. For the CH^+ fragment, it is assumed that the charge is located on the carbon with a mass of 13. The initial velocities of the fragments are assumed to be zero. Geometrical structures were obtained using the level of theory described above.

The angular dependence of the ionization rate from HOMO and HOMO-1 was calculated using Time-Dependent Density Functional Theory (TDDFT) [181]. Bond length have been set to their optimized neutral parameters value, that is, HCCH geometries parameters are CH=0.110 nm and CC=0.122 nm. The CC bond was set to be parallel to the z-axis. For each spin orbital, KohnSham molecular orbital, the time-dependent ionization probability was calculated. From this, we have extracted the ratio of HOMO-1 and HOMO presented in Figure 7.3(b)).

7.3 Results

7.3.1 Single-pulse experiment

Signatures of proton migration in $C_2H_2^+$ have recently been demonstrated at the FEL in Hamburg [90] with XUV light (38 eV). Indications of time-dependent acetylene vinylidene isomerization, photoinitiated via ionization to the A-state of the acetylene cation appear in the KER of correlated C^+ and CH_2^+ fragments at energies above 5.8 eV (ref. [90]. As an initial experiment, we set out to find this signature by using single laser pulses of 266 nm central wavelength and varying pulse duration and peak power. The experimental scheme in terms of relevant electronic and ionic states and excitation pathways is described in Figure 7.1. The A-state of the acetylene cation is reached by absorption of four 266 nm photons (corresponding to 4 x 4.66 eV = 18.64 eV). Once on the A-state, proton migration occurs, which is then followed by ionization to a dissociative state of the dication within the same laser pulse. Results of a single 266 nm pulse experiment are shown in Figure 7.3(a), containing the KER distributions of the two-fragment correlation channel of vinylidene for 32 fs (green and red), 110 fs (black) and 250 fs (blue) pulse duration and various pulse powers. Already a short pulse of moderate pulse power (green solid line) leads to a KER distribution broadened on the high-energy side. With increasing pulse duration, a strongly pronounced high-energy shoulder appears. The shoulder obtained with 250 fs pulses (blue solid line) agrees very well with data obtained at the FEL using 38 eV (open circles) [90]. This shoulder was assigned to proton migration initiated by ionizing acetylene to the A-state of its cation [90, 118, 92, 119]. The proton migration that we observe is essentially

pulse duration dependent and only secondarily intensity dependent. The intensities of the short 32 fs pulses (3×10^{14} and 6×10^{14} W/cm^2), which are higher by a factor of five than those for the long pulses, indicate that increasing the intensity alone will not lead to a strongly pronounced high-energy shoulder. Fragmentation occurs in the doubly charged state that is accessed here in a sequential process within a single pulse; this means the complete sequence, of first pump followed by proton migration and finally probe, is taking place underneath the envelope of the 266 nm pulse and we observe the accumulated signal of molecules that have undergone the full sequence. This effect is therefore most pronounced for the longest pulses (250 fs) that are also of the lowest intensity.

In addition, we used 800 nm, 200 fs pulses (grey shaded). The energetically narrow KER distribution from 800 nm excitation confirms the observation of Alnaser *et al.* [4]. In this case, we do not obtain high-energy fragments as a signature of isomerization in the acetylene cation, and similar results were obtained at 400 nm (not shown). This was a primary motivation for our study at 266 nm in order to confirm that UV excitation is essential to populate the A-state.

7.3.2 Initial State Assignment (I)

Assignment of the electronic states involved in the isomerization can be more demanding in a multiphoton scheme compared with a single photon scheme pumped by one VUV photon. In both cases, however, multiple states can be populated, for example, the ground and the first excited state of the cation. In our experiment, while the cationic A-state is excited by four photons, the ground state of the cation $X^2\Pi_u$ is populated in a three-photon process. However, the documented energy barrier separating the acetylene and vinylidene isomers will prohibit proton migration from low-lying vibrational levels on the electronic ground state [20], so its contribution will only show up around the main peak of KER in Figure 7.3(a). To confirm that the experimentally observed high-energy shoulder arises from ionization to the A-state [90],we investigate the angular distribution of the molecular fragments from the KER spectrum obtained with the 110 fs, 266 nm pulse shown as a black solid line in Figure 7.3(a). Initially, all population is in the $X^1\Sigma_g^+$ electronic state of the neutral acetylene. Following Koopmans approximation [100], ionization to the $A^2\Sigma_g^+$ state of the acetylene cation requires the removal of one electron from the HOMO-1, which is a σ_g orbital. In general, the probability for ionization from this orbital is largest for those molecules aligned parallel to the polarization of the laser field [1] (this corresponds to the angle θ=0°, consistent with the definition given in the inset of Figure 7.1). Our experimental situation of strong field multiphoton ionization represents an uncommon case located between weak field multiphoton ionization and tunnel ionization. State of the

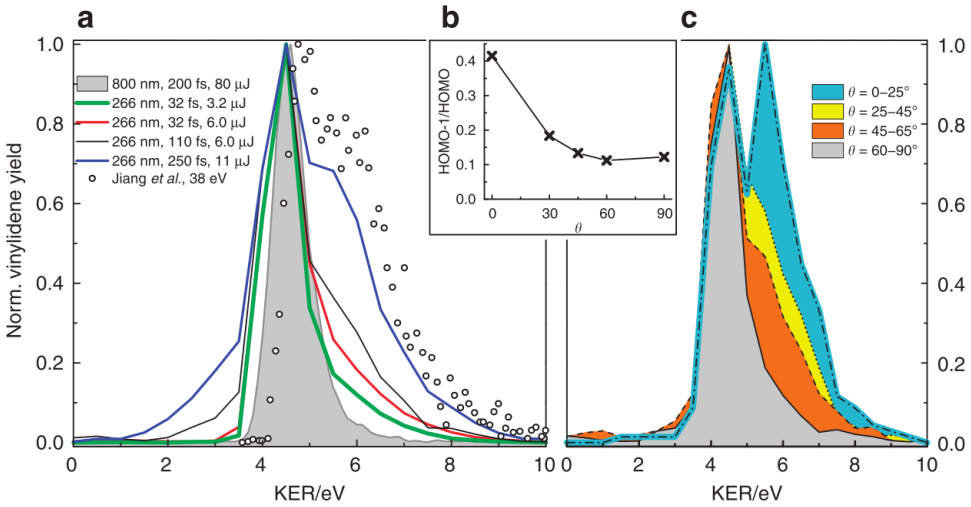

Figure 7.3: (a) Wavelength, pulse duration and energy dependence (with estimated intensities) on the vinylidene yield versus total KER $C^+ + CH_2^+$. Filled grey curve: 800 nm excitation, 200 fs pulse duration, 80 mJ, 4×10^{14} W/cm^2; green curve: 266 nm excitation, 32 fs pulse duration, 3.2 mJ, 3×10^{14} W/cm^2; red curve: 266 nm excitation, 32 fs pulse duration, 6.0 mJ, 6×10^{14} W/cm^2; black curve: 266 nm excitation, 110 fs pulse duration, 6.0 mJ, 1×10^{14} W/cm^2; blue curve: 266 nm excitation, 250 fs pulse duration, 11 mJ, 1×10^{14} W/cm^2; open circles: excitation with 38 eV from an FEL [90].(b) TDDFT calculations showing the ratio of ionization rate of HOMO-1 to HOMO versus angle θ. Pulse parameters were: wavelength: 266 nm, pulse duration: 24 fs (27 cycles), intensity: 3×10^{14} W/cm^2.(c) Cuts of the angular distribution of the 266 nm, 110 fs spectrum shown as black solid line in (a). Cyan corresponds to angles θ between 0 - 25° (note that the high-energy peak exceeds the main peak here); yellow corresponds to 25 - 45°, orange to 45 - 60° and grey to 60 - 90°. All curves are normalized to the peak maximum. Reprinted with permission from NPG.

art literature [178] proposes TDDFT to represent exactly this situation. Our TDDFT calculations of the ionization rates of HOMO-1 and HOMO confirm the anticipated angular dependence. As expected, their ratio in Figure 7.3(b) shows a well-pronounced maximum for angle θ=0°. Note that this is also exactly where the maximum in the high-energy shoulder of the angular-resolved KER distribution is observed (see cyan shaded curve of Figure 7.3(c). The high-energy maximum of this particular angular slice is significantly more pronounced than for all other angular distributions and even exceeds the main peak. Thus, we can confidently assign this region to ionization to the $A^2\Sigma_g^+$ state. Although higher electronic states with Σ symmetry exist in the cation, the probability of them being populated under the current experimental condition is significantly lower than for the A-state.

7.3.3 Pump-probe study of the two-body breakup process

Next, we used pump-probe CEI to image the dynamics resulting from multiphoton ionization with 266 nm pulses. We investigate two chemical reactions: (i) proton migration – one of the fundamental processes in chemistry and biology; and (ii) the first observation of C=C bond breaking on highly excited states of the acetylene and vinylidene cation.

We focus first on the isomerization process: as shown in the experimental scheme of Figure 7.1, a 266 nm pump-pulse ionizes the system to $[HC{=}CH]^+$ in a four-photon process, thereby initiating proton migration dynamics. A time-delayed, 800 nm probe-pulse tunnel ionizes the molecule to doubly and triply charged states of acetylene or vinylidene. Its electric field stripes off electrons, leaving behind positively charged fragments that undergo Coulomb explosion. As in the single-pulse experiments, proton migration dynamics shows up in pump-probe experiments in the high-energy region obtained by correlating two fragments. This dynamics corresponds to the region V3 of the vinylidene channel ($C^+ + CH_2^+$) in Figure 7.4(a). We observe an increase of the yield in this high-energy shoulder in the temporal window of 60 100 fs followed by a decrease. (We will leave the details about the proton migration dynamics and vinylidene formation until we have direct evidence from three-fragment correlations in the next section.) Note that this high-energy shoulder is less pronounced in the pump-probe experiment of Figure 7.4 compared with the single-pulse experiment in Figure 7.3(a), in which the complete two-step ionization process occurs many times beneath a single-pulse envelope. Therefore, for long single-pulse durations (110 and 250 fs), the excited state dynamics can be initiated on a larger number of molecules and this gives rise to an accumulated vinylidene formation compared with the 32 fs in case of the pump-probe experiment.

The mid-energy region V2 in Figure 7.4(a) has been previously [90] assigned to a sequential double ionization. In addition, we observe a new peak emerging in the low-energy region V1. This peak is first visible around 80 fs, and occurs as well in the lowenergy region A1 of the acetylene channel ($CH^+ + CH^+$; Figure 7.4(b) and has, to our knowledge, never been observed before for $C_2H_2^+$. Since it occurs for both vinylidene and acetylene, we attribute it to a stretching of the C=C bond. In both channels, it migrates to smaller energies (indicating an increase in the CC internuclear distance) with increasing time delay. The peak strength continuously increases with increasing time delay, which is consistent with a lowering of the ionization potential as the C=C bond length increases. We separate the KER structure of the acetylene channel into only two areas, A1 and A2, since no proton migration is observed in this channel. A2 contains contributions from a direct ionization to the dication as well as a subsequent ionization from the cation to the dication, and is not further investigated in this paper.

Using Coulomb potentials for analysis, the peak at 1 eV corresponds to an elongation of the C=C bond to $< 4r_{eq}$, where r_{eq} is the equilibrium distance, implying that the molecule has largely dissociated. Similar dissociation effects have been observed in $C_2H_2^{2+}$ [204] and 1,3-butadiene [197]. While none of the lowlying electronic states of $C_2H_2^+$ is dissociative along the CC stretch coordinate, if a fifth photon is absorbed during the pumppulse, the molecule will have energy in excess of the lowest CC dissociation asymptotes (Figure 7.1). Since the dissociation dynamics occur in both the acetylene and vinylidene channels, they are likely to be triggered by the same event, namely absorption of a photon to higher lying excited states of the cation. From there, it can proceed to dissociative states of the vinylidene cation. This dissociation pathway has not been observed at a FEL [90], given that for one-photon absorption, once ionized, no further coupling between electronic states occurs. We predict that in a multiphoton experiment with shorter pump-pulses, this sequential coupling after ionization is also likely to be suppressed.

7.3.4 Pump-probe study of the three-body breakup process

This new dissociation channel also shows up in the three-body breakup $C_2H_2^{3+} \longrightarrow H^+ + C^+ + CH^+$, in which two electrons are removed by the probe-pulse. Before we address the rich information present in this channel though, we first need to prove that it is indeed what we claim, and that the probe-pulse is only showing us dynamics of the cation. As a first step in doing so, we compare the KER features in the two-body channel (Figure 7.4), which we have established to show us time-dependent processes that must originate in the cation, with those of the three-body channel in Figure 7.5. Figure 7.5(a) contains the total KER during the Coulomb explosion. The peak maximum migrates from ≈ 15 eV at time

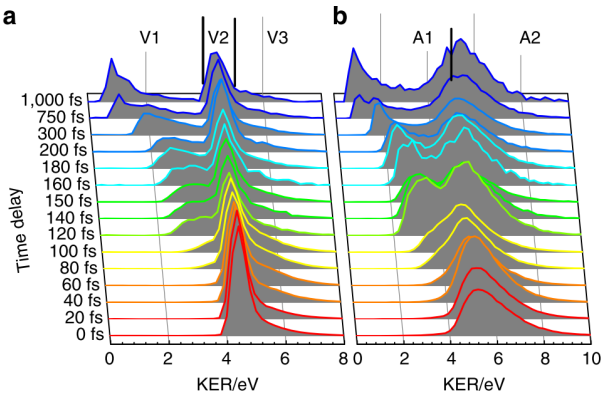

Figure 7.4: Vinylidene channel $C^+ + CH_2^+$ is shown in (a) and acetylene channel $CH^+ + CH^+$ in (b) with increasing time delay from 0 fs (red) to 1000 fs (blue). The vinylidene spectrum contains three different regions: V1: the low-energy range below 4 eV; V2: the intermediate energy range between 4 and 5 eV; and V3: the TDDFT calculations of the high-energy range, >5 eV. The acetylene channel is divided into two regions: the low-energy region A1: <4 eV, and the high-energy region A2: >4 eV. Spectra are normalized by the number of correlated counts, to account for varying acquisition times at different time steps, as well as for minor fluctuations in pulse power or gas pressure. This normalization allows comparison of the absolute count number in each channel at each time delay. Reprinted with permission from NPG.

zero to 7 eV at a time delay of a picosecond, indicating the presence of the dissociative channel described in the previous section. To uncover the close analogy between two- and three-body breakup, we take advantage of the fact that in the three-body channel an H^+ fragment is created, which, because of conservation of momentum, is responsible for carrying away most of the increased and broadband energy release. If the 3+ channel is observing the same dynamics, we expect strong similarities in the energy sum of correlated $C^+ + CH^+$ fragments of the three-body channel, with the total energy released in the two-body channel. To extract hidden sub-structures of Figure 7.5(a), we look at the 3+ KER reduced by the proton energy in Figure 7.5(b), leading to a double-peak structure with one peak ≈ 6 eV, and another one emerging for longer times and moving to 1 eV at 1 ps. The overall KER is still slightly higher compared with the two-body breakup since here Coulomb potentials are more closely approximated. The key difference being that while both of the main peaks are well separated in the two-body case, the peaks in Figure 7.5(b) are much broader, leading to an overlap of the dominant spectral features. This is due to the additional broadband energy both, the remaining CH^+, and the C^+ fragments gather when the proton is removed from either CH_2^+ or CH^+. The temporal evolution of the KER by the single fragments is shown in Supplementary Figure 7.3, which indicates that apart from the CC bond the CH bond dissociates. The low-energy peak in Figure 7.5 follows precisely the evolution that was observed for the peak assigned to dissociation in the two-body breakup in Figure 7.4. This constitutes strong evidence that we observe the same cation dynamics in the two-body and in the three-body breakup. The KER spectra for the three-body breakup are too broad to clearly observe the high-energy shoulder associated with the launching of proton migration. However, since dissociation in the cationic states requires the absorption of a fifth photon, compared with the four photons required to initiate proton migration dynamics on the A-state, it is most likely that the latter process as well is initiated on the cation and probed via ionization to the triply charged states.

In the three-body breakup channel, we have access to the direction in which the proton is emitted, allowing us to follow the proton migration process in detail. At its simplest, if the proton trajectory is close to the direction of the CH^+ fragment, it means that the molecule was close to the vinylidene isomer while undergoing Coulomb explosion. While, if the proton is close to the C^+ fragment direction, the molecule is closer to acetylene. Such an analysis allows for the construction of a molecular movie of the proton migration reaction in momentum space. Key frames of this molecular movie are represented by the Newton plots in Figure 7.6 as described in the figure caption and the Methods section. Since proton migration in the acetylene cation initiated on the A-state results in a bound vinylidene cation (that is, non- dissociative), its Coulomb explosion will yield in a high KER. Therefore, the dynamics of interest were isolated by filtering the total three-body

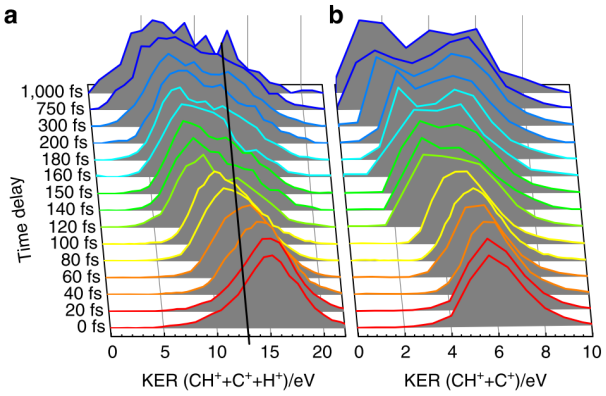

Figure 7.5: Peak values are normalized to the maximum. (a) Total KER $CH^+ + C^+ + H^+$; (b) KER from $CH^+ + C^+$ fragments. The black line in (a) indicates the energy cutoff for the Newton plots of Figure 7.6. Binning was adjusted according to the number of correlated counts available for each time delay. Note that the data for a time delay of 1 ps contain significantly less statistics than other time delays, displayed sub-maxima are related to this. Reprinted with permission from NPG.

KER data, selecting only those correlated events above 13 eV, thereby excluding the CC bond dissociation events visible in Figures 7.4 and 7.5. The cutoff for energy filtering is indicated as a black line in Figure 7.5(a). In Figure 7.6, proton fragment momenta are presented in the molecular frame [191], in concert with classically calculated values (shown as symbols) that assume Coulomb potentials and are included to serve as a visual guide. Since the triply charged states populated in the experiment substantially deviate from a Coulomb potential, the observed momentum in the experiment is lower than the classically calculated one. Despite this deviation, the agreement between this simple calculation and the experimental data is very good. Starting from the linear geometry of neutral acetylene in the ground state, the trans-configuration is reached after 20 fs, indicated by a depletion in signal at $(x = -1.0|y = 0.0)$, which is shown in blue and an increased signal at $(x = -0.3|y = 0.7)$ shown in green. This matches a half-period of the trans-bent vibrational mode. At 40 fs, the centre of mass reaches the classically calculated transition state $(x = 0.0|y = 1.0)$. This agrees with timescales predicted by our semi-classical simulations for a population transfer to the ground state mediated by the conical intersection. A maximum in vinylidene formation (classically calculated value $(x = 0.6|y = 0.8)$) is observed around 100 fs, after which the population maximum swings back to the acetylene side (with a vinylidene population minimum $\approx$ 150 fs). This oscillation continues with the next vinylidene population maximum observed at 180 fs. All time values are

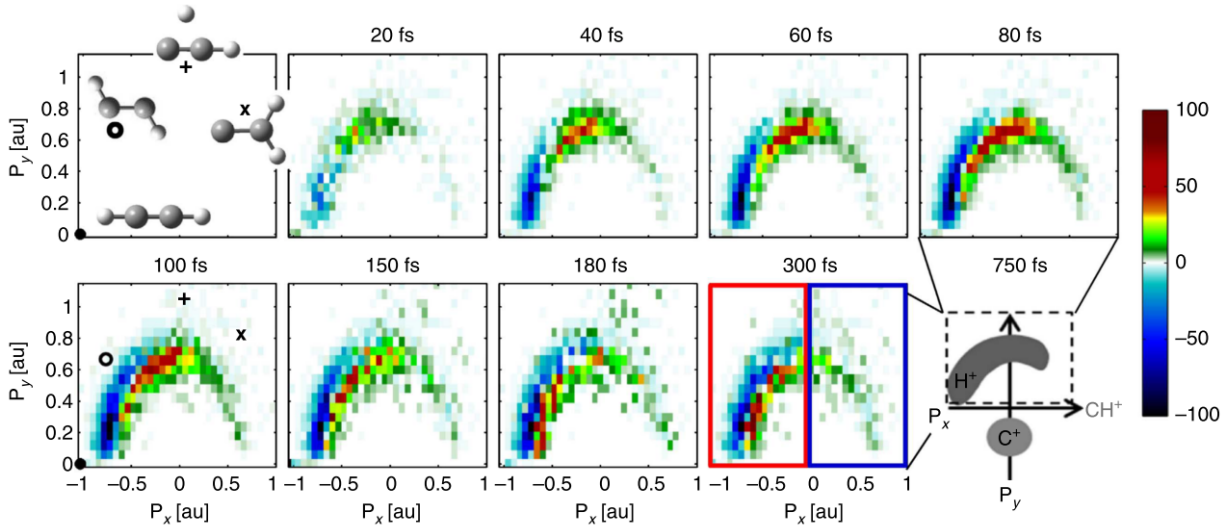

Figure 7.6: Newton plots filtered for KER $>$ 13 eV. Symbols show classically calculated results assuming Coulomb potentials for linear configuration (.), trans-configuration (o), transition state (+) and vinylidene (x), given in the upper left corner. As indicated on the lower right, all molecules are rotated such that the momentum vector of CH^+ points towards the positive x-axis, the relative momentum of C^+ is confined to the negative y-axis. Here, we plot only data of the momentum vector of H^+ after subtracting the distribution at δt=0. The plots show the evolution of H^+ momenta with increasing time delay from 0 to 300 fs, normalized to the integral. The distribution appears localized at 20 fs (dark green data points) and spreads out towards the CH^+ ion with increasing time delay. C^+ is considerably heavier than H^+ and thus localized, while the light H^+ propagates with time being transferred from the acetylene configuration to the vinylidene one. White colours correspond to zero, blue colours to negative contributions (after subtraction, that is, where the population originates) and other colours to positive contributions (that is, where the population is going). Reprinted with permission from NPG.

associated with an error of ±5 fs.

The to and fro isomerization behaviour of Figure 7.6 is perfectly reproduced by the *ab initio* trajectory simulations of the vibronic dynamics as evinced in Figure 7.7. While a single recurrence had also been observed in $C_2D_2^{2+}$ (refs [126, 79]), we now see further oscillations associated with the evolution of the nuclear wavepacket. We deduce from these results the following proton migration process: Both X- and A-states are populated in a three- and four-photon process, respectively; (Fig 7.1). According to our calculations and reference [118], the A-state population is depleted by roughly half in the first 40 - 50 fs via a trans-bent conical intersection to hot vibrational states of the ground electronic state of $[HC{=}CH]^+$. Formation of vinylidene takes place exclusively here, where the isomerization barrier can be overcome in both directions, which is why we observe the to and fro isomerization between acetylene and vinylidene (green arrow in Figure 7.1). The initial X-state population does not contribute to isomerization since its energy is too low to overcome the isomerization barrier. The isomerization process itself is 'primed' by the pre-eminence of motion along the trans-bending mode in the excited state. The solid lines in Figure 7.7 represent the total ground- and excited-state populations of acetylene (red) and vinylidene (blue) cation. As evidenced in Figure 7.7, the agreement is excellent up to 150 fs. From a single exponential fit, we estimate the initial isomerization time to be ∼41 fs (theory) and 43±10 fs (experiment), which is in accord with previous results [90]. The temporal resolution achieved results from the fact that both the pump and the probe step are highly nonlinear.

7.3.5 Initial state assignment (II)

In order to validate the proposed interpretation of the three-fragment correlation data, we confirm that the imaged dynamics occur on the state of interest, that is, the A-state of the cation. Evidence for a low-lying electronic state of Σ symmetry (such as the A-state) has already been presented in the single-pulse experiments of Figure 7.3 with the appearance of a high-energy shoulder analogous to observations at the FEL and its angular dependence, which reveals ionization from the HOMO-1. While Coulomb explosion occurs in the triply charged molecule $C_2H_2^{3+}$, there exist multiple combinations of pump- and probe- pulses that may be used to reach this ionic state. To verify that it is indeed dynamics on the cationic state that are being probed rather than the neutral or the subsequently prepared dicationic surface, we first note that we expect negligible dicationic populations to be prepared by the pump step since the ratio of parent ion $C_2H_2^+$ to $C_2H_2^{2+}$ in the time of flight (TOF) spectrum is > 100:1, demonstrating that the pump step strongly favours preparation of the cation over the dication. In addition, neither pump- nor probe-pulses alone contribute

$> 0.3\%$ to the correlated counts of the two-body breakup compared with their joined interaction. Of course, our method is only sensitive to the combination of pump and probe step, and thus an extremely efficient (but here undesirable) probe step for the transition from the $2^+ \rightarrow 3^+$ states compared with the $1^+ \rightarrow 2^+$ could, in principle, compensate for the pump efficiency. We therefore estimated the tunnel ionization rates for these processes based on the Keldysh theory. The results show the $1^+ \rightarrow 2^+$ ionization process to be clearly saturated, which holds for the intensity ranges accessible during our experiment. This means that the preference of populating the cation over the dication in the pump step is preserved in the probe step such that the overwhelming cation population created by the pump is the one imaged by the probe step. This is consistent with (and perhaps a necessary precondition for) the observation of the triply charged species. Combining the efficiencies of pump and probe step, it appears therefore extremely unlikely that we observe dication dynamics in the case of three-fragment correlation, which is also supported by the fact that the same dissociation dynamics is observed both in the dication (Figure 7.4) and the trication (Figure 7.5), as discussed earlier. While for low pump powers, we observe a four-photon absorption that matches the ionization potential of the A-state energetically, for higher pump powers it is indicated that we are driving the pump step in saturation. This saturation effect also holds for the experimental condition of the pump-probe experiment. Thus, by the arrival time of the probe-pulse, there are no neutral molecules left in the jet. Finally, this assignment is strongly supported by the excellent agreement with new high-level theoretical simulations of the $C_2H_2^+$ A-state initiated dynamics, as shown in Figure 7.7.

In summary, if one aims to populate the excited states of charged molecules whose difference in ionization potentials is too large to be overcome by 800 nm photons, our experimentally rather simple approach provides an alternative to demanding VUV sources. Indeed, given the limited availability, repetition rate, pulse stability and timing jitter of FELs, our approach provides tremendous benefits in terms of statistics and temporal resolution. Combining pump-probe CEI with multiphoton absorption of UV light opens the door to time-resolved imaging of chemical reactions and very rich dynamics since a variety of electronic states is accessed simultaneously. Careful consideration, as here, makes it possible to identify their origins unambiguously. Combined with theoretical simulations, our results present the most complete picture of proton migration and C=C bond breaking on the ground and excited states of $C_2H_2^+$ to date.

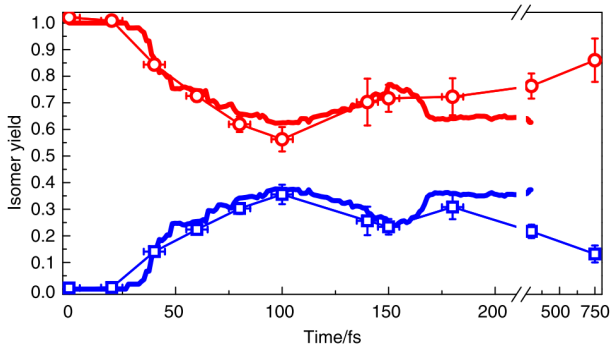

Figure 7.7: Comparison of Theory and Experiment. Comparison of theory (thick lines) and experiment (open symbols) for acetylene (red) and vinylidene (blue) yield: Theoretical curves show the superposition of acetylene and vinylidene yield in both the ground state and excited states of the cation as a function of time. Experimental values are obtained by integrating the Newton plots of Fig. 5 for negative P_x (acetylene, circles) or positive P_x (vinylidene, squares), as indicated there by the red and blue box at 300 fs. Note the broken axis for long time delays. Experimental data are corrected by offset and scaling factor to fit the theoretical points. Reprinted with permission from NPG.

7.4 Acknowledgements

We gratefully acknowledge research funding from NSERC (Natural Sciences and Engineering Research Council of Canada), FQRNT (Fonds de recherche du Quebec - Nature et technologies) and CIPI (Canadian Institute for Photonic Innovations). H.I. acknowledges financial support from the NSERC-Banting Postdoctoral Fellowships Program. S.B. and V.W. are thankful for financial support from NSERC.

Chapter 8

Proton Migration in Ethylene

8.1 Experimental Design

The CEI apparatus, laser system, and data acquisition used in this experiment the same as that used for the work published in [87] and discussed in 7.2. Slight modifications to experimental parameters include the specific pump and probe intensities as well as the specific pump-probe time delays.

The pump and probe laser parameters (including pulse energy and pulse length) were optimized to maximize measurement statistics without saturating the detector. Since this experiment focuses on time resolution of physical processes, the pulse durations were minimized, realizing 38 fs and 32 fs pulse lengths for the pump and probe respectively. As described in Chapter 7, the physical phenomena of interest in this work are insensitive to small changes in the laser field intensity, so long as it stays within the multiphoton regime. For the measurements described in this chapter, the laser pump pulse energies are between 31 uJ and 45 uJ while that of the probe pulse are between 2.4 uJ and 3.2 uJ. Applying the formulae for intensity described in 3.1, an upper limit an upper limit of 7×10^{15} W/cm^2 is calculated. Although the beam intensity was not measured throughout this campaign, previous measurements of intensity on the same laser system for both 800 nm and 266 nm yielded intensities on the order of 10^{14} W/cm^2 [1].

[1] Private communication with Heide Ibrahim, July 7th, 2017

8.2 Results

8.2.1 Preliminary Analysis

Singly and multiply ionized ethylene is capable of fragmenting into a plethora of channels. To minimize these possibilities, relatively low laser intensities on the order of $10^{14}\,\mathrm{W/cm^2}$ for the pump and probe fields were used. The possible fragmentation channels are initially visualized in the TOF spectrum in Figure 8.1.

The ionization of ethylene produces a large breadth of fragments. These fragments appear in the measured time of flight spectrum (Figure 8.1) as both narrow and broad peaks. The sharp peaks are associated with ion fragments that have little dissociative kinetic energy; while the broad peaks are associated with ions that dissociate along repulsive PES and therefore have a ranges of kinetic energy in the TOF dimension.

Due to the discrete mass distribution among ethylene's constituent atoms (carbon mass 12 amu, hydrogen mass 1 amu), the time of flight spectrum is clustered into carbon-centric groups. Namely, groups with two carbon atoms and a charge of +1; one carbon atom and a charge of +1 (or, due to the mass-charge degeneracy, two carbon atoms and a charge of +2); one carbon atom and a charge of +2; and zero carbon atoms. In each of these carbon-centric groups exist moieties of varying hydrogen content - namely between one and four hydrogen atoms.

Building on the analysis of the TOF spectrum, the fragmentation production can be further understood by examining the coincidence plot in Figure 8.2. As described in [60] [2], the linear off-diagonal correlation peaks indicate coincident events between fragmentation ions with considerable kinetic energy. From Figure 8.2, there are strong, high energy channels, producing the fragment pairs listed in Table 8.1. Due to the relatively strong bond between the carbon atoms, most of these channels feature the ejection of molecular hydrogen coincident with a two-carbon based ion. Though the TOF spectrum indicates significant production of protons, the coincidence map cannot resolve correlations among the rich array of fragmentation pathways. On the other hand, the rare trihydrogen cation is easily observed to be produced in coincidence with C_2H^+ and to a small degree C_2^+.

A unique feature not intended to be observed in CEI experiments is the long trail beginning at approximately [500, 3500] and extending smoothly along the off-diagonal to [1900, 2500]. The source of this signal is located where $H^+ + C_2H_3^+$ are coincident,

[2] Although this publication speaks to the covariance mapping technique, this qualitative feature is present in both techniques

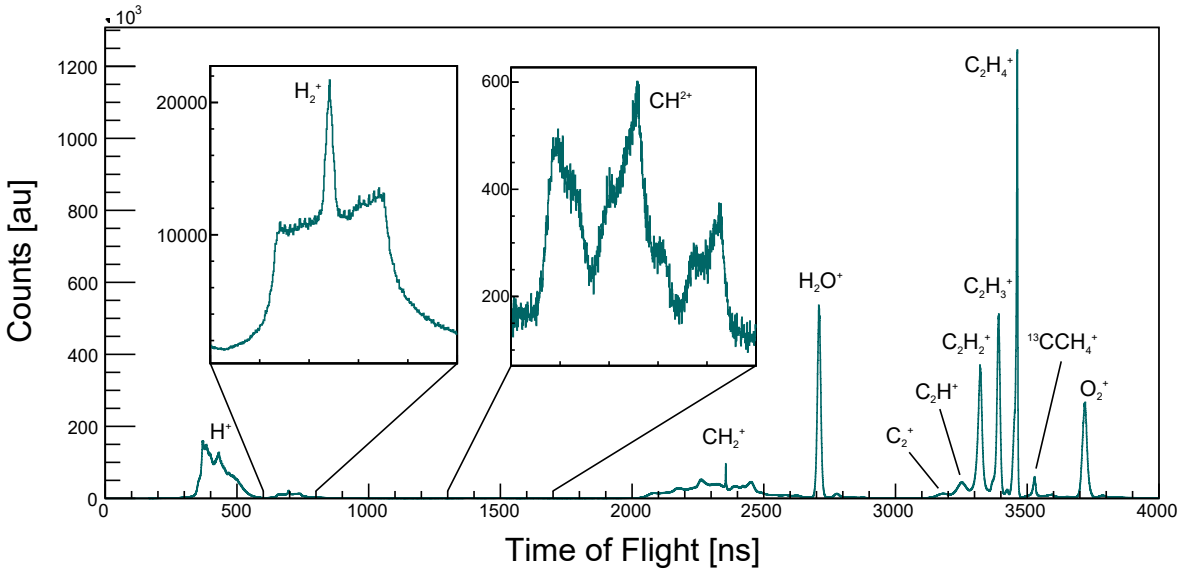

Figure 8.1: Measured time of flight spectrum with 0 fs pump-probe delay. Inserts show low signal regions

eventually fading near the CH_n^+ region. These coincident events are the result long-lived $C_2H_4^{2+}$ species that fragment into $H^+ + C_2H_3^+$ only after hundreds of nanoseconds (also observed by Larimian *et al.* [107]). Two much weaker signals can be seen parallel to this curve, most likely resulting from the long lived channel $C_2H_4^{2+} \longrightarrow H_2^+ + C_2H_2^+$ and $^{13}CCH_4^{2+} \longrightarrow H^+ + {}^{13}CCH_3^+$ (an isotope contaminant discussed later).

Lastly, an assortment of methyl (CH_3), methylene (CH_2), CH, and carbon ions are observed to be produced in coincidence. To better resolve this region of coincident TOF measurements, the covariance mapping technique is employed [60] and shown in Figure 8.3. This covariance map reveals several channels where the carbon-carbon bond is broken as part of a two- or three-body fragmentation process. Naturally, the autocorrelation of CH_2^+ ions produce narrow peaks in the covariance map due to equal momentum being imparted on the constituent ions during break-up. Similarly, the two-ion breakup into CH^+ and CH_3^+ also yields a narrow distribution. For coincident ions pairs in this region with fewer than four hydrogen atoms, a spread in the covariance signal indicates energy lost to the ejection of a hydrogen atom or proton. These include the carbon-based pairs indicated in Table 8.1 where some hydrogen is indicated as a third ion.

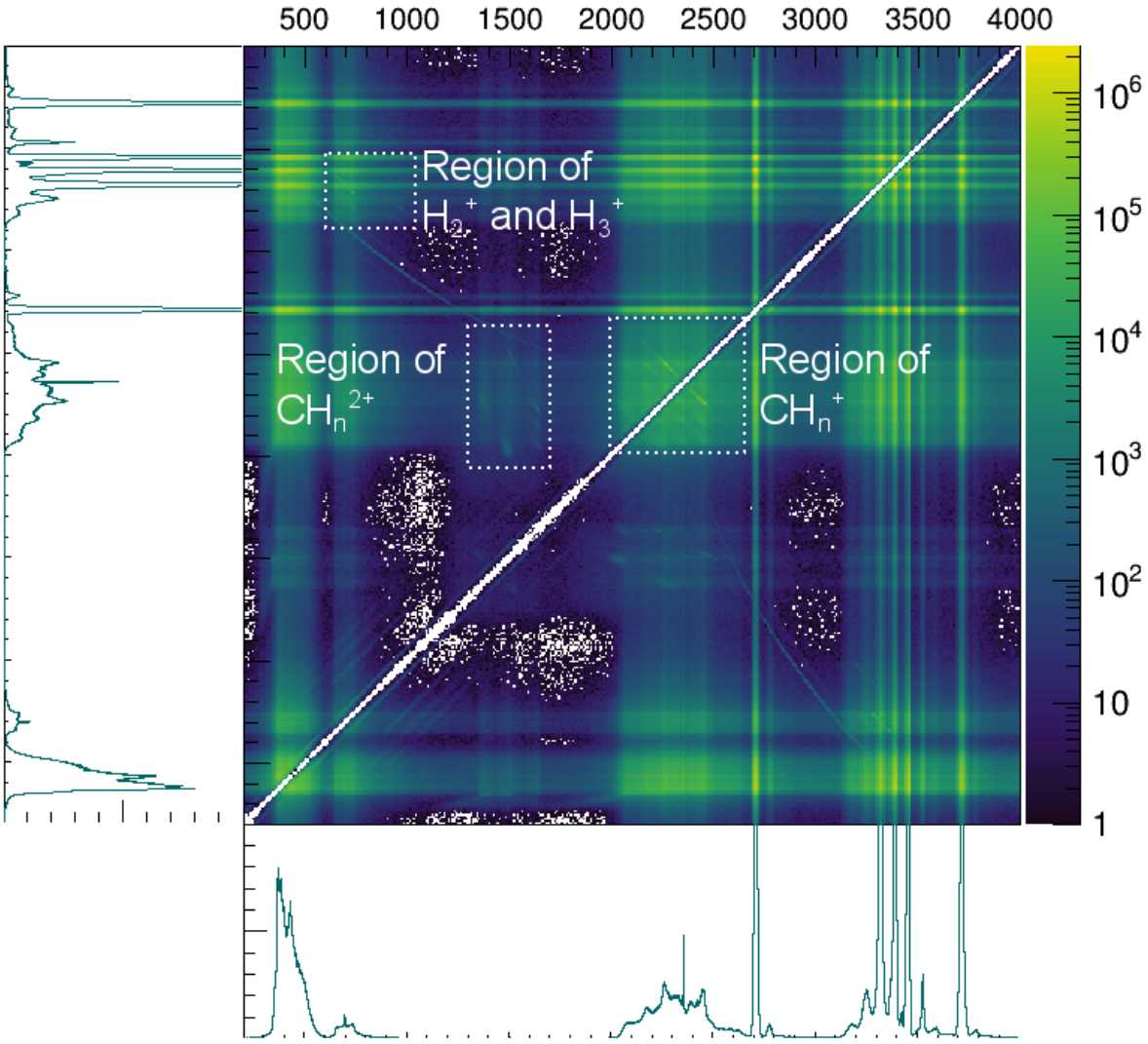

Figure 8.2: Coincidence Map with 0 fs pump-probe delay. Log scale used to highlight low-signal structures.

Region	Ion 1	Ion 2	Ion 3	Counts
H^+	H^+	$C_2H_3^+$	–	239610
H_2^+ and H_3^+	H_2^+	$C_2H_2^+$	–	57930
	H_2^+	C_2H^+	H	4731
	H_2^+	C_2H^+	H^+	0
	H_2^+	C_2^+	H_2	0
	H_2^+	C_2^+	H_2^+	84
	H_3^+	C_2H^+	–	2292
CH_n^+	CH^+	CH_3^+	–	12462
	CH_2^+	CH_2^+	–	603753
	C^+	CH^+	H_3^+	0
	C^+	CH_2^+	H_2^+	224
	CH^+	CH^+	H_2^+	0
	CH^+	CH_2^+	H	8703
	CH^+	CH_2^+	H^+	4568
CH_n^{2+}	CH_2^{2+}	CH_2^+	–	4168

Table 8.1: Fragmentation pairs of C_2H_4 observed in the coincidence map in Figure 8.2

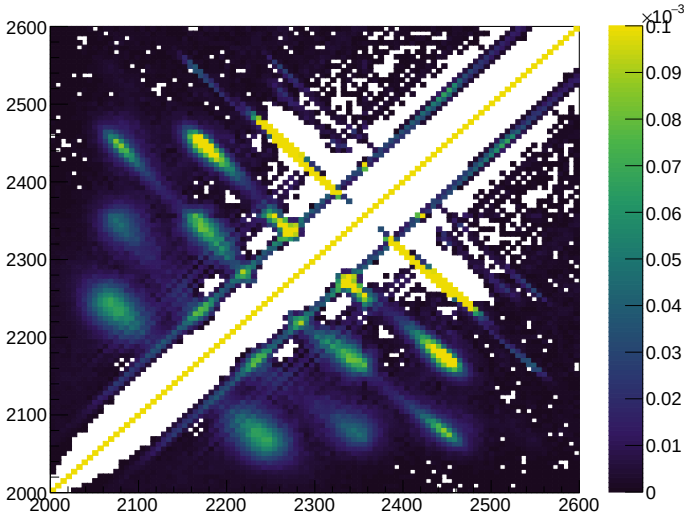

Figure 8.3: Covariance Map focusing on the CH_n^+ region of Figure 8.2

8.2.2 2-Ion Momentum Imaging

With a preliminary view of the fragmentation channels available to ethylene under the ionization conditions used in this experiment, the momentum imaging analysis technique is applied to each channel of interest. In this section, analysis is performed only on those fragmentation channels where momentum is split between two ions.

Absolute and Measured Count Rates

Absolute count rates for the six most common 2-ion channels are shown in figure 8.6. The unit *Events / Laser Shot* technically indicates the number of *measured* events and not *produced* events - the result of using a detector with less than 100% detection efficiency. Since the detector efficiency is identical for each ion [174], this suggests that the measured event rates and the produced event rates are related by a single scaling factor across all channels. However, there are two more factors that effect such a scaling factor and are unique to each channel.

The first effect to consider is the detector dead-time. By examining the diagonal on the coincidence map in Figure 8.2, an estimate of the effective detector dead-time is measured as the gap in TOF signal between successive events. For this experiment, a dead-time

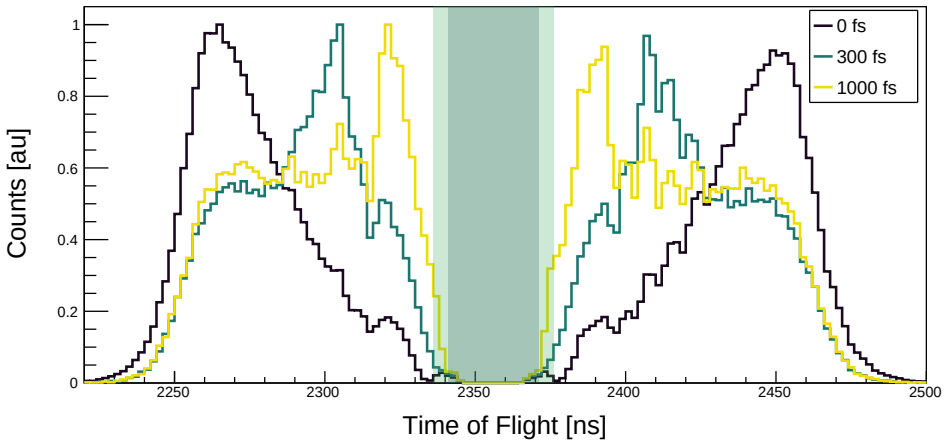

Figure 8.4: TOF spectrum of coincident events in the $CH_2^+ + CH_2^+$ channel for pump-probe delays of 0, 300, and 1000 fs. The blue and green regions denote estimated detector dead-time regions with durations of 30 and 40 ns respectively.

of 30 ns is estimated. For most channels, this dead-time is of little significance as the sequential detection of events occurs over hundreds to thousands of nanoseconds. However, the $CH_2^+ + CH_2^+$ channel uniquely has identical ions which arrive at the detector in close succession when energetic, and arrive at the same time when produced in a low KER process. An examination of the TOF spectrum of coincident events in this channel reveal that the dead-time effects few events in the 0 fs delay measurement as evidenced by the lack of signal in the blue-green region of Figure 8.4. The steady decline of signal approaching the dead-time region in the 0 fs delay measurement is contrasted with the sharp decline in signal at the edge of the dead-time region for the 1000 fs delay measurement. This sudden drop in signal appears in measurements made at delays greater than 300 fs. This suggests that event rates reported in such long delay times in fact under-estimate the count rates when compared with similar other 2-ion channels and those channels made with shorter delay times.

The second effect the reduces detection efficiency for different channels uniquely is the PSD inhomogeneity. As a MCP is bombarded with ions, its sensitivity in high-traffic regions reduces. For CEI experiments that produce low-energy ions (such as singly charged parent ions), a significant reduction in detection efficiency is created in the small region projected by the focal spot. This dead-spot is easily resolved in the distributions of ion positions shown in Figure 8.5 for the $CH_3^+ + CH^+$ channel at both short (0 fs) and long (1000 fs) pump-probe delays. Although both long and short time delays experience a

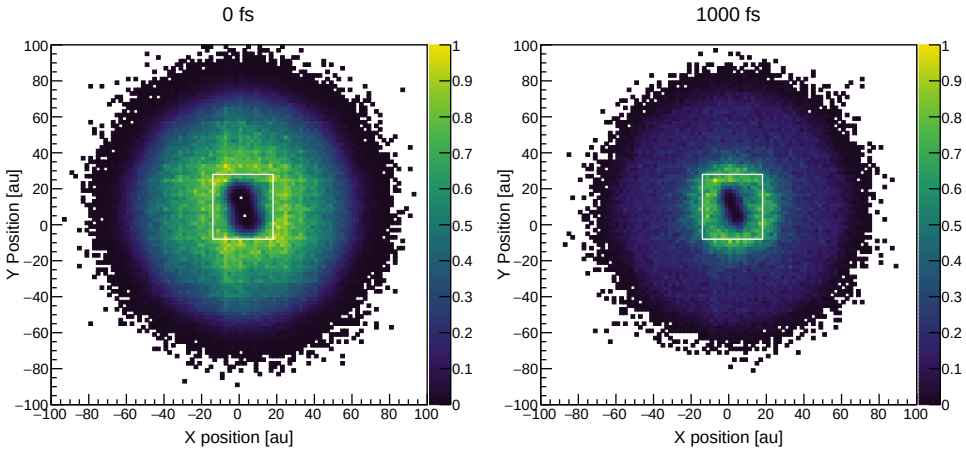

Figure 8.5: Distribution of ion positions on the PSD from events in the channel CH_3^+ + CH^+ produced at the two pump-probe delays 0 and 1000 fs. The white box indicates the integration area used to highlight the unequal reduction in count rates across pump-probe delays.

reduction in count rates, the tendency for the long time delay to produce low-energy ions results in a *relatively* higher reduction in events. To quantify this, the integral of events in and around the dead-spot for both channels is measured and compared with the full channel signal. For the short time delay, 12% is measured within the dead-spot region while 34% is measured for long time-delay. The higher density of events localized in and around the dead-spot for long time-delays confirms that the scaling between measured and produced events is not the same for all pump-probe delays.

Combined, the two effects of detector dead-time and dead-spot result in reduced count rates for low-energy ions overall and reduced count rates for low-energy identical ions especially (relevant only for the CH_2^+ + CH_2^+ channel). The exact reduction factor is not measured, but analysis across all pump-probe delays shows that only delays larger than 300 fs are effected.

Fragmentation Channel Production

A general trend between these channels is observed: there is always a peak at or near time-zero. This is expected as the multiphotonic ionization process is nonlinear with respect to the laser-field intensity. As such, there will always be an increased probability to access states when both pump and probe fields overlap in time. Now, specific trends are discussed.

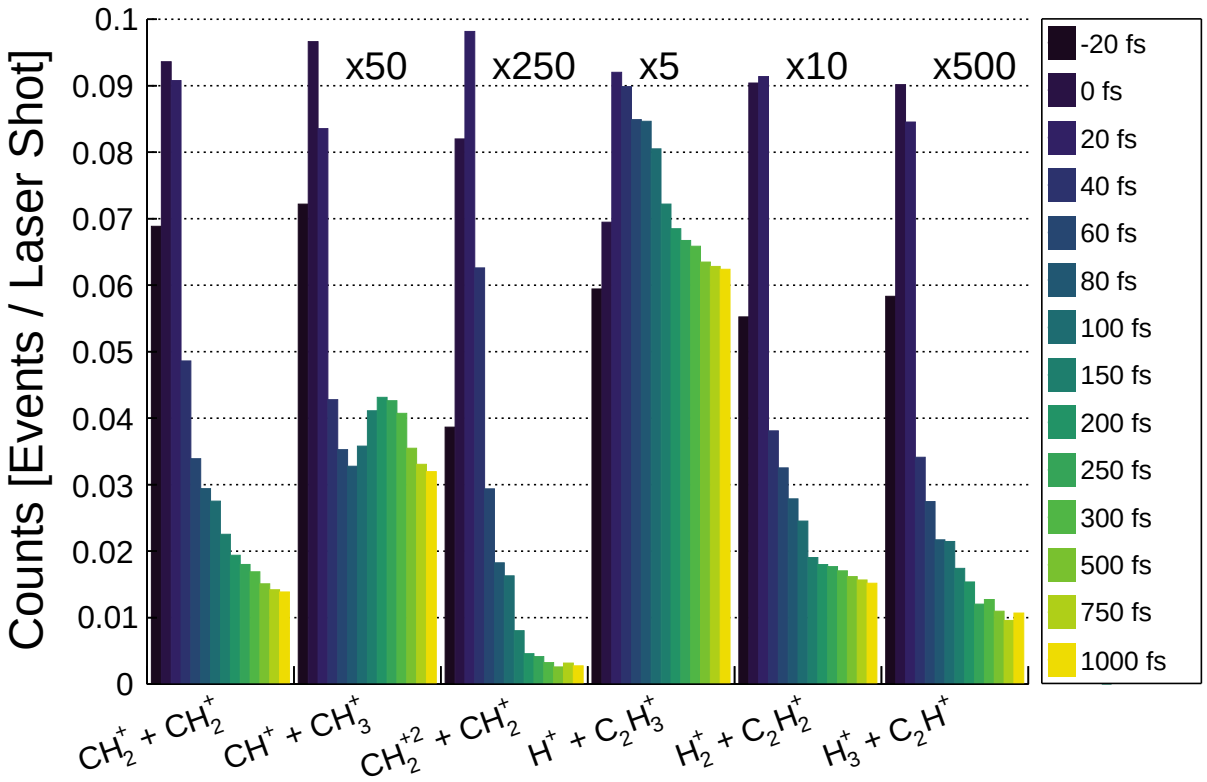

Figure 8.6: Absolute count rates for the top six most common 2-ion channels for various pump-probe time delays. Due to the large differences in count rates, five of the channels have been scaled individually.

Across short pump-probe time delays, breaking of the C-C bond, producing two identical, singly charged ions ($C_2H_4^{2+} \longrightarrow CH_2^+ + CH_2^+$) is overwhelmingly common. As the delay time increases, the production of ions in this channel reduces exponentially until there a steady state at or near 750 fs and 1000 fs. As discussed earlier, the measured count rates for long pump-probe time delays under count the absolute count rates more than those measured for short pump-probe time delays. The decaying trend of absolute count rates should, therefore, rise up for delays beyond 300 fs.

The second most populated channel, $C_2H_4^{2+} \longrightarrow H^+ + C_2H_3^+$, produces a similar trend to the symmetric breakup of ethylene. There are three noteworthy features regarding the absolute values. One, the count rates for this channel surpass that of the earlier described symmetric breakup ($C_2H_4^{2+} \longrightarrow CH_2^+ + CH_2^+$) for time delays above approximately 150 fs. Two, the production rate across all time-delays varies significantly less than every other channel. That is, the trend sits atop a large background production rate that appears to be insensitive to the pump-probe delay itself. And lastly, this channel uniquely produces the fewest events when the pump-probe is reversed (a delay of -20 fs). Taken together, these features suggest that the ionization process leaving dicationic ethylene in states that release a proton require fewer photons (due to less sensitivity at pump-probe overlap).

The next most populated channel $C_2H_4^{2+} \longrightarrow H_2^+ + C_2H_2^+$ is the first one to be discussed that results in molecular formation through the breaking of two C-H bonds and the creation of one H-H bond. Despite this fundamentally different process, the production rate dependence on pump-probe time delay mimics that of the simplest case: the breaking of the C-C bond discussed above.

The only triply charged state shown here, $C_2H_4^{3+} \longrightarrow CH_2^{2+} + CH_2^+$, features the largest relative change in count rates across time delays. This increased signal at and near time-zero is likely due to the non-linear dependence of triply ionizing ethylene. However, since the peak occurs at a delay of 20 fs and not 0 fs, there is likely evidence of bond-length dependent enhanced ionization.

The last two channels to be discussed are relevant for the isomerization of ethylene - fragmentation into $CH^+ + CH_3^+$ and $H_3^+ + C_2H^+$. The former has the unique property of an undulation in its signal - producing a second peak in production at 200 fs. However, production of the trihydrogen cation, a signifier of proton migration, does not observe the same trend. What's more, this fragmentation channel peaks at 20 fs time delay instead of time-zero, commensurate with the expectation that some time for migration is needed to maximize production of this cation.

To investigate further the dynamics of the common two-body breakup channels of $C_2H_4^+$, KER plots are shown for 14 time-delays in Figures 8.7 and 8.8. For a single channel,

each of the 14 histograms have been integral normalized to highlight the movement of signal from one energy peak to another.

For the four channels shown, two common trends appear. For the first, a strong peak appears at or near 5.5 eV, regardless of whether a C-C or C-H bond is broken. This peak energy release is maintained from −20 fs through 1 ps, indicating that relatively stable states are accessed. The shape of this main energy spectrum for the three channels $CH_2^+ + CH_2^+$, $CH_3^+ + CH^+$, and $H_3^+ + C_2H^+$ are very similar: exhibiting short low energy tails and long high energy tails; while $CH_2^+ + CH_2^+$ uniquely has low energy shoulder. The proton channel, however, is flipped in shape: exhibiting a relatively sharp drop in high energy events.

The second distinct trend is a time-dependent signal originating at the strong, time-zero peak, and approaching zero KER for long time-delays. All four channels produce this behaviour, while the relative sizes of the time-dependent signal with respect to the time-independent signal are unique to each channel. When the C-H bond is broken, this time-dependent signal is relatively weak, ultimately reducing the events in the main peak very little. When the C-C bond is broken in an isomerized geometry ($CH_3^+ + CH^+$), most of the signal migrates from the stable peak to the time-dependent one. Though not as pronounced, a similar trend is seen in the symmetric breakup. Recalling that the experimental aparatus cannot effectively measure low energy events in the $CH_2^+ + CH_2^+$ channel, it can be estimated that the low energy time-dependent signal is under-represented, suggesting that approximately half of the signal eventually moves from the main peak into this temporal peak.

Careful examination of the main peak locations in the C-C bond breaking channels reveals a slight undulation at and around 150 fs. This dip in the peak KER may be an artefact of the time-dependent peak described above. The superposition of the distributions artificially shift the peaks towards one another, when in fact a deconvolution of this signal would resolve a main peak location similar to that for the short and long time-delays.

8.2.3 Contamination

The coincident fragmentation events identified hereto assume that an ethylene monomer of mass 28 amu was targeted. However, it is immediately clear from the TOF spectrum that molecules with mass larger than ethylene are probed in this experiment. These contaminants produce fragments through their own channels that populate the TOF spectrum and, more importantly, overlap with the ethelyene fragmentation channels. In order to confidently state that any measured fragmentation channel is populated solely by fragments

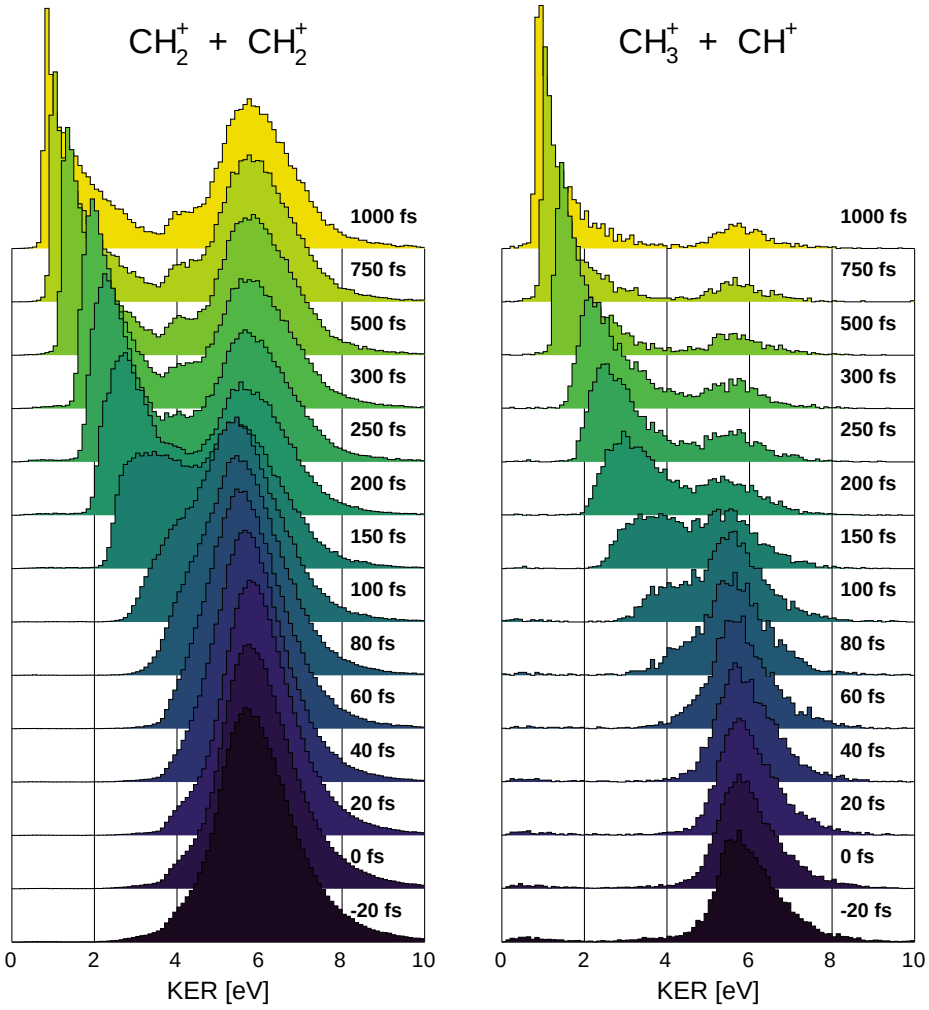

Figure 8.7: Kinetic Energy Release in the channel $C_2H_4^{2+} \longrightarrow CH_2^+ + CH_2^+$ and $C_2H_4^{2+} \longrightarrow CH_3^+ + CH^+$ over various pump-probe delays. Each histogram is integral normalized.

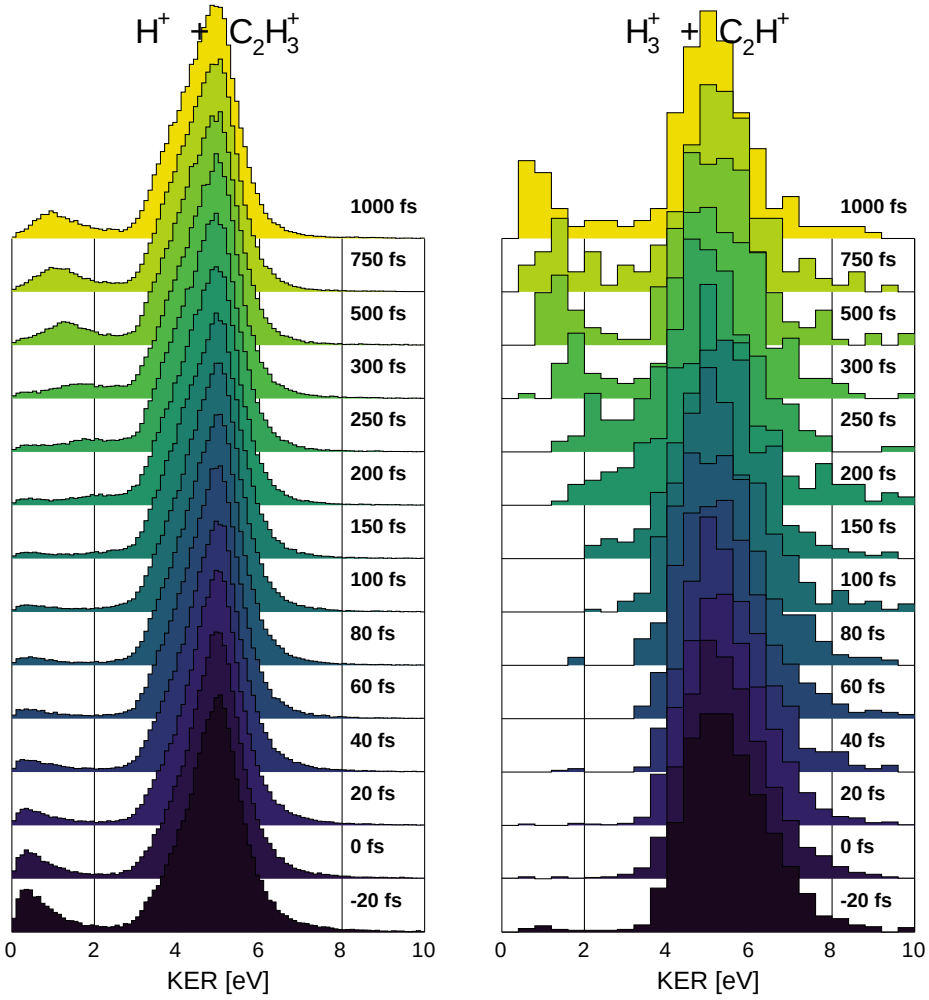

Figure 8.8: Kinetic Energy Release in the channel $C_2H_4^{2+} \longrightarrow H^+ + C_2H_3^+$ and $C_2H_4^{2+} \longrightarrow H_3^+ + C_2H^+$ over various pump-probe delays. Each histogram is integral normalized.

C_2H_4	C_2DH_3		$^{13}CCH_4$
$CH_2^+ + CH_2^+$	$CHD^+ + CH_2^+$		$CH_2^+ + {}^{13}CH_2^+$
603753	1.4%†		1.4%†
$H^+ + C_2H_3^+$	$D^+ + C_2H_3^+$	$H^+ + C_2DH_2^+$	$H^+ + {}^{13}CCH_3^+$
91854	0.8%§	1.8%‡	1.8%‡
$H_2^+ + C_2H_2^+$	$DH^+ + C_2H_2^+$	$H_2^+ + C_2DH^+$	$H_2^+ + {}^{13}CCH_2^+$
57930	0.3%	1.3%§	1.3%§
	$D^+ + CH^+ + CH_2^+$		
	0.09%		$H^+ + {}^{13}CH^+ + CH_2^+$
$H^+ + CH^+ + CH_2^+$	$H^+ + CD^+ + CH_2^+$		1.4%*
4568	1.4%*		$H^+ + CH^+ + {}^{13}CH_2^+$
	$H^+ + CH^+ + CDH^+$		1.8%**
	1.8%**		

Table 8.2: Total measured events for common fragmentation channels in ethylene and the two isotopes C_2DH_3 and $^{13}CCH_4$. Percentages indicate the number of events in the isotope channel compared with the C_2H_4 channel. Counts indicated by †,§,‡,*, and ** are identical due to an indistinguishability in their mass to charge ratio.

from the presumed target, an analysis of potential contamination is performed. The three contributors examined are as follows: ethylene with a carbon isotope, $^{13}CCH_4$ (due to its natural abundance); ethylene with a deuterium isotope, C_2DH_3 (due to its possible cross-over contamination from previous experiments); and ethylene dimers, $C_2H_4 \cdot C_2H_4$ (due to its natural abundance).

At first glance, the mass 29 peak suggests a significant production of isotopes - approximately 4% compared with the $C_2H_4^+$ peak. This is not a reliable measure of contamination as the high detection rates result in under-counting extremely high probability events such as $C_2H_4^+$ production. For a more accurate measure, specific fragmentation channels are examined using the coincident-momentum algorithm.

Table 8.2 compares the total events measured from ethylene and its isotopes fragment-

ing into the top three most common 2-ion channels and the most common 3-ion channel. Due to the degeneracy in the mass to charge ratio of several fragments, not all fragmentation channels are uniquely identified. Several of the deuterium fragmentation channels are indistinguishable from heavy carbon fragmentation channels (indicated by matching superscript symbols). To determine which of the two isotope channels are to account for the detected events, it is enough to note that a natural background of 1% ^{13}C is expected in the source, resulting in approximately 2% of the two-carbon ethylene molecules having one heavy carbon atom. The measured count rates from $^{13}CCH_4$ channels nearly match this expectation, supporting the argument that heavy carbon dominates the contamination.

An additional argument against the possibility that these detected events are sourced from C_2DH_3 molecules can be made by considering the ratio of recorded events from a class of deuterium based channels. For example, the third channel in Table 8.2 shows two possible fragmentation channels of C_2DH_3. Using the undeuterated channel as reference, it is expected that replacing any of the hydrogen atoms with a deuterium atom in the channel $H_2^+ + C_2H_2^+$ would result in production of the two channels $DH^+ + C_2H_2^+$ and $H_2^+ + C_2DH^+$ with equal probability. Since the measured count rates are not equal, it can be concluded that these events are misidentified as deuterium based channels, and in fact come from heavy carbon based channels of equal mass (indicated by identical superscripts). Though not listed, the 0.3% events detected for the channel $DH^+ + C_2H_2^+$ would identify properly as the heavy carbon channel $H_3^+ + {}^{13}CCH^+$.

The same line of reasoning applies to the three ion fragmentation channel $H^+ + CH^+ + CH_2^+$ where it is expected that the three possible deuterated channels appear in the ratio $1 : 1 : 2$, but in fact appear as $0.09 : 1.4 : 1.8$, or, approximately $1 : 15 : 20$. Ultimately, it can be concluded that there is no contamination from deuterized ethylene and that the heavy carbon isotope of ethylene makes up less than 2% of the gas target.

This leaves the ethylene dimer and trimers for consideration. Such dimers and trimers are known to exist in varying abundances among volumes of ethylene and, furthermore, are known to undergo several fragmentation pathways post-ionization [31, 129]. Ceyer and Meisels unveiled several fargmentation channels of singly ionized ethylene dimers and trimers, resulting in rich TOFMS spectra that included strong fingerprints of the monomer, dimer, and trimer states as well a plethora of fragments resulting from various dynamics. The TOF spectrum presented here does not show a significant peak at mass 56 (ethylene dimer), suggesting there is little to no ethylene dimer molecules in the target source. However, there are small peaks in the 41 - 44 amu range as well as broad peaks in the 66 - 73 amu mass range. It is possible these peaks originate from dimer and trimer reactions that result in $C_3H_5^+$-like ions and $C_5H_9^+$-like ions, but contribute little to the overall signal.

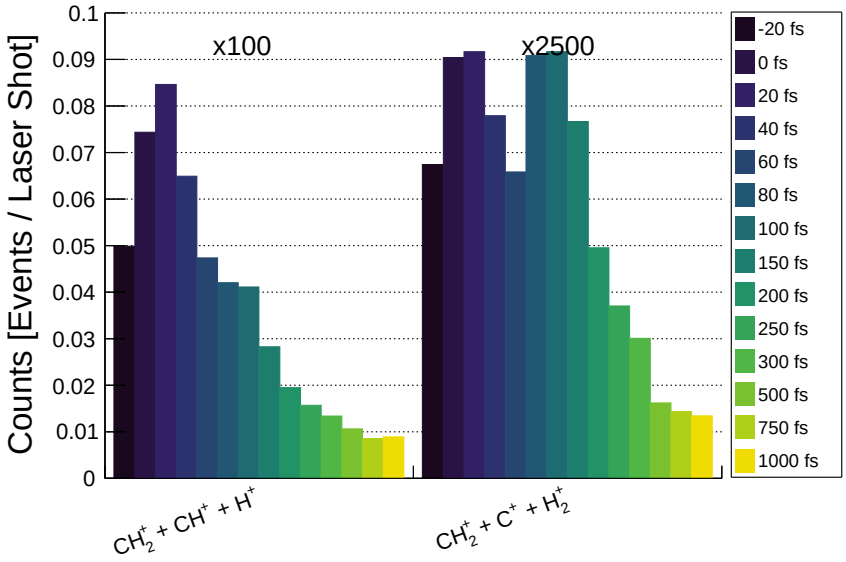

Figure 8.9: Absolute count rates for the top two most common 3-ion channels for various pump-probe time delays. Scale is set to match that from the 2-ion channesls in figure 8.6

8.2.4 3-Ion Momentum Imaging

Applying the same analysis technique for triple ion coincidences yielded far fewer events. The channel with the strongest signal was the fragmentation pathway yielding $CH_2^+ + CH^+ + H^+$. This yielded approximately 4500 events for the zero femtosecond time delay, while the next strongest channel, $CH_2^+ + C^+ + H_2^+$ yielded just 200 events. Count rates are shown in Figure 8.9. KER spectra for these channels are shown in Figure 8.10. The KER spectra for the $CH_2^+ + CH^+ + H^+$ channel mimics the 2-ion spectra in that a single mode exists for roughly 80 fs (this time peaked at ~16 eV) when a second distribution starts to emerge as a low energy shoulder, which increases in size while decreasing further in energy for higher pump-probe delays. The $CH_2^+ + C^+ + H_2^+$ channel shows the same behaviour but with the 16 eV peak all but disappearing by high delays .

Isomerization

As seen from figure 8.6, production of the ethylene isomer ethylidene ($HCCH_3$) is apparent from the C-C bond breaking channel $CH^+ + CH_3^+$. What's more, the production of this channel peaks after a time delay of 200 fs, suggesting that proton migration into the

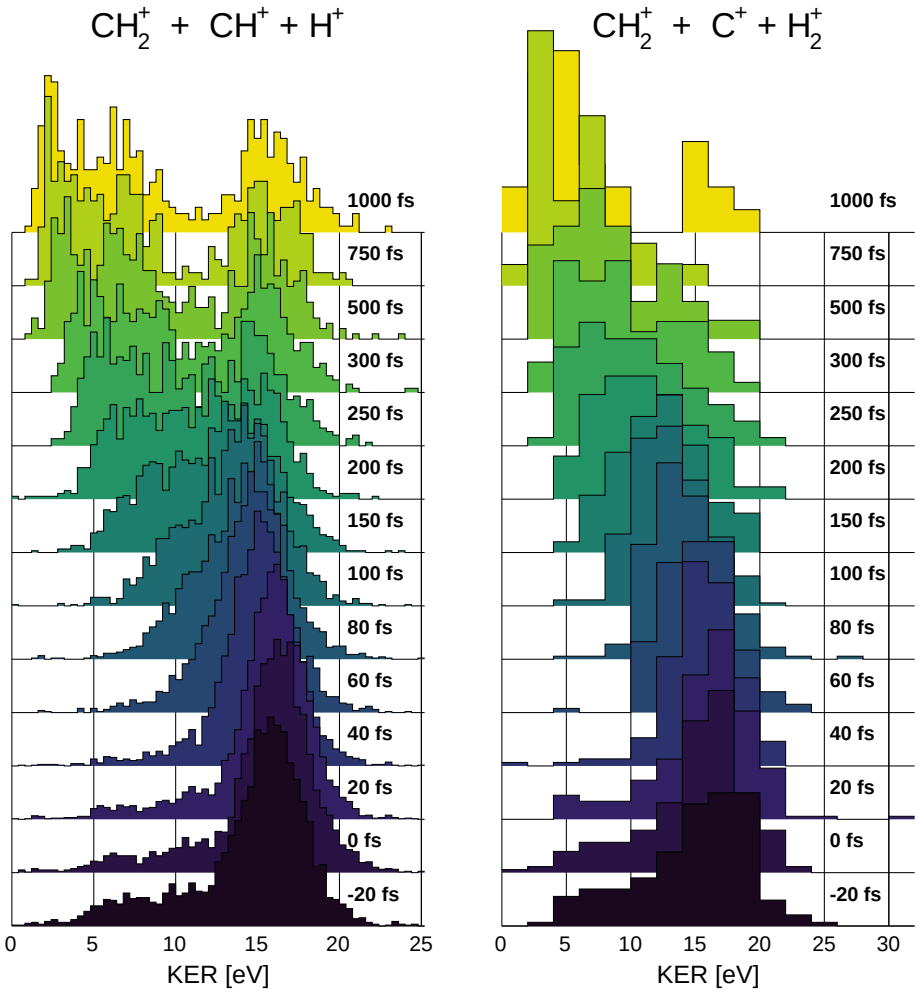

Figure 8.10: Kinetic Energy Release in the 3-ion channels $C_2H_4^{2+} \longrightarrow CH_2^+ + CH^+ + H^+$ and $C_2H_4^{2+} \longrightarrow CH_2^+ + C^+ + H_2^+$ over various pump-probe delays. Each histogram is integral normalized.

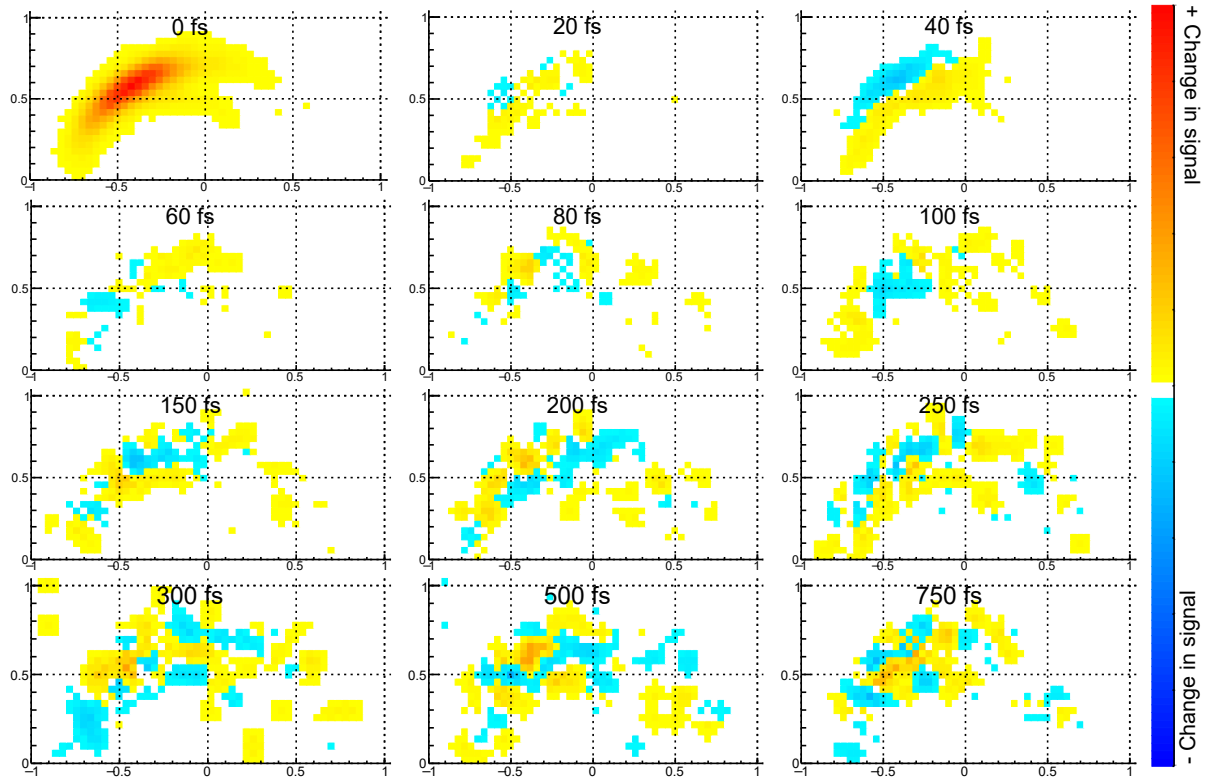

Figure 8.11: Difference Newton plots for H^+ in the $C_2H_4^{2+} \longrightarrow CH_2^+ + CH^+ + H^+$ channel. Momentum vectors are rotated such that CH_2^+ points along x-axis and the CH^+ momentum is fixed below the x-axis. 0 fs shows raw data, while all subsequent plots show changes in the signal from one pump-probe delay earlier. That is, [H^+(20 fs) - H^+(0 fs)] is shown under 20 fs, and [H^+(80 fs) - H^+(60 fs)] is shown under 80 fs. Signal shown result from high energy filtering. Specifically, KER > 14 eV

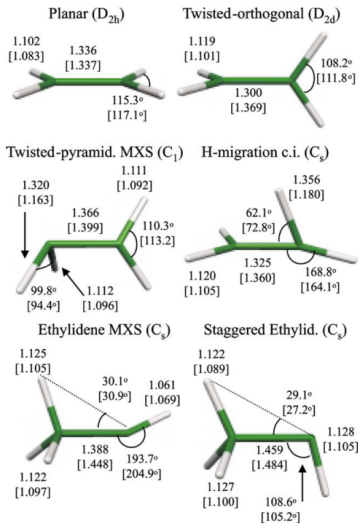

Figure 8.12: Selected geometrical structures of Ethylene studied by Barbatti *et al.*. [11] Reprinted with permission from Elsevier.

ethylidene state maximizes at 200 fs. To better understand this, the proton migration is imaged using Newton plots shown in Figure 8.11. In these figures, the H^+ momentum is fixed to the upper two quadrants, and the CH_2^+ is fixed to the lower two quadrants (not shown). These are both plotted with respect to the heaviest ion (CH_2^+) along the positive x-axis. The peak of the H^+ signal with 0 fs delay makes an angle of approximately 120° with respect to the CH_2^+ momentum vector. The coincident signal from the CH^+ ion (not shown) also points in the negative x-axis. This confirms that the majority of the H^+ signal with 0 fs delay originates from breakup in the ethylene geometry. The H^+ signal also demonstrates a smeared arc. This signal results from H^+ ejecting at various positions along the ethylene molecule.

This last feature - indicative of isomerization - generally produces little less signal and little variation among pump-probe delays. To extract the time-dependent nature of the H^+ momentum vector, signal from successive Newton diagrams are subtracted from one another. The results are shown in Figure 8.11 for time delays 20 - 750 fs. For these time delays, yellow-red indicate increases in signal and cyan-blue indicate decreases in signal. After 20 fs, there is relatively little change in the H^+ momentum vector signal. Between 20 fs and 40 fs, the magnitude of the H^+ ion momentum reduces, and signal begins to appear in two regions: in the positive x-axis and very close to the x-axis itself near x=-0.7. At this pump-probe delay, the KER spectrum has not changed, so the reduced H^+ momentum

is not the result of an overall relaxation. It must be that the H^+ ion has migrated to a position where it ejects with less energy compared to the CH^+ and CH_2^+ fragments. The signal appearing at positive x values shows the H^+ moving in the same direction as the CH_2^+ ion, while the signal at x=-0.7, shows H^+ moving opposite the CH_2^+ ion. Signal in the positive x and positive y quadrant increases for increasing pump-probe delay up until 200 fs where a reduction in signal appears. At 250 fs, an increase in signal reappears. From here on, the signal-to-noise ratio is too poor to image any structures.

The number of geometric configurations available to ethylene (a selection shown in Figure 8.12) greatly complicates the interpretation of the Newton Plot signal shown in Figure 8.11 and may explain its noisy descent beyond 300 fs. Referring to the structures in Figure 8.12, it is possible the reduction in H^+ momentum seen at 20 and 40 fs results from the ethylene rotating into the twisted-orthogonal state. More clearly, the ejection of H^+ in the direction of CH_2^+ suggests that the structure formed at this time is more similar to the HC_2H_3 geometry than the $H_2C_2H_2$ geometry. To quantify the extent to which this latter isomerization occurs, integration of the H^+ signal in the positive x direction is performed and plotted in Figure 8.13. The isomer signal remains low for the first 20 fs then increases to a maximum at 100 fs, confirming the images of H^+ migration shown in the Newton plots. A decrease in signal at 200 fs is seen, followed by an increase at 300 fs suggesting that the to-and-fro motion of the proton across the ethylene molecule has been imaged in Figure 8.11. The 100 fs timescale for this isomerization channel has been measured by Jiang *et al.* with an XUV pump-probe ionization scheme at FLASH [91]. Jiang *et al.* measure the signal yield in of high KER events (KER>4 eV)in the isomerized channel $CH^+ + CH_3^+$. In a separate VUV-XUV pump-probe ionization scheme, Allison *et al.* measured the isomerization yield in the channel $CH^+ + CH_3^+$, reporting a similar peak at 100 fs.

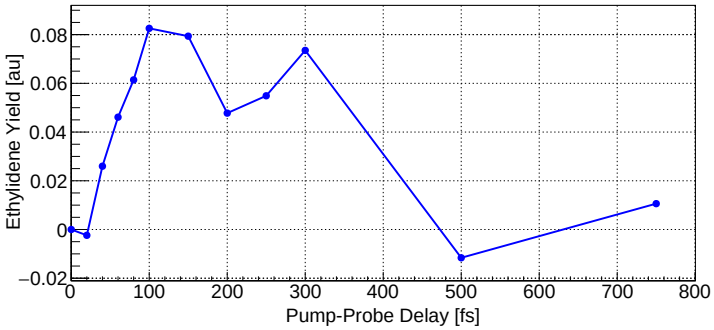

Figure 8.13: Relative ethylidene yield calculated using the integral on raw Newton plots from Figure 8.11. The range $x > -0.1$ is used since little isomerization into the ethylidene structure is seen beyond $x = -0.1$ after 20 fs.

8.3 Conclusion

The time-dependent fragmentation of ethylene into various channels has been observed and respective KER distributions measured. The isomerization of ethylene into the $HCCH_3$ geometry has been confirmed through the fragmentation channel $CH^+ + CH_3^+$ as well as through the production of the trihydrogen cation in the channel $C_2H^+ + H_3^+$. This isomerization process has been imaged for the first time by measuring the proton ejection momentum vector with respect to the C-C bond. This time-dependent isomerization signal peaks at 100 fs, matching previous studies on this process.

Chapter 9

Conclusions

9.1 Ultrafast Process Imaging

The breadth of the Coulomb Explosion Imaging technique has been expanded to include new sources of ionization - specifically synchroton-based soft x-rays and ultraviolet-infrared pump-probe lasers. Combined with new measurements using variable pulse-length infrared femtosecond lasers and previous measurments with highly charged ion impact, an expansive study on molecular structure undergoing ultrafast processes has been performed.

For the first time, complete three-dimensional momentum coincidence measurements of the carbonyl sulfide molecule using soft x-ray ionization has been performed. The tunable photon energy allowed observation of a strict KER threshold - the first observation of its kind. Concerted and sequential breakup of triply and quadruply charged OCS was observed. Dalitz plot analysis of the sequential process $OCS^{3+} \longrightarrow CO^{2+} + S^{+} \longrightarrow O^{+} + C^{+} + S^{+}$ revealed enhanced bending of the OCS^{3+} molecular ion when ionized by 167 eV - the result of accessing the $\pi^{*}_{1/2}$ state.

Using the FEMPULS technique, measurements on the structural deformation of OCS ions were made. Various sequential breakup channels were documented including the hereto unseen channel, $OCS^{4+} \longrightarrow CO^{2+} + S^{2+} \longrightarrow C^{+} + O^{+} + S^{2+}$. Through the choice of laser pulse length, the branching ratio into metastable fragmentation pathways is shown to be controlled. Lastly, controlled isomerization of OCS into two extremely bent states was achieved, with the bending timescale measured at $\sim$150 fs.

The ultrafast isomerization process of acetylene into vinylidene has been measured using a UV-IR pump-probe table-top setup, with time-dependent isomer yields matching

theory. The success of this proof of principle experiment opened the door to the ultrafast imaging of state-specific processes without the need for x-ray FEL systems.

The scalability of the acetylene measurements was shown by performing a similar experiment with ethylene. For this target, various measurements associated with the proton migration process isomerizing ethylene into ethylidene were made, showing similar isomerization timescales to acetylene.

9.2 Future Work

With the current range of ionization sources and imaging apparatuses available there is a limit on the size of the next step into structural imaging. Increased detection efficiency made available with the use of super MCP detectors combined with commercially available 100 kHz laser sources make it possible to acquire coincidence measurements of rare processes and those processes producing several fragments. Although detection of rare events scales well with these improvements in instrumentation, the ability to reconstruct absolute geometries scales at a chaotic rate as evidenced by the sheer rarity of published structures through the use of CEI. By way of example, consider the complete fragmentation and geometry reconstruction of the five-atom molecule CHISOF [61]. Gagnon *et al.* successfully reconstructed just five molecules, with the rest of the events converging with unacceptable fitness. The exhaustive analysis by Ramadhan [152] further confirms this. Instead, then, the focus of CEI measurements should be on rare processes with distinct features measurable when undergoing fragmentation - not necessarily complete geometric imaging.

Building off of the FEMPULS measurements of OCS, a relatively simple IR-IR pump-probe scheme could be used to image the metastable break-up of OCS^{3+} and OCS^{4+}, imaging directly, for the first time, the rotating CO^{2+} and CS^{2+} molecular ions. Furthermore, the isomerization process identified in the (1,2,1) channel could be confirmed using the long 200 fs pulse overlapped with a short 7 fs pulse. Such a pump-probe design would allow for direct imaging of this newly measured isomerization process.

Upgrading the pump-probe scheme to the VUV range would allow for shorter pulses and more control on state access in targets. Combining this ionization scheme with higher repetition rate lasers and more efficient detectors, higher resolution snapshots of acetylene and ethylene isomerization can be taken. In lieu of increasing the resolution of this particular proton migration process, a more efficient system could be used to investigate the isomerization of ethylene into its various structural configurations, such as the twisted-orthogonal state. Because this geometry does not exist in a plane, imaging it would require

coincident detection of at least four ions - a feat not yet achieved with CEI, but ultimately possible.

References

[1] H. Akagi, T. Otobe, A. Staudte, A. Shiner, F. Turner, R. Dorner, D. M. Villeneuve, and P. B. Corkum. Laser Tunnel Ionization from Multiple Orbitals in HCl. *Science*, 325(5946):1364–1367, 2009.

[2] C J Allan, K Siegbahn, U Gelius, D A Allison, G Johansson, H Siegbahn, and K Siegbahn. ESCA Studies of CO_2, CS_2 and COS. *Journal of Electron Spectroscopy and Related Phenomena*, 1:131–151, 1972.

[3] T. K. Allison, H. Tao, W. J. Glover, T. W. Wright, A. M. Stooke, C. Khurmi, J. Van Tilborg, Y. Liu, R. W. Falcone, T. J. Martnez, and A. Belkacem. Ultrafast internal conversion in ethylene. II. Mechanisms and pathways for quenching and hydrogen elimination. *Journal of Chemical Physics*, 136(12), 2012.

[4] A S Alnaser, I Litvinyuk, T Osipov, B Ulrich, A Landers, E Wells, C M Maharjan, P Ranitovic, I Bochareva, D Ray, and C L Cocke. Momentum-imaging investigations of the dissociation of D_2^+ and the isomerization of acetylene to vinylidene by intense short laser pulses. *Journal of Physics B: Atomic, Molecular and Optical Physics*, 39(13):S485–S492, 2006.

[5] M. V. Ammosov, N. B. Delone, and V. P. Krainov. Tunnel ionization of complex atoms and of atomic ions in an alternating electromagnetic field. *Soviet Physics JETP*, 64(6):1191–1194, 1986.

[6] Toshiaki Ando, Akihiro Shimamoto, Shun Miura, Katsunori Nakai, Huailiang Xu, Atsushi Iwasaki, and Kaoru Yamanouchi. Wave packet bifurcation in ultrafast hydrogen migration in CH_3OH^+ by pump-probe coincidence momentum imaging with few-cycle laser pulses. *Chemical Physics Letters*, 624:78–82, 2015.

[7] U. Ankerhold, B. Esser, and F. von Busch. Decay of CS_2 and OCS after sulphur 1s photoexcitation: II. Dissociation channels and kinematics. *Journal of Physics B: Atomic, Molecular and Optical Physics*, 30:1207–1222, 1997.

[8] U. Ankerhold, B. Esser, and F. von Busch. Ionization and fragmentation of OCS and CS_2 after photoexcitation around the sulfur 2p edge. *Chemical Physics*, 220(3):393–407, 1997.

[9] S. Augst, D. D. Meyerhofer, D. Strickland, and S. L. Chint. Laser ionization of noble gases by Coulomb-barrier suppression. *Journal of the Optical Society of America B*, 8(4):858–867, 1991.

[10] L Avaldi and A Huetz. Photodouble ionization and the dynamics of electron pairs in the continuum. *Journal of Physics B: Atomic, Molecular and Optical Physics*, 38(9):S861–S891, 2005.

[11] M. Barbatti, G. Granucci, M. Persico, and H. Lischka. Semiempirical molecular dynamics investigation of the excited state lifetime of ethylene. *Chemical Physics Letters*, 401(1-3):276–281, 2005.

[12] Anton Barty, Jochen Küpper, and Henry N. Chapman. Molecular Imaging Using X-Ray Free-Electron Lasers. *Annual Review of Physical Chemistry*, 64(1):415–435, 2013.

[13] Michal Ben-Nun and Todd. J. Martínez. Ab Initio Quantum Molecular Dynamics. *Advances in Chemical Physics*, 121:439–512, 2002.

[14] R. Bergmann, H. Daniel, T. von Egidy, F. J. Hartmann, J. J. Reidy, and W. Wilhelm. Measurement of the Coulomb capture ratio of negative muons and the muonic Lyman-series intensities on solid solutions of Nb-V at five stoichiometric ratios. *Physical Review A - Atomic, Molecular, and Optical Physics*, 20(3):633–638, 1979.

[15] V R Bhardwaj, C P Safvan, K Vijayalakshmi, and D Mathur. On the spatial alignment of bent triatomic molecules by intense, picosecond laser fields. *Journal of Physics B: Atomic, Molecular and Optical Physics*, 30:3821–3831, 1997.

[16] Cosmin I. Blaga, Junliang Xu, Anthony D. DiChiara, Emily Sistrunk, Kaikai Zhang, Pierre Agostini, Terry A. Miller, Louis F. DiMauro, and C. D. Lin. Imaging ultrafast molecular dynamics with laser-induced electron diffraction. *Nature*, 483(7388):194–197, 2012.

[17] Irina Bocharova, Reza Karimi, Emmanuel F. Penka, Jean Paul Brichta, Philippe Lassonde, Xiquan Fu, Jean Claude Kieffer, André D. Bandrauk, Igor Litvinyuk, Joseph Sanderson, and François Légaré. Charge resonance enhanced ionization of CO_2 probed by laser coulomb explosion imaging. *Physical Review Letters*, 107(6), 2011.

[18] P. Bolognesi, P. O'Keeffe, and L. Avaldi. The OCS S L_3MM auger spectrum and angular distributions studied by photoelectron-auger electron coincidence experiments. *Journal of Physical Chemistry A*, 113(52):15136–15141, 2009.

[19] C Bomme, R Guillemin, T Marin, L Journel, T Marchenko, N Trcera, R K Kushawaha, M N Piancastelli, M Simon, M Stener, and P Decleva. Molecular-frame photoelectron angular distribution imaging studies of OCS S1s photoionization. *Journal of Physics B: Atomic, Molecular and Optical Physics*, 45(19):194005, 2012.

[20] Séverine Boyé-Péronne, Dolores Gauyacq, and Jacques Liévin. Vinylidene-acetylene cation isomerization investigated by large scale ab initio calculations. *Journal of Chemical Physics*, 124(21):214305, 2006.

[21] W. H. Breckenridge and Henry Taube. Ultraviolet Absorption Spectrum of Carbonyl Sulfide. *The Journal of Chemical Physics*, 52(4):1713–1715, 1970.

[22] Vincent Brems, Bernd M Nestmann, and Sigrid D Peyerimhoff. Ab initio study of the core-excited OCS molecule : assignment of the L -shell excitation spectrum. *Chemical Physics Letters*, 287:255–262, 1998.

[23] M. Brewczyk and L. J. Frasinski. Thomas-Fermi-Dirac strong laser fields. *Journal of Physics B: Atomic, Molecular and Optical Physics*, 24:L307–L313, 1991.

[24] J P Brichta, S J Walker, R Helsten, and J H Sanderson. Ultrafast imaging of multielectronic dissociative ionization of CO_2 in an intense laser field. *Journal of Physics B: Atomic, Molecular and Optical Physics*, 40(1):117–129, 2007.

[25] Jean Paul Brichta, Aden N. Seaman, and Joseph H. Sanderson. Ultrafast imaging of polyatomic molecules with simplex algorithm. *Computer Physics Communications*, 180(2):197–200, 2009.

[26] V. Brites, J. H D Eland, and M. Hochlaf. OCS^2+ dication spectroscopy and electronic states. *Chemical Physics*, 346(1-3):23–33, 2008.

[27] W. A. Bryan, W. R. Newell, J. H. Sanderson, and A. J. Langley. Observation of multiple ionization pathways for OCS in an intense laser field resolved by three-dimensional covariance mapping and visualized by hierarchical ionization topology. *Physical Review A - Atomic, Molecular, and Optical Physics*, 74(5):1–11, 2006.

[28] Thomas A. Carlson, Patrick Gerard, Manfred O. Krause, Grant Von Wald, James W. Taylor, Frederick A. Grimm, and B. P. Pullen. Resonant auger processes for molecules as studied with angle resolved electron spectrometry. *Journal of Electron Spectroscopy and Related Phenomena*, 47(C):227–243, 1988.

[29] Thomas A. Carlson and Manfred O. Krause. Electron shake-off resulting from K-shell ionization in neon measured as a function of photoelectron velocity. *Physical Review*, 140(4A):A1057–A1064, 1965.

[30] T X Carroll, De Ji, and T. D. Thomas. Cabon and Oxygen KLL and Sulfur LMM Auger Spectra of OCS. *Journal of Electron Spectroscopy and Related Phenomena*, 51:471–486, 1990.

[31] S. Ceyer, P. Tiedemann, C. Ng, B. Mahan, and Y. Lee. Photoionization of ethylene clusters. *The Journal of Chemical Physics*, 70(5):2138, 1979.

[32] H. N. Chapman and Et Al. Femtosecond X-ray protein nanocrystallography. *Nature*, 470(7332):73–78, 2011.

[33] S Chelkowski, A Conjusteau, T Zuo, and A D Bandrauk. Dissociative ionization of H_2^+ in an intense laser field: Charge-resonance-enhanced ionization, Coulomb explosion, and harmonic generation at 600 nm. *Phys. Rev. A*, 54(4):3235–3244, 1996.

[34] S. Chelkowski, P. Corkum, and A. Bandrauk. Femtosecond Coulomb Explosion Imaging of Vibrational Wave Functions. *Physical Review Letters*, 82(17):3416–3419, 1999.

[35] S. L. Chin, F. Yergeau, and P. Lavigne. Tunnel ionisation of Xe in an ultra-intense CO_2 , laser field (10^{14} W cm^{-2}) with multiple charge creation. *Journal of Physics B: Atomic, Molecular and Optical Physics*, 18(8):L213–L215, 1985.

[36] K Codling and L J Frasinski. Dissociative ionization of small molecules in intense laser fields. *Journal of Physics B: Atomic, Molecular and Optical Physics*, 26:783–809, 1993.

[37] K. Codling, L. J. Frasinski, and P. A. Hatherly. Multiphoton ionisation of H_2 and D_2 using an intense sub-picosecond laser. *Journal of Physics B: Atomic, Molecular and Optical Physics*, 21:L433–L438, 1988.

[38] K Codling, L J Frasinski, and P A Hatherly. On The Field Ionisation of Diatomic Molecules by Intense Laser Field. *Journal of Physics B: Atomic, Molecular and Optical Physics*, 22(12):L321–L327, 1989.

[39] E. Constant, H. Stapelfeldt, and P. Corkum. Observation of Enhanced Ionization of Molecular Ions in Intense Laser Fields. *Physical Review Letters*, 76(22):4140–4143, 1996.

[40] G. R. Cook and M. Ogawa. Photoionization and Absorption Coefficients of OCS. *The Journal of Chemical Physics*, 51(2):647–652, 1969.

[41] C. Cornaggia, J. Lavancier, D. Normand, J. Morellec, and H. X. Liu. Intensity dependence of the multielectron dissociative ionization of N_2 at 305 and 610 nm. *Physical Review A*, 42(9):5464–5472, 1990.

[42] Rh Dalitz. CXII. On the analysis of τ-meson data and the nature of the τ-meson. *Philosophical Magazine*, 44(357):1068–1080, 1953.

[43] Aloke Das, E. D. Poliakoff, R. R. Lucchese, and John D. Bozek. Mode-specific photoionization dynamics of a simple asymmetric target: OCS. *Journal of Chemical Physics*, 130(4):044302, 2009.

[44] N. B. Delone and V. P. Krainov. *Atom in a Strong Optical Field [in Russian].* Energoatomizdat, 2nd ed. edition, 1984.

[45] J Delwiche, MJ Hubin-Franskin, G Caprace, and P Natalis. On the He (I) and Ne (I) photoelectron spectra of OCS. *Journal of Electron Spectroscopy and Related Phenomena*, 21:205–218, 1980.

[46] Jacques Delwiche, MarieJeanne HubinFranskin, PaulMarie Guyon, and Irène Nenner. Autoionization of OCS by threshold photoelectron spectroscopy. *The Journal of Chemical Physics*, 74(8):4219–4227, 1981.

[47] Xiaoyan Ding, M. Haertelt, S. Schlauderer, M. S. Schuurman, A. Yu Naumov, D. M. Villeneuve, A. R.W. McKellar, P. B. Corkum, and A. Staudte. Ultrafast Dissociation of Metastable CO_2^+ in a Dimer. *Physical Review Letters*, 118(15):1–5, 2017.

[48] R. Dörner, T. Vogt, V. Mergel, H. Khemliche, S. Kravis, C. Cocke, J. Ullrich, M. Unverzagt, L. Spielberger, M. Damrau, O. Jagutzki, I. Ali, B. Weaver, K. Ullmann, C. Hsu, M. Jung, E. Kanter, B. Sonntag, M. Prior, E. Rotenberg, J. Denlinger, T. Warwick, S. Manson, and H. Schmidt-Böcking. Ratio of Cross Sections for Double to Single Ionization of He by 85400 eV Photons. *Physical Review Letters*, 76(15):2654–2657, 1996.

[49] N. Douguet, T. N. Rescigno, and A. E. Orel. Time-resolved molecular-frame photoelectron angular distributions: Snapshots of acetylene-vinylidene cationic isomerization. *Physical Review A - Atomic, Molecular, and Optical Physics*, 86(1):1–7, 2012.

[50] Masahiro Ehara, Mayumi Ishida, and Hiroshi Nakatsuji. Fine theoretical spectroscopy using symmetry adapted cluster-configuration interaction general-R method : Outer- and inner-valence ionization spectra of CS_2 and OCS. *Journal of Chemical Physics*, 117:3248–3255, 2002.

[51] Maximilian Eichberger, Hanjo Schäfer, Marina Krumova, Markus Beyer, Jure Demsar, Helmuth Berger, Gustavo Moriena, Germán Sciaini, and R. J. Dwayne Miller. Snapshots of cooperative atomic motions in the optical suppression of charge density waves. *Nature*, 468(7325):799–802, 2010.

[52] J H D Eland. The dynamics of three-body dissociations of dications studied by the triple coincidence technique PEPIPICO. *Molecular Physics*, 61(3):725–745, 1987.

[53] J. H D Eland, M. Hochlaf, P. Linusson, E. Andersson, L. Hedin, and R. Feifel. Triple ionization spectra by coincidence measurements of double Auger decay: The case of OCS. *Journal of Chemical Physics*, 132(1):014311, 2010.

[54] J. H D Eland, F. S. Wort, P. Lablanquie, and I. Nenner. Mass spectrometric and coincidence studies of double photoionization of small molecules. *Zeitschrift für Physik D Atoms, Molecules and Clusters*, 4(1):31–42, 1986.

[55] P. Erman, A Karawajczyk, Elisabeth Rachlew, M. Stankiewicz, and K.Y. Franzén. High-resolution angular-resolved measurements of the fragmentation of the core-excited OCS molecule. *Physical Review A*, 56(4):2705, 1997.

[56] Renfei Feng, Glyn Cooper, and C. E. Brion. Quantitative studies of the photoabsorption of carbonyl sulphide in the valence-shell, S 2p, 2s and C 1s inner-shell regions (4-360 eV) by dipole electron impact spectroscopies. *Chemical Physics*, 252:359–378, 2000.

[57] Renfei Feng, Glyn Cooper, Yasuhiro Sakai, and C E Brion. Dipole (e,e+ion) coincidence studies of the ionic photofragmentation and photoionization of carbonyl sulfide in the valence shell and S 2p , 2s and C 1s inner shell regions (10-300 eV). *Chemical Physics*, 255:353–368, 2000.

[58] K Yoshiki Franzen, P Erman, P. A. Hatherly, A Karawajczyk, E Rachlew, and M Stankiewicz. Quasi two-step dissociation effects observed in the core excited OCS molecule. *Chemical Physics*, 285:71–76, 1998.

[59] L. J. Frasinski, K. Codling, P. Hatherly, J. Barr, I. N. Ross, and W. T. Toner. Femtosecond dynamics of multielectron dissociative ionization by use of a picosecond laser. *Physical Review Letters*, 58(23):2424–2427, 1987.

[60] L. J. Frasinski, K. Codling, and P. A. Hatherly. Covariance Mapping: A Correlation Method Applied to Multiphoton Multiple Ionization. *Science*, 246(4933):1029–1031, 1989.

[61] J. Gagnon, Kevin F. Lee, D. M. Rayner, P. B. Corkum, and V. R. Bhardwaj. Coincidence imaging of polyatomic molecules via laser-induced Coulomb explosion. *Journal of Physics B: Atomic, Molecular and Optical Physics*, 41(21):215104, 2008.

[62] M. Gaillard, D. Gemmell, G. Goldring, I. Levine, W. Pietsch, J. Poizat, A. Ratkowski, J. Remillieux, Z. Vager, and B. Zabransky. Experimental determination of the structure of H_3^+. *Physical Review A*, 17(6):1797–1803, 1978.

[63] Deepanwita Ghosh, Bhaskar Mondal, Sabyasachi Bagchi, and Abhijit Kumar Das. Isomers of OCS and their reaction with H_2O on singlet potential energy surface. *Molecular Physics*, 108(24):3353–3364, 2010.

[64] Emily A. Gibson, Ariel Paul, Nick Wagner, Ra'anan Tobey, David Gaudiosi, Sterling Backus, Ivan P. Christov, Andy Aquila, Eric M. Gullikson, David T. Attwood, Margaret M. Murnane, and Henry C. Kapteyn. Coherent Soft X-ray Generation in the Water Window with Quasi-Phase Matching. *Science*, 302(5642):95–98, 2003.

[65] A. Giusti-Suzor, F. H. Mies, Louis F. DiMauro, E. Charron, and B. Yang. Dynamics of H_2^+ in intense laser fields. *Journal of Physics B: Atomic, Molecular and Optical Physics*, 28:309–339, 1995.

[66] A V Golovin, J Adachi, S Motoki, M Takahashi, and A Yagishita. Inner-shell photoelectron angular distributions from fixed-in-space OCS molecules. *Journal of Physics B: Atomic, Molecular and Optical Physics*, 38(3):L63–L68, 2005.

[67] S. Haessler, J. Caillat, W. Boutu, C. Giovanetti-Teixeira, T. Ruchon, T. Auguste, Z. Diveki, P. Breger, A. Maquet, B. Carré, R. Taïeb, and P. Salières. Attosecond imaging of molecular electronic wavepackets. *Nature Physics*, 6(3):200–206, 2010.

[68] R I Hall, L Avaldi, G Dawber, A G Mcconkey, M A Macdonald, and G C King. Double photoionization of CO_2, OCS, C_2H_2, CF_4, and C_6H_6 studied by threshold photoelectrons coincidence (TPEsCO) spectroscopy. *Chemical Physics*, 187:125–135, 1994.

[69] T. Hartman, P. N. Juranic, K. Collins, B. Reilly, N. Appathurai, and R. Wehlitz. Large molecules reveal a linear length scaling for double photoionization. *Physical Review Letters*, 108(2):1–4, 2012.

[70] T. Hartman, P. N. Juranić, K. Collins, B. Reilly, E. Makoutz, N. Appathurai, and R. Wehlitz. Photo-double-ionization mechanisms in aromatic hydrocarbons. *Physical Review A - Atomic, Molecular, and Optical Physics*, 87(6):1–8, 2013.

[71] Hirokazu Hasegawa, Akiyoshi Hishikawa, and Kaoru Yamanouchi. Coincidence imaging of Coulomb explosion of CS_2 in intense laser fields. *Chemical Physics Letters*, 349(1-2):57–63, 2001.

[72] P. A. Hatherly, L. J. Frasinski, K. Codling, and J. R M Barr. Multiphoton ionisation of n-alkanes using an intense sub-picosecond laser. *Chemical Physics Letters*, 149(5-6):477–481, 1988.

[73] P. Herwig, K. Zawatzky, M. Grieser, O. Heber, B. Jordon-Thaden, C. Krantz, O. Novotny, R. Repnow, V. Schurig, D. Schwalm, Z. Vager, A. Wolf, O. Trapp, and H. Kreckel. Imaging the Absolute Configuration of a Chiral Epoxide in the Gas Phase. *Science*, 342(6162):1084–1086, 2013.

[74] Y Hikosaka, P Lablanquie, E Shigemasa, T Aoto, and K Ito. Sub-natural linewidth spectroscopy on corevalence doubly ionized states of OCS. *Journal of Physics B: Atomic, Molecular and Optical Physics*, 41(2):025103, 2008.

[75] Yasumasa Hikosaka, Hideo Hattori, Takumi Hikida, and Koichiro Mitsuke. Superexcited states of OCS probed by using photoelectron spectroscopy for autoionizing atomic sulfur. *Journal of Chemical Physics*, 107(8):2950–2961, 1997.

[76] A Hishikawa, A Iwamae, K Hoshina, M Kono, and K Yamanouchi. Coulomb Explosion Dynamics of N_2O in Intense Laser-Field: Identification of New Two-Body

and Three-Body Fragmentation Pathways. *Research in Chemical Intermediates*, 24(7):765–784, 1998.

[77] Akiyoshi Hishikawa, Atsushi Iwamae, Kennosuke Hoshina, Mitsuhiko Kono, and Kaoru Yamanouchi. Mass-resolved two-dimensional momentum imaging of the Coulomb explosion of N_2 and SO_2 in an intense laser field. *Chemical Physics Letters*, 282(3-4):283–291, 1998.

[78] Akiyoshi Hishikawa, Atsushi Iwamae, and Kaoru Yamanouchi. Ultrafast Deformation of the Geometrical Structure of CO_2 Induced in Intense Laser Fields. *Physical Review Letters*, 83(6):1127–1130, 1999.

[79] Akiyoshi Hishikawa, Akitaka Matsuda, Mizuho Fushitani, and Eiji J. Takahashi. Visualizing recurrently migrating hydrogen in acetylene dication by intense ultrashort laser pulses. *Physical Review Letters*, 99(25):10–13, 2007.

[80] Akiyoshi Hishikawa, Eiji J. Takahashi, and Akitaka Matsuda. Electronic and nuclear responses of fixed-in-space H_2S to ultrashort intense laser fields. *Physical Review Letters*, 97(24):15–18, 2006.

[81] Akiyoshi Hishikawa, Masakuni Ueyama, and Kaoru Yamanouchi. Probing the ultrafast nuclear motion in CS_2^{2+} in intense laser fields. *Journal of Chemical Physics*, 122(15):1–5, 2005.

[82] U. Hohm. Dipole Polarizability and Bond-dissociation Energy. *Journal of Chemical Physics*, 101(7):6362–6364, 1994.

[83] D. M. P. Holland and M A Macdonald. A photoelectron Study of the Inner Valence Molecular Orbitals of OCS. *Chemical Physics*, 144:279–287, 1990.

[84] Kennosuke Hoshina, Yusuke Furukawa, Tomoya Okino, and Kaoru Yamanouchi. Efficient ejection of H_3^+ from hydrocarbon molecules induced by ultrashort intense lalifeser fields. *Journal of Chemical Physics*, 129(10), 2008.

[85] Y. F. Hu, L. Zuin, G. Wright, R. Igarashi, M. McKibben, T. Wilson, S. Y. Chen, T. Johnson, D. Maxwell, B. W. Yates, T. K. Sham, and R. Reininger. Commissioning and performance of the variable line spacing plane grating monochromator beamline at the Canadian Light Source. *Review of Scientific Instruments*, 78(8):083109, 2007.

[86] Heide Ibrahim, Benji Wales, Samuel Beaulieu, Bruno E Schmidt, Nicolas Thiré, Éric Bisson, Christoph T Hebeisen, Vincent Wanie, Mathieu Giguére, Jean-Claude Kieffer, Michael Spanner, André D Bandrauk, Michael S Schuurman, Joseph Sanderson, and François Légaré. Tabletop imaging using 266nm femtosecond laser pulses, for characterization of structural evolution in, single molecule, chemical reactions. *Journal of Physics: Conference Series*, 635(11):112128, 2015.

[87] Heide Ibrahim, Benji Wales, Samuel Beaulieu, Bruno E. Schmidt, Nicolas Thiré, Emmanuel P. Fowe, Éric Bisson, Christoph T. Hebeisen, Vincent Wanie, Mathieu Giguére, Jean-Claude Kieffer, Michael Spanner, André D. Bandrauk, Joseph Sanderson, Michael S. Schuurman, and François Légaré. Tabletop imaging of structural evolutions in chemical reactions demonstrated for the acetylene cation. *Nature Communications*, 5:4422, jul 2014.

[88] O Jagutzki, H Schmidt-Böcking, V Mergel, A Cerezo, and M Huang. Device and method for two-dimensional detection of particles or electromagnetic radiation, 2003.

[89] M R Jana, B Ray, P N Ghosh, and C P Safvan. Dissociation of carbonyl sulfide by 150 keV Ar+ ion impact. *Journal of Physics B: Atomic, Molecular and Optical Physics*, 43(21):215207, 2010.

[90] Y. H. Jiang, A. Rudenko, O. Herrwerth, L. Foucar, M. Kurka, K. U. Kühnel, M. Lezius, M. F. Kling, J. Van Tilborg, A. Belkacem, K. Ueda, S. Düsterer, R. Treusch, C. D. Schröter, R. Moshammer, and J. Ullrich. Ultrafast extreme ultraviolet induced isomerization of acetylene cations. *Physical Review Letters*, 105(26):1–4, 2010.

[91] Y H Jiang, A Rudenko, M Kübel, O Herrwerth, L Foucar, M Kurka, K U Kühnel, A Senftleben, M F Kling, F P Sturm, J van Tilborg, A Belkacem, K Motomura, A Yamada, K Ueda, S Düsterer, R Treusch, C D Schröter, R Moshammer, and J Ullrich. Time-resolved XUV-induced isomerization and H_3 formation in C_2H_4 cation. *Journal of Physics: Conference Series*, 388(January):32014, 2012.

[92] Y H Jiang, A Senftleben, M Kurka, A Rudenko, L Foucar, O Herrwerth, M F Kling, M Lezius, J V Tilborg, A Belkacem, K Ueda, D Rolles, R Treusch, Y Z Zhang, Y F Liu, C D Schröter, J Ullrich, and R Moshammer. Ultrafast dynamics in acetylene clocked in a femtosecond XUV stopwatch. *Journal of Physics B: Atomic, Molecular and Optical Physics*, 46(16):164027, 2013.

[93] U Johann, T S Luk, I A McIntyre, A McPherson, A P Schwarzenbach, K Boyer, and C K Rhodes. Multiphoton ionization in intense ultraviolet laser fields. *AIP Conference Proceedings*, 142, 1986.

[94] T. Kaneyasu, M. Ito, Y. Hikosaka, and E. Shigemasa. Stability and Fragmentation of OCS^{2+} Studied by Using Auger-Electron-Ion Coincidence Measurement. *Journal of the Korean Physical Society*, 54(915):371–375, 2009.

[95] E. P. Kanter, P. J. Cooney, D. S. Gemmell, K. O. Groeneveld, W. J. Pietsch, A. J. Ratkowski, Z. Vager, and B. J. Zabransky. Role of excited electronic states in the interactions of fast (MeV) molecular ions with solids and gases. *Physical Review A*, 20(3):834–854, 1979.

[96] Reza Karimi, Eric Bisson, B. Wales, Samuel Beaulieu, Mathieu Giguere, Zijian Long, Wing-Ki Liu, Jean Claude Kieffer, Francois Légaré, and Joseph Sanderson. N_2O ionization and dissociation dynamics in intense femtosecond laser radiation, probed by systematic pulse length variation from 7 to 500 fs. *Journal of Chemical Physics*, 138(20), 2013.

[97] Reza Karimi, Benji Wales, Eric Bissone, Francois Légaré, Jean-Claude Kieffer, and Joseph Sanderson. Coulomb explosion dynamics of triatomic molecules in laser pulses ranging from 7 to 200fs. *Journal of Physics: Conference Series*, 388(3):032049, 2012.

[98] L. V. Keldysh. Ionization in the field of a strong electromagnetic wave. *Soviet Physics JETP*, 20(5):1307–1314, 1965.

[99] A. Knapp, M. Walter, Th Weber, A. L. Landers, S Schössler, T. Jahnke, M Schöffler, J. Nickles, S. Kammer, O. Jagutzki, L. Ph H. Schmidt, T. Osipov, J. Rösch, M. H. Prior, H. Schmidt-Böcking, C. L. Cocke, J. Feagin, and R. Dörner. Energy sharing and asymmetry parameters for photo double ionization of helium 100 eV above threshold in single-particle and Jacobi coordinates. *Journal of Physics B: Atomic, Molecular and Optical Physics*, 35(23):L521–L526, 2002.

[100] T Koopmans. Über die Zuordnung von Wellenfunktionen und Eigenwerten zu den Einzelnen Elektronen Eines Atoms. *Physica*, 1(1-6):104–113, 1934.

[101] K. Kosma, S. A. Trushin, W. Fuss, and W. E. Schmid. Ultrafast dynamics and coherent oscillations in ethylene and ethylene-d_4 excited at 162 nm. *Journal of Physical Chemistry A*, 112(33):7514–7529, 2008.

[102] M Kotani, K Ohno, and K Kayama. Quantum Mechanics of Electronic Structure of Simple Molecules. In *Handbuch der Physik*, page Vol. XXXVII/2. Springer Berlin Heidelberg, 1961.

[103] Branka Kovac. The He i photoelectron spectra of CO_2, CS_2, and OCS: Vibronic coupling. *The Journal of Chemical Physics*, 78(4):1684–1692, 1983.

[104] A. A. Krasnoperova, E. S. Gluskin, and L. N. Mazalov. $L_{II,III}$-Absorption spectra of sulfur in the CS_2 and SCO molecules. *Journal of Structural Chemistry*, 18:206–210, 1977.

[105] E Kukk, J D Bozek, J A Sheehy, P W Langhoff, and N Berrah. Angular distribution of molecular-field- and spin-orbit-split sulfur 2p photoemission in OCS: a sensitive probe of the molecular environment. *Journal of Physics B: Atomic, Molecular and Optical Physics*, 33:L51–L57, 2000.

[106] J. Laksman, D. Ceolin, M. Gisselbrecht, and S. L. Sorensen. Nuclear motion in carbonyl sulfide induced by resonant core electron excitation. *Journal of Chemical Physics*, 133(14):144314, 2010.

[107] Seyedreza Larimian, Sonia Erattupuzha, Erik Lötstedt, Tamás Szidarovszky, Raffael Maurer, Stefan Roither, Markus Schöffler, Daniil Kartashov, Andrius Baltuška, Kaoru Yamanouchi, Markus Kitzler, and Xinhua Xie. Fragmentation of long-lived hydrocarbons after strong field ionization. *Physical Review A*, 93(5):1–8, 2016.

[108] J. Lavancier, D. Normand, C. Cornaggia, J. Morellec, and H. X. Liu. Laser-intensity dependence of the multielectron ionization of CO at 305 and 610 nm. *Physical Review A*, 43(3):1461–1469, 1991.

[109] T. LeBrun, M. Lavollée, Marc Simon, and P. Morin. Dissociation dynamics of core excited N_2O. *Journal of Chemical Physics*, 98(4):2534, 1993.

[110] B. Leclerc, a. Poulin, D. Roy, M.-J. Hubin-Franskin, and J. Delwiche. Study of OCS by electron energy loss spectroscopy. *The Journal of Chemical Physics*, 75(11):5329–5348, 1981.

[111] F. Légaré, Kevin F. Lee, I. V. Litvinyuk, P. W. Dooley, A. D. Bandrauk, D. M. Villeneuve, and P. B. Corkum. Imaging the time-dependent structure of a molecule as it undergoes dynamics. *Physical Review A - Atomic, Molecular, and Optical Physics*, 72(5):1–4, 2005.

[112] F. Légaré, Kevin F. Lee, I. V. Litvinyuk, P. W. Dooley, S. S. Wesolowski, P. R. Bunker, P. Dombi, F. Krausz, A. D. Bandrauk, D. M. Villeneuve, and P. B. Corkum. Laser Coulomb-explosion imaging of small molecules. *Physical Review A - Atomic, Molecular, and Optical Physics*, 71(1):2–6, 2005.

[113] F. Légaré, I. V. Litvinyuk, P. W. Dooley, F. Quéré, A. D. Bandrauk, D. M. Villeneuve, and P. B. Corkum. Time-Resolved Double Ionization with Few Cycle Laser Pulses. *Physical Review Letters*, 91(9):0930021–0930024, 2003.

[114] M. Lezius, V. Blanchet, D. M. Rayner, D. M. Villeneuve, Albert Stolow, and Misha Yu Ivanov. Nonadiabatic multielectron dynamics in strong field molecular ionization. *Physical Review Letters*, 86(1):51–54, 2001.

[115] Lide D R. *CRC Handbook of Chemistry and Physics*. CRC Press, 84 edition, 2003.

[116] Lide D R. *CRC Handbook of Chemistry and Physics*. CRC Press, 88 edition, 2007.

[117] H. Lischka. COLUMBUS, an ab initio electronic structure program, 2012.

[118] Mohamed El Amine Madjet, Zheng Li, and Oriol Vendrell. Ultrafast hydrogen migration in acetylene cation driven by non-adiabatic effects. *Journal of Chemical Physics*, 138(9), 2013.

[119] Mohamed El Amine Madjet, Oriol Vendrell, and Robin Santra. Ultrafast dynamics of photoionized acetylene. *Physical Review Letters*, 107(26):1–5, 2011.

[120] M. Magnuson, J. Guo, C. Såthe, J.-E. Rubensson, J. Nordgren, P. Glans, L. Yang, Paweł Sałek, and Hans Ågren. Competition between decay and dissociation of core-excited carbonyl sulfide studied by x-ray scattering. *Physical Review A*, 59(6):4281–4287, 1999.

[121] T. H. Maiman. Stimulated Optical Radiation in Ruby. *Nature*, 187(4736):493–494, 1960.

[122] Toshio Masuoka. Dissociation dynamics of doubly- and triply-charged molecules studied by the triple photoelectron-photoion-photoion coincidence method. *Journal of Chemical Physics*, 98(9):6989–6994, 1993.

[123] Toshio Masuoka and Hiroyuki Doi. Single-, double-, and triple-photoionization cross sections of carbonyl sulfide (OCS) and ionic fragmentation of OCS+, OCS2+, and OCS3+. *Phys. Rev. A*, 47(1):278–288, 1993.

[124] Toshio Masuoka and Inosuke Koyano. Dissociative single, double , and triple photoionization of OCS in the region hv = 20-100 eV studied by mass spectrometry and the photoion-photoion coincidence method. *Journal of Chemical Physics*, 95(2):909–917, 1991.

[125] Toshio Masuoka, Inosuke Koyano, and Norio Saito. Kinetic-energy release in the dissociative double photoionization of OCS. *The Journal of Chemical Physics*, 97(4):2392–2399, 1992.

[126] Akitaka Matsuda, Mizuho Fushitani, Eiji J. Takahashi, and Akiyoshi Hishikawa. Visualizing hydrogen atoms migrating in acetylene dication by time-resolved three-body and four-body Coulomb explosion imaging. *Physical Chemistry Chemical Physics*, 13(19):8697, 2011.

[127] J. F. McCann and J. H. Posthumus. Molecular dynamics in intense laser fields. *Philosophical Transactions of the Royal Society A: Mathematical, Physical and Engineering Sciences*, 357:1309–1329, 1999.

[128] B. K. McFarland, J. P. Farrell, P. H. Bucksbaum, and M. Guhr. High Harmonic Generation from Multiple Orbitals in N_2. *Science*, 322(5905):1232–1235, 2008.

[129] G G Meisels. Radiolysis of Ethylene. IV. Unimolecular Dissociation of Intermediate Ion-Molecule Complexes. *The Journal of Chemical Physics*, 42(7):2328–2334, 1965.

[130] R. J Dwayne Miller, Ralph Ernstorfer, Maher Harb, Meng Gao, Christoph T. Hebeisen, Hubert Jean-Ruel, Cheng Lu, Gustavo Moriena, and German Sciaini. Making the molecular movie: First frames. *Acta Crystallographica Section A: Foundations of Crystallography*, 66(2):137–156, 2010.

[131] P Millie, I Nenner, P Archirel, P Lablanquie, P Fournier, and J H D Eland. Theoretical and experimental studies of the triatomic doubly charged ions CO_2^{2+}, OCS^{2+}, CS_2^{2+}. *Journal of Chemical Physics*, 84(3):1259–1269, 1986.

[132] Tatsumi Mizogawa, Yohko Awaya, Yasuhito Isozumi, Rintaro Katano, Shin Ito, and Nobuhiro Maeda. New readout technique for two-dimensional position-sensitive detectors. *Nuclear Instruments and Methods in Physics Research, Section A: Accelerators, Spectrometers, Detectors and Associated Equipment*, 312(3):547–552, 1992.

[133] Tatsumi Mizogawa, Michiyuki Sato, and Yohko Awaya. Application of the "MBWC" two-dimensional position readout technique to a multiwire proportional counter. *Nuclear Instruments and Methods in Physics Research, Section A: Accelerators, Spectrometers, Detectors and Associated Equipment Inst. and Methods in Physics Research, A*, 366(1):129–136, 1995.

[134] Yonezo Morino, Yoshikazu Kikuchi, Shuji Saito, and Eizi Hirota. Equilibrium Structure and Potential Function of Sulfur Dioxide from the Microwave Spectrum in the-Excited Vibrational State. *Journal of Molecular Spectrocopy*, 13:95–118, 1964.

[135] I Nenner and P. Morin. Electronic and nuclear relaxaction of core-excited molecules. In U Becker and D Shirley, editors, *VUV and Soft X-Ray photoionization*, pages 291–354. Springer US, 1996.

[136] N. Neumann, D. Hant, L. Ph H Schmidt, J. Titze, T. Jahnke, A. Czasch, M. S. Schöffler, K. Kreidi, O. Jagutzki, H. Schmidt-Böcking, and R. Dörner. Fragmentation dynamics of CO_2^{3+} investigated by multiple electron capture in collisions with slow highly charged ions. *Physical Review Letters*, 104(10):1–4, 2010.

[137] John J. Neville, Tolek Tyliszczak, and Adam P. Hitchcock. Photofragmentation of OCS at the S 1s edge. *Journal of Electron Spectroscopy and Related Phenomena*, 101-103:119–124, 1999.

[138] Amos S Newton. Triple Ionization in Small Molecules. *Journal of Chemical Physics*, 40(607):607–608, 1964.

[139] Hiromichi Niikura, F Légaré, R Hasbani, a D Bandrauk, Misha Yu Ivanov, D M Villeneuve, and P B Corkum. Sub-laser-cycle electron pulses for probing molecular dynamics. *Nature*, 417(6892):917–922, 2002.

[140] J. Niskanen, V. Carravetta, O. Vahtras, H. Ågren, H. Aksela, E. Andersson, L. Hedin, P. Linusson, J. H D Eland, L. Karlsson, J. E. Rubensson, and R. Feifel. Experimental and theoretical study of core-valence double photoionization of OCS. *Physical Review A - Atomic, Molecular, and Optical Physics*, 82(4):1–10, 2010.

[141] M. Nisoli, S. De Silvestri, and O. Svelto. Generation of high energy 10 fs pulses by a new pulse compression technique. *Applied Physics Letters*, 68(20):2793–2795, 1996.

[142] M. Nisoli, S. De Silvestri, O. Svelto, R. Szipöcs, K. Ferencz, Ch. Spielmann, S. Sartania, and F. Krausz. Compression of high-energy laser pulses below 5 fs. *Optics Letters*, 22(8):522–524, 1997.

[143] Peng Peng, Shichang Peng, Hongtao Hu, Na Li, Ya Bai, Peng Liu, HuaiLiang Xu, Ruxin Li, and Zhizhan Xu. Intensity-dependent study of strong-field Coulomb explosion of H_2. *Optics Express*, 23(14):18763, 2015.

[144] Emmanuel Penka Fowe and Andre D. Bandrauk. Nonperturbative time-dependent density-functional theory of ionization and harmonic generation in OCS and CS_2 molecules with ultrashort intense laser pulses: Intensity and orientational effects. *Physical Review A - Atomic, Molecular, and Optical Physics*, 84(3):1–5, 2011.

[145] A. M. Perelomov, V. S. Popov, and M. V. Terent'ev. Ionization of atoms in an alternating electric field. *Soviet Physics JETP*, 23(5):924–934, 1966.

[146] M. Pitzer, M. Kunitski, A. S. Johnson, T. Jahnke, H. Sann, F. Sturm, L. P. H. Schmidt, H. Schmidt-Bocking, R. Dorner, J. Stohner, J. Kiedrowski, M. Reggelin, S. Marquardt, A. Schiesser, R. Berger, and M. S. Schoffler. Direct Determination of Absolute Molecular Stereochemistry in Gas Phase by Coulomb Explosion Imaging. *Science*, 341(6150):1096–1100, 2013.

[147] Martin Pitzer, Gregor Kastirke, Maksim Kunitski, Till Jahnke, Tobias Bauer, Christoph Goihl, Florian Trinter, Carl Schober, Kevin Henrichs, Jasper Becht, Stefan Zeller, Helena Gassert, Markus Waitz, Andreas Kuhlins, Hendrik Sann, Felix Sturm, Florian Wiegandt, Robert Wallauer, Lothar Ph H Schmidt, Allan S. Johnson, Manuel Mazenauer, Benjamin Spenger, Sabrina Marquardt, Sebastian Marquardt, Horst Schmidt-B??cking, J??rgen Stohner, Reinhard D??rner, Markus Sch??ffler, and Robert Berger. Absolute Configuration from Different Multifragmentation Pathways in Light-Induced Coulomb Explosion Imaging. *ChemPhysChem*, 17:2465–2472, 2016.

[148] J. H. Posthumus, L. J. Frasinski, A. J. Giles, and K. Codling. Dissociative ionization of molecules in intense laser fields: a method of predicting ion kinetic energies and appearance intensities. *Journal of Physics B: Atomic, Molecular and Optical Physics*, 28:L349–L353, 1995.

[149] J H Posthumus, a J Giles, M R Thompson, and K Codling. Field-ionization, Coulomb explosion of diatomic molecules in intense laser fields. *Journal of Physics B: Atomic, Molecular and Optical Physics*, 29(23):5811–5829, 1996.

[150] A. W. Potts and T. A. Williams. The observation of "forbidden" transitions in He II photoelectron spectra. *Journal of Electron Spectroscopy and Related Phenomena*, 3(1):3–17, 1974.

[151] S D Price and J H D Eland. Single photon double ionization of the oxygen molecule. *J. Phys. B*, 24(20):4379–4389, 1991.

[152] Ali Ramadhan. *Molecular Movies and Geometry Reconstruction Using Coulomb Explosion Imaging*. PhD thesis, University of Waterloo, 2017.

[153] Ali Ramadhan, Benji Wales, Isabelle Gauthier, Reza Karimi, Michael MacDonald, Lucia Zuin, and Joe Sanderson. Molecular dynamics of dissociative ionization in OCS probed by soft X-ray synchrotron radiation. *Journal of Structural Chemistry*, 49(21):1–22, 2016.

[154] H Rottke, C Trump, and W Sandner. Multiphoton ionization and dissociation of H_2O. *Journal of Physics B: Atomic, Molecular and Optical Physics*, 31:1083–1096, 1998.

[155] C.P. Safvan and M.R. Jana. Fragmentation of OCS^{3+} formed by 150 keV Ar^+ ion impact on OCS. *Journal of Physics: Conference Series*, 388(1):012020, 2012.

[156] K Saha, S B Banerjee, and B Bapat. Dissociation of OCS upon various S(2p) Auger decay transitions. *Journal of Physics: Conference Series*, 488(10):102020, 2014.

[157] James A R Samson. Proportionality of electron-impact ionization to double photoionization. *Physical Review Letters*, 65(23):2861–2864, 1990.

[158] J. Sanderson, T. Nishide, H. Shiromaru, Y. Achiba, and N. Kobayashi. Near-Coulombic behavior in the dissociative ionization of CO2 due to impact by Ar8+. *Physical Review A*, 59(6):4817–4820, 1999.

[159] J. H. Sanderson, A. El-Zein, W. A. Bryan, W. R. Newell, A. J. Langley, and P. F. Taday. Geometry modifications and alignment of H_2O in an intense femtosecond laser pulse. *Physical Review A*, 59(4):R2567–R2570, 1999.

[160] J. H. Sanderson, T. R J Goodworth, A. El-Zein, W. A. Bryan, A. J. Langley, and P. F. Taday. Coulombic and pre-Coulombic geometry evolution of carbonyl sulfide in an intense femtosecond laser pulse, determined by momentum imaging. *Physical Review A. Atomic, Molecular, and Optical Physics*, 65(4):434031–434038, 2002.

[161] J H Sanderson, R V Thomas, W A Bryan, W R Newell, A J Langley, and P F Taday. Alignment and bending of CO_2 by intense femtosecond laser pulses. *Journal of Physics B: Atomic, Molecular and Optical Physics*, 31:L599–L606, 1998.

[162] J H Sanderson, R V Thomas, W A Bryan, W R Newell, I D Williams, A J Langley, and P F Taday. High-intensity femtosecond laser interactions with vibrationally excited CO_2. *Journal of Physics B: Atomic, Molecular and Optical Physics*, 31:L59–L64, 1998.

[163] Yukio Sato, Hirohiko Kono, Shiro Koseki, and Yuichi Fujimura. Description of molecular dynamics in intense laser fields by the time-dependent adiabatic state approach: Application to simultaneous two-bond dissociation of CO_2 and its control. *Journal of the American Chemical Society*, 125(26):8019–8031, 2003.

[164] Bruno E Schmidt, Waldemar Unrau, Aldo Mirabal, Shaohui Li, Marcel Krenz, Ludger Wöste, and Torsten Siebert. Poor man's source for sub 7 fs: a simple route to ultrashort laser pulses and their full characterization. *Optics Express*, 16(23):18910–18921, 2008.

[165] Tamar Seideman, M. Yu. Ivanov, and P. B. Corkum. Role of Electron Localization in Intense-Field Molecular Ionization. *Physical Review Letters*, 74(15):2819–2822, 1995.

[166] Sason Shaik. The Lewis Legacy: The Chemical Bond-A Territory and Heartland of Chemistry. *Journal of Computational Chemistry*, 28(1):51–61, 2007.

[167] T. K. Sham, B. X. Yang, J. Kirz, and J. S. Tse. K-edge near-edge x-ray-absorption fine structure of oxygen- and carbon-containing molecules in the gas phase. *Physical Review A*, 40(2):652–669, 1989.

[168] J. A. Sheehy and P. W. Langhoff. Photoionization of Carbonyl Sulfide: Threshold Resonance Features in Outer-Valence-Shell Partial Cross Sections. *Chemical Physics Letters*, 135(1):109–118, 1987.

[169] B. Siegmann, U. Werner, H.O. Lutz, and R. Mann. Complete Coulomb fragmentation of CO_2 in collisions with 5.9 MeV u^{-1} Xe^{18+} and Xe^{43+}. *Journal of Physics B: Atomic, Molecular and Optical Physics*, 35(17):3755–3765, 2002.

[170] N. Sivakumar, G. E. Hall, P. L. Houston, J. W. Hepburn, and I. Burak. Stateresolved photodissociation of OCS monomers and clusters. *The Journal of Chemical Physics*, 88(6):3692–3708, 1988.

[171] Olga Smirnova, Yann Mairesse, Serguei Patchkovskii, Nirit Dudovich, David Villeneuve, Paul Corkum, and Misha Yu. Ivanov. High harmonic interferometry of multi-electron dynamics in molecules. *Nature*, 460(7258):972–977, 2009.

[172] J F Stanton. CFOUR, a quantum chemical program package, 2014.

[173] Henrik Stapelfeldt, Hirofumi Sakai, Eric Constant, and Paul B. Corkum. Formation and measurement of molecular quantum picostructures. *Physical Review A*, 55(5):R3319–R3322, 1997.

[174] H C Straub, M A Mangan, B G Lindsay, K A Smith, and R F Stebbings. Absolute detection efficiency of a microchannel plate detector for kilo-electron volt energy ions. *Review Of Scientific Instruments*, 70(11):4238–4240, 1999.

[175] Donna Strickland and Gerard Mourou. Compression of amplified chirped optical pulses. *Optics Communications*, 56(3):219–221, 1985.

[176] Orazio Svelto. *Principles of Lasers*. Springer US, Boston, MA, 2009.

[177] Eiji J. Takahashi, Pengfei Lan, Oliver D. Mücke, Yasuo Nabekawa, and Katsumi Midorikawa. Attosecond nonlinear optics using gigawatt-scale isolated attosecond pulses. *Nature Communications*, 4:1–9, 2013.

[178] Dmitry A. Telnov and Shih I. Chu. Effects of electron structure and multielectron dynamical response on strong-field multiphoton ionization of diatomic molecules with arbitrary orientation: An all-electron time-dependent density-functional-theory approach. *Physical Review A - Atomic, Molecular, and Optical Physics*, 79(4):041401, 2009.

[179] P. Tzallas, E. Skantzakis, L. A. A. Nikolopoulos, G. D. Tsakiris, and D. Charalambidis. Extreme-ultraviolet pumpprobe studies of one-femtosecond-scale electron dynamics. *Nature Physics*, 7(10):781–784, 2011.

[180] Masakuni Ueyama, Hirokazu Hasegawa, Akiyoshi Hishikawa, and Kaoru Yamanouchi. Concerted and sequential Coulomb explosion processes of N_2O in intense laser fields by coincidence momentum imaging. *Journal of Chemical Physics*, 123(15):1–9, 2005.

[181] C A Ulrich and A D Bandrauk. Time-Dependent Density Funct. Theory SE. In M L Marques, editor, *Time-Dependent Density Funct. Theory SE*, pages 357–375. Springer Berlin Heidelberg, 2006.

[182] Z. Vager, E.P. Kanter, G. Both, P.J. Cooney, A. Faibis, W. Koenig, B.J. Zabransky, and D. Zajfman. Direct Determination of the Sterochemical Structure of CH_4^+. *Physical Review Letters*, 57(22):2793–2795, 1986.

[183] Z Vager, R Naaman, and E P Kanter. Coulomb Explosion Imaging of Small Molecules. *Science*, 244(4903):426–431, 1989.

[184] J van Tilborg, T K Allison, T W Wright, M P Hertlein, R W Falcone, Y Liu, H Merdji, and A Belkacem. Femtosecond isomerization dynamics in the ethylene

cation measured in an EUV-pump NIR-probe configuration. *Journal of Physics B: Atomic, Molecular and Optical Physics*, 42(8):081002, 2009.

[185] Giorgi Veshapidze, Tatsuhiro Nishide, Haruo Shiromaru, Nobuo Kobayashi, and Tatsumi Mizogawa. A time- and position-sensitive detector using a resistive film anode combined with a "modified backgammon with weighted capacitors" readout pad. *Japanese Journal of Applied Physics, Part 1: Regular Papers and Short Notes and Review Papers*, 41(2 A):871–875, 2002.

[186] D. Villeneuve, M. Ivanov, and P. Corkum. Enhanced ionization of diatomic molecules in strong laser fields: A classical model. *Physical Review A*, 54(1):736–741, 1996.

[187] C. Vozzi, M. Negro, F. Calegari, G. Sansone, M. Nisoli, S. De Silvestri, and S. Stagira. Generalized molecular orbital tomography. *Nature Physics*, 7(10):822–826, 2011.

[188] B Wales, R Karimi, E Bisson, S Buleau, M Giguère, T Motojima, R Anderson, J Matsumoto, J-C Kieffer, F Légaré, H Shiromaru, and J Sanderson. Comparing Coulomb explosion dynamics of multiply charged triatomic molecules after ionization by highly charged ion impact and few cycle femtosecond laser pulses. *Physica Scripta*, T156:014068, 2013.

[189] Benji Wales, Eric Bisson, Reza Karimi, Samuel Beaulieu, Ali Ramadhan, Mathieu Giguère, Zijian Long, Wing Ki Liu, Jean Claude Kieffer, Francois Légaré, and Joseph Sanderson. Coulomb imaging of the concerted and stepwise break up processes of OCS ions in intense femtosecond laser radiation. *Journal of Electron Spectroscopy and Related Phenomena*, 195:332–336, 2014.

[190] Benji Wales, Eric Bisson, Reza Karimi, Jean Claude Kieffer, Francois Légaré, and Joseph Sanderson. A coincidence detection algorithm for improving detection rates in coulomb explosion imaging. *Nuclear Instruments and Methods in Physics Research, Section A: Accelerators, Spectrometers, Detectors and Associated Equipment*, 667:11–15, 2012.

[191] Benji Wales, Tomonori Motojima, Jun Matsumoto, ZiJian Long, Wing-Ki Liu, Haruo Shiromaru, and Joseph Sanderson. Multiple ionization and complete fragmentation of OCS by impact with highly charged ions Ar^{4+} and Ar^{8+} at 15 keV q^{-1}. *Journal of Physics B: Atomic, Molecular and Optical Physics*, 45(4):045205, 2012.

[192] Lai Sheng Wang, J. E. Reutt, Y. T. Lee, and D. A. Shirley. High resolution UV photoelectron spectroscopy of CO_2^+, COS^+ and CS_2^+ using supersonic molecular beams. *Journal of Electron Spectroscopy and Related Phenomena*, 47(C):167–186, 1988.

[193] Julia A. Weinstein and Neil T. Hunt. Ultrafast chemical physics: In search of molecular movies. *Nature Chemistry*, 4(3):157–158, 2012.

[194] E Wells, C E Rallis, M Zohrabi, R Siemering, Bethany Jochim, P R Andrews, U Ablikim, B Gaire, S De, K D Carnes, B Bergues, R de Vivie-Riedle, M F Kling, and I Ben-Itzhak. Adaptive strong-field control of chemical dynamics guided by three-dimensional momentum imaging. *Nature communications*, 4:2895, 2013.

[195] H J Worner, J B Bertrand, D V Kartashov, P B Corkum, and D M Villeneuve. Following a chemical reaction using high-harmonic spectroscop. *Nature*, 466(7306):604–607, 2010.

[196] C. Y. Robert Wu and D. L. Judge. Study of sulfurcontaining molecules in the EUV region. II. Photoabsorption cross section of COS. *The Journal of Chemical Physics*, 76(6):2871–2874, 1982.

[197] Huailiang Xu, Tomoya Okino, Katsunori Nakai, Kaoru Yamanouchi, Stefan Roither, Xinhua Xie, Daniil Kartashov, Li Zhang, Andrius Baltuska, and Markus Kitzler. Two-proton migration in 1,3-butadiene in intense laser fields. *Physical chemistry chemical physics : PCCP*, 12(40):12939–42, 2010.

[198] F. Yergeau, S. L. Chin, and P. Lavigne. Multiple ionization of rare-gas atoms by an intense CO_2 laser (10^{14}Wcm^{-2}). *Journal of Physics B: Atomic, Molecular and Optical Physics*, 19, 1986.

[199] D. Zeidler, A. Staudte, A. B. Bardon, D. M. Villeneuve, R. Dörner, and P. B. Corkum. Controlling attosecond double ionization dynamics via molecular alignment. *Physical Review Letters*, 95(20):1–4, 2005.

[200] A. H. Zewail. Femtochemistry: Atomic-Scale Dynamics of the Chemical Bond Using Ultrafast Lasers (Nobel Lecture). In *Femtochemistry*, pages 1–73. Wiley-VCH Verlag GmbH, 2001.

[201] A. H. Zewail. Four-Dimensional Electron Microscopy. *Science*, 328(5975):187–193, 2010.

[202] A. M. Zheltikov. Keldysh parameter, photoionization adiabaticity, and the tunneling time. *Physical Review A - Atomic, Molecular, and Optical Physics*, 94(4):1–6, 2016.

[203] T. Zuo and A. D. Bandrauk. Charge-resonance-enhanced ionization of diatomic molecular ions by intense lasers. *Physical Review A*, 52(4):R2511–R2514, 1995.

[204] T. S. Zyubina, Y. A. Dyakov, S. H. Lin, A. D. Bandrauk, and A. M. Mebel. Theoretical study of isomerization and dissociation of acetylene dication in the ground and excited electronic states. *Journal of Chemical Physics*, 123(13), 2005.

APPENDICES

Appendix A

Data Analysis

A.1 Calibration and Optimization

In calculating the 3D momenta of ionic fragments from the momentum equations 2.6, 2.7, and 2.8, a few assumptions are made. The first assumptions is that ions are produced instantaneously on a timescale much shorter than the TOF resolution. The second is that the location of the ionization occur in a volume with dimensions smaller than what is resolvable by the PSD.[1] These assumptions are met sufficiently with the current state of PSD sensitivity in both space and time.

In calculating the expected zero TOF using equation 2.5, several physical parameters are needed. Since the ionization distance d is often difficult to measure (and may vary from experiment to experiment), it is easier to *measure* the zero TOF of several ionic species, plot the relationship between t_0 and $\sqrt{m/q}$, perform a linear fit, and use these fit parameters as system calibrations. The calculation for the zero-time-of-flight after calibration then follows Equation A.1 where T_{scale} encodes the apparatus geometry and extraction field and T_{shift} accounts for time delays in the electrical signals initiating ionization and ion detection.

$$t_{0,m,q} = T_{scale}\sqrt{\frac{m}{q}} + T_{shift} \tag{A.1}$$

[1] In the chapter on ethylene, a fragmentation process with a lifetime much longer than the TOF resolution is measured. Despite not strictly measuring the 3D momentum, interesting physics can still be gleamed in this CEI experiment.

A.2 Newton Plot

The Newton plot is an effective tool for visualizing momentum vector distributions measured in coincident 3-ion CEI experiments. Effectively, the distribution resolves the momentum vectors in the molecular frame. In this representation, the orientation of each momentum vector relative to one another is conserved, while information on the orientation of each momentum vector with respect to the lab frame is lost. Since the momentum vectors are measured from fragmentations yielding zero-momentum sum, 3-ion momentum vectors are planar, and therefore result in a 2D distribution. For this same reason, 2-ion coincident measurements require a 1D distribution, and 4-ion require a 3D distribution. Only the 3-ion case is considered here.

The rotation of 3 momentum vectors out of the 3D lab frame and into the 2D molecular frame is trivial. Before doing so, a polar axis must be chosen to define the orientation of molecular-frame vectors. It is customary (though not necessary) to use one of the fragment momentum vectors as a polar reference. Since there are three to chose from, it is best practice to create Newton plots in triplet, where each fragment is used as a reference. Generally, the plot that is easiest to interpret is that where the heaviest terminal ion is used as the reference (such as S^+ in OCS^{n+} fragmentation) due to the limited distribution in momentum imparted on such ions.

Once the reference vector has been selected, it is customary, though not necessary, to plot the reference vector along the positive x or $y-$axis. The momenta for the other two vectors are rotated into the plane of the 2D distribution with a specified handedness such that one vector necessarily appears on the one side, while the other on its opposite. A sample of data plotted in this manner and a schematic indicating the regions for each ion momentum vector is shown in Figure A.1.

The histogram resulting from this plotting scheme is in fact 3 overlaid distributions. Since the reference vector is locked into a linear space, it doesn't resolve anything meaningful and is often left out, leaving behind just two momentum distributions (though it is plotted in Figure A.1 for completeness). By leaving out the reference distribution, there is some ambiguity built into these distributions. To solve this problem, a second Newton plot exists: the normalized Newton plot (shown in Figure A.2). Such plots are created by first following the same algorithm as before for rotating the vectors into place, then normalizing the magnitudes of each vector before building the histogram. The magnitude of each vector is scaled such that the reference vector's magnitude is unity. Again, the reference vector is not plotted as it would yield a single, high value dot along the x or $y-$axis. The other two vectors are plotted normally. The interpretation of these plots is made easy. Since

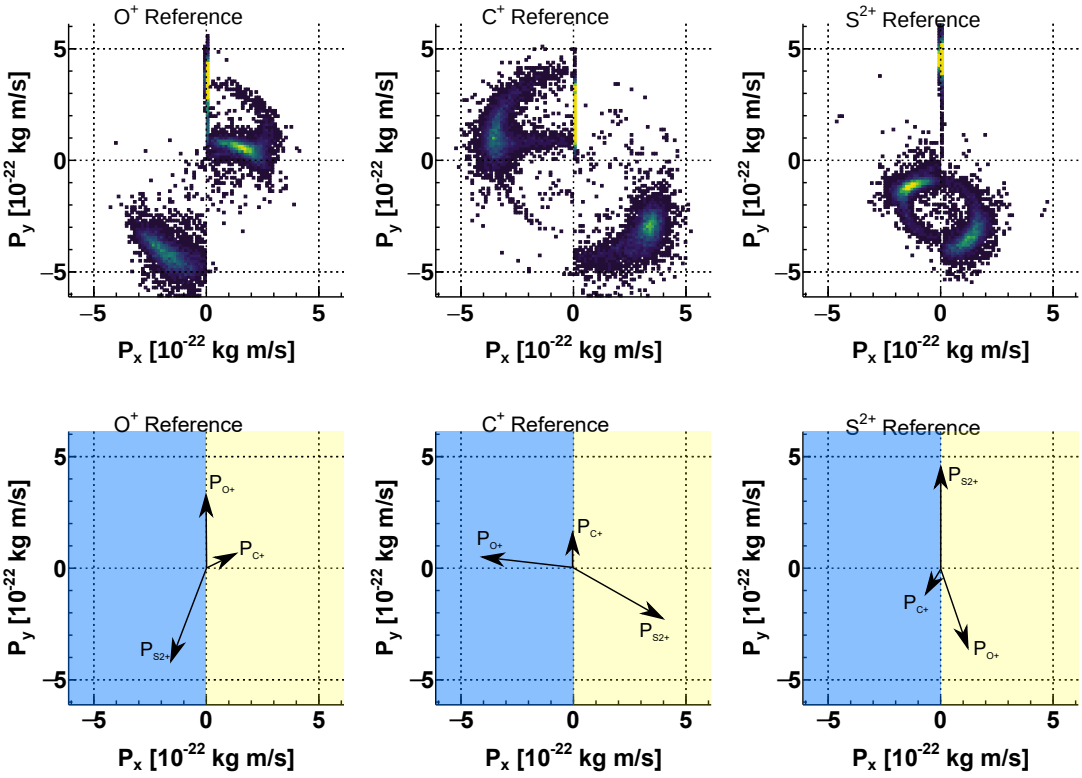

Figure A.1: [TOP ROW] Newton plots for the 3-ion channel $OCS^{4+} \longrightarrow O^+ + C^+ + S^{2+}$. Each histogram is an overlay of 3 distributions. The colour scale is over-saturated for the reference momentum vector (along the y-axis) in order to highlight the signal from the other two vectors. [BOTTOM ROW] Schematic of Newton plot. Reference ion momentum is plotted along y-axis; other two momentum vectors are rotated into the left and right halves respectively.

the momentum vector of the reference ion is known ($\vec{p} = 1[au]\hat{j}$ in the examples shown), any point in the momentum space for the second ion *determines* the coincident point in the momentum space of the third ion since the three momentum vectors must equate to zero. Examples of this type of normalized Newton plot along with schematics are shown in Figure A.2.

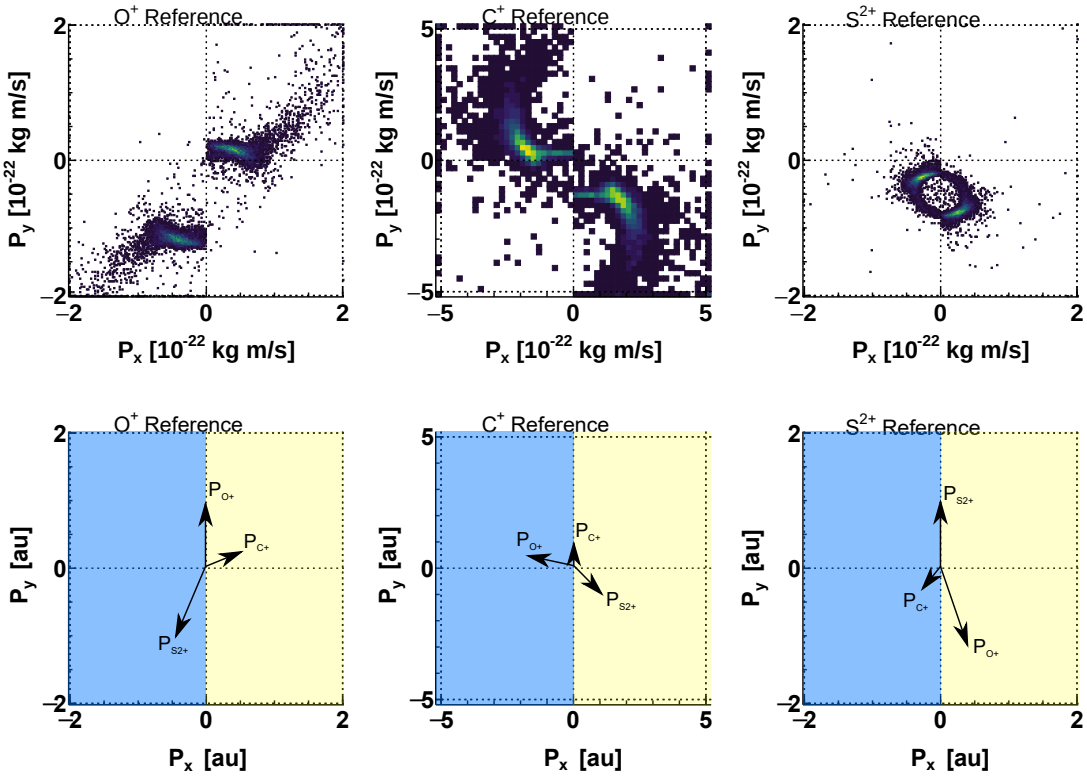

Figure A.2: [TOP ROW] Normalized Newton plots for the 3-ion channel $OCS^{4+} \longrightarrow O^+ + C^+ + S^{2+}$. Each histogram is an overlay of 2 distributions. The reference vector is not shown (but would resolve a single peak at $(0, 1)$). Note the arbitrary axis units and scales. [BOTTOM ROW] Schematic of Normalized Newton plot. Reference ion momentum is plotted along y-axis; other two momentum vectors are rotated into the left and right halves respectively.

A.3 Dalitz Plot

The Dalitz plot is an effective tool for displaying coincident triple particle data in a 2D histogram. It was developed by Richard Henry Dalitz [42] for use in particle physics experiments and has recently been popularized in CEI experiments due to the similarity in the nature of their coincidence measurements.

The Dalitz plot has two representations: one in momentum space and one in energy space. The latter has been implemented in the research here, but the former is also used in this field. The phenomena that can be resolved by both tools appears to be the same, only the shape by which they manifest in the plot differs. Here, the energy plot will be considered.

To create a Dalitz plot, the fragment and total KER of triple coincidences needs to be calculated. Then, the fractional energy of each fragment is calculated. Taking for example the channel $OCS^{3+} \longrightarrow O^+ + C^+ + S^+$, the fractional energies would be $\epsilon_{O^+} = KER_{O^+}/KER_{OCS^{3+}}$, $\epsilon_{C^+} = KER_{C^+}/KER_{OCS^{3+}}$, and $\epsilon_{S^+} = KER_{S^+}/KER_{OCS^{3+}}$. The Dalitz energy distribution is created by plotting the fractional energy from the gemoetrically central fragment along the $y-$axis and the difference between the terminal fragments along the $x-$axis. A shift in the $y-$values and a scaling of the $x-$values is also done to be consistent with previous work [136], but is not necessary.

An example of the resulting 2D histogram is shown right in Figure A.3. The phase space is bound by an oval, a result of the strict zero-momentum-sum condition. Events that appear outside this region therefore indicates incomplete energy measurements. Furthermore, each location coordinate within this space has with it an associated orientation of momentum vectors (shown left in Figure A.3). Similar to the Normalized Newton plots described in A.2, each set of 3 momentum vectors maintain only the magnitudes and directions relative to each other, with the absolute magnitudes and directions relative to the lab-frame lost.

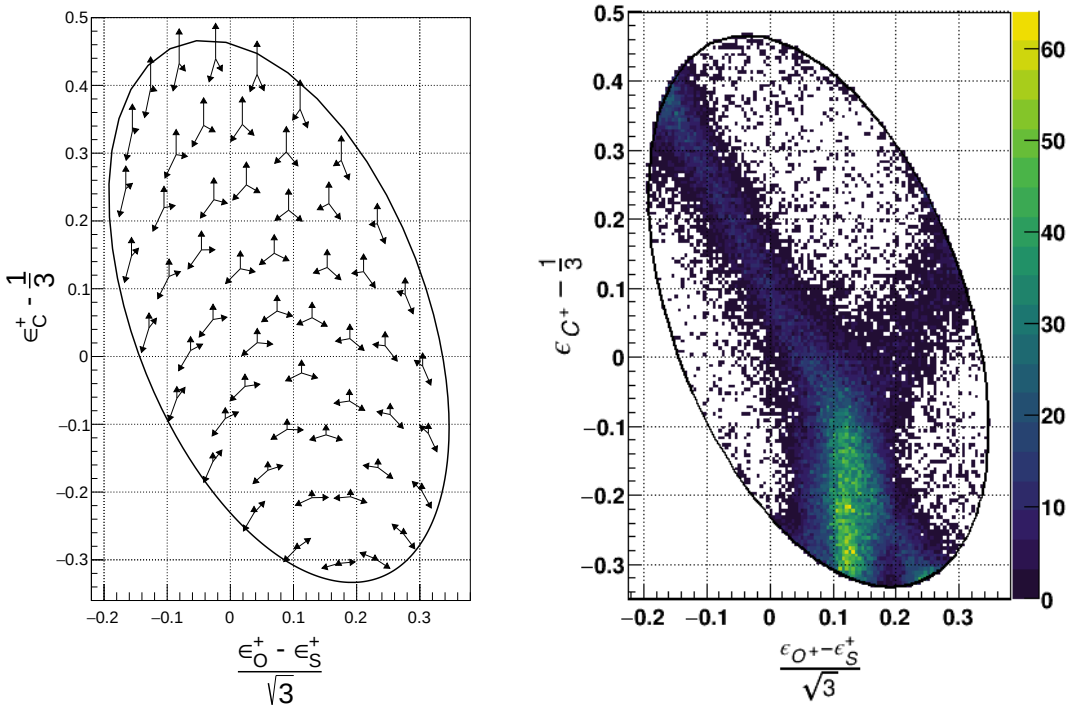

Figure A.3: [LEFT] Schematic of Dalitz Plot for the 3-ion channel $OCS^{3+} \longrightarrow O^+ + C^+ + S^+$, showing sample sets of momentum vectors at specific coordinates. [RIGHT] Sample data from the same channel

Appendix B

Additional CEI Apparatus Elements

B.1 Mirror Mount

For future CEI experiments at UW, a 1 cm f=10 cm focusing mirror will be used to initiate ionization on a super sonic beam gas target. This mirror is mounted to an XYZ stage similar to that used in the CLS experiments. To reduce the perturbing effect of this metallic element on the extraction field, it is biased to the average voltage between the plates it sits closest to. Since the XYZ stage is itself grounded, the mirror mount was additionally designed to be electrically insulated. The final design (and its Computer Aided Design (CAD) mock-ups) are shown in the following figures. The vacuum compatible materials used are teflon, copper, and stainless steel.

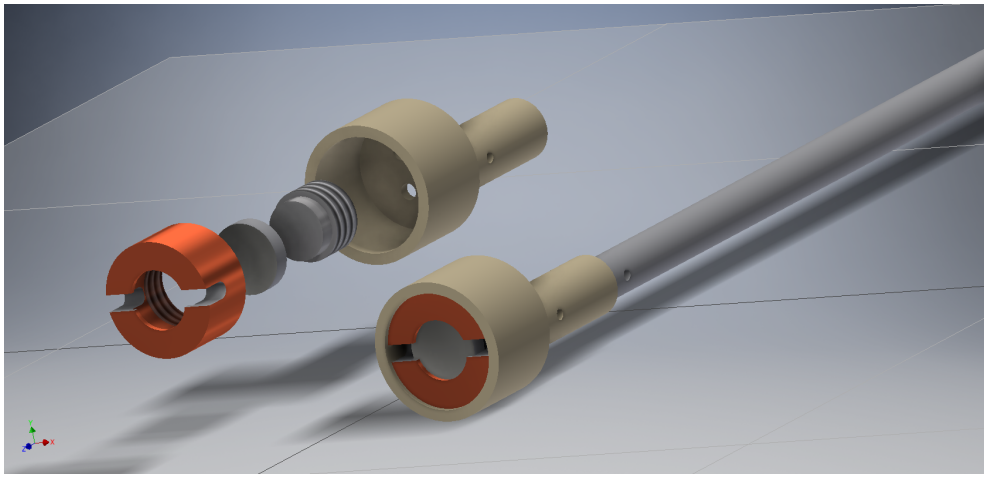

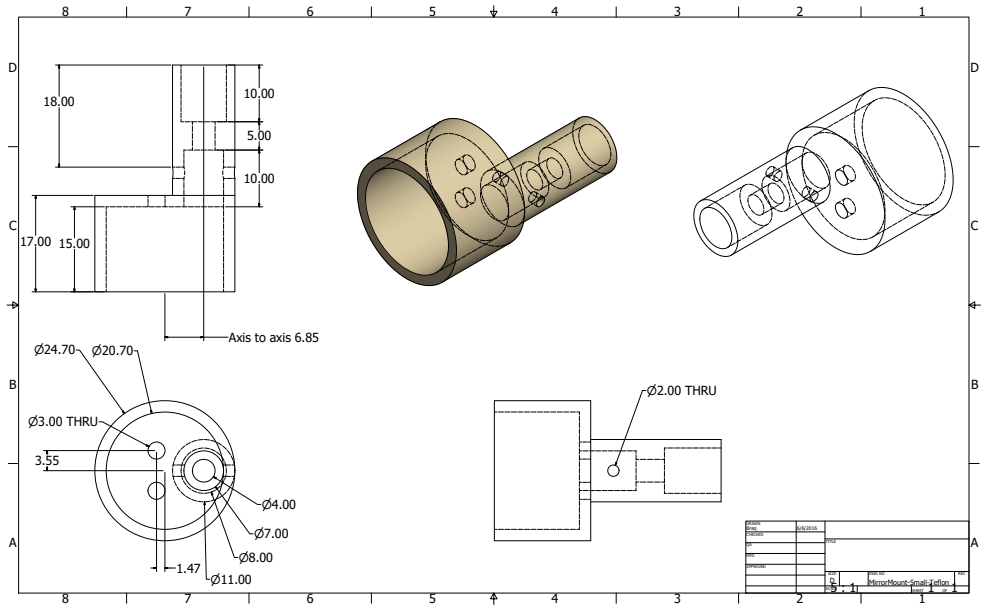
18.00
10.00
5.00
10.00
17.00
15.00
Axis to axis 6.85
Ø24.70
Ø20.70
Ø3.00 THRU
3.55
Ø4.00
Ø7.00
Ø8.00
1.47
Ø11.00
Ø2.00 THRU
MirrorMount-Small-Teflon

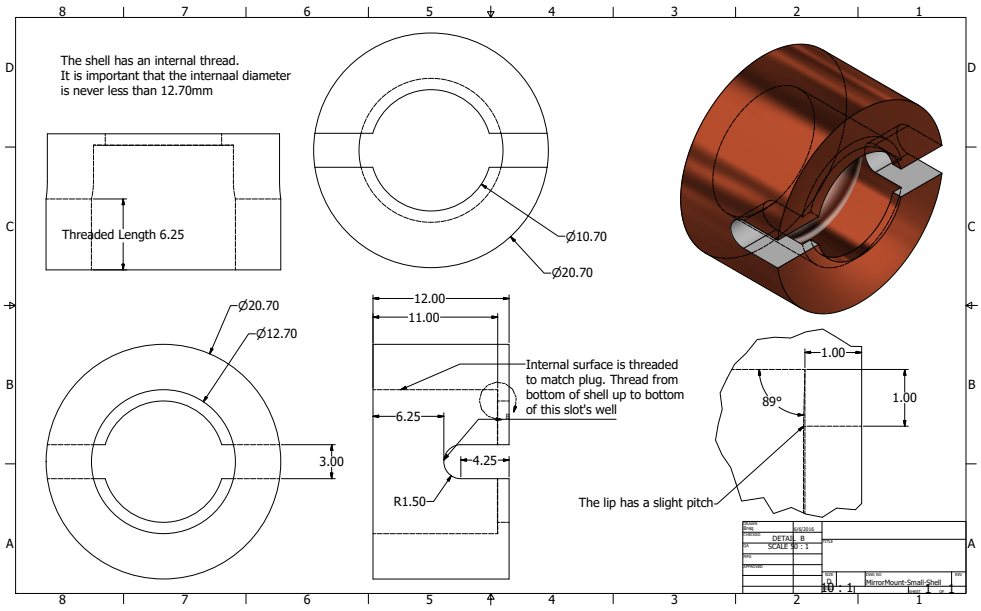
The shell has an internal thread.
It is important that the internaal diameter
is never less than 12.70mm
Threaded Length 6.25
Ø10.70
Ø20.70
Ø20.70
Ø12.70
3.00
12.00
11.00
Internal surface is threaded
to match plug. Thread from
bottom of shell up to bottom
of this slot's well
6.25
4.25
R1.50
1.00
89°
1.00
The lip has a slight pitch
DETAIL B
SCALE 50 : 1
MirrorMount-Small-Shell
10 : 1

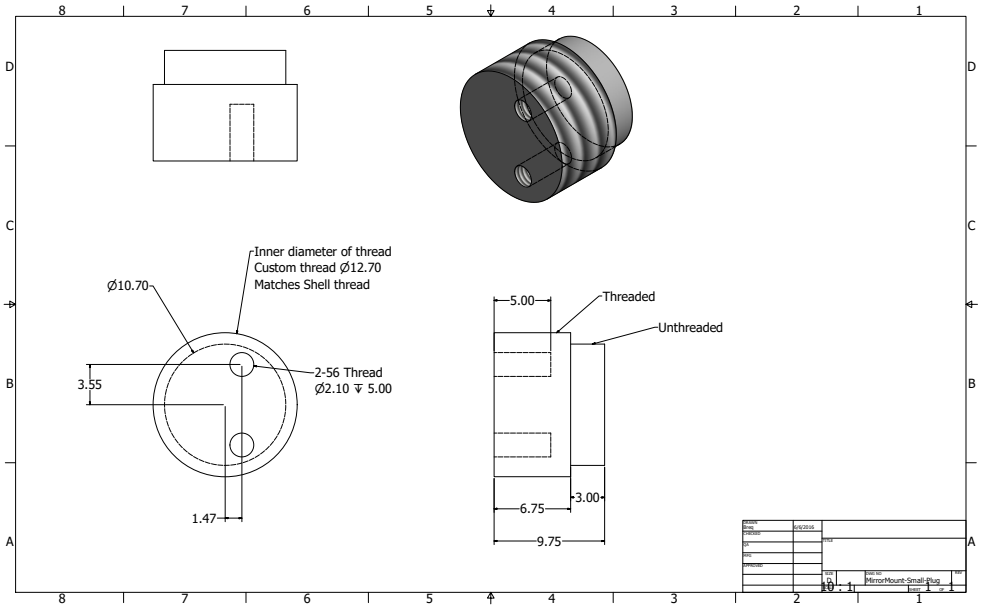
Inner diameter of thread
Custom thread Ø12.70
Matches Shell thread
Ø10.70
2-56 Thread
Ø2.10 ↧ 5.00
3.55
1.47
5.00
Threaded
Unthreaded
3.00
6.75
9.75
MirrorMount-Small-Plug
10 : 1